



# UNIVERSITÀ DEGLI STUDI DI PADOVA

Dipartimento di Ingegneria Industriale

SCUOLA DI DOTTORATO DI RICERCA IN  
SCIENZA E INGEGNERIA DEI MATERIALI

XXVI CICLO

## INNOVATIVE PATTERNABLE MATERIALS FOR MICRO- AND NANO- FABRICATION

**Direttore della Scuola:** Ch.mo Prof. Gaetano Granozzi

**Supervisore:** Prof.ssa Giovanna Brusatin

**Dottoranda:** ERIKA ZANCHETTA



*To my special  
and amazing family*

*“Slipping through my fingers all the time  
I try to capture every minute  
The feeling in it  
Slipping through my fingers all the time  
Do I really see what's in her mind  
Each time I think I'm close to knowing  
She keeps on growing  
Slipping through my fingers all the time”*





# CONTENTS

<b>ABSTRACT .....</b>	<b>9</b>
<b>ESTRATTO .....</b>	<b>11</b>
<b>INTRODUCTION.....</b>	<b>13</b>
<b>CHAPTER 1 LITHOGRAPHIC TECHNIQUES FOR MICRO- AND NANO- FABRICATION..</b>	<b>19</b>
1.1. TRADITIONAL LITHOGRAPHIC PROCESS VS DIRECT PATTERNING.....	20
1.1.1. <i>Pattern transfer</i> .....	23
1.1.2. <i>Metallic or ceramic etching masks</i> .....	26
1.1.3. <i>Direct patterning</i> .....	29
1.2. UV LITHOGRAPHY (UVL OR PHOTOLITHOGRAPHY).....	30
1.3. X-RAY LITHOGRAPHY (XRL) .....	35
1.4. ELECTRON BEAM LITHOGRAPHY (EBL).....	37
1.4.1. <i>Elements of electron optics</i> .....	38
1.4.2. <i>Electron beam Physics</i> .....	40
1.5. NANOIMPRINT LITHOGRAPHY (NIL).....	42
<b>CHAPTER 2 INTRODUCTION TO MATERIALS FOR MICRO- AND NANO- LITHOGRAPHY: FROM ORGANIC TO COMPLETELY INORGANIC RESISTS.....</b>	<b>53</b>
2.1. PHOTORESISTS: A SURVEY .....	54
2.2. TRADITIONAL PHOTORESISTS - ORGANIC RESISTS .....	61
2.3. INORGANIC RESISTS.....	72
2.4. HYBRID ORGANIC-INORGANIC MATERIALS .....	74
2.4.1. <i>Hybrid organic-inorganic resists</i> .....	79
2.5. NIL RESISTS .....	86
<b>CHAPTER 3 TITANIA BASED SYSTEMS AS HIGH REFRACTIVE INDEX RESISTS.....</b>	<b>95</b>
3.1. LITERATURE BACKGROUND: TiO <sub>2</sub> SOL-GEL SYNTHESIS STARTING FROM TITANIUM ALKOXIDES .....	96
3.2. SYNTHESIS OF TWO TITANIA BASED MATERIALS: IN AND EX-SITU .....	103
3.2.1. <i>Materials and methods</i> .....	104
3.3. CHARACTERIZATION OF THE SYNTHESIZED EX-SITU AND IN-SITU SOL-GEL MATERIALS .....	108
3.3.1. <i>UV-Vis characterization</i> .....	109
3.3.2. <i>FTIR characterization</i> .....	110
3.3.3. <i>Rutherford back scattering RBS</i> .....	120
3.3.4. <i>DTA/TGA and DSC</i> .....	121
3.3.5. <i>Rheology of in-situ and ex-situ films</i> .....	122

3.3.6. Crystalline structures of ex-situ and in-situ films after UV and thermal treatments: XRD and TEM characterization .....	124
3.4. FROM MICRO- TO NANO- LITHOGRAPHY .....	127
3.5. UV LITHOGRAPHY .....	128
3.5.1. Chemical understanding of the double tone processes of in-situ system .....	134
3.6. NANOIMPRINT LITHOGRAPHY .....	137
3.6.1. FTIR and ellipsometric characterization of nanoimprint process .....	138
3.6.2. Nanoimprint lithography of in-situ and ex-situ films .....	141
<b>CHAPTER 4 HIGH SELECTIVE ETCHING MASKS: ALUMINA BASED RESIST .....</b>	<b>153</b>
4.1. ALUMINA RESIST SYNTHESIS .....	157
4.2. CHARACTERIZATION .....	157
4.2.1. Characterization of the as deposited alumina-based resist .....	158
4.2.2. Characterization of the thermally treated alumina-based resist .....	160
4.2.3. Characterization of the alumina-based resist exposed to UV or X-rays .....	161
4.3. UV LITHOGRAPHY .....	163
4.3.1. Chemical modification of alumina system during lithographic process .....	165
4.3.2. Chemical understanding of the double tone processes of alumina system .....	168
4.4. X-RAYS LITHOGRAPHY .....	170
4.5. EBL .....	172
4.5.1. First lithographic results .....	172
4.5.2. Casino® simulations .....	173
4.5.3. Optimized lithographic results .....	175
4.6. NANOIMPRINT LITHOGRAPHY .....	177
4.7. ETCHING RESISTANCE TESTS .....	178
<b>CHAPTER 5 ZIRCONIA BASED MATERIALS FOR ADAPTIVE OPTICS AND STEM CELLS DIFFERENTIATION DEVICES .....</b>	<b>185</b>
5.1. SYNTHESIS AND CHARACTERIZATION OF TWO ZR- BASED MATERIALS: PHOTSENSITIVE AND THERMOSETTING RESISTS .....	186
5.1.1. Synthesis of GZ system .....	187
5.1.2. GZ characterization .....	188
5.1.3. Synthesis of TMSPM-Zr system .....	193
5.1.4. TMSPM-Zr characterization .....	194
5.2. ADAPTIVE OPTICS DEVICES: FABRICATION AND TESTS .....	200
5.2.1. Introduction .....	200
5.2.2. Deformable gratings .....	204
5.2.3. Digital grating .....	207
5.2.4. Blazed grating .....	215
5.3. MICRO- AND NANO- INSERTS FOR MICRO- INJECTION MOULDING .....	219

5.3.1. Stamp inserts realization .....	221
5.3.2. Stamp replication with micro-injection moulding technique.....	225
5.3.3. Mesenchymal Stem Cells (MSC) differentiation: literature background.....	228
5.3.4. Mesenchymal Stem Cells (MSC) growth and differentiation on PS micro and nano patterned replica.....	233
<b>CONCLUSIONS .....</b>	<b>241</b>
<b>FUTURE PERSPECTIVES .....</b>	<b>245</b>
A) ONGOING EXPERIMENTS ON TITANIA AND ALUMINA SYSTEMS .....	245
B) PATTERNING OF SMART POROUS MATERIAL.....	247
<b>ACKNOWLEDGMENTS .....</b>	<b>253</b>



## *Abstract*

The research activity of this thesis is focused on the development and optimization of new directly patternable organically modified TiO<sub>2</sub>, Al<sub>2</sub>O<sub>3</sub> and ZrO<sub>2</sub> based sol-gel materials whose peculiar characteristics and performances were optimized and exploited for the final specific application.

In particular, the main strategy that lies at the basis of all the thesis work is the combination of top down and- bottom up approach for the final device realization. In fact, special attention has been set to materials design and synthesis (bottom up) and subsequently to the micro- and nano- fabrication of patterns on the corresponding film surface with different lithographic techniques (top down) in order to achieve the required properties, according to the final application.

As it concerns the *bottom up approach*, the sol-gel has been assumed as the main synthetic method since, by mixing different organic-inorganic precursors, new materials with unique properties and microstructures can be created. In fact, by using organically modified precursors (such as trimethoxyphenylsilane, 3-glycidoxypropyltrimethoxysilane, 3-(Trimethoxysilyl)propyl methacrylate) or organic monomers it was possible to produce hybrid materials with the organic and inorganic components intimately mixed at a molecular scale, with the twofold effect of obtaining new properties and conferring them the patternability. Moreover, the addition of tetrafunctional precursors (Titanium isopropoxide, Zirconium butoxide, Aluminum-tri-sec-butoxide) allowed to increase the reticulation degree, taking part to the inorganic network formation, to improve the material mechanical properties (such as scratch, abrasion, plasma etching resistance) and to confer particular characteristics to the final materials, i.e. to modulate the refractive index.

On the other hand, as it regards the *top down approach*, different lithographic techniques (photolithography, X-ray lithography, electron beam lithography and nanoimprint lithography) have been exploited in the realization of high refractive index patterns, high selective etching masks features, adaptive-optics devices and stamps for microinjection moulding directly with the synthesized materials. The structural and chemical changes induced inside the material by the interactions with the source used in the lithographic process

have been deeply investigated in order to optimize both the synthesis of the best sol-gel systems and the final lithographic procedures.

In conclusion the development of all the above mentioned advanced materials and innovative processing was pushed by the main target of improving, simplifying and decreasing costs and time of the overall micro- and nano- fabrication process in order to obtain better final features quality, with respect to traditional lithographic procedures.

## *Estratto*

L'attività di ricerca del presente lavoro di tesi è stata finalizzata allo sviluppo e all'ottimizzazione di nuovi materiali sol-gel a base di ossidi di  $\text{TiO}_2$ ,  $\text{Al}_2\text{O}_3$  e  $\text{ZrO}_2$ , organicamente modificati, per diverse applicazioni, sfruttando alcune delle loro caratteristiche peculiari e ottimizzandone le prestazioni.

Nella fase iniziale del lavoro particolare attenzione è stata rivolta alla sintesi e all'ingegnerizzazione dei materiali stessi (approccio bottom up). Nella fase successiva i materiali sviluppati sono stati micro- e nano- strutturati mediante tecniche litografiche differenti (approccio top down) al fine di valorizzarne proprietà specifiche a seconda della particolare applicazione finale. La combinazione tra l'approccio top down e quello bottom up è stata dunque la principale strategia adottata al fine di raggiungere gli obiettivi prefissati.

Per quanto riguarda l'*approccio bottom up*, la strategia di sintesi adottata è stata il metodo sol-gel. Infatti, l'utilizzo di precursori organico-inorganici permette di sintetizzare nuovi materiali con proprietà e microstrutture uniche. Utilizzando precursori organicamente modificati, come ad esempio trimetossifenilsilano, glicidossipropiltrimetossisilano, metacrilossipropiltrimetossisilano, è stato possibile infatti ottenere materiali ibridi avanzati le cui componenti, organica e inorganica, sono intimamente mescolate a livello molecolare. Inoltre, in fase di sintesi, possono essere aggiunti precursori tetra funzionali, tra cui Titanio isopropossido, Zirconio butossido, Alluminio-tri-sec-butossido, per: aumentare il grado di reticolazione, poiché partecipano alla formazione del network inorganico, con relativo incremento delle proprietà meccaniche del materiale (resistenza al graffio, all'abrasione, all'attacco con plasma), e conferire particolari caratteristiche al materiale finale, come ad esempio la modulazione dell'indice di rifrazione.

I materiali così sintetizzati sono stati quindi direttamente micro- e nano- strutturati mediante tecniche litografiche differenti (fotolitografia, litografia a raggi X e a elettroni, litografia nanoimprint), *approccio top down*, al fine di ottenere pattern ad elevato indice di rifrazione, maschere per il silicio altamente selettive, dispositivi per ottica adattiva e stampi per microiniezione. Uno studio approfondito dell'interazione del materiale con le sorgenti utilizzate nei vari processi litografici ha permesso inoltre di ottimizzare sia la sintesi dei sistemi sol-gel stessi sia i parametri di processo litografico.

Quindi, lo sviluppo e l'ottimizzazione contemporanei dei materiali avanzati e dei processi litografici innovativi appena citati hanno permesso di ridurre in termini di costi e tempo l'intero processo di micro- e nano- fabbricazione dei dispositivi finali realizzati, rispetto al processo litografico tradizionale, ottenendo strutture qualitativamente superiori.



## *Introduction*

The development of new miniaturized devices for application in optics, electronics, mechanics, energy, biology and medicine has considerably increased together with the need for materials with advanced functional and structural properties. In particular, the more and more stringent specifications required to the final micro and nano-structured devices depend on two combined features of the lithographic process: the resists chemistry (bottom up approach) and the lithographic machines (top down approach). Resists are imaging or recording materials that undergo photochemical reaction when exposed to a particular source (UV light, X-rays or electrons), changing their solubility in specific developers. When exposed, for example through a mask, they can produce micro- and nano- patterned features that act as protective layers for the transferring of the pattern into the underlying active substrate. Different lithographic techniques (top down approach), such as optical lithography and, more recently, advanced lithographic techniques including extreme UV lithography, soft and hard X-ray lithography, e-beam and focused ion beam writing, imprinting and soft lithography techniques have been developed to facilitate the fabrication of ever smaller structures [<sup>1</sup>] on resists materials.

Recently, the research on novel photosensitive systems which could replace the existing sacrificial commercial photoresists is greatly focused on the possibility of adding innovative and advanced materials features, in order to directly exploit these patternable materials also as final constituents of the device. The idea at the basis of the development of these directly patternable resists is that they allow to combine the bottom up approach with the top down within a single functional material without the need for pattern transfer processes. As a consequence, these resists allow to reduce problems of degradation of the surface/film which is usually observed at the end of a multi-steps process, time consuming, surface roughness and adhesion between photoresist and device substrate typical of sacrificial commercial polymeric resists.

In particular, increasing attention has been devoted to sol-gel materials as potential innovative resists with functional and advanced capabilities (e.g. etching resistance, high refractive index, porosity, etc.) conferring outstanding advantages beyond the simple patterning ability to these class of materials. In fact one of the major advances of the sol-gel processing is

undoubtedly the synthesis of organic-inorganic hybrid (HOI) materials, taking advantage of the mild conditions involved in the synthesis. Innovative and advanced materials that exhibit the flexibility and functionality of organics and many of the useful properties of inorganics, including thermal stability, hardness and chemical resistance, can then be achieved.

Considering the great number of parameters that influence the final material properties, a deep understanding and control of sol-gel hybrid structure represents an important task that has been faced to develop and design at molecular level advanced materials exploiting their bottom up approach of the synthesis. The great number of precursors, especially metal alkoxides and organically modified silicon alkoxides, allows an incredible number of possible materials. On the one hand, by using silicon precursors modified with organic groups, such as phenyls or methyls, or polymerizable organic functionalizations, such as epoxide and methacrylic groups, it is possible to produce hybrid materials with the organic and inorganic components intimately mixed at a molecular scale thanks to the covalent C-Si bonds that remains stable under the synthesis conditions since it is not sensitive to the hydrolytic cleavage. On the other hand, tetrafunctional precursors are usually introduced to increase the reticulation degree, taking part to the inorganic network formation and to improve the material mechanical properties (such as scratch, abrasion, plasma etching resistance) or to confer particular characteristics to the final materials, i.e. to modulate the refractive index, or as carriers of special functions as for example catalytic properties of TiO<sub>2</sub> clusters.

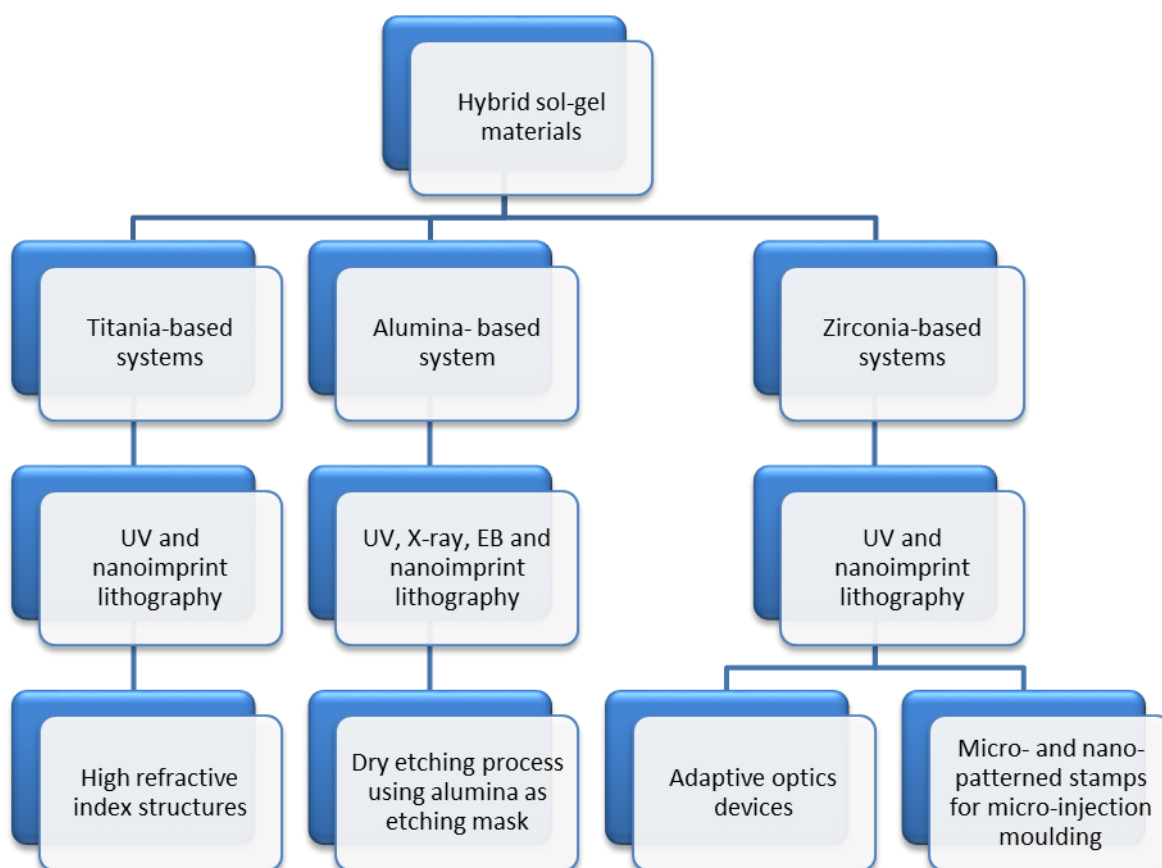
Moreover, the organic component of the organic-inorganic sol-gel hybrids is of paramount importance not only to provide the materials with the specific properties but also to confer the patternability on them in order to obtain “directly patternable” resists. Generally, in literature two different approaches are exploited in the direct patterning of sol-gel materials:

- the use of specific organically modified alkoxides (3-glycidoxypropyltrimethoxysilane GPTMS, 3-(Trimethoxysilyl)propyl methacrylate TMSPM, trimethoxyphenylsilane) in which the organic part (double bonds C=C in vinylic, acrylic, methacrylic compounds and epoxy rings) can be polymerized in solid state by irradiation [<sup>2</sup>],
- or the chemical modification of metal-alkoxides with  $\beta$ -diketones or chelate rings that degrade upon irradiation [<sup>3</sup>].

In this work, new hybrid or inorganic directly patternable TiO<sub>2</sub>, Al<sub>2</sub>O<sub>3</sub>, ZrO<sub>2</sub> based materials have been developed. On the one hand ZrO<sub>2</sub> based HOI nanostructured features were obtained starting with sol-gel precursors with polymerizable groups (such as epoxy rings as in the case of GPTMS or methacrylic groups as for TMPSM), on the other hand TiO<sub>2</sub> and Al<sub>2</sub>O<sub>3</sub> based

inorganic structures were fabricated using precursors (such as phenylsilanes or organic monomers) whose organic component undergoes degradation upon exposure to different radiations (UV, X-rays, electrons) exploiting either the presence of photocatalytic TiO<sub>2</sub> or their direct photosensitivity. In the context of inorganic resists, the distinctive and innovative feature of the presented systems is that they could be made almost inorganic at low temperature, simply by exposing them to a particular source (electrons, X-rays, UV) or in combination with mild thermal treatments (< 300°C). A new method for patterning inorganic material at low temperature is then described.

An outline of the work is schematically represented in the following diagram:



The structure of the thesis, regarding the subjects faced, is organized as follow:

**Chapter 1:** a survey of the main micro and nano patterning lithographic methods is provided (top down approach), focusing the attention on the techniques used in the present work.

**Chapter 2:** a short introduction on materials used as resists in micro- and nano- fabrication, from organic to hybrid organic-inorganic.

**Chapter 3:** experimental chapter on the synthesis of Ti-based systems obtained either by loading a HOI system with commercial anatase nanoparticles (ex situ system) or by obtaining the titania clusters during synthesis starting with Ti-isopropoxide (in situ system). In particular experimental results concerning the chemical and structural modifications occurring during thermal treatment and UV exposure of titania films are presented, with special attention to the refractive index changes. Finally micro- and nano- fabrication of high refractive index structures through UV and nanoimprint lithography (carried out in collaboration with *École polytechnique fédérale de Lausanne EPFL, Lausanne, Switzerland* and *Micro Resist Technology MRT, Berlin, Germany*) is presented [4].

**Chapter 4:** a new alumina based hybrid system showing both high resolution and extremely high selectivity toward silicon (up to 100:1) in fluorine based plasma etching process is presented. The synthesized material can be patterned with different lithographic techniques, such as UV, X-ray, EB and nanoimprint lithography. Moreover, selecting the development chemistry it showed both positive and negative tone behaviour. The chapter describes the investigation and optimization of all the process parameters involved in the different lithographic procedures, finally presenting the outstanding achievements when using the patterned material as mask for silicon in dry etching process. This work has been carried out in collaboration with *Elettra synchrotron* and *TASC-INFM National Laboratory of Trieste* [5,6].

**Chapter 5:** synthesis of two different hybrid organic-inorganic materials belonging to Zr-based systems, organically modified with 3-glycidoxypropyltrimethoxysilane (GPTMS) and 3-(Trimethoxysilyl)propyl methacrylate (TMSPM). After characterization in terms of UV sensitivity, as in the case of TMSPM-based system, and thermal curing, as for GPTMS-based material, the systems were used as resist for UV and nanoimprint lithography for two different applications. First, the realization and characterization of a double-grating monochromator for ultrafast pulses in the XUV region obtained using deformable gratings (collaboration with *CNR-IFN, LUXOR Laboratory, Padova*) is presented [7,8]. Moreover, the fabrication of micro- and nano- patterned stamps as alternative inserts to the metallic ones for micro injection moulding technique is reported (collaboration with *Te.Si. Laboratory of Rovigo*). The inserts were designed in order to obtain polystyrene replicas, with micro and nano structured surfaces, engineered to induce differentiation of mesenchymal stem cells to osteoblasts.

---

## References

- <sup>1</sup> A. Pimpin, W. Srituravanich, *Engineering Journal* **2012**, 16, 37-55.
- <sup>2</sup> X. Luo , C. Zha, B. Luther-Davies, *Optical Materials* **2005**, 27, 1461–1466.
- <sup>3</sup> H. Segawa, *Journal of the ceramic society of Japan* **2008**, 116, 251-259.
- <sup>4</sup> E. Zanchetta, V. Auzelyte, J. Brugger, A.V. Savegnago, G. Della Giustina, G. Brusatin, *Microelectron. Eng.* **2012**, 98, 176–179.
- <sup>5</sup> G. Greci, G. Della Giustina, A. Pozzato, E. Zanchetta, M. Tormen, G. Brusatin, *Microelectron. Eng.* **2012**, 98, 134–137.
- <sup>6</sup> E. Zanchetta , G. Della Giustina , G. Greci , A. Pozzato , M. Tormen , G. Brusatin, *Adv.Mater.* **2013**, 25, 6261–6265.
- <sup>7</sup> S. Bonora, F. Frassetto, E. Zanchetta, G. Della Giustina, G. Brusatin, L. Poletto, *Rev. Sci. Instrum.***2012**, 83, 123106.
- <sup>8</sup> F. Frassetto, S. Bonora, C. Vozzi, S. Stagira, E. Zanchetta, G. Della Giustina, G. Brusatin, L. Poletto, *Optics Express* **2013**, 21,12996-13004.



---

# *Chapter 1*

## *LITHOGRAPHIC TECHNIQUES*

### *FOR MICRO- AND NANO- FABRICATION*

Microolithography and nanolithography refer specifically to lithographic patterning methods capable of structuring material on a fine scale. Typically features smaller than 10 micrometers are considered microlithographic, and features smaller than 100 nanometers are considered nanolithographic. For decades, micro- and nanolithography technology has contributed to the manufacturing of integrated circuits (ICs) and microchips, as well as fabrication of sensors, microreactors, combinatorial arrays, microelectromechanical (MEMS), microanalytical and micro-optical systems.

Methods used to generate nanoscale structures and nanostructured materials are commonly characterized as “top-down” and “bottom-up”. The top-down approach, focus of this chapter, uses various lithography techniques to pattern nanoscale structures, typically in two-dimensions (2D) over length scales approximately 4 orders of magnitude larger (in linear dimension) than an individual structure. On the other hand the bottom-up approach uses interactions between molecules or colloidal particles to assemble discrete nanoscale structures in two and three dimensions.

Lithography techniques are divided into two types by the use of masks or templates: masked lithography (photolithography, X-ray lithography, soft lithography, nanoimprint lithography) and maskless lithography (electron beam lithography, focused ion beam lithography, scanning probe lithography). Masked lithography makes use of masks or molds to transfer patterns over a large area simultaneously, thus, enabling a high-throughput fabrication up to several tens of wafers/hr, while maskless lithography fabricates arbitrary patterns by a serial writing without the use of masks, allowing an ultrahigh-resolution patterning of arbitrary shapes with a minimum feature size as small as a few nanometers but limited throughput. The most powerful microfabrication technique is photolithography, i.e. the lithography using a UV light source and a photosensitive material as resist, and essentially all integrated circuits (IC) are fabricated using this technology.

Advanced lithographic techniques currently being explored as potential substitutes for conventional photolithography in the regime  $<100$  nm include extreme UV (EUV) lithography, interferential lithography, soft X-ray lithography, e-beam writing, focused ion beam (FIB) writing, and proximal-probe lithography. These techniques have the capability to generate extremely small features (as small as a few nm), but their development into economical methods for mass-production (or manufacturing) of nanostructures still requires substantial effort. As an exception, certain electron beam lithography equipment, capable of higher patterning resolution (sometimes as small as a few nanometers), is commercially important, primarily for its use in the manufacture of photomasks.

In this chapter, a general explanation of the conventional lithographic process has been reported in comparison to the direct patterning, with a special deepening about UV, X-ray, Electron Beam (EB) and Nanoimprint lithography.

### ***1.1. Traditional lithographic process vs Direct patterning***

Lithography is a relatively complex process whereby a desired micro or nanometric pattern is transferred into a substrate (silicon, glass, GaAs, etc.) or a thin film (e.g. polymeric, sol-gel film), by using a photoresist. The photoresist is an active material layer that can be patterned by selective exposure to different sources (UV, X-ray, Electrons, Ion beam) and that must “resist” chemical and physical attack of the underlying substrate, after the development step.

The main steps of the lithographic process generally used are (Figure 1.1):

1. *Resist Deposition*: the precursor solution of a photosensitive material (*resist*) is spin-coated on a clean substrate, for instance a silicon wafer, to form a very thin, uniform layer.
2. *Soft Bake*: the layer is thermally treated at a low temperature to evaporate the residual solvent.
3. *Alignment and Exposure*: a *latent image* is formed in the resist e.g. (a) via exposure to ultraviolet or X-ray light through a photomask with opaque and transparent regions or (b) by direct writing using an electron beam.
4. *Post-Exposure Bake*
5. *Development*: the areas of the resist that have (or have not) been exposed are removed by rinsing with an appropriate solvent.



6. *Pattern Transfer Process*: wet or dry etching, lift-off.
7. *Resist Stripping*: the resist is removed at the end of the process

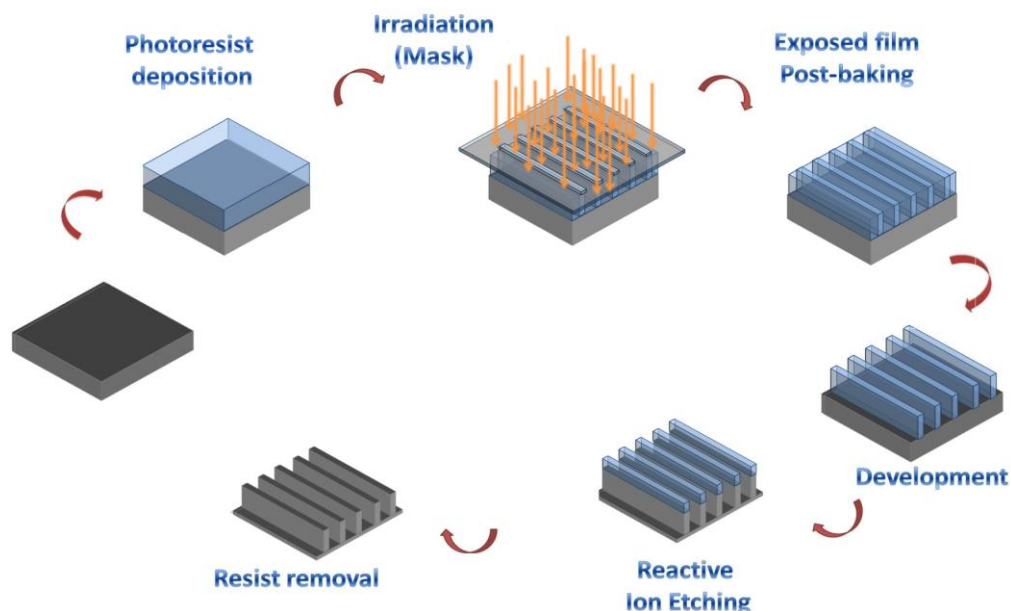


Figure 1.1 Traditional photolithographic process steps

Firstly, before resist deposition the surface substrate has to be cleaned to remove any traces of contamination from the surface of the wafer such as dust, organic, ionic and metallic compounds and a layer of silicon dioxide is formed by a wet or dry oxidation process. Then, after an accurate substrate cleaning, a thin resist layer, which is a radiation sensitive polymer blends based multicomponent material, is applied by standard spin coating techniques. The viscosity of the resist solution is dependent on the solid content and the spin rate can be used to tailor the resist thickness. After the resist deposition on the substrate, the sample is soft baked in an oven or on a hot plate at different temperatures and time according to the resist. This procedure is important to evaporate the residual solvent (1-3%) and increase the adhesion between the resist and the substrate. This is a critical step because on the one hand incomplete removal of the solvent affects the resist profile and, on the other hand, excessive baking destroys photoactive compound and reduces sensitivity. A typical bake is 1-15 minutes on a 90-150°C hot plate. Thick resists may benefit from a longer baking time.

At this point, the resist is ready to be patterned via lithography to form (sub)micrometer-scale features. The resist film is in fact selectively irradiated through a photomask which possesses opaque and transparent regions, forming a submicrometer-scale pattern of dark and

illuminated regions in the resist layer - the *latent image*. Chemical and physical changes occur in the exposed areas of the resist layer allowing to classify resists as *positive* or *negative*, depending on how they respond to radiation, Figure 1.2.

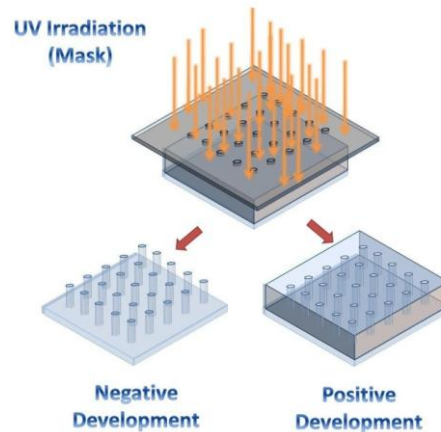


Figure 1.2 Positive and negative behaviour of photoresists

For positive resist, the exposed region becomes more soluble and thus removable in the following development step. The net result is that the pattern produced (also called *image*) in the positive resist is the same as the one of the mask. For negative resists the exposed regions become insoluble because of molecular weight increase due to the polymerization, and the patterns formed in the negative resist are the reverse of the mask patterns (please refer to Chapter 2 for further details and a deep explanation of resists chemistry and behaviour).

To further promote the reaction activated by the exposition and improve the contrast, as well as the resolution, the sample is *post-baked* after exposure. The heat treatment is necessary to increase the difference in the weight of the polymeric chains between exposed and unexposed areas, thus changing the solubility of the polymer. For example, it can improve the resist wet and dry etch resistance making it more difficult to be removed by aggressive etches. This treatment is also applied to reduce the effect of light intensity standing waves produced by reflection from the substrate which causes levels of resist with high and low exposure [1]. It can also affect the resist profile.

After the post-bake, the latent image is developed and a pattern is formed on the photoresist. The *development* consists in the selective removal of the resist by rinsing the exposed sample with an appropriate solvent. It is a critical step in the formation of a good pattern, with temperature and time both influencing uniformity and reproducibility of the final outcome. Developers are generally matched to a type of photoresist. Though they may be

interchangeable to some extent, changing the type of developer used in a process will usually change the exposure time necessary to resolve the pattern. Each developer used has a different dilution, and some require longer development times than others.

### 1.1.1. Pattern transfer

The pattern on the resist can be used as a mask in the following process step. For example, areas of the underlying substrate that are not protected by the patterned resist may be etched or doped. In particular, the etching process allows to transfer the resist pattern to the substrate or to the underlying active film. Etching processes are often divided into two classes, wet etching and dry etching [2].

When a material is attacked by a liquid or vapour etchant, it is removed isotropically (equally in all directions) or anisotropically (in vertical direction). The difference between isotropic etching and anisotropic etching is shown in Figure 1.3. Material removal rate for wet-etching is usually faster than dry etching processes and it can easily be changed by varying the temperature or the concentration of active species.

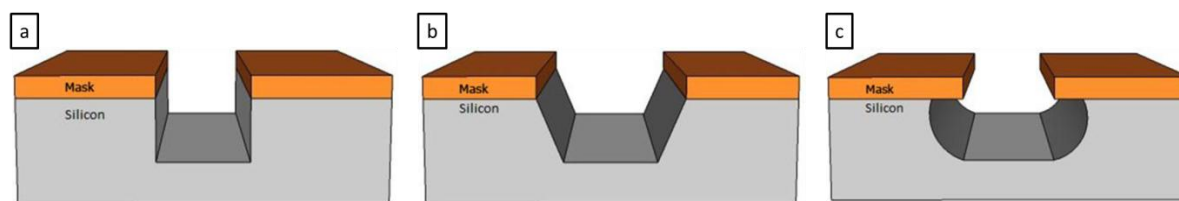


Figure 1.3 (a) Completely anisotropic (b) Partially anisotropic and (c) Isotropic etching of silicon [3]

*Wet etching* consists in the removal of the material by immersion in a liquid bath of the chemical etchant. A wet etching process involves multiple chemical reactions that consume the original reactants and produce new reactants. The wet etch process can be described by three basic steps. (1) Diffusion of the liquid etchant to the structure that is to be removed. (2) Reaction between the liquid etchant and the material being etched away. A reduction-oxidation (redox) reaction usually occurs. This reaction entails the oxidation of the material then dissolving the oxidized material. (3) Diffusion of the byproducts in the reaction from the reacted surface. Some of the anisotropic wet etching agents for silicon are potassium hydroxide (KOH), ethylenediamine pyrocatechol (EDP), or tetramethylammonium hydroxide (TMAH). For isotropic wet etching of silicon, a mixture of hydrofluoric acid, nitric acid, and acetic acid (HNA) is the most common etchant solvent.

*Dry etching* refers to the removal of material, by exposing the material to a bombardment of ions (usually a plasma of nitrogen, chlorine and boron trichloride oxygen) that dislodge portions of the material from the exposed surface. The material removal can occur through 1) chemical reactions that consume the material, using chemically reactive gases or plasma; 2) physical removal of the material, usually by momentum transfer (ion beam milling); or 3) a combination of both physical removal and chemical reactions.

Physical dry etching requires high kinetic energy beams to etch off the substrate atoms. The material evaporates when the high energy particles (ion, electron, or photon) knock out the atoms from the substrate surface. There is no chemical reaction taking place and therefore only the material that is unmasked is removed. The physical reaction taking place is illustrated in Figure 1.4.

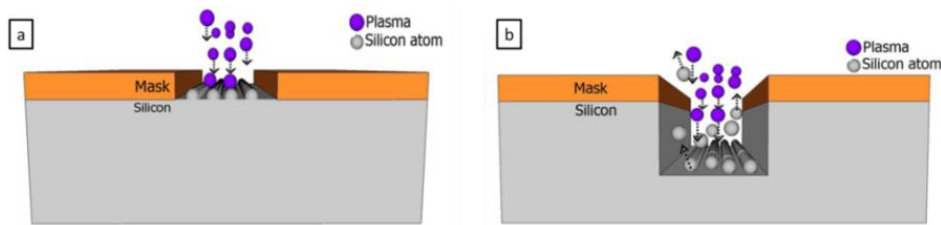


Figure 1.4 The plasma hits the silicon wafer with high energy to knock-off the Si atoms on the surface. (a) The plasma atoms hitting the surface. (b) The silicon atoms being evaporated off from the surface [3].

Chemical dry etching (also called vapour phase etching) does not use liquid chemicals or etchants. This process involves a chemical reaction between etchant gases to attack the silicon surface. Anisotropic dry etching has the ability to etch with finer resolution and higher aspect ratio than isotropic etching. Due to the directional nature of dry etching, undercutting can be avoided. Figure 1.5 shows the reaction that takes place in chemical dry etching. Some of the ions that are used in chemical dry etching is tetrafluoromethane ( $\text{CF}_4$ ), sulfur hexafluoride ( $\text{SF}_6$ ), nitrogen trifluoride ( $\text{NF}_3$ ), chlorine gas ( $\text{Cl}_2$ ), or fluorine ( $\text{F}_2$ ).[4]

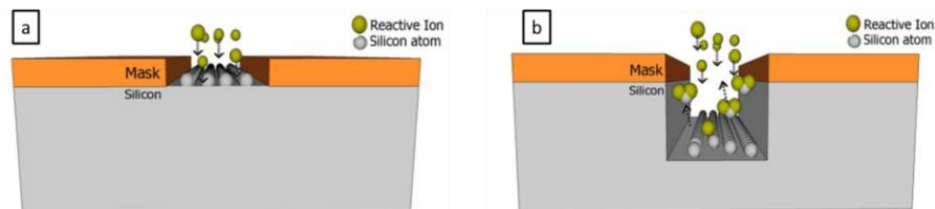


Figure 1.5 Process of a reactive ion interacting with the silicon surface. (a) The interaction between the reactive ion and the silicon atom. (b) A bond between the reactive ion and the silicon atom then chemically remove the silicon atoms from the surface [3].

An example of dry etching is *Reactive Ion Etching (RIE)*, one of the most diverse and most widely used processes in industry and research, which utilizes reactive ion generated by plasma discharge in chlorine base ( $\text{SiCl}_4$  and  $\text{Cl}_2$ ) or fluorine base ( $\text{CF}_4$ ,  $\text{CHF}_3$ ,  $\text{C}_2\text{F}_6$ ) reactive gas. Typical RIE gases used for the etching of different substrates are reported in Table 1.1 together with the corresponding selectivity when resists, ceramic or metal patterns are used as etching masks. In the RIE-process, cations are accelerated with high energy to the substrate and chemically react with the silicon. This process use both physical and chemical mechanisms to achieve high levels of resolution as well as a high speed. The high energy collision from the ionization helps to dissociate the etchant molecules into more reactive species. RIE is a very anisotropic etching process that removes material in the vertical direction only. This property is very desirable, since it faithfully follows the mask patterns on the wafer, leaving any material covered by mask untouched. Practically, if isotropic chemical reactions occur, then attack in the horizontal direction can consume a portion of the material covered by the mask, leading to the phenomenon known as “undercutting”.

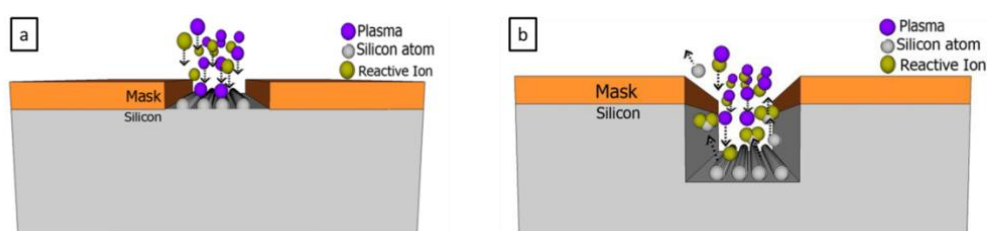


Figure 1.6 Scheme of the physical and chemical reactions involved in material removal in Reactive Ion Etching technique [3]

### Typical RIE Gases

Material	Gas	Etching Rate (Å/min)	Mask	Selectivity
Si (a-Si)	1) $\text{CF}_4$ 2) $\text{SF}_6$ 3) $\text{BCl}_2 + \text{Cl}_2$	~ 500	Resist Metal (Cr, Ni, Al)	~ 20:1 ~ 40:1
$\text{SiO}_2$	1) $\text{CHF}_3 + \text{O}_2$ 2) $\text{CF}_4 + \text{H}_2$	~ 200	Resist Metal (Cr, Ni, Al)	~ 10:1 ~ 30:1
$\text{Si}_3\text{N}_4$	1) $\text{CF}_4 + \text{O}_2 (\text{H}_2)$ 2) $\text{CHF}_3$	~ 100	Resist Metal (Cr, Ni, Al)	~ 10:1 ~ 20:1
GaAs	1) $\text{Cl}_2$ 2) $\text{Cl}_2 + \text{BCl}_3$	~ 200	$\text{Si}_3\text{N}_4$ Metal (Cr, Ni)	~ 10:1 ~ 20:1
InP	1) $\text{CH}_4/\text{H}_2$	~ 200	$\text{Si}_3\text{N}_4$ Metal (Cr, Ni, Al)	~ 40:1
Al	1) $\text{Cl}_2$ 2) $\text{BCl}_3 + \text{Cl}_2$	~ 300	Resist $\text{Si}_3\text{N}_4$	~ 10:1
Resist / Polymer	1) $\text{O}_2$	~ 500	$\text{Si}_3\text{N}_4$ Metal (Cr, Ni)	~ 50:1

Table 1.1 Typical RIE gases used for the etching of different substrates and corresponding selectivity when resists, metal or ceramic patterns are used as etching masks.

In order to achieve deep etches in silicon using an ICP-RIE, three basic etch requirements must be met. First, the etch must have a relatively high etch rate. A slow etch rate is cost prohibitive in a high throughput, industrial process and has the potential for the introduction of process variations, leading to etch failures. Second requirement is that the etch must have a high selectivity, or preference, to etch the silicon as compared to the etch mask. Insufficient selectivity limits the maximum etch depth or requires complicated thick masks to compensate for erosion, limiting the minimum feature size. Finally, the etch must remain anisotropic throughout the etching process. If lateral etching occurs, pattern transfer begins to fail as the etching continues vertically. The ultimate test of a mask is the fidelity of pattern transfer into the silicon over the entire etching period [5]. Another important consideration concerns the formation of highly volatile reaction by-products. The desorption of the reaction by-products from the surface of the material being plasma etched is of equal importance to the chemical reactions that decompose the material. If such desorption fails to occur, then etching cannot occur even if the chemical reactions have been completed.

The final step of the lithographic process is the removal of the patterned photoresist after pattern transfer. There are a number of methods to accomplish the stripping process. The choice depends on the materials present on the wafer and the resist nature. The most important thing is that the stripping procedure must not damage or contaminate the layer below.

It has to be pointed out that the obtained structured device could be the final output of the fabrication process or it could be an intermediate product further used as a template for the fabrication of many replicas, like e.g. in NanoImprinting Lithography (NIL) or Injection moulding technology.

### ***1.1.2. Metallic or ceramic etching masks***

The actual quality of the final obtained structures is related not only to the performances of wet or dry etcher, but depends strongly on the characteristic of the mask material used (i.e. selectivity toward the substrate in the chosen plasma chemistry) and on the aspect ratio required. In fact, central to the success of these top-down manufacturing methods is not only the ability of the imaging layer to capture fine features with high fidelity, but also the imaging layer needs to play the role of etch mask: it needs to be resistant to plasma etching to allow pattern transfer into the underlying material. Thereby, there is a growing demand on

developing high resolution, high selectivity mask for etching processes, which could be easily removed after the pattern transfer, leaving the substrate patterned with high quality nano-structures.

Traditional resist materials, however, are usually carbon-based polymeric systems and have little resistance to plasma etching. Although thicker resist layer can be exploited to achieve the desired etch resistance, the requirements on lateral resolution impose an upper limit to the usable thickness. With each advance in photolithography technology, the depth-of-focus is reduced, requiring ever thinner imaging layers in order to achieve high lateral resolution to ensure a focused image of the pattern throughout the thickness of the layer. Moreover, the imaging layer thickness is further constrained by the need to prevent pattern collapse during the development and drying process. Surface tension of the wet developer and rinse chemicals, as well as drying flux of air or nitrogen can exert sufficient force to mechanically distort the printed patterns (Figure 1.7), especially when the aspect-ratio is large [6].

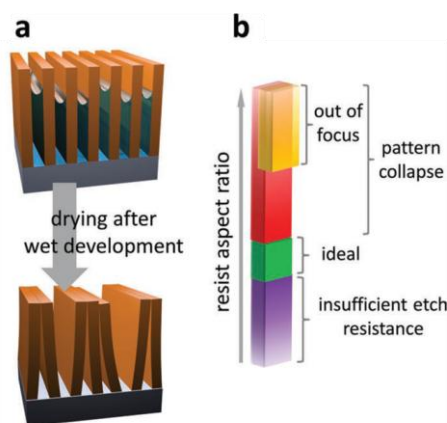


Figure 1.7 Limitations of top-down patterning a) Pattern collapse of high aspect-ratio resist structures due to capillary forces during post-development drying. b) Summary of constraints on aspect-ratio of resist structures [6].

Therefore, even if polymeric resist masks offer the simplicity of a single processing step, they generally exhibit poor dry etching selectivity, which results in significant degradation of the mask pattern, such as sloped sidewalls. This non-ideality is circumvented by first transferring patterns to an intermediate layer (hard mask) that has greater etch resistance before being etched into the desired material (Figure 1.8). Hard etch mask based on  $\text{SiO}_2$ ,  $\text{SiN}$  and  $\text{SiGe}$  typically offer high selectivity and improved structured sidewall profiles, but with the added cost of more complicated patterning [7]: the oxide layer must be grown or deposited, followed by pattern transfer from another material or resist into the oxide mask. Increasing the number of processing steps increases the effort needed for accurate pattern transfer as well as the potential for reduction in mask fidelity and significant investments in processing equipment.



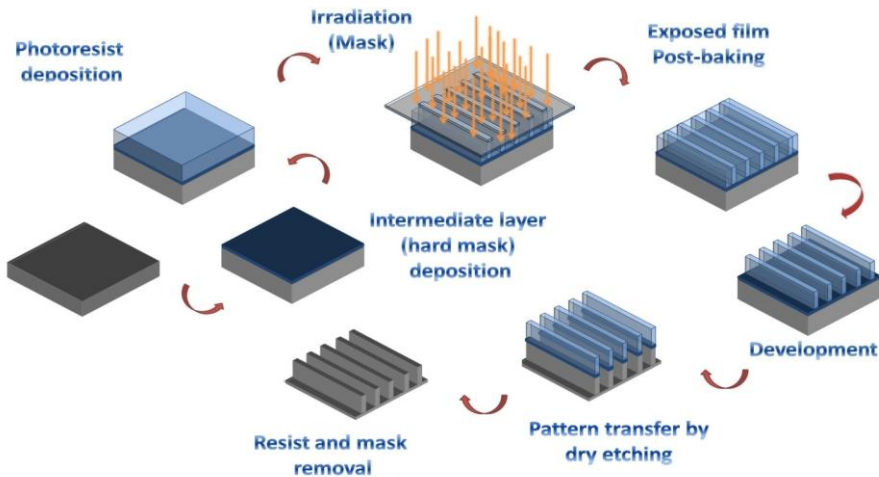


Figure 1.8 Pattern transfer using hard masks due to low plasma etch resistance of resists.

On the other hand, metal masks such as Aluminium, Copper, Chromium and Nickel have high selectivity with respect to Silicon. This is primarily due to their lack of chemical reactivity with the etch gas molecules and their mechanical strength. Metal masks are generally patterned by "Lift-off" process. A metallic film is blanket-deposited all over the substrate, for example through evaporation or sputtering, covering the patterned photoresist and areas in which the photoresist has been cleared. During the actual lift-off, the photoresist under the film is removed with solvent, taking the film with it, and leaving only the film which was deposited directly on the substrate, see Figure 1.9.

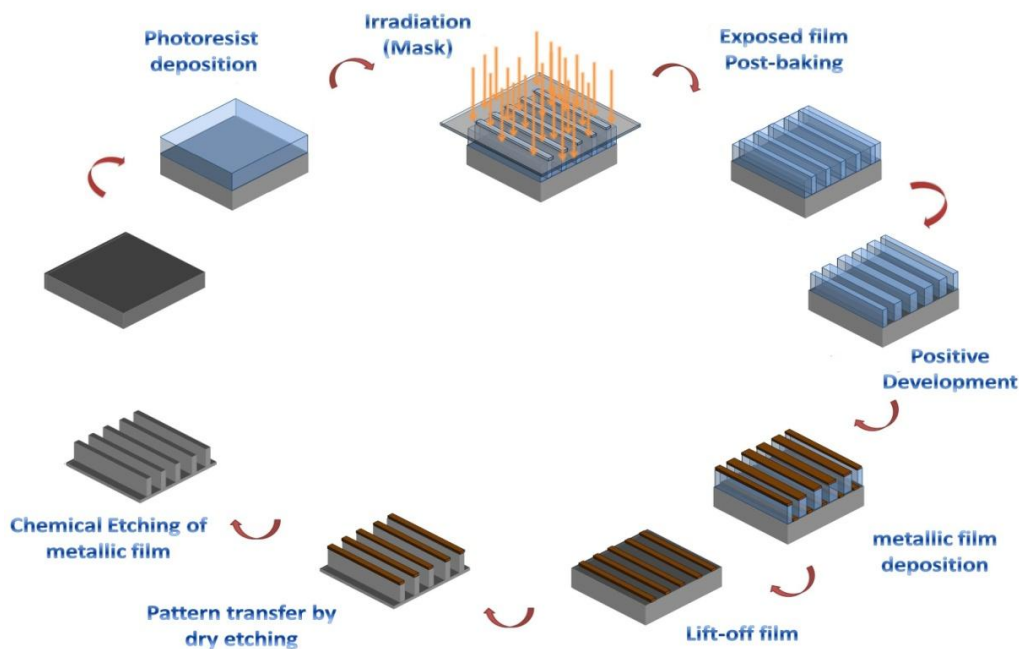


Figure 1.9 Patterning process using metallic masks deposition and lift-off



### 1.1.3. Direct patterning

More recently a new approach to pattern active materials has appeared, also called direct patterning. This approach, assumed as the main patterning method used during this thesis work, consists in the patterning like standard resists, by radiation exposure and development, of engineered materials which can also constitute the final active material of the device, unlike common resists that are typically used as simply sacrificial layers in traditional fabrication process. Of technological interest is the possibility of engineering the final functional properties of the resist film by tailoring its chemical synthesis, allowing to envisage an enormous number of applications, ranging from sensing to photonics. From a fabrication point of view, a direct patterning process brings enormous advantages in terms of cost and time of the overall process: pattern transfer to the active layer, and eventually lift-off process, is avoided together with the reduction of problems of adhesion between substrate and photoresist, film degradation and pattern roughness introduction during the traditional multi-step process (Figure 1.10).

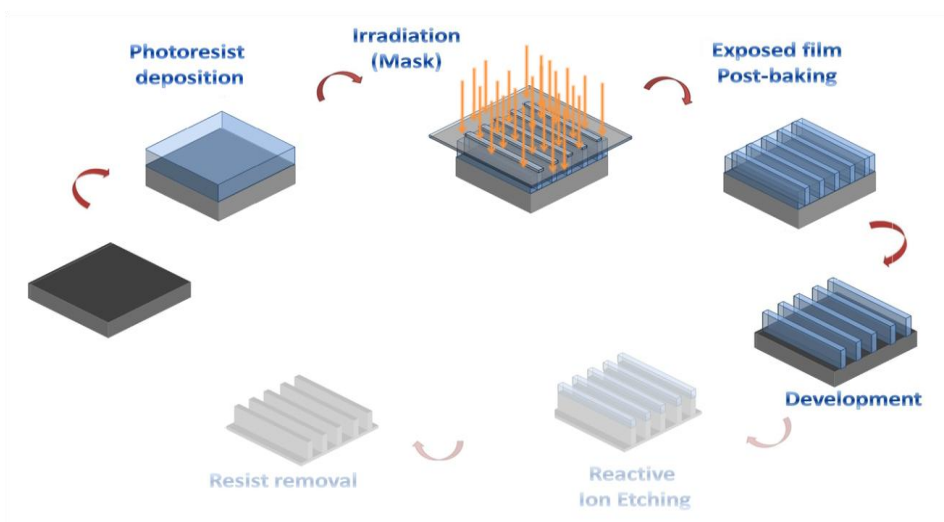


Figure 1.10 Direct patterning process: no need for pattern transfer step

Many photolithography and processing cycles may be performed to directly create complex devices: Table 1.2 resumes the main characteristics and applications of each lithographic tools. Since the purpose of this work was to obtain large-scale patterns of different materials, in particular Titania, Alumina and Zirconia based systems, through different top-down approaches, such as photolithography (UVL), X-ray lithography (XRL), electron-beam lithography (EBL) and nanoimprint lithography (NIL), an outline of these lithographic processes will be described in the following section of this chapter.

Lithography Technique	Minimum Feature Size	Throughput	Applications
Photolithography (contact & proximity printings)	2-3 $\mu\text{m}$ <sup>[22]</sup>	very high	typical patterning in laboratory level and production of various MEMS devices
Photolithography (projection printing)	a few tens of nanometers (37 nm) <sup>[2]</sup>	high - very high (60-80 wafers/hr) <sup>[1]</sup>	commercial products and advanced electronics including advanced ICs <sup>[1]</sup> , CPU chips
Electron beam lithography	< 5 nm <sup>[23]</sup>	very low <sup>[1, 3]</sup> (8 hrs to write a chip pattern) <sup>[1]</sup>	masks <sup>[3]</sup> and ICs production, patterning in R&D including photonic crystals, channels for nanofluidics <sup>[23]</sup>
Focused ion beam lithography	~20 nm with a minimal lateral dimension of 5 nm <sup>[2]</sup>	very low <sup>[3]</sup>	patterning in R&D including hole arrays <sup>[125, 134]</sup> , bull's-eye structure <sup>[132]</sup> , plasmonic lens <sup>[137]</sup>
Soft lithography	a few tens of nanometers to micrometers <sup>[2, 13]</sup> (30 nm) <sup>[2]</sup>	high	LOCs for various applications <sup>[13, 96]</sup>
Nanoimprint lithography	6-40 nm <sup>[14, 15, 18]</sup>	high (> 5 wafers/hr) <sup>[1]</sup>	bio-sensors <sup>[17]</sup> , bio-electronics <sup>[18]</sup> , LOCs: nano channels, nano wires <sup>[97, 102, 104]</sup>
Dip-pen lithography	a few tens of nanometers <sup>[39, 40, 43]</sup>	very low – low, possibly medium <sup>[39]</sup>	bio-electronics <sup>[43]</sup> , bio-sensors <sup>[40]</sup> , gas sensors <sup>[42]</sup>

Table 1.2 Specifications and applications of the major lithography techniques<sup>[8]</sup> and refs therein].

## 1.2. UV lithography (UVL or Photolithography)

Over the years, optical lithography has become a powerful method for patterning large areas with high throughput, being employed for pattern generation in manufacturing of ICs, microchips and commercial MEMS devices. This technique utilizes an exposure of a light-sensitive polymer (photo-resist) to ultraviolet (UV 193-436 nm) light to define a desired pattern, by using a pre-fabricated quartz photomask with chromium as photo-absorber material, from which the final pattern is derived. A chrome-on-glass photomask is called a binary mask, because there is either a transmission or a blockade. Moreover, if the mask is mostly covered by chrome, with only a small percentage of open area, it is said to be a dark field mask; if it is mainly transparent with only small percentage of chrome, it is designated a light or bright field mask.

Historically, ultraviolet light is produced by gas-discharge lamps using mercury, sometimes in combination with noble gases such as xenon. These lamps produce light across a broad spectrum with several strong peaks in the ultraviolet range. This spectrum is filtered to select

a single spectral line, usually the "g-line" (436nm) or "i-line" (365nm). More recently, lithography has moved to "deep ultraviolet", produced by excimer lasers (KrF and ArF excimer lasers with emission wavelengths between 248–193 nm).

There are three forms of photolithography: contact printing, proximity printing and projection printing as schematically illustrated in Figure 1.11.

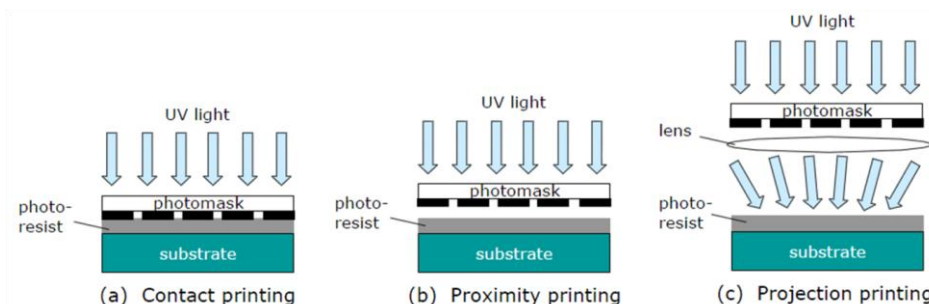


Figure 1.11 Schematic illustration of three forms of photolithography: (a) contact printing; (b) proximity printing; and (c) projection printing [8]

The simplest photolithographic technique is contact lithography: the photomask and the wafer coated with the resist are brought into intimate contact and exposed to UV light. Mask dimensions and diffraction at mask edges determine the final resolution of the obtainable pattern. Extremely small patterns can be made in principle but the production of photomask with submicron features is prohibitively expensive. Mask damage is frequent when the mask and the wafer are in direct contact, making contact printing not very production worthy. To reduce the wear and tear to the chromium mask under repeated contact, the wafer can be placed in close proximity (from 3 to 50  $\mu\text{m}$  gap) to the mask instead of hard contact with it, giving an optical proximity print.

Perfectly vertical resist walls ( $90^\circ$ ) are difficult to make. Positive resists usually have a slightly positive slope,  $85^\circ$  to  $89^\circ$ , negative resists have similar retrograde profile. This is a natural consequence of exposure light intensity through the mask. The nonsharpness of the edge of the shadow is caused not only by a noncollimated illumination but also by Fresnel diffraction. For collimated illumination, the wavefront traversing the mask is diffracted by the mask pattern and Fresnel diffraction formulae have to be used to estimate the minimum linewidth that can be printed:

$$l_m \cong \sqrt{\lambda g}$$

where  $\lambda$  is the wavelength of the exposure radiation and  $g$  is the gap between the mask and the wafer and includes the thickness of the resist. Values of  $g < 5\mu\text{m}$  are difficult in practice because of non-flatness of the wafer; hence achieving sub-micrometer resolution with visible and ultraviolet wavelengths is also difficult. Both contact and proximity lithography can be done in the same machine where the gap is an adjustable parameter. Contact/proximity systems are 1X: the image is the same size as the original. Generally, contact and proximity printings are capable of making patterns as small as a few micrometers. Therefore, they are typically used in the fabrication of moderate-resolution patterns especially in laboratories and small to medium-sized companies. It should be noted that photolithography in most of research works normally refers to contact or proximity printings.

In contrast, a projection printing system utilizes an optical lens system to project a deep-UV pattern from an excimer laser (wavelength of 193 or 248 nm) on the photo-resist enabling pattern-size reduction by 2-10 times. Fraunhofer far-field diffraction governs the optics of projection systems. Since only one sample at a time can be exposed, this requires a step-and-repeat system to totally cover the wafer area (*stepper* machine). One of the most significant advantages in projection optical system is that the mask is not in physical contact with the wafer, greatly improving mask lifetime. Furthermore pattern size reduction makes mask-making much easier. Errors in both resist image and the etched chrome image on the mask are reduced, leading to tighter linewidth tolerances on the wafer.

Projection printing is by far the most widely used system in micro-fabrication and can yield superior resolutions compared to contact and proximity methods: it is capable of fabricating high-resolution patterns as small as a few tens of nanometers (37 nm) [<sup>9</sup>] at a high throughput (60-80 wafers/hr) [<sup>10</sup>].

In the projection system the resolution is given by the Rayleigh relations:

$$I_m = k_l \lambda / NA$$

where  $NA$  is the numerical aperture of the imaging system ( $NA = n \sin\theta$ , with  $n$  the index of refraction in the image medium and  $\theta$  is the half-angle of the cone of light converging to a point image at the wafer),  $\lambda$  is again the exposure wavelength and  $k_l$ , usually referred as “k-factor“, whose typical value is 0.4.

Therefore, resolution can be improved by either reducing the wavelength and  $k_l$  or increasing  $NA$  or both. However the depth of focus,  $\Delta z$ , that can be expressed as:

$$\Delta z = \frac{\pm \frac{l_m}{2}}{\tan \theta} \approx \frac{\pm \frac{l_m}{2}}{\sin \theta} = \frac{\pm n\lambda}{2(NA)^2}$$

degrades much more rapidly by increasing NA than by decreasing  $\lambda$ .

Therefore, since the resolution depends on the source wavelength used  $\lambda$ , high pressure mercury lamp is adequate (436 nm g-line and 365 nm i-line) for above 0.25  $\mu\text{m}$  minimum line width, while between 0.25 and 0.13  $\mu\text{m}$  deep UV sources such as excimer lasers (248 nm KrF and 193 nm ArF) are required, Table 1.3.

In recent years, immersion lithography, using 193 nm and optics with numerical apertures  $NA$  exceeding 1.0, allows improved imaging resolution (below 0.13  $\mu\text{m}$ ) by increasing the refractive index of the medium between the imaging lens and the imaging plane. Increasing the index of the fluid (from air with  $n=1$  to water with  $n=1.47$  at 193 nm) between the final lens element and the imaging plane improves depth of focus while also allowing lenses with larger capture angles (numerical aperture) to be used in the imaging system. However, the technical challenges of contacting the photoresist-coated substrate and mask with water (or another solvent) must be solved before immersion lithography can be implemented.

Wavelength	Numerical aperture	Rayleigh resolution	Year of first use	Light source
436 nm	0.30	0.89 $\mu\text{m}$	1982	Hg arc lamp (g-line)
365 nm	0.45	0.49 $\mu\text{m}$	1990	Hg arc lamp (i-line)
365 nm	0.60	0.37 $\mu\text{m}$	1994	Hg arc lamp (i-line)
248 nm	0.50	0.30 $\mu\text{m}$	1994	Hg arc lamp or KrF excimer laser
248 nm	0.60	0.25 $\mu\text{m}$	1997	KrF excimer laser
248 nm	0.70	0.22 $\mu\text{m}$	1999	KrF excimer laser
193 nm	0.75	0.16 $\mu\text{m}$	2001	ArF excimer laser
193 nm	0.85	0.14 $\mu\text{m}$	2003	ArF excimer laser

Table 1.3 Typical parameters for stepper optics

To pattern still smaller features, photolithography will require further advances, such as decreasing the imaging wavelength to 157 nm or to soft X-rays ( $\sim 13.5$  nm) known in the microelectronics industry as extreme ultraviolet (EUV) light. The shift to shorter wavelengths of light requires new photoresists as new light sources and, especially, new types of optics based on reflection rather than transmission to focus the light [<sup>11</sup>and refs therein].

As it will be seen in the following paragraph, X ray lithography is a proximity lithography, but with much smaller wavelength:  $\lambda \sim 1$  nm is used, and therefore much smaller lines can be printed. One particularly ambitious approach to overcome the wavelength limitation on resolution in optical lithography is the absorbance modulation optical lithography (AMOL) [12]. AMOL employs simultaneous exposure at two different wavelengths and is shown schematically in Figure 1.12. Twenty-nanometer lines and spaces have been reported corresponding to a  $k_1$  value of 0.05.

## Absorbance Modulation Optical Lithography (AMOL)

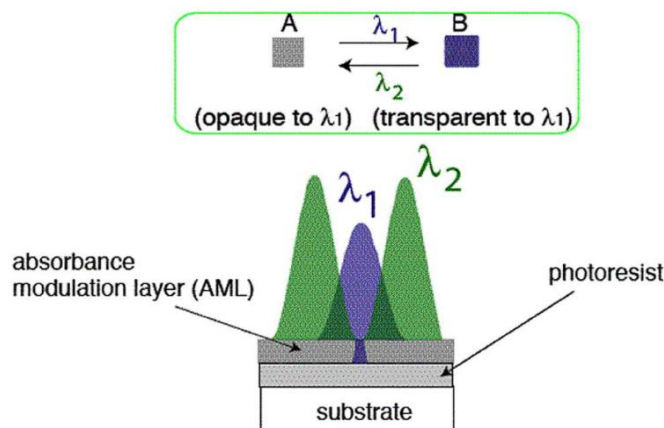


Figure 1.12 An example of an ambitious approach to achieving features sizes for  $k_1 < 0.25$ , AMOL. Under exposure at one wavelength, the absorbing modulation layer (AML) turns opaque and transparent at the other. Thus a simultaneous exposure at  $\lambda_1$  and  $\lambda_2$  can achieve an arbitrarily small transparent opening in the AML, which is then transferred to the photoresist by the same exposure at  $\lambda_1$ . To achieve closely packed features, the operation must be repeated prior to developing. (Courtesy of H. I. Smith.) [10]

Moreover the resolution can be improved acting on  $k_1$  which is a complex factor of several variables in the photolithography process, such as the quality of the photoresist, and the use of resolution enhancement techniques (RET), such as phase shift masks, off-axis illumination (OAI) and optical proximity correction (OPC). As it concerns the resists, the industry is developing better resist chemistry for example through chemical amplification in which the exposure gives rise to an acid that on subsequent heating catalyses the desired chemical reaction, with the drawback of the diffusion of the acid limiting the sharpness of the features (refer to Chapter 2 for resists chemistry). As it concerns RET, phase-shifting masks [13] presents alternate clear features with a phase change in the transmitted light so that they destructively interfere and give rise to a region of zero intensity between them, OAI consists in well matching the angle of illumination and the angle of diffraction in order to enhance the

amount of light diffracted and finally OPC mask presents a distorted image on the mask that is design to produce a perfect image on the resist (examples are reported in Figure 1.13).

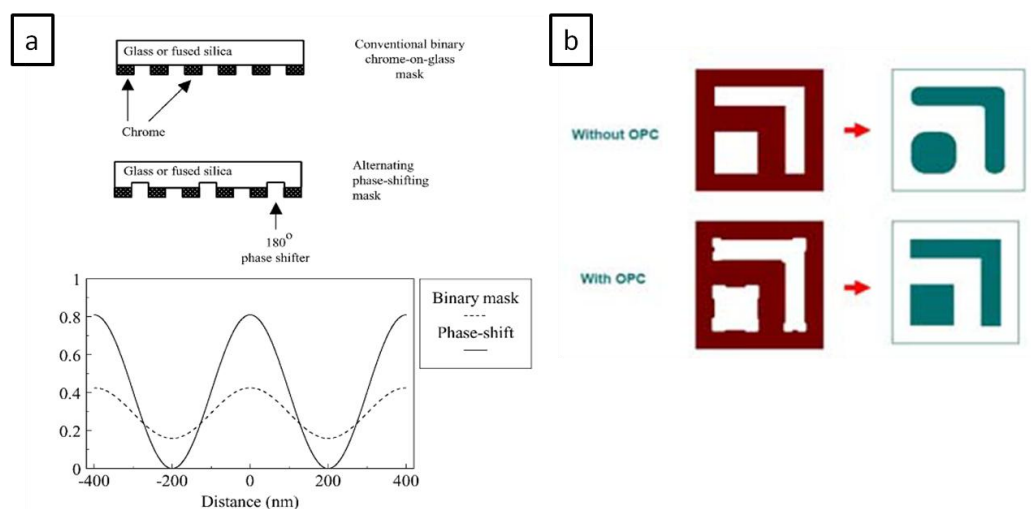


Figure 1.13 (a) The alternating area PSM (M. D. Levenson, IEDM 1982) compared with the conventional binary mask. The resultant intensity curves show clearly the better contrast in the image of the PSM. This was probably the earliest example of treating the mask as a diffractive element rather than an object to be faithfully imaged. (b) optical proximity correction (OPC)

Finally, since the main drawback in photolithography is the time and cost required to fabricate the photomask, a photolithographic method that can produce simple patterns (e.g., diffraction gratings) without using a photomask has been developed. This technique, named *interferential lithography*, involves the constructive and destructive interference of multiple laser beams at the surface of the photoresist [14].

### 1.3. X-ray lithography (XRL)

X-ray lithography is the main contender for sub 250 nm lithography. X-ray lithography uses collimated X-rays with wavelengths  $\lambda$  in the range 0.01-0.1nm, with the subset 0.6-44 often called soft X-ray, as the exposing energy to transfer a geometric pattern from a mask to a light-sensitive chemical photoresist on the substrate. Because it's difficult to use optical diffraction components for imaging in the X-ray regime, X-ray lithography is carried out as a simple 1:1 shadow projection technique with a proximity gap between mask and resist-coated wafer. The mask consists in a X-ray absorber, typically of gold or compounds of tantalum or tungsten, on a membrane that is transparent to X-rays, typically a low atomic number material such as diamond, beryllium, polyimide, or a thin membrane of a higher atomic number material such as silicon or silicon carbide.



X-ray are generated in atoms when an electron from a higher atomic orbital decays into a core hole, leading to the emission of a photon of energy equal to the difference in energy between the two levels, i.e. by fluorescence. Because of the competing Auger process, the fluorescence becomes efficient only for relatively heavy atoms ( $Z > 28$ ). Another process is the emission of radiation by a high energy accelerated electron, by direct coupling of the moving charge with the electromagnetic field. At present, only two types of X-ray sources have enough power to be considered viable candidates for XRL- based manufacturing. They are based on plasmas or electron accelerators. Until now only the electron storage rings, called synchrotrons, accelerators capable of producing stable beams of particles with very high energies, in the million (MeV) to billion (GeV) electronvolt range, have reached a very mature stage of development to be exploited in the lithographic applications. As it will be seen in Chapter 4, part of this PhD work has been performed at the LILIT beamline at ELETTRA synchrotron source facility (Trieste), Figure 1.14. [<sup>15,16</sup>]

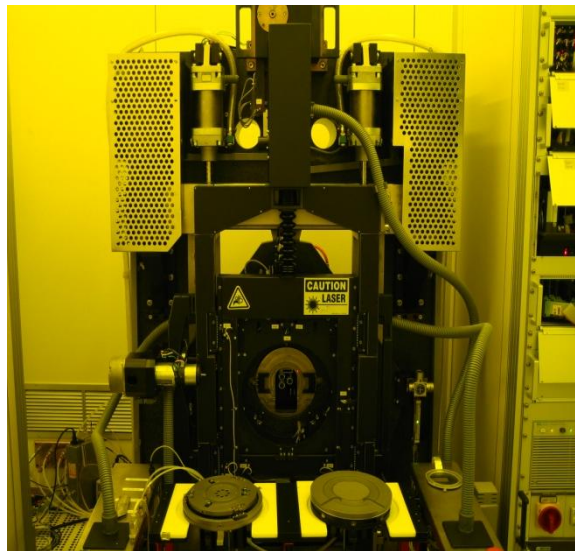


Figure 1.14 X-ray stepper located at the LILIT beamline (Trieste) in a 10 class clean room

In the case of soft X-rays, which are frequently used in high resolution X-ray lithography, the absorption process is dominated by the photoelectric effect. At energy around 1-2 keV, the electric field of radiation couples most efficiently with the atom' inner electron. The absorption of a photon results in the excitation of a photoelectron from a bound atomic state to the unbound continuum, thus yielding an absorption spectrum characterized by edges rather than lines. The macroscopic response of a system is described by its dielectric function. In general the strength of the interaction of a material with a radiation beam depends on how



many electrons are available for the interaction, i.e. on the polarizability of the material at that frequency. Hence materials with large number of electrons per  $\text{cm}^3$  will interact more strongly than material with fewer electrons. High density materials and materials containing elements of large atomic numbers (such as Au, W, Pt, etc.) will have larger absorption compared to lighter ones (i.e.  $\text{H}_2\text{O}$ , organic materials, Si,  $\text{N}_2$ , etc.). The absorption coefficients can be approximated by  $\mu \approx \lambda^2 Z^2$  and for X-rays all their values are around  $0.1\text{-}1 \mu\text{m}^{-1}$ . Hence the interaction between X-rays and materials can be considered as “weak”, since the radiation must propagate for hundreds of wavelengths before appreciable variation in the optical path [17]. This explains the high X-ray penetration power and the relatively large resist thickness (100-1000  $\mu\text{m}$ ) of resist that can be uniformly exposed.

Therefore, the lithographic resolution comes from the extremely short wavelength used, which overcomes the diffraction limits of optical lithography, and the high penetration from the transparency of most materials in this region of the spectrum. Moreover, because of good collimation, very fine features with vertical sidewalls and very large depth of focus can be obtained, enabling resist height to width ratios above 100:1.

In conclusion, X-ray lithography has many advantages over optical lithography but traditional X-ray sources are not bright enough to produce reasonable throughput. Moreover some technical issues remain open, such as the availability of strong, stable, collimated, single frequency X-ray sources (synchrotron light only fits this requirements but with high cost and huge size), sensitivity of typical resist (need for long time exposure), mechanical and radiation stability of the mask, the availability of high throughput e-beam system for mask making and the reliability of high accuracy alignment.

#### ***1.4. Electron beam lithography (EBL)***

Electron beam lithography (EBL) has been consider one of the more flexible methods that can undertake the realization of submicron devices [18]. This is possible due to the very small spot size of the electrons whereas the resolution in optical lithography is limited by the wavelength of light used for exposure. The electron beam has wavelength so small ( $\lambda < 1 \text{ \AA}$  for 10-50 keV electrons) that diffraction no longer defines the lithographic resolution. This latter depends on electron scattering and on the size of the beam, which can reach  $\sim 5 \text{ nm}$ .

EBL is a form of maskless lithography: the final features are created directly from a digital representation on a computer, by controlling an electron beam as it scans across a resist-

coated substrate, such as polymethylmethacrylate (PMMA) dissolved in trichlorobenzene (positive) or polychloromethylstyrene (negative)[<sup>19</sup>], in a dot-by-dot fashion to generate patterns in sequence. It is then flexible because design can be changed immediately by rewriting the code.

The advantages of electron beam lithography include:

- ♦ the generation of micron and submicron resist geometries,
- ♦ highly automated and precisely controlled operation,
- ♦ greater depth of focus than that available from optical lithography,
- ♦ direct patterning on a semiconductor wafer without using a mask
- ♦ maximum high resolution below 10 nm.

The biggest disadvantage of electron lithography is its low throughput (approximately 5 wafers / hour at less than 0.1  $\mu\text{m}$  resolution), in fact e-beam writing is several orders of magnitude slower than optical lithography with photomask. Therefore, electron lithography is primarily used in the production of photomasks and in situations that require small number of custom circuits. However the equipment for EBL is complex and sensitive and it requires a lot of servicing and maintenance for an ultimate resolution and reasonable uptime.

As in the other lithographic techniques, the sample (wafer) is covered with an electron sensitive resist. This material undergoes a substantial change in its chemical or physical properties, when it is exposed to the electron beam. The beam position and intensity are computer-controlled, and the electrons are delivered only to certain areas to get the desired pattern. After the exposure, a part of the resist is dissolved away and the sample can be further processed with etching procedures to get the final structure. The number of incoming electrons (*dose*), that are needed to fully develop the resist thickness, is a function of beam current intensity, so the amount of electronic charge, distance between exposure points (*stepsize*) and the time that beam remains in each point to deliver the correct dose (*dwelltime*). The dose depends on the exact resist sensitivity at certain exposure and development conditions.

#### ***1.4.1. Elements of electron optics***

A typical e-beam system consists of a column of electron optics for forming and controlling the electron beam, a sample stage and a control electronics. The column includes principally

an electron source, magnetic lenses, a beam blanker and a mechanism for deflecting the beam, Figure 1.15.

The e-beam gun is usually part of a scanning electron microscope (SEM), although transmission electron microscopes (TEM) can also be used. The electron gun is a device that can generate a beam of electrons with a suitable current density; a tungsten thermo-ionic-emission cathode or a single-crystal lanthanum boride ( $\text{LaB}_6$ ) can be used for the electron gun. Accelerating voltage of electron emitted is typically around 10-100KeV. Condenser lenses are used to focus the electron beam to a spot size of 0.01 to 0.1  $\mu\text{m}$  in diameter. Beam-blanking plates (to turn the electron beam on and off) and beam deflection coils are computer-controlled and operated at high rates to direct the focused electron beam to any location in the scan field substrate. Because the scan field is much smaller than the substrate dimension, a precision mechanical stage, controlled by interferometer, is used to position the substrate to be patterned. The choice of the substrate is important for the determination of the final resolution: conductive or semi-conductive substrates are preferred.

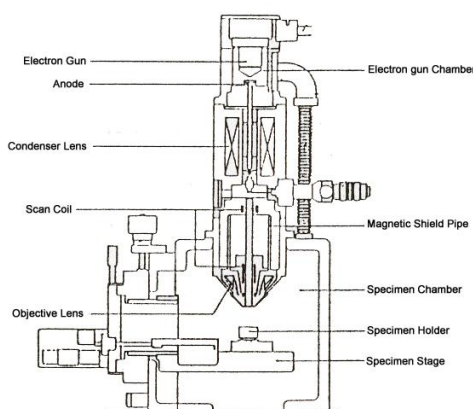


Figure 1.15 Scheme of EBL column

There are two main e-beam writing strategies: projection printing and direct writing. In projection printing, a large e-beam pattern is projected parallel through a mask onto a resist coated substrate by using a high-precision lens system. In direct writing, a small e-beam spot is moved with respect to the wafer to expose the wafer one pixel at a time, eliminating the expensive and time-consuming production of the masks.

There are basically two ways to scan the focused electron beam: *raster scan* and *vector scan*. The simplest writing strategy is termed *raster scan*: the patterns are written by a beam that moves through a regular pattern (vertically oriented). It uses a single Gaussian beam and

divides the pattern to be drawn into small rectangles and makes an “exposure-no-exposure” decision for each rectangles. In the *vector scan* the beam is directed only to the requested pattern features and jumps from feature to feature, skipping empty (not exposed) spaces and making the systems much faster. Variable shaped beam is another improvement over raster scan: when larger than minimum pixel size structures are drawn, writing speed is enhanced dramatically. Electron beam writing area is very small: about 250x250  $\mu\text{m}$ , which is the region that can be scanned electromagnetically. If an area larger than 250x250  $\mu\text{m}$  has to be drawn, additional movement must be introduced. The stage scan is a mechanical movement, controlled by an interferometer. Pattern placement in different subfield is thus a sum of two different mechanisms.

#### **1.4.2. Electron beam Physics**

Electron may be emitted from a conducting material either by heating it to the point where the electrons have sufficient energy to overcome the work function barrier of the conductor (thermo ionic sources) or by applying an electric field enough strong that they tunnel through the barrier (field emission sources)[<sup>17</sup>].

When high energy (10-50kV) electrons hit the resist, they scatter. Even if the beam spot on resist top surface is very small, scattering broadens the beam inside the resist and the resist is exposed on a larger area than the initial spot.

In fact in EBL when electrons penetrate the resist film and underlying substrate, they undergo collisions, that lead to energy losses and path changes. Electrons experience many small angle scattering (forward scattering) events, and they occasionally undergo large angle scattering events (backscattering) when they penetrate through the resist into the substrate. Forward scattering is not the major effect for resist component: most of the film exposure comes from a cascade of low voltage electrons called secondary electrons that have been created when the beam slows down. These electrons are responsible for the resist reaction, such as polymerization, polymer cross-linking or chain scissor as well as more complex processes. These 2 to 50 eV have a range of few nanometre in the resist, allowing the minimum practical resolution of 20 nm observed in the highest resolution systems. Thus the incident electrons spread out as they travel through the material until either all of their energy is lost or they leave the material due to backscattering. Backscattered electrons cause the proximity effect, where the dose that a pattern feature receives is affected by electron scattering from other features nearby, limiting the minimum spacing between pattern features. The range of

backscattered electrons- defined as the distance a typical electron travels in the bulk material before losing all its energy- depends on both the energy of primary electrons and the type of substrate [17]. Finally, the dose distribution looks like a sharp peak of the forward contribution superimposed with a back-scattered fog. Thus, although electron wavelengths on the order of 1Å can be easily achieved, electron scattering in the resist limits the attainable resolutions to > 10 nm.

Beam spots down to 5 nm diameter are not limited by the wavelength of electrons ( $\lambda= 8$  pm for 25 kV) but rather by the electron source size, optics aberrations and diffraction for highly collimated beams. Furthermore, interactions in solid limit the minimum size and the increase in effective beam diameter due to forward scattering is given by:

$$d_{\text{eff}} (\text{nm})= 0.9 (t/V)^{1.5}$$

where  $t$  is the resist thickness in nm and  $V$  is the voltage in kV [20]. This effect is minimized by using the thinnest possible resist and the highest accelerating voltage.

In fact, the penetration depth of the electrons in the matter depends on focusing depth and acceleration voltage applied to the beam (thus kinetic energy of the charges). In e-beam lithography at low energy (between 2 and 20keV), the penetration depth of electrons is limited requiring thin resist layers. In this case, electrons will lose almost all their energy in the resist layer, increasing the exposure efficiency and the throughput of the lithographic tool, reducing damage and charging but at the expense of a high resolution. At higher acceleration voltages, resolution is higher, but also substrate heating and damage in the crystalline structure increase. The electron efficiency is inversely proportional to the acceleration voltage, i.e. increasing incoming energy implies that dose should be higher.

Another common problem is the exposure of a resist on insulating substrate, whereby substrate charging causes considerable distortion. A simple solution for exposure energy higher than 10 kV is to evaporate a thin (10 nm) layer of gold, chrome or aluminium on top of the resist. Electrons travel through the metal with minimum scattering, exposing the resist.

In conclusion, EBL is a technique with high resolution potentiality and great flexibility, but at present it is not compatible with mass production nanofabrication.

### 1.5. *Nanoimprint lithography (NIL)*

Unlike the above forms of patterning that employ radiation (photons, electrons, or ions) to delineate a pattern in a resist, non-radiation-based patterning techniques allow to realize features in a resist primarily using mechanical or chemical means or both. Mechanical patterning uses a mould (also called template) that shapes a material into features (i.e., nanoimprinting) or a stamp that transfers an ink onto a surface (nanoprinting or soft-lithography), Figure 1.16.

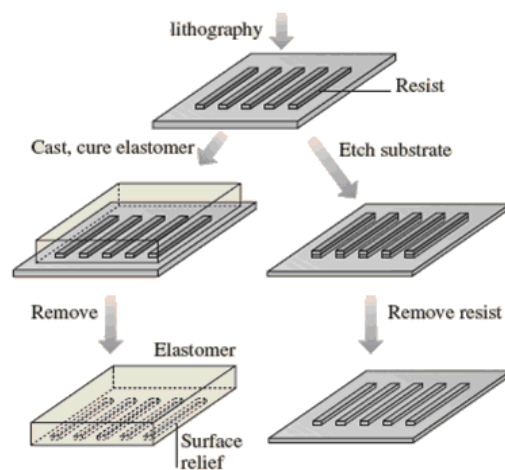


Figure 1.16 Schematic illustration of two methods for producing high resolution stamps. The first step involves patterning a resist thin layer, on a flat substrate, such as a silicon wafer. It is convenient to use an established technique, such as photolithography or electron beam lithography, for this purpose. This structure, known as the master, is converted to a stamp either by etching or moulding. In the first case, the resist acts as a mask for etching the underlying substrate. Removing the resist yields a stamp. This structure can be used directly as a stamp to print patterns, or to produce additional stamps. In the moulding approach, a prepolymer is cast against the relief structure formed by the patterned resist on the substrate. Curing (thermally or optically) and then peeling the resulting polymer away from the substrate yields a stamp. In this approach, many stamps can be made with a single master, and each stamp can be used many times.

Compared with radiation-based nanopatternings, nonradiation-based patternings have three major advantages due to fundamentally different physical principles. First, they do not have a diffraction limit in resolution; secondly, they are easy for 3-D patterning; and thirdly, they can directly pattern functional materials to reduce fabrication steps and cost. They also eliminate expensive, complicated particle source and optical systems [10].

*Soft lithographic techniques* – replica molding, micromolding in capillaries, microtransfer moulding, near-field conformal photolithography using an elastomeric phaseshifting mask, etc. [21,22]- arose from the innovation of using a relatively soft polymer stamp to imprint a solution. This technique, first introduced by Bain and Whitesides in 1989 [23], requires inexpensive materials and employs non-specialized equipment. It is mainly for patterning of

micrometer sizes or features greater than 100 nm because it is very difficult to control the amount and flow of a liquid ink and the stamps are not sufficiently rigid. The feature resolution of the printing is poorer than nanoimprint, where a hard mould and embossing are used. To overcome the problem of ink flow and amount control, a process called nanotransfer printing can be used, which can be separated into two main steps: the fabrication of a patterned polymer stamp, and the use of this stamp to transfer molecules in geometries defined by the element's relief structure, Figure 1.17. The uniqueness of this technique is on the utilization of a soft stamp for pattern transferring, thus it allows a conformal contact between the stamp and the substrate resulting in a patterning capability on flexible or curved substrates.

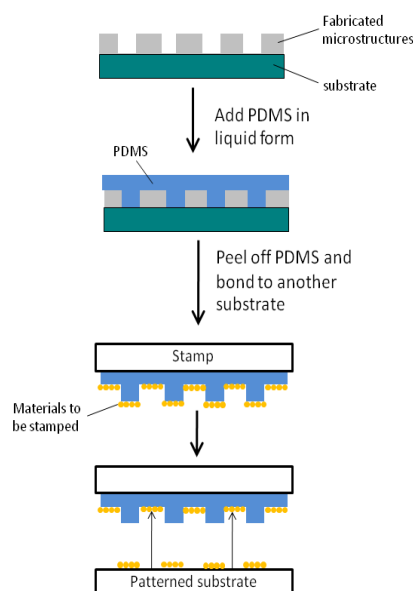


Figure 1.17 Nanotransfer printing [8]

Similar to soft lithography, nanoimprint lithography utilizes a hard mould to imprint into a polymer film for nanoscale patterning, making use of the differences between the mechanical properties of a structured stamp and a moulding material.

*Nanoimprint lithography (NIL)*, a potential candidate for the next generation lithography technology, has become more and more popular because of its low-cost, high-throughput and high-resolution [24]. The first stage of the NIL process is the moulding of a thin thermoplastic film using a hard master. During a process cycle the resist material is made viscous by heating over the glass transition temperature, and shaped by applying pressure. Tg temperature, stiffness, strength, viscoelasticity, toughness and viscosity of the polymer is influenced by its

molecular weight. The reduced viscosity of the polymer at higher temperature is a result of the increasing ability of the chains to move freely while Van der Waals interaction of the chains are reduced. The thermoplastic film is compressed between the stamp and the substrate and the viscous polymer is forced to flow into the cavities of the mould, conforming exactly to the surface relief of the stamp. When the cavities of the stamps are filled, the polymer is cooled down, while the pressure is maintained. The molten structure is then frozen. After relieving the pressure, the stamp can be retrieved (demoulded) without damage, and reused for the next moulding cycle. The imprint resists can be also thermal curable materials, which are initially in liquid state and become solid by curing them with heat (thermoset resists). The imprinted material can serve as a resist for pattern transfer, after removal of the residual layer by homogeneously thinning down the resist in an (ideally) anisotropic etching process. (as in conventional lithography and being removed later), or can be a part of the devices to be built and stay on the wafer (direct imprint of functional materials), Figure 1.18.

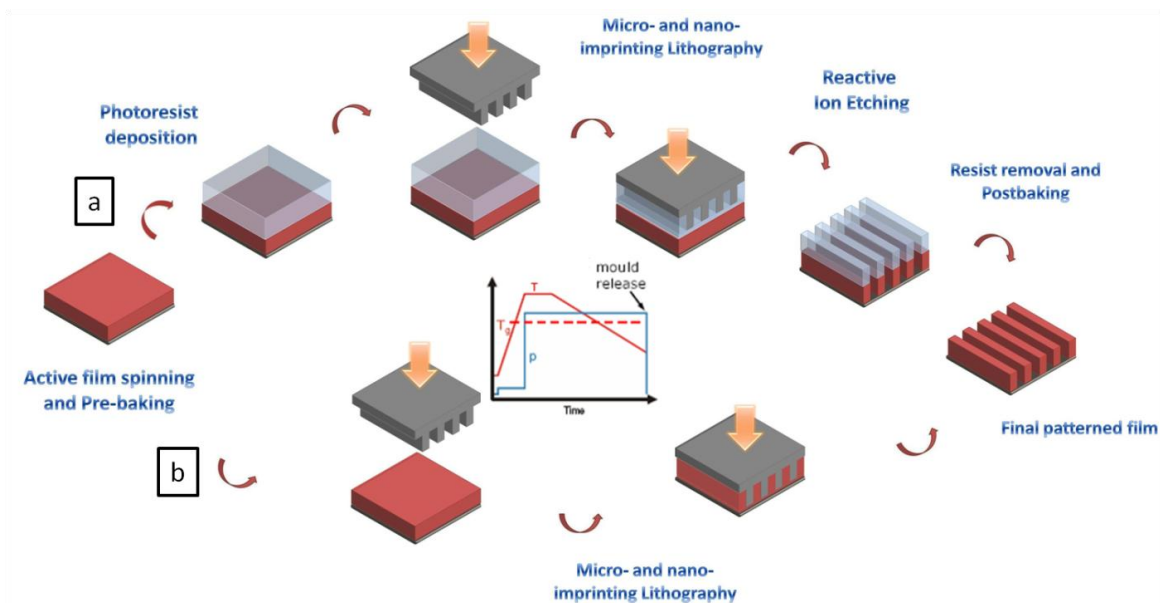


Figure 1.18 Nanoimprint lithography process: (a) imprinted material serves as a resist for pattern transfer, (b) direct imprint of functional materials

NIL was first introduced by S.Y. Chou as thermoplastic moulding, and is therefore often referred to as “hot embossing technique”, enabling the definition of features with lateral sizes down to sub-10 nm [24,25]. Since pattern delineation in nanoimprint lithography is not based on the modification of the chemical structure of a resist by radiation, its resolution is not limited by the factors that limit the resolution of conventional lithography: wave diffraction, scattering and interference in a resist, backscattering from a substrate, and the chemistry of



resist and of its development. In fact, the limits of resolution mainly is reliable to the ability in making the features on the mould. Moreover, NIL has been demonstrated to have high fidelity in pattern transfer, accurately reproducing original mould patterns and maintaining smooth vertical sidewalls in the imprint resist, unlike in conventional lithography, which can produce sloped sidewalls and line edge roughness due to a Gaussian shape of the light profile, light scattering, and other noise. Furthermore, other two advantages offered by NIL are: the NIL exposure area (area patterned in a single step) can be much larger than the exposure field of a conventional photolithography stepper ( $\sim 1 \text{ in}^2$ ) because NIL does not require high precision optics nor a well-conditioned monochromatic light source; NIL can be much cheaper than photolithography since it does not use complicated and expensive optics systems and laser sources.

A simple model for the squeezed polymer flow underneath the stamp protrusion is obtained by treating the polymer as an incompressible liquid of constant viscosity, and solving the Navier-Stokes equation with non-slip boundary conditions at the stamp and substrate surfaces. According to this model, given for line-shaped stamp protrusions and cavities, it is possible to find the following expression, known as Stefan's equation, for the film thickness  $h(t)$  when a constant imprint force  $F$  per length is applied to the stamp protrusion:

$$\frac{1}{h^2(t)} = \frac{1}{h_0^2} + \frac{2F}{\eta_0 L s^3} t$$

where  $\eta_0$  is the zero shear viscosity,  $s$  the protrusion width and  $L$  the protrusion length.

Inserting the final thickness  $h_f = h(t_f)$  in the previous relation, gives the embossing time:

$$t_f = \frac{\eta_0 L s^3}{2F} \left( \frac{1}{h_f^2} - \frac{1}{h_0^2} \right)$$

For many practical cases, where a constant pressure under each stamp protrusion  $p = F/(sL)$  is assumed, this formula gives:

$$t_f = \frac{\eta_0 s^2}{2p} \left( \frac{1}{h_f^2} - \frac{1}{h_0^2} \right)$$

As a direct consequence of the Stefan's equation it can be seen that small (narrow) stamp protrusions will sink faster than the large (wide) ones. The stamp geometry can therefore be optimized by reducing the dimensions of protrusions.

While stamps with nano-protrusions would allow fast embossing of some seconds, using standard NIL process parameters, protrusions of some hundreds of microns would already

increase embossing times to some hours. The strong dependence of the embossing time on the pressing area has the consequence that, for fully inserted stamp relief (full contact over the total stamp area), the flow practically stops (Figure 1.19). For this case,  $s$  becomes larger and the flow continues only towards the stamp borders. The stamp geometry can therefore be optimized by reducing the dimensions of the protrusions.

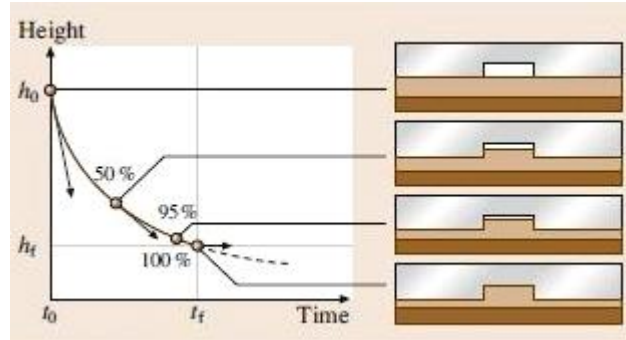


Figure 1.19 Schematics of the squeeze flow of a compressed polymer film into the cavity [26].

Hirai et al. were the first to investigate the polymer deformation process by numerical simulations [27,28]. They studied the pressure required for successful imprinting and the filling rate into the grooves of the mould as a function of the aspect ratio of the pattern, the initial thickness of the polymer, and the duty cycle of the structure for a periodic pattern. It was found that the required pressure increased not only for high-aspect-ratio patterns, but for low-aspect-ratio patterns as well. This is because for wide trenches the pressure is not evenly distributed as a result of the polymer flow resistance, and the polymers fill in from the edges with a slower filling rate than at the centre of the cavity. The pressure also increases when the initial thickness of the polymer film decreases to less than twice the mould depth. This again can be attributed to the increased resistance of polymer flow in the confined nanofluidic channels formed between the mould protrusion and the substrate surface.

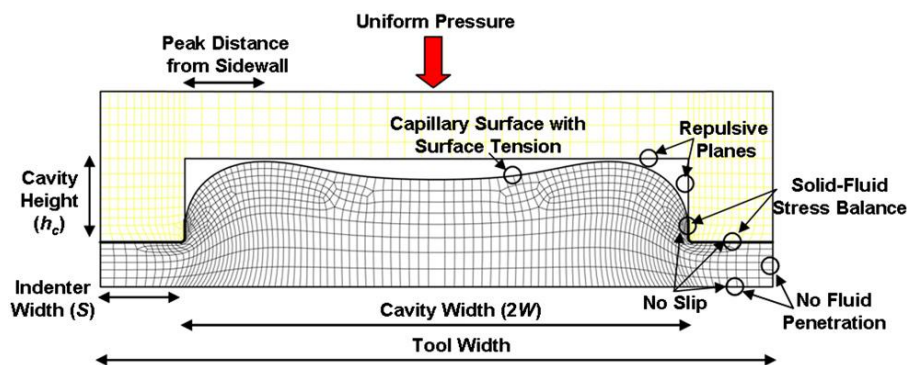


Figure 1.20 Nanoimprint lithography cavity and deforming polymer, showing simulation boundary conditions, geometry variables and polymer peak deformation location measurement.

There are various forms of nanoimprint technology. The earliest is the already described thermal nanoimprint lithography (thermal-NIL), originated in 1994, that imprints a thermoplastic resist at temperatures higher than its glass transition temperature  $T_g$  and removes the residual layers of the imprinted materials to expose the substrate. With the integration of light sources into imprint machines and the introduction of a low-viscosity UV-curable monomer, UV-NIL was developed for photo-curable resists. After imprinting on a liquid UV-curable monomer layer by a moderate pressure, broadband UV light radiation directly through the backside of the transparent mould causes the monomer to crosslink, forming a rigid polymer. It can reduce imprint pressures significantly and avoid time consuming as well as stress induced during high temperature cycle. Step-and-flash imprint lithograph (SFIL) is a photo-NIL process in which drops of a resist liquid are dispensed and imprinted on one single die area at a time. All the processes have their specific advantages, e.g. while UV-NIL can be performed at room temperature, hot embossing is low cost since non-transparent stamps can be used. The major characteristics of the process are summarized in Table 1.4.

Type of NIL / properties	NIL (T-NIL) hot embossing	UV-NIL UV-imprint
<b>basic process sequence</b> (see Figs. 8.3 and 8.6)	1) spin-coat thermoplastic film 2) place stamp on film 3) heat until viscous 4) emboss at high pressure 5) cool until solid 6) demold stamp	1) dispense liquid resin 2) parallel alignment of stamp with defined gap 3) imprint at low pressure 4) expose with UV light through stamp and crosslink 5) demold stamp
Pressure $p$	20–100 bar	0–5 bar
Temperature $T_{\text{mold}}$	100–200 °C	20 °C (ambient)
Temperature $T_{\text{demold}}$	20–80 °C	20 °C (ambient)
Resist	solid, thermoplastic $T_R \approx 60\text{--}100\text{ °C}$	liquid, UV-curable
Viscosity $\eta$	$10^3\text{--}10^7$ Pas	$10^{-2}\text{--}10^{-3}$ Pas
Stamp material	Si, SiO <sub>2</sub> opaque	glass, SiO <sub>2</sub> transparent
Stamp area	full wafer, > 200 mm diameter	25 × 25 cm <sup>2</sup> , limited by control of gap
Stamp contact	facilitated by bending	planarization layer
Embossing time	from seconds to minutes	< 1 min (per exposure)
Advantage	low-cost large-area equipment and stamps	low viscosity, low pressure, alignment through stamp
Challenge	process time, thermal expansion due to thermal cycle	step and repeat needed for large areas
Development needed	alignment, residual layer homogeneity	material variety
<b>Hybrid approaches</b>	thermoset resists: embossing and curing before demolding	thermoplastic resists: hot molding and UV-curing before demolding
Advantage	low temperature variation cycle: demolding at high temperature possible	solid resist: full-wafer single imprint possible

Table 1.4 Comparison of hot embossing (NIL) and UV imprinting (UV-NIL), with typical parameters of current processes [29].

The most commonly used materials for mould have been quartz and silicon that are kinds of hard material. Typically, mould features are patterned by using conventional lithographic techniques such as photolithography, interferential lithography or electron beam lithography. A hard material offers a number of advantages for nanofabrication. The rigidity retains nanoscale features with minimal local deformation. Moreover, a hard mould is thermally stable at high temperature.

Although nanoimprint lithography has made a great progress in a relatively short time, there are few issues to be resolved. One of them is life time of the mould. Heating/cooling cycles and high pressure, applied during embossing, cause stress and wear on moulds. This stress also presents a problem of alignment for multi-layer fabrication. Viscosity of embossed material is also an important issue. It appears to be a limiting factor for minimizing pattern size and increasing feature density.

Moreover, a mould for imprint lithography typically has a high density of nanoscale protrusion features on its surface. This effectively increases the total surface area that contacts the imprinted polymer, leading to strong adhesion of the imprinted polymer to the mould. This effect can easily be seen by the sticking of a resist material to a mould without any special treatment. Solutions to this problems are (I) incorporating an internal release agent into the resist formulation, (ii) applying a low-surface-energy coating to the mould to reduce its surface energy, and (iii) choosing a mould material with an intrinsically low surface energy. Anti-adhesion layers on the mould can reduce polymer laceration and friction forces during this step, but they have to be thin and durable. A low-surface-energy release layer on the stamp surfaces not only helps to improve imprinting qualities, but also significantly increases the stamp lifetime by preventing surface contamination. The most widely adopted approach is to form a self-assembled monolayer of fluorinated trichlorosilanes with different carbon chain lengths on the mould surface (e.g. 1H,1H,2H,2H-perfluorodecyl-trichlorosilane), either by a solution phase or a vapour-phase reaction, due to their low surface energy, high surface reactivity and high resistance against temperature and pressure. Vapour phase coating has been shown to provide better imprint results for nanoscale features because it avoids the difficulty of liquid wetting of the nanoscale trench features on the mould. This approach can be readily applied to oxide surfaces, or to Si surfaces that have been oxidized with a piranha soak to generate required terminal hydroxyl groups. Silanization of oxidized silicon with a  $\text{RSiCl}_3$  precursor begins with hydrolysis of the polar head group, which converts the  $\text{Si-Cl}$  bonds to  $\text{Si-OH}$  (silanol) groups. The silanol groups generated,

which are strongly attracted to the hydrophilic surface of oxidized silicon, condense and react with the hydroxyl group on the surface as well as other monomer silanol group to form networks of covalent siloxane bonds, Si–O–Si. Such covalent bonding makes the surfactant coating layer chemically and thermally stable.

## References

- <sup>1</sup> Y. Xia, G. M. Whitesides, *Annu. Rev. Mater. Sci.* **1998**, 28, 153.
- <sup>2</sup> S. Franssila, *Introduction to microfabrication*, Wiley&Sons, **2004**.
- <sup>3</sup> A. Nayak, Logeeswaran V.J, M. Saif Islam, “Wet and Dry Etching”, *Encyclopedia of Nanotechnology*, **2012**.
- <sup>4</sup> M. J. Madou, *Fundamentals of Microfabrication: The Science of Miniaturization*, 2 ed.: CRC Press, **2002**.
- <sup>5</sup> M. Shearn, X. Sun, M. D. Henry, A. Yariv, A. Scherer, Chapter 5, Advanced Plasma Processing: Etching, Deposition, and Wafer Bonding Techniques for Semiconductor Applications, *Semiconductor Technologies*, ed. Jan Grym, **2010**.
- <sup>6</sup> Y. Tseng , A. U. Mane , J. W. Elam, S. B. Darling, *Adv. Mater.* **2012**, 24, 2608.
- <sup>7</sup> M. Serry, M. Ibrahim, S. Sedky, *2012 IEEE 25th International Conference on Micro Electro Mechanical Systems (MEMS)* **2012**, 321 – 324.
- <sup>8</sup> A. Pimpin, W. Srituravanich, *Engineering Journal* **2012**, 16.
- <sup>9</sup> B. D. Gates, Q. Xu, M. Stewart, D. Ryan, C. G. Willson, G. M. Whitesides, *Chem. Rev.* **2005**, 105.
- <sup>10</sup> R. F. Pease, S. Y. Chou, *Proc. IEEE* **2008**, 96, 248-270.
- <sup>11</sup> B. D. Gates, Q. Xu, M. Stewart, D. Ryan, C. G. Willson, G. M. Whitesides, *Chem. Rev.* **2005**, 105, 1171-96.
- <sup>12</sup> R. Menon and H. I. Smith, *J. Opt. Soc. Amer.* **2006**, A 23, 2290.
- <sup>13</sup> M. D. Levenson, N. S. Viswanathan, R. A. Simpson, *IEEE Trans. Electron Devices* **1982**, ED-29, 1828–1836.
- <sup>14</sup> G. Della Giustina, G. Zacco, E. Zanchetta, M. Gugliemi, F. Romanato, G. Brusatin, *Microelectronic Engineering* **2011**, 88, 1923–1926.
- <sup>15</sup> E. Di Fabrizio, A. Nucara, M. Gentili, R. Cingolani,, *Rev. Sci. Instrum.* **1999**, 70, 1605.
- <sup>16</sup> F. Romanato, E. Di Fabrizio, L. Vaccari, M. Altissimo, D. Cojoc, L. Businaro, S. Cabrini, *Microelectron. Eng.* **2001**, 57, 101.
- <sup>17</sup> P. Rai-Choudhury, *Handbook of Microlithography, Micromachining and Microfabrication*, Vol. 1. Spie Optical Engineering Press, **1994**.
- <sup>18</sup> P. Rai-Choudhury, *Micromachining and Microfabrication*, ed. Handbook of Microlithography, SPIE, Bellingham **1997**.

- 
- <sup>19</sup> L. Ming, C. Bao-qin, Y. Tian-Chun, Q. He, X. Qiuxia, Proc. *6<sup>th</sup> Int. Conf. Solid-State and Integrated-Circuit Technol.* (IEEE), **2001**.
- <sup>20</sup> S. Franssila, *Introduction to microfabrication*, Wiley&Sons, **2004**.
- <sup>21</sup> Y. Xia, J. A. Rogers, K. E. Paul, G. M. Whitesides, *Chem. Rev.* **1999**, 99, 1823–1848.
- <sup>22</sup> Y. Xia, G. M. Whitesides, *Angew.Chem. Int.Ed.***1998**, 37, 550-575.
- <sup>23</sup> C. Bain and G. M. Whitesides, *Angew. Chem., Int. Ed.* **1989**, 28, 506-512.
- <sup>24</sup> S.Y. Chou, P.R. Krauss, P.J. Renstrom, *Science* **1996**, 272, 85.
- <sup>25</sup> S. Y. Chou, P. R. Krauss, *Microelectronic Eng.* **1997**, 35, 237-240.
- <sup>26</sup> *Handbook of Nanotechnology*, Chapter 8, Springer, **2010**.
- <sup>27</sup> Y. Hirai, M. Fujiwara, T. Okuno, Y. Tanaka, M. Endo, S. Irie, K. Nakagawa, M. Sasago, *J. Vac. Sci. Technol. B* **2001**, 19(6).
- <sup>28</sup> Y. Hirai, T. Konishi, T. Yoshikawa, S. Yoshida, *J. Vac. Sci. Technol. B: Microelectronics and Nanometer Structures* **2004**, 22 , 3288-3293.
- <sup>29</sup> *Handbook of nanofabrication*, Chapter 8 Nanoimprint lithography, Springer, **2010**.





---

## *Chapter 2*

# ***INTRODUCTION TO MATERIALS FOR MICRO- AND NANO- LITHOGRAPHY: FROM ORGANIC TO COMPLETELY INORGANIC RESISTS***

The semiconductor industry owes a significant tribute to lithography for having made possible much of the tremendous progress in integrated circuit technology and performance over the past 30 years. Higher speed transistors, higher packing densities and lower power dissipation in complementary metal oxide semiconductor (CMOS) circuits were obtainable thanks to advances in lithographic technology capable of achieving increasingly smaller features.

However, the more and more stringent specifications required as final outcome of the lithographic process (such as dimension tolerances of 10 nm or less and positioning accuracy of 1 nm or less) depend on two distinguished but combined features: the lithographic machines (exposure tools) and the resists chemistry (imaging or recording media). These two main components, that can be also called *top-down* or *bottom-up* approaches, are now fully recognized as forming a crucial and highly interdependent foundation for advanced lithography. In particular, the combination of top-down and bottom-up techniques will allow for even more functionality to be joint within a single miniaturized device.

Up to 2000, scientists mainly struggled to improve the resolution of lithographic machines, i.e., decrease the critical dimension (CD) from several micrometers to several tens of nanometers, considering resist technologies as less critical since the traditional photoresists, such as poly(methyl methacrylate) (PMMA) or DNQ-Novolac (DNQ is diazonaphthaquinone), could largely accommodate the sub-micrometer resolution of industrial lithographic machines available on the early 1990s.<sup>[1,2,3]</sup> Therefore, extreme ultraviolet (EUVL), X-ray (XRL), electron beam (EBL), and ion beam (IBL) lithographies have been developed so far to achieve smaller and smaller features down to 5 nm (refer to Table 1.2), since it is widely accepted that the shorter the radiation wavelength the finer the resolution, as already discussed in Chapter 1.

It is then clear that with the advent of prototypes of sub-100 nm resolution exposure tools the need for higher performance and higher contrast resists was imperative. Photoresists generally belong to *polymer* systems (PMMA, novolac), but they have posed some deficiencies, such as etch resistance, high-temperature stability, pattern collapse, line-edge roughness. Recently, other classes of materials have then attracted the attention. In fact, it has been demonstrated that inorganic resists are capable of exhibiting a higher contrast and etch resistance than standard organic resists; however their intrinsic lower sensitivity and complex deposition methods make them more suitable for IBL. Hence, the strategy of mixing properties of both organic and inorganic resists led to the development of engineered hybrid organic-inorganic resists which offer an optimum combination of high contrast for sub-100 nm resolution and high sensitivity for a large throughput, acting as optimum resists for a given lithographic technology [4].

Therefore, the research activity on new lithography materials, alternative to widespread used polymeric systems, has known increasing development in recent years, in particular as regards the synthesis of sol-gel resists with innovative properties, suitable to avoid a material sacrificial use in the lithographic process and to satisfy specific performance demands (i.e. refractive index, porosity, etc.).

The next section highlights selected organic and inorganic resists. Finally, an in-depth analysis of hybrid organic-inorganic materials and their use as resists will be given.

## **2.1. Photoresists: a survey**

*Photoresists* are sensitive materials that undergo photochemical reaction when exposed to a particular source (UV light, X-rays or electrons). The chemical modifications upon irradiation produce a change in solubility in specific developers. The main role of a photoresist is to "resist" the actual pattern formation steps, i.e. etching, ion implantation, metal deposition. Therefore the resist film that remains after the development functions also as a protective mask. The resist film must "resist" the etchant and protect the underlying substrate while the bared areas are being etched.

As previously discussed, resist materials can be one of two kinds: (1) a sacrificial resist, where the material is used as an etch mask to create patterns in a substrate or (2) a functional material, where the patterned material directly becomes part of a device. Functional materials are more difficult to design as they have to satisfy both the lithographic process constraints for

achieving a high-fidelity micro and nanopattern, and satisfy the properties required by the device over the course of the life of the device.

The typical photoresist mixture is made up of a resin, which is the binder that provides mechanical properties (adhesion, chemical resistance), a solvent used to dissolve the resin, allowing the resin to be applied in a liquid state, eventually a photoactive compound (PAC) which inhibits or promotes the dissolution of the resin in the developer.

As previously mentioned in Chapter 1, photoresists are classified into two groups: positive resists and negative resists depending on the leachable areas of the exposed film after irradiation through a mask, Figure 2.1.

- A *positive resist* is a type of photoresist in which the portion of the photoresist that is exposed to light becomes soluble to the photoresist developer. In these resists, exposure to UV light changes the chemical structure of the resist so that it becomes more soluble in the developer. The exposed resist is then washed away by the developer solution, leaving windows of the bare underlying material. The mask, therefore, contains an exact copy of the pattern which is to remain on the wafer, as a stencil for subsequent processing.
- A *negative resist* is a type of photoresist in which the exposed areas of the photoresist become crosslinked/polymerized, and more difficult to dissolve in developer. Therefore, the negative resist remains on the surface of the substrate where it is exposed, and the developer solution removes only the unexposed areas. Masks used for negative photoresists, therefore, contain the inverse or photographic "negative" of the pattern to be transferred.

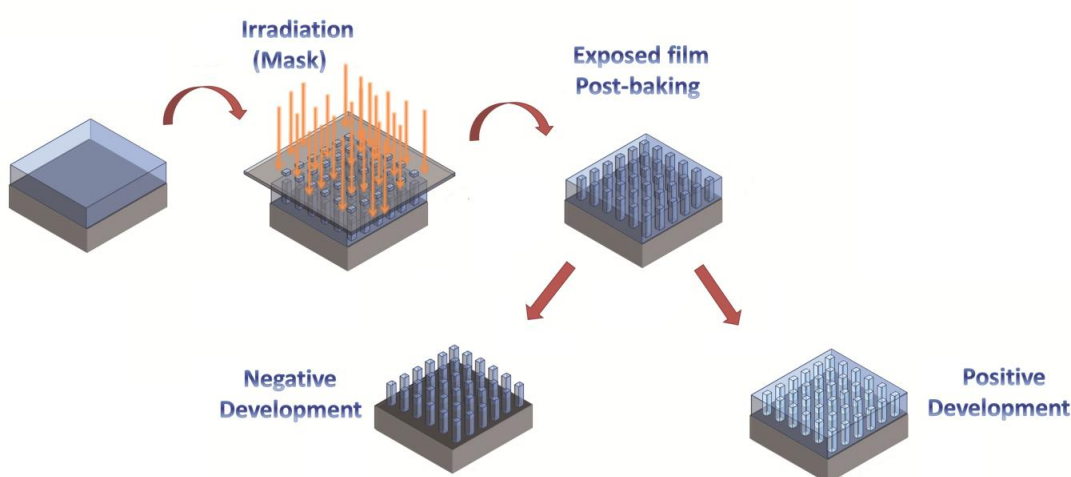


Figure 2.1 Pattern realization in a negative and positive resist

As stated by the Grotthuss and Draper Law (1817) the chemical changes that can only be produced in a system by absorbed radiation is the Principle of Photochemical Activation. Therefore, to produce a change in electronic structure of a molecule (bonds), the absorbed energy should be comparable with the bond energy. For instance, the C-H, C-C and C-O bonds possess energy around 3.5eV, corresponding to radiation in the UV range (5-3eV). A rearrangement in the chemical bonds of the materials can then be produced through photoexcitation, i.e. electron excitation by photon absorption, that can lead either to bond breakage (photolysis) or to the formation of new bonds between the excited molecules (polymerization and crosslinking). This principle is at the basis of the different behaviour of positive and negative resists, Figure 2.2.

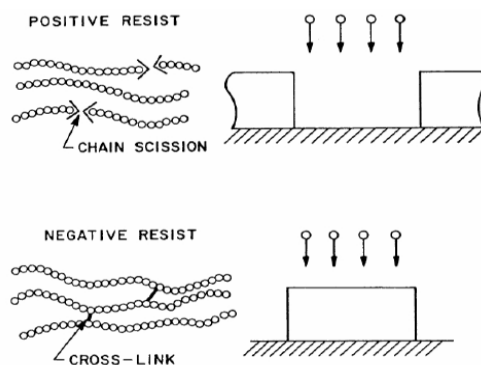


Figure 2.2 Positive and negative resist mechanism: photolysis and polymerization or crosslinking

In the simplest positive resists (i.e. PMMA, PS), several different free radicals are generated upon exposure to light (photoproducts) and the final outcome is the breakage of the polymer backbone bonds, leaving fragments of lower molecular weight. A solvent developer selectively washes away the lower molecular weight fragments, thus forming a positive tone pattern in the resist film: the exposed areas are removed. Positive resists can be superior to negative photoresists because they do not swell during development, they are capable of finer resolution and they are reasonably resistant to plasma processing operations. A photoactive component can be added to the photoresist mixture but it has to accomplish to some physical requirements: its absorption spectrum needs to overlap with the emission spectrum of the exposure source, e.g. a Hg lamp, it has to be bleachable at the exposure wavelength so that the photoreaction is able to reach the resist-substrate interface, it has to be compatible with the base resin (for example novolac) so that the two form a single, miscible phase and finally it

has to possess high thermal stability so that the photoactive dissolution inhibitor does not break down at prebake temperatures.

In a negative resist, after exposure the sensitive compound adsorbs the optical energy and converts it into chemical energy to initiate a chain reaction cross-linking the polymer chains together, making them less soluble from the developer. The polymerization often occurs via a free-radical or acid-catalyzed (ionic) mechanism, Figure 2.3. The former mechanism generally uses photoinitiators which generates active species upon irradiation that react with the monomers. In the latter the curing agents belong to the ionic photo-acid generator compound and, for example to onium salt family: the light promotes the generation of a cationic-radical specie that react with the monomers.

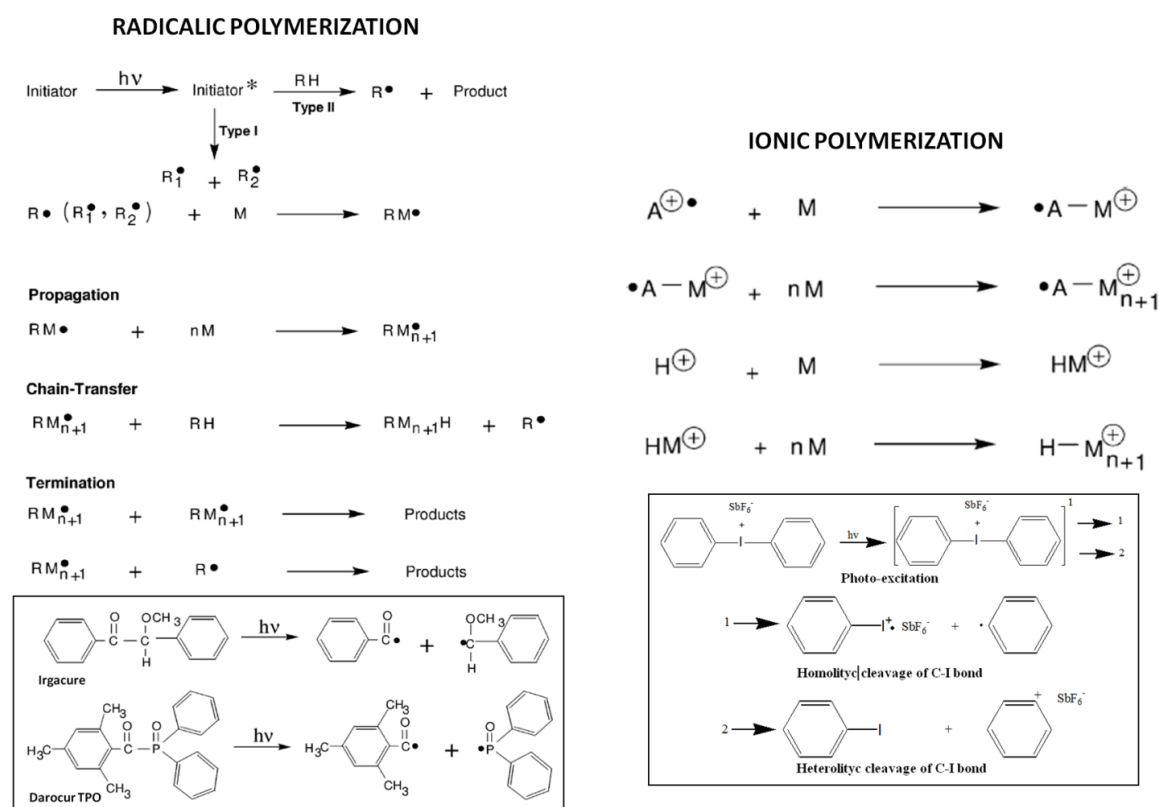


Figure 2.3 Mechanism reaction of radicalic and ionic polymerization together with examples of the corresponding photoinitiators: Irgacure and Darocur TPO for the former, diaryliodonium salt for the latter

Problems such as scum (insoluble residue in exposed areas), swelling during development, and bridging between features can all contribute to reduce the quality of the polymerized material. Moreover, the desired cross-linking that makes negative resist physically and chemically stable, also makes the photoresist removal difficult. A reasonable starting point for developing a negative resist process is to choose a development time twice as long as the time

needed to clear the unexposed resist and an exposure dose just sufficient to ensure an acceptable resist thickness loss on all the present features (e.g., no more than 10%) [17].

A key parameter, that influences both resolution and profiles, is the sensitivity and, thus, the resist contrast. By general convention, the *sensitivity*  $S$ , is related to the thickness,  $d$ , of the resist layer measured after exposure and development, and is obtained from exposure characteristic curves. The resist fraction remaining after development in an uniformly illuminated resist versus the logarithm of the applied exposure dose are described in the contrast curve. Idealized contrast curves for positive and negative resists are shown in Figure 2.4 by dot lines. To be precise the contrast curve is a property not only of the resist but it is a function of the entire resist process such as bake temperature and time, developer normality and time.

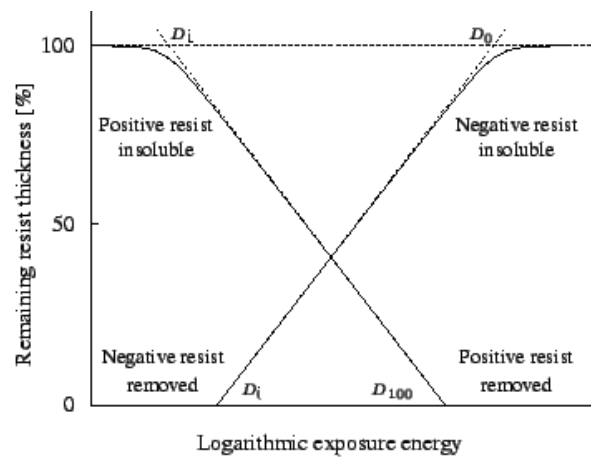


Figure 2.4 The contrast curve is a logarithmic sensitivity plot showing resist thickness versus exposure energy. The contrast is defined as the linear slope of the transition region and describes the ability of the resist to distinguish between light and dark areas.

In the case of positive resists,  $S \equiv D^{100}$  corresponds to the exposure light dose required to completely remove the irradiated polymer from the substrate, i.e. the dose at which the normalized thickness of the resist layer is equal to zero,  $d_{irr}/d_0=0$ . The sensitivity of a positive resist is defined as the energy required to produce complete solubility in the exposed region. Thus,  $D^{100}$  corresponds to the sensibility. In addition to  $D^{100}$ , a parameter  $\gamma$ , the *contrast ratio*, is defined to characterize the resist:

$$\gamma \equiv \left[ \ln \left( \frac{D^{100}}{D_i} \right) \right]^{-1}$$

where  $D_i$  is the energy obtained by drawing the tangent at  $D^{100}$  to reach the 100% resist thickness as shown in Figure 2.4. Typical  $\gamma$  values range from 2-3. A large  $\gamma$  implies a more rapid solubility of the resist with an incremental increase of exposure energy and results in sharper images. The edge of the resist image corresponds to the position where the total absorbed optical energy equals the threshold energy  $D^{100}$ .  $D$  is the product of the light intensity and irradiation time, and is commonly given in units of  $\text{mJ cm}^{-2}$ .

The negative resist remains completely soluble in the developer solution for the exposure energies lower than the threshold energy  $D_0$ . After  $D_0$ , more of the resist film remains after development. The sensitivity is reported as  $S \equiv D^{0.5}_0$  or sometimes as  $S = D^{0.8}_0$  or  $S = D^{0.9}_0$ , corresponding to  $d_{irr} = 0.5D_0$ ,  $d_{irr} = 0.8D_0$  or  $d_{irr} = 0.9D_0$ , respectively. The contrast is calculated as:

$$\gamma \equiv \left[ \ln \left( \frac{D_0}{D_i} \right) \right]^{-1}.$$

A higher sensitivity, corresponding to a lower exposure dose, implies a faster production rate. Differently, for nanoimprinting technique, the “resist” is not structured by radiation but by pressure (see paragraph 1.5 and 2.5) and heating, such as thermoplastic material.

With the concept of resist contrast now defined, it is now possible to discuss the importance and impact of resist contrast in the lithographic process. The most common exposure method in use today is projection printing: an image of the mask pattern is projected onto the resist coated wafer, refer to paragraph 1.2. Due to distortions introduced by the imaging system, the “latent image” or intensity distribution at the wafer plane is not a perfect step function representation of the mask (see Figure 2.5). [5,6] It is the job of the photoresist to translate the smoothly varying aerial image projected by the exposure tool back into a crisp binary style relief pattern of the mask features. It is clear from Figure 2.6 that a non-linear response of the dissolution rate of the resist to exposure dose is required to accomplish this imaging task. In fact, for a resist with an infinitely high contrast (i.e. a resist that possesses a step function for a contrast curve), it would be possible to resolve images of a mask as long as there was any finite difference in intensity produced at the wafer plane by the exposure tool. The contrast of a photoresist is determined by a complex set of factors, and discussions of this subject can be found in the literature. [7]

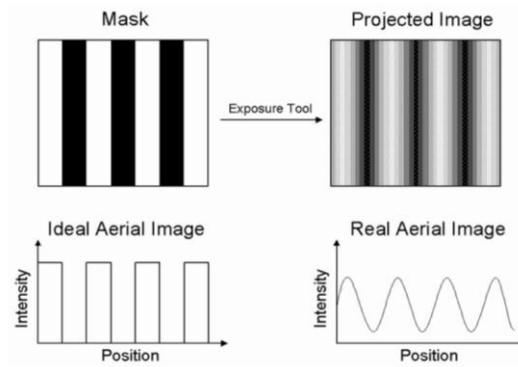


Figure 2.5 Comparison of real aerial image produced by projection exposure tools with ideal mask pattern.

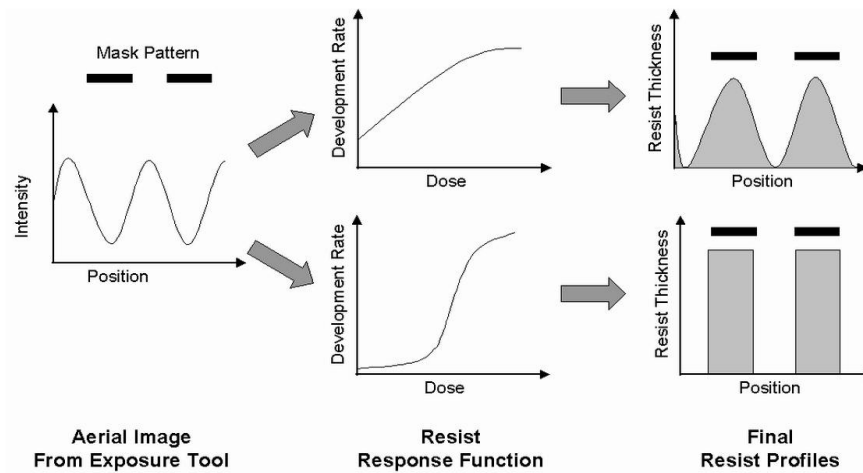


Figure 2.6 Illustration of the importance of a non-linear resist response to exposure dose. A resist that displays a linear rate versus dose behavior will reproduce the sinusoidal behavior of the aerial image, while a non-linear resist response can reproduce the desired binary image from the mask in the final resist profiles.

In conclusion a resist material to be useful in device fabrication has to possess the following features:

- It must be applicable by spin coating into a thin and uniform film that adheres to various substrates such as metals, semiconductors, and insulators
- It must possess high radiation sensitivity and contrast
- It must possess high resolution capability, dictated by molecular size, weight of the resist, chemical structure, reactivity to electrons or light, compositional non-uniformity
- It must give high aspect ratio structures withstanding pattern collapse during development



- It must withstand extremely harsh environments, for example, high temperature, strong corrosive acids, and plasmas used in subsequent etching, doping and sputtering operations.

## 2.2. Traditional photoresists - Organic resists

Over the past decades, many different types of resist materials have been investigated. Between 1952 and 1974, a negative resist called KODAK KTFR was widely used in semiconductor industry, Figure 2.7. It was composed of partially cyclized *cis*-isoprene (with single, double or triple ring structures), as crosslinker agent a diazido benzophenone, mixed in a 4:1 wt ratio and as a solvent: a mixture of butylacetate, ethylacetate and 2-butanol. Hg lamps were used as exposure tools.

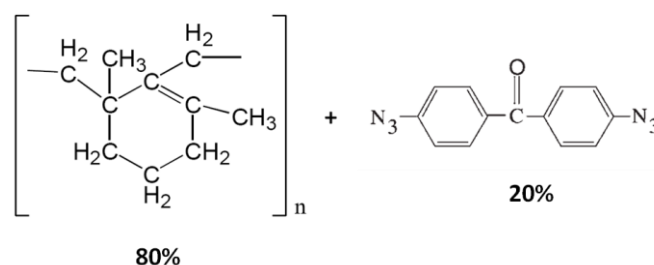


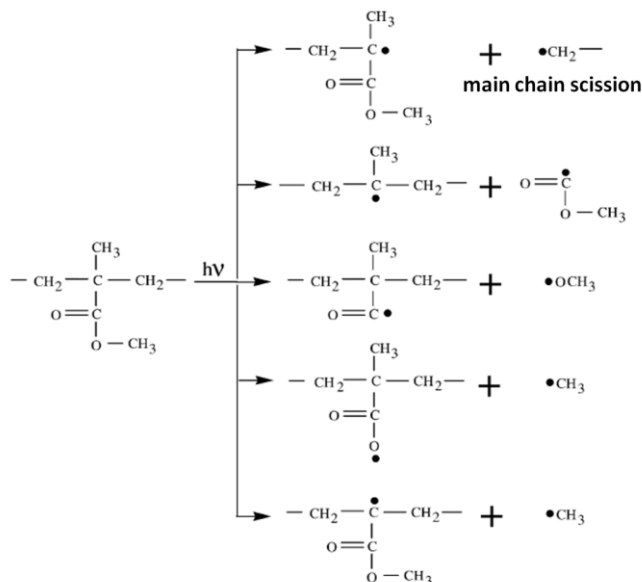
Figure 2.7 Negative resist KODAK KTFR formulation: poli-*cis*-isoprene and diazido benzophenone (crosslinker agent), mixed in a 4:1 wt ratio

Nowadays, traditional polymeric materials can be either single or multiple component formulations. Among these, two types of resists have received special attention. One is chain-scission resists designed for EBL. The other is chemically amplified (CA) resists designed for both deep ultraviolet (DUV) and EBL.

The simplest chain-scission resists are *single component materials* such as poly(methyl methacrylate), or PMMA, which is used as a resist in electron beam lithography. PMMA is dissolved in a casting solvent, for example, polypropylene glycol methyl ether acetate (PGMEA). Thin films are obtained on silicon wafers by spin-casting from the PMMA solution. The wafers are prebaked at a suitable temperature to remove the solvent. The films are then exposed to an electron beam, followed by developing in a suitable developer solution. The molecular weights of the polymer in the exposed regions are decreased via chain-scission by e-beam irradiation.

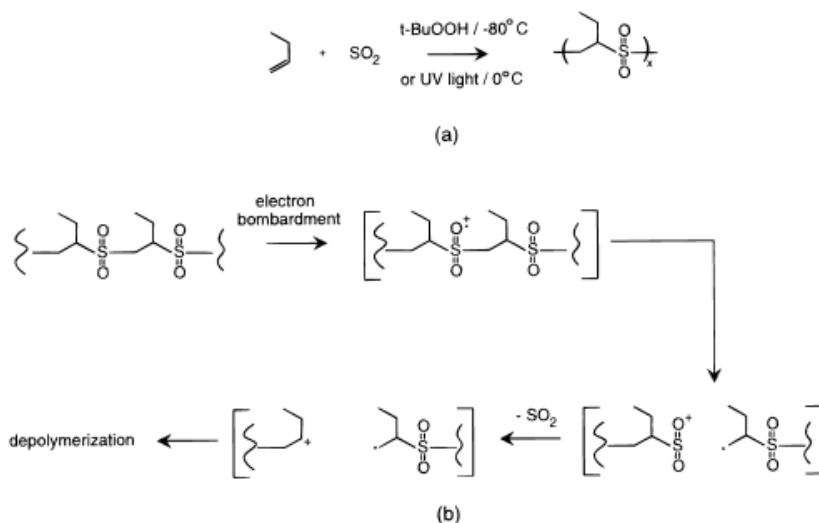
PMMA can undergo several reactions upon exposure to UV with formation of a multiplicity of photoproducts, Scheme 2.1. However the breakage of the principal chain is not favoured

and its use as a photoresist is possible due to the leakage of the functional groups that alters the chemical-physical properties of the polymer. This reduction in molecular weight causes the PMMA to dissolve orders of magnitude faster in the appropriate developing solvent, resulting in the ability to pattern the resist. PMMA is typically used for EBL because it offers high resolution with low cost and ease of process.



Scheme 2.1 PMMA chain scission upon UV exposure

Other commercial e-beam resists include ZEP520 (Nippon Zeon Co), poly(butene-1-sulfone) (Scheme 2.2) and poly(2,2,2-trifluoroethyl- $\alpha$ -chloroacrylate) (EBR-9, Toray Inc.).



Scheme 2.2 Electron-beam resist chemistry, illustrated for poly(butene-1-sulfone): (a) polymer synthesis, (b) proposed polymer fragmentation pathway

With its higher sensitivity [8] and etching resistance than PMMA, ZEP520 (positive-tone, Zeon Corp.) is arguably the second most popular chain-scission-type positive EBL resist: it shows in fact a sensitivity of 3-9  $\mu\text{C}/\text{cm}^2$  compared to  $\sim 100\text{-}300 \mu\text{C}/\text{cm}^2$  of PMMA [9]. ZEP-520 is a copolymer of  $\alpha$ -chloromethacrylate and  $\alpha$ -methylstyrene (Mw approx. 55 000) which has been used to pattern features as small as 10 nm with high energy (70 keV) exposures [10]. The molecular formula and some examples of patterns obtained using ZEP-520 are reported in Figure 2.8.

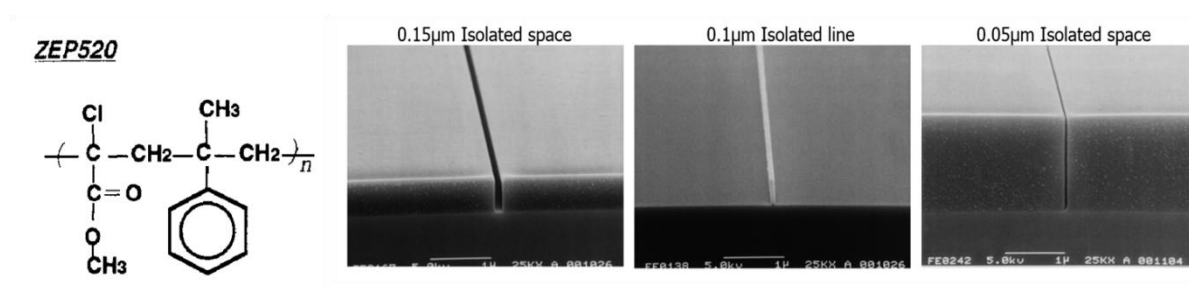


Figure 2.8 ZEP520 molecular formula; examples of patterns obtained with ZEP520 (positive-tone, Zeon Corp.)

However, for some applications, such as the fabrication of hole arrays in a metal film by using lift-off, negative resist would offer substantially shorter exposure time, except when using a more complicated "resist tone reversal" process [11]. Unfortunately, there is no negative resist that gains similar popularity as PMMA and ZEP520. A negative resist like PMMA, which is a simple polymer with low cost and practically unlimited shelf life, that can be dissolved easily using various solvents to give the preferred film thickness is polystyrene. This resist undergoes crosslinking when exposed to deep UV light or an electron beam. Dense periodic patterns with 40-nm period lines have been demonstrated using low molecular weight polystyrene resist [12], and the ultimate resolution (half-pitch for dense periodic structure) was demonstrated to be 20-nm-period lines and 15-nm-period 2D dot arrays, Figure 2.9. Besides ultrahigh resolution, polystyrene is more (by approximately  $3 \times$ ) resistant to dry etching than PMMA. Its major drawback is its low sensitivity compared to PMMA, which would limit its application to small scale nano-patterning [13].

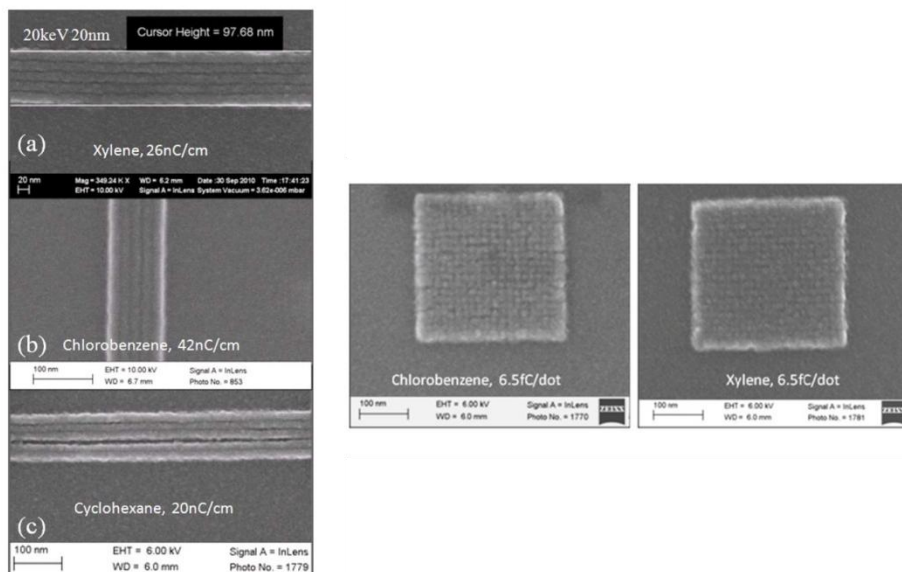
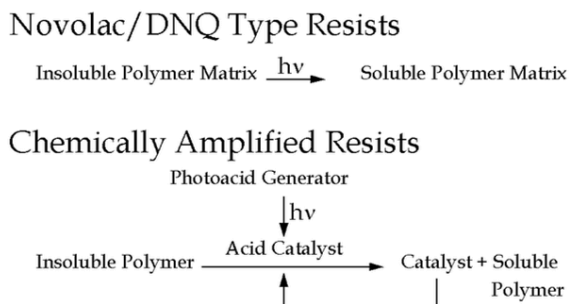


Figure 2.9 On the left: dense line arrays with a period of 20 nm exposed at 20 keV and developed at room temperature for 90 s using (a) xylene; (b) chlorobenzene; and (c) cyclohexane. The lines in (c) collapsed due to capillary force during resist drying; On the right: dense 2D dot array with a period of 15-nm exposure at 5 keV and developed by chlorobenzene and xylene for 1.5 min at room temperature.

The majority of resists used in semiconductor production today are *multi-component formulations*. In general, these multi-component resists can be classified as either non-chemically amplified (diazonaphthoquinone-novolac type resists) or chemically-amplified (CA). The basic operation of these two types of resists is shown in Scheme 2.3. The diazonaphthoquinone-novolac, or DNQ-novolac, resists have been the workhorse for the semiconductor industry for over 20 years and continue to be the most widely used resist technology in high volume semiconductor production today. [14]



Scheme 2.3 Comparison of chemically amplified and non-chemically amplified resist function.

DNQ-novolac resists consist of a phenolic novolac resin, a diazonaphthoquinone (DQ) type dissolution inhibitor, and an organic casting solvent. The novolac resin provides the physical

properties required in the photoresist such as good film forming characteristics, etch resistance, and thermal stability. The DQ provides a photochemical route to modify the dissolution rate of the resist in aqueous alkaline developers. Finally, the organic solvent has properties that provide the ability to spin coat the resist to form uniform, glassy thin films.

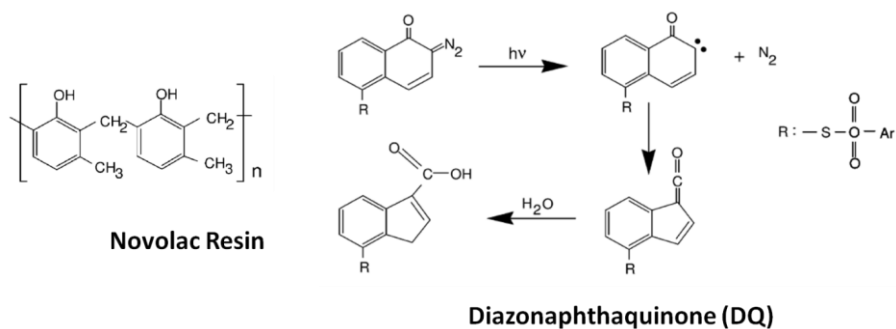


Figure 2.10 two main components of DNQ-Novolak Resists; the reaction of DQ upon irradiation

The phenolic novolac resins are generally hydrophilic because of the presence of the OH groups, therefore are readily dissolved by aqueous alkaline solutions. However with addition of diazonaphthaquinone (DQ), a hydrophobic and nonionizable compound, the phenolic resins become hydrophobic and their dissolution is greatly inhibited. After exposure, DQ is converted into indene carboxylic acid (ICA) which is hydrophilic and very ionizable, Figure 2.11. This allows the developer to wet and penetrate the novolac resin. Phenolic resins which contain ICA instead of DQ are readily dissolved by aqueous alkaline developers (such as TMAH). In order for the novolac resin to dissolve into the aqueous solution, hydroxide ions from the solution must first deprotonate some of the phenolic sites on the novolac chain. In this way, dissolution of novolac into aqueous developers is more similar to an etching process, such as copper dissolving in an acidic solution.

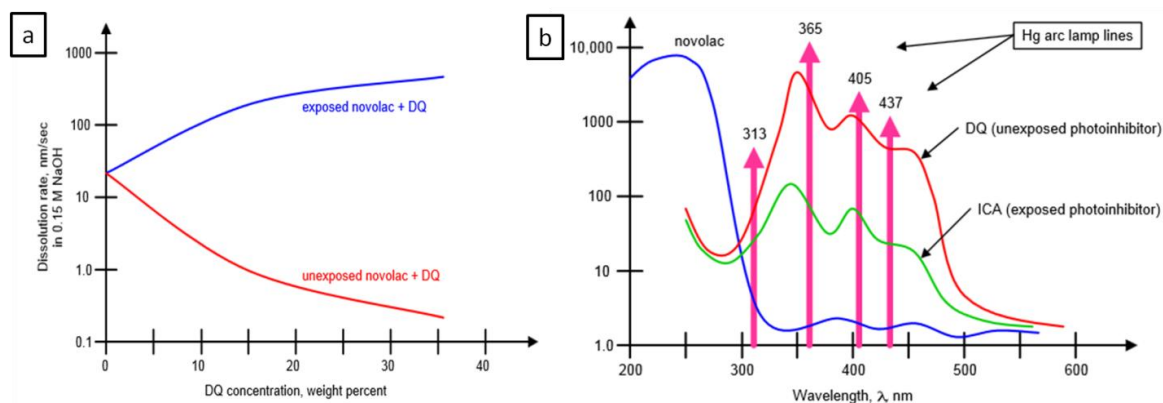
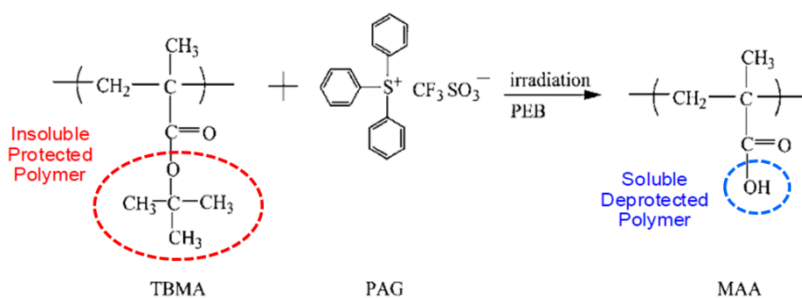


Figure 2.11 (a) development rate of unexposed and fully exposed mixtures of a DQ type inhibitor and a novolac resin; (b) UV-Vis absorption spectrum of novolac resin, DQ and ICA

Unfortunately these resists are not suitable for use at deep-ultraviolet (DUV) wavelengths (250 nm), the succeeding evolutionary step in the progression of optical lithography tools to higher resolution. In fact in DUV exposure tools based on KrF excimer sources the requirements imposed by the design of the exposure tool projection optics (specifically the introduction of optical line narrowing elements to minimize the effects of chromatic aberration) leads to a significant reduction of the light intensity at the wafer plane. In practice, regardless of the light source, DUV photoresists require approximately a 10x improvement in photoefficiency compared to DQ-based resists. One way of achieving this increased efficiency is via the photochemical generation of an initiating species or catalyst that is active in subsequent thermal reactions, such as in chemically amplified (CA) resists.

CA resists function by a different mechanism.<sup>[15]</sup> They are called CARs because a single photon can produce a reactive species, usually an acid, which can catalytically carry out multiple additional reactions. Thus, the required number of photons, or dose, to effect an equivalent solubility change is greatly reduced in CARs relative to non-CARs. Instead of chain scission, the solubility differentiation between the exposed and unexposed regions is realized by an acid-catalyzed deprotection reaction, which changes the polarity of the polymer in the exposed regions. CA resist consists of a matrix copolymer, whose key component is a deprotection unit, and a photoacid generator (PAG). PAG loadings are typically 1-5 wt% of the total solids, although the proportion is increasing in newer formulations. Upon irradiation, for example, of DUV or e-beam, the PAG generates a strong acid which, in the subsequent postexposure-bake (PEB) process, catalyzes the deprotection reaction. The overall outcome is that the solubility of the resist in a developer is differentiated between the exposed and unexposed regions, allowing to obtain either positive or negative images



Scheme 2.4 Deprotection reaction in a CA resist containing tert-butyl methacrylate (TBMA) as deprotection units

Scheme 2.4 depicts the deprotection reaction in a CA resist containing tert-butyl methacrylate (TBMA) as deprotection units. Other components of CA resists include methyl methacrylate,

acrylic acid, and moieties to increase high carbon content, such as aromatics or bicyclics, e.g., norbornene which is incorporated to increase the reactive ion etch resistance (RIE) for pattern transfer to the substrate. Moreover, it is believed that the CA concept offers the dominant strategy for the design of new resists not only for optical but also for EBL and XRL.

Other chemically amplified resists to use in the DUV spectral range are epoxide rings-containing polymers: the strong acid formation due to the presence of a photoacid generator leads to the ring opening and the crosslinking of the polymer which becomes insoluble in particular solvents (negative tone).

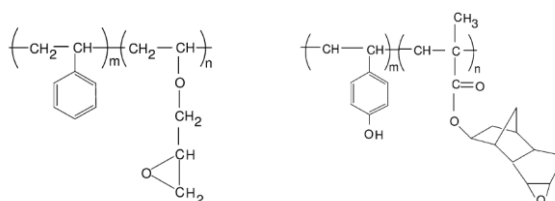


Figure 2.12 Epoxide rings opening in negative-tone resists

Another chemically amplified resist being developed at IBM originally designed as a deep-UV and as a potential projection EBL resist (KRS-XE) is based on the partial protection of poly(hydroxy styrene) with an acid sensitive ketal group of low volatility. The protecting group has a low deblocking activation energy and an extremely high reaction rate. Therefore the chemical amplification occurs rapidly after exposure at room temperature without a postexposure bake, in contrast to most chemically amplified resist systems. This resist also contains triphenyl sulfonium triflate as an acid generator and a proprietary additive. [16] It shows high contrast (>10), and resolution down to 30nm allowing to obtain images with aspect ratios as high as 6.

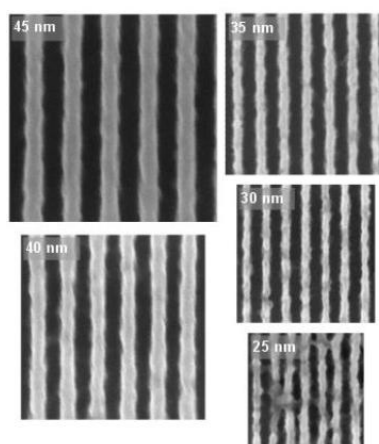


Figure 2.13 Equal Line Space Images Ranging from 45 to 25 nm Printed in Experimental KRS Resist Provided by IBM. The imaging performance degrades rapidly for sizes below 35 nm, indicating a resist limit [17]

Other chemically amplified negative EBL resists are SU-8 and mr-L 6000 (Microresist Technology) which, in comparison to ZEP520, offer superior sensitivity, but with low contrast and resolution (more strictly speaking, half-pitch for dense periodic line array patterns), which is limited by the diffusion of the photoacid generator during postbaking. The SU-8 is a negative, epoxy-type, near-UV photoresist based on EPON SU-8 epoxy resin (from Shell Chemical) that has been originally developed, and patented (US Patent No. 4882245 (1989) and others) by IBM. Two companies have now bought a license from IBM to sell the photoresist: Microchem Corp. and Gersteltec SARL. The resist is supplied as a liquid consisting of an epoxy resin, a solvent (GBL or cyclopentanone depending on formulation) and a photo-acid generator. Upon exposure to UV radiation, a strong acid (HSbF<sub>6</sub>) is generated which causes the epoxy resin to form a ladder-like structure with a high cross-linking density when heated above a critical temperature provided in a post-exposure bake. The unexposed material is then removed with a solvent, such as 1-Methoxy-2-propanol acetate.

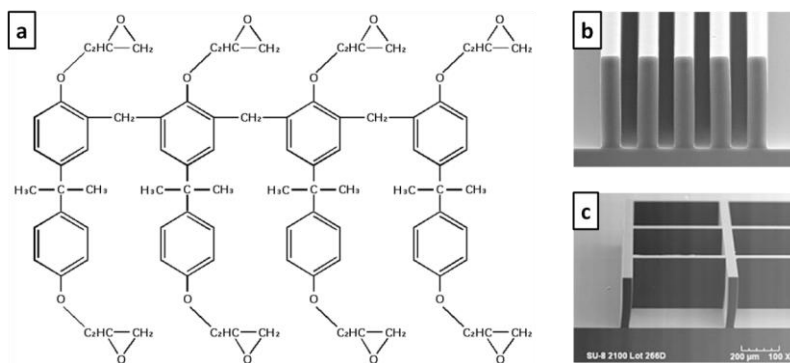


Figure 2.14 (a) SU-8 molecule; (b) 10 μm features in 50 μm SU-8 3000 (contact expose) (c) 25 μm wide, 125 μm high SU-8 2000 (Source: MicroChem)

SU-8 is highly transparent in the ultraviolet range. This allows for the fabrication of relatively high aspect ratio ( $> 20$ ) structures (thanks to the high viscosity which allows to obtain thick-hundreds of micrometers-films) with nearly vertical side walls. Because of the highly cross-linked matrix in the exposed material, it is thermally stable (up to 200°C) and chemically stable after development. It is now mainly used in the fabrication of microfluidics (mainly via soft lithography, but also with other imprinting techniques such as nanoimprint lithography) and microelectromechanical systems parts.

However, a drawback in most of CARs is that spatially nonuniform distribution of acid formed by the imaging exposure as well as photoacid diffusion in the exposed regions of the



film to effect deprotection can cause a decrease of resolution and definition of the pattern with problems of image blur and line edge roughness (Figure 2.15).

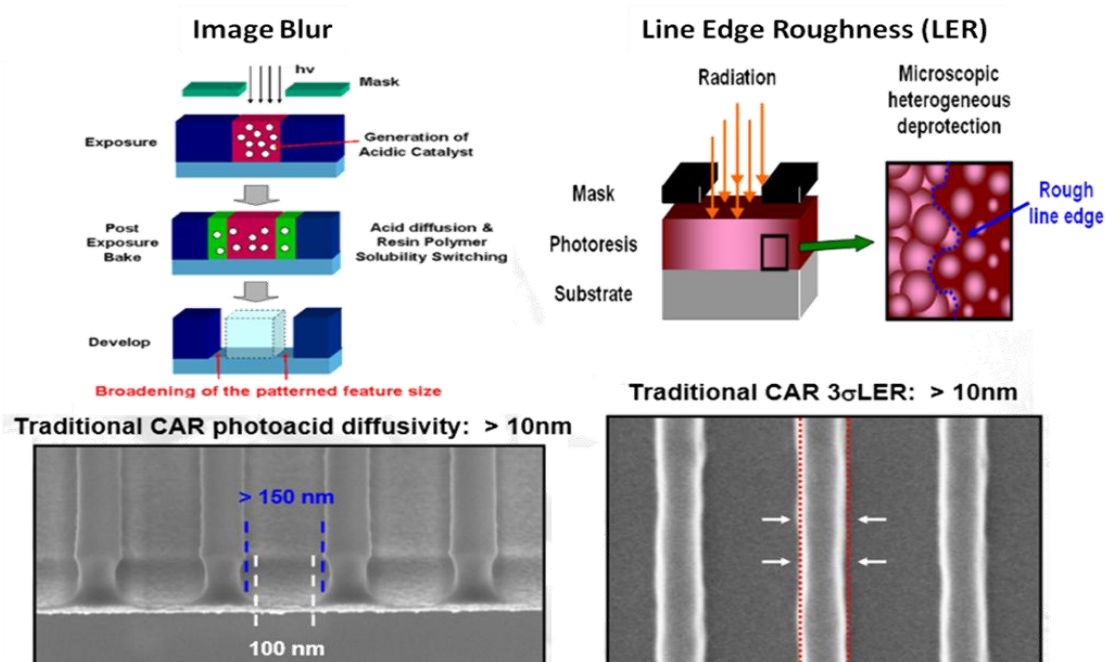


Figure 2.15 image blur and line edge roughness problems in CAR [18]

The other major new family of resists that has been developed to improve performance and overcome the drawbacks of the above mentioned resists is *molecular glass resists or molecular resists*. Molecular glasses are low molecular-weight organic compounds that readily form stable amorphous glasses and show glass transitions usually associated with polymers. They were developed considering that the resolution of the resist depends not only on the chemical structure or on its reactivity to electrons or light, but also on its molecular size and weight, Figure 2.16.

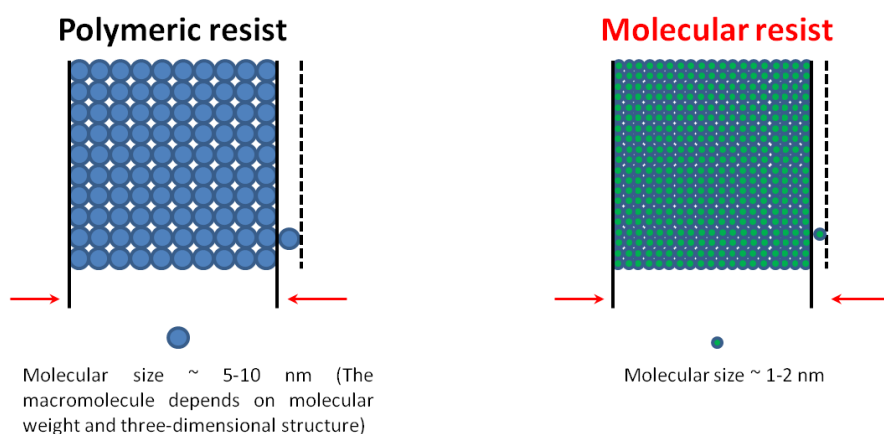


Figure 2.16 Increased resolution for molecular resist compared to polymeric resist

Therefore their monodispersity, unique dissolution behaviour, and very low molecular weight can produce significantly different behaviour and patterning performance as compared to polymeric resist materials using similar imaging reactions and functional groups.

Molecular glasses were first reported to be used as photoresists in 1995 by Fujita *et. al.*, who used a calixarene derivative (hexa acetate *p*-methylcalix[6]arene) to obtain sub-10nm resolution using electron beam (e-beam) lithography, Figure 2.17.[<sup>19</sup>]

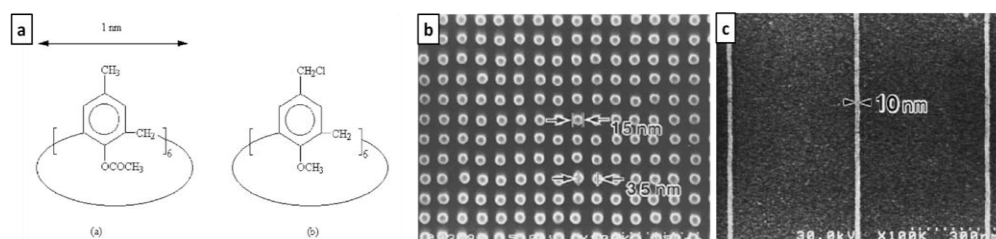


Figure 2.17 (a) Calixarene derivatives: a) Hexaacetate *p*-methylcalix[6]arene (MC6AOAc), b) hexachloromethoxycalix[6]arene (CMC6AOMe). Molecular weights ( $M_w$ ) are 972 and 996, respectively. The molecular diameter is approximately 1 nm for both. (b) MC6AOAc dots pattern: 15 nm diameter, 35 nm pitch [<sup>20</sup>]; (c) SEM image of calixarene resist pattern on Ge [<sup>19</sup>].

Calixarene is a discrete molecule, and therefore monodisperse, with a molecular weight of 972 and a molecular diameter of about 1 nm (Figure 2.17a). In contrast, other phenol-based resists have molecular weight dispersions from 1000 to 10000, which set a resolution limit. Hexaacetate *p*-methylcalix[6]arene exhibited high durability to halide plasma etching, allowing to obtain little line edge roughness at 10 nm resolution, but a low sensitivity (20 times lower than that of PMMA).

Since then, several molecular glasses based on star-shaped molecules, calixarene derivatives, dendrimers, polyphenols, and cholates have been applied as resist materials. Examples of molecular resists are reported in Figure 2.18.

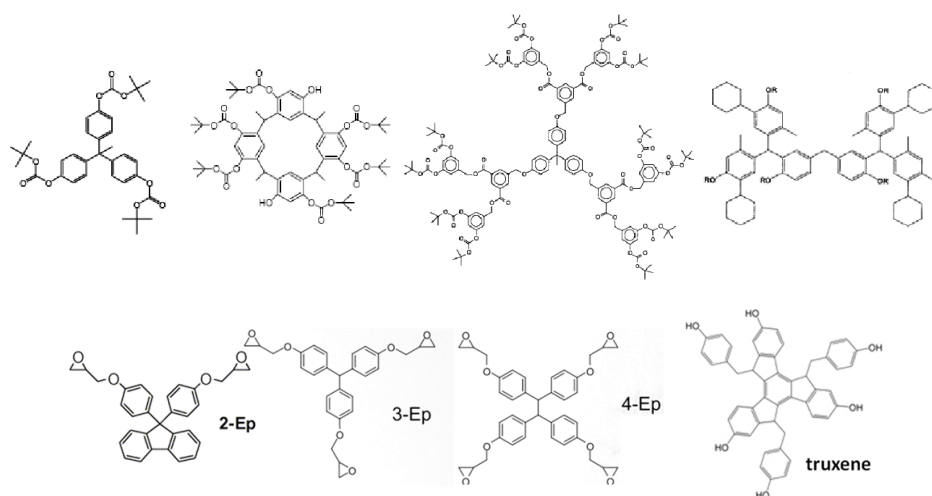


Figure 2.18 Examples of molecular resists

Fullerene and its derivatives have also been used as e-beam molecular resists by themselves and in mixture with ZEP 520 for nanolithography, Figure 2.19. Fullerene  $C_{60}$  is a small molecule approximately 1 nm in diameter, whose photon-induced polymerization reduces its solubility in toluene allowing to use it as a e-beam negative resists. Patterns with a resolution of 20 nm in silicon were obtained. [21] Fullerene  $C_{60}$  derivatives were also used, such as the tris fullerene derivative (TrAF), showing a better sensitivity and a different response mechanism to the e-beam: a fragmentation mechanism of the  $C_{60}$  cage instead of a polymerization reaction as in  $C_{60}$ . [22]

The sub-nm  $C_{60}$  molecules were also incorporated into ZEP520 [23,24]. The basic idea behind the design of this concept was that the  $C_{60}$  molecule (diameter of approx. 0.7 nm, which corresponds to the length of four to five C-C bonds in the ZEP520 molecules) can reduce the free volume in the polymer resist thin films, leading to a higher softening transition ( $T_g$ ), increased rigidity due to increased density of the film leading to improved mechanical and etch resistance.

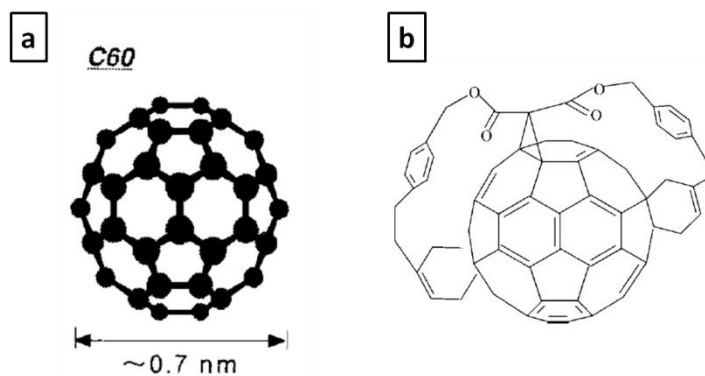


Figure 2.19 (a) Sub-nm  $C_{60}$  molecule (b)  $C_{60}$  tris adduct fullerene (TrAF) [4].

Therefore, it has been assumed that molecular glasses offer advantages over polymeric resists:

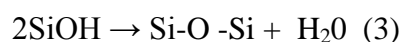
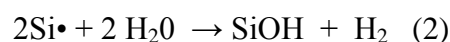
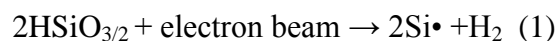
- they are much smaller in molecular size, thus leading to improved line edge roughness;
- they do not suffer from intermolecular chain entanglement like polymers that can lead to internal stress or swelling and pattern distortion
- they are identical molecules and monodisperse, producing homogeneous films, with no segregation
- they are single molecules, allowing to control their properties and functionality

- they are about the same size as many resist additives such as PAGs which could potentially result in more uniform distribution of resist additives due to better phase compatibility.

However, due to the difficulty in finding organic materials with acceptable absorbance characteristics for Deep and EUV lithography other inorganic molecular resists were developed. Among them Hydrogen silsesquioxane (HSQ) will be discussed in the next paragraph “Inorganic Resists”.

### 2.3. *Inorganic resists*

HSQ ( $\text{HSiO}_{3/2}$ , Dow Corning), Figure 2.20a, belongs to the POSS family, Polyhedral Oligomeric Silsesquioxane (POSS), cage compounds with defined mono-disperse molecular weights and size approximately 1-1.5 nm. They generally consist in a silicon-based inorganic cage ( $\text{Si}_8\text{O}_{12}$ ) surrounded by eight organic corner groups, which in the case of HSQ are simply hydrogens H. HSQ is an inorganic three-dimensional polymeric-type material that upon electron irradiation undergoes cross-linking via Si-H bond scission, exhibiting a negative tone behaviour. It can be cross-linked by exposure to e-beam or EUV radiation with wavelengths shorter than 157 nm. The crosslinking mechanism is as follow: Si-H bonds, which are weaker than Si-O-Si bonds, are broken by e-beam, consequently siloxane bonds are formed via unstable silanol Si-OH, resulting from reaction to moisture.



This cross-linking results in HSQ having an amorphous structure similar to  $\text{SiO}_2$  that is relatively insoluble in alkaline hydroxide developers. Aggregates in HSQ are small owing to its three dimensional framework. In addition the excellent development property of HSQ avoids any influence from polymer aggregates on development. Consequently, linewidth fluctuation can be reduced to less than 2 nm. The resolution is then very high (below 10 nm) [25], thanks to its small molecular size and lack of swelling during development [26], as well as the dry etch resistance toward silicon (around 5-10) exhibited by HSQ, Figure 2.20. However, it exhibits low sensitivity and it is not suitable for liftoff unless when used with a double layer resist stack, such as HSQ coated on PMMA. Moreover, HSQ is unstable, and so spin coating, baking, exposure, and development must be done quickly [27].

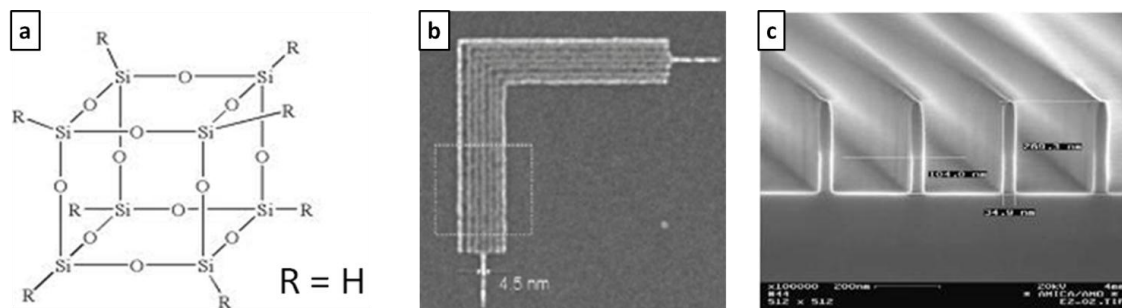


Figure 2.20 (a) HSQ cage ; (b) SEM image of 9-nm-pitch nested-L structures patterned in 10-nm-thick HSQ [25]  
 (c) 34nm polySi gate etch, HSQ masked, stopping on 3nm SiO<sub>2</sub> (Source: AMO).

Silica and Metal halides resists have actually demonstrated better resolution than HSQ, but they are not practical resists due to their extremely low sensitivity and inability to form arbitrary patterns [28].

Positive inorganic spin-On-Glass (SOG) materials have also been developed, such as Accuglass 512B (Honeywell Co. Ltd.) and Nano Imprint Mold Oxide-Positive tone 0701 (NIMO-P0701). Both resists have a siloxane structure which includes Si–O–R and Si–R (R=CH<sub>3</sub>), which are converted into Si–OH when exposed to EB readily soluble in BHF. However they exhibit lower sensitivity and resolution with respect to negative e-beam resists [29].

Regarding inorganic materials directly patterned and not used as sacrificial layers as the ones reported so far, it is worth mentioning the patterning of ceramic films by the so-called soft lithography techniques developed by the Whitesides Group at Harvard University in the 1990s [30-31-32]. In 2004 the Aksay Group published a general review on submicrometer-scale parallel patterning of ceramic materials [33,34] and Masuda and co-workers reported on the strategy of using UV-patterned SAMs for site-selective deposition of functional oxides [35-36]. Over the years, patterning of inorganic features obtained through the sol-gel method became a field that have attracted progressively more attention because of its important role and advantages in device realization. The versatility of sol-gel process can be exploited to synthesize functional sol-gel systems that at the same time behave as resist allowing the realization of selected patterns, strongly simplifying the realization of active devices. In most cases, the sol-gel structures are obtained by the deposition of a sol-gel solution on EB pre-pattern structure realized using commercial resists (resist template) [37]. After thermal treatment, the resist template is removed by a chemical solution, leaving only the sol-gel features, as shown in Figure 2.21.

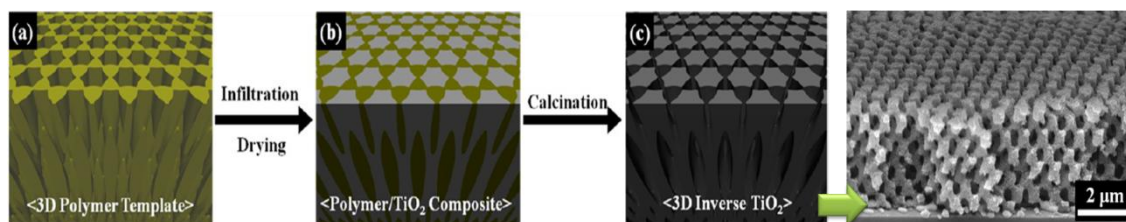


Figure 2.21 (a) Three-dimensional SU-8 polymer template. (b) Infiltrated polymer/titania sol-gel composite. (c) Three-dimensional titania inverse structures after calcinations and SEM image of an example of obtained titania 3D pattern

In conclusion, inorganic resists exhibit higher contrast, stability and etching resistance than standard organics, but they generally suffer from intrinsic lower sensitivity, complex processing and short shelf life. Therefore, organic resists are being combined with inorganic constituents to engineer hybrid organic-inorganic (HOI) resists as an emerging alternative class of resists for micro and nanolithography, having both solution processability together with higher performance, stability and wider choice of properties. In particular, thermal resistance ( $<300^{\circ}\text{C}$ ), mechanical strength (antiscratch) and chemical endurance (dissolution) typical of polymers can be improved by using HOI resists. Before describing the literature on HOI resists published so far a brief description of what the words “hybrid materials” stand for will be given.

#### 2.4. Hybrid organic-inorganic materials

The field of functional hybrid materials has been widely recognized as one of the most promising and rapidly emerging research areas in materials chemistry.

Hybrid organic-inorganic materials are not simply physical mixtures. A hybrid material is termed a molecular or nano-composites with organic (or bio) and inorganic components intimately mixed, if at least one of the components, organic or inorganic, has a dimension ranging from a few Å to several nanometers. Components making up the hybrids could be molecules, oligomers or polymers, aggregates and even particles.

In many cases the organic component allows an easy shaping and better processing of the materials while the inorganic components provide mechanical and thermal stability, but also new functionalities that depend on the chemical nature, the structure, the size, and crystallinity of the inorganic phase (silica, transition metal oxides, metallic phosphates, nanoclays, nanometals, metal chalcogenides). Indeed, the inorganic component can

implement or improve electronic, magnetic and redox properties, density, refraction index, etc., see Table 2.1.

Properties	Organics (polymers)	Inorganics (SiO <sub>2</sub> , TMO)
Nature of bonds	covalent [C-C] (+ weaker van der Waals or H bonding)	ionic or ionic-covalent [M-O]
$T_g$ (glass transition)	low (-100 °C to 200 °C)	high (>200 °C)
Thermal stability	low (<350 °C, except polyimides, 450 °C)	high (>>100 °C)
Density	0.9–1.2	2.0–4.0
Refractive index	1.2–1.6	1.15–2.7
Mechanical properties	elasticity plasticity rubbery (depending on $T_g$ )	hardness strength fragility
Hydrophobicity, permeability	hydrophilic hydrophobic $\pm$ permeable to gases	hydrophilic low permeability to gases
Electronic properties	insulating to conductive redox properties	insulating to semiconductors (SiO <sub>2</sub> , TMO) redox properties (TMO) magnetic properties
Processability	high: • molding, casting • machining • thin films from solution • control of the viscosity	low for powders (needs to be mixed with polymers or dispersed in solutions) high for sol-gel coatings (similar to polymers)

Table 2.1 Comparison of properties of conventional organic and inorganic components [<sup>38</sup>]

Numerous hybrid materials have been synthesized and processed by different chemical routes based on:

- *polymers and sol-gel chemistry*: starting from oligomers or polymers, the purpose is to improve or modulate mechanical, thermal or adhesion properties by the addition of an inorganic component, preserving a number of advantages due to the organic polymeric nature of the system (high flexibility, low density, ...). The conventional process is to mix together the polymer (or a prepolymer) and the inorganic particles or to obtain in situ the inorganic nanoparticles, leading to a more homogeneous material.

- *inorganic and sol-gel chemistry*: they can be obtained either through the impregnation of organic components (dyes or monomers) within sol-gel derived organosilicas-or hybrid metallic oxides or through the organic functionalization of nanofillers, nanoclays or other compounds with lamellar structures;

- *heterofunctional metallic alkoxides or silsesquioxanes*: precursors of this kind have the formula  $R_xM(OR')_{n-x}$  or  $_3(R'O)Si-R-Si(OR')_3$ . The hydrolysis of alkoxy groups (OR') followed by a condensation reaction will form the mineral network and the R groups will imprint in the network the organic function.

- self-assembly or templated growth, nano-building block approaches, hydrothermally processed hybrid zeolites or microporous metal organic frameworks, integrative synthesis or coupled processes, bio-inspired strategies, etc.



Consequently the properties of hybrid materials are not only the sum of the individual contributions of both phases, but the role of their inner interfaces could be predominant. The nature of the interface has been used to grossly divide these materials into two distinct classes:

- *Class I:* includes hybrids systems where one of the components (organic, biologic or inorganic) is entrapped within a network, Figure 2.22. Such systems are essentially based on weak-type interactions between the hosting network and the entrapped species such as Van der Waals, hydrogen bonding or electrostatic interactions. In the case of sol-gel synthesis, this type of materials is usually obtained by the simple mixing in a common solvent of the mineral precursor prior to hydrolysis with organic molecules or macromolecules. By this way, numerous materials have been prepared embedding organic dyes or optically active molecules. Silicon, titanium or zirconium alkoxides can also be mixed with various polymers dissolved in a common solvent leading to the in situ formation of mineral fillers. Class I materials can also be obtained by the simultaneous formation of the two components generally leading to high interpenetrating networks.

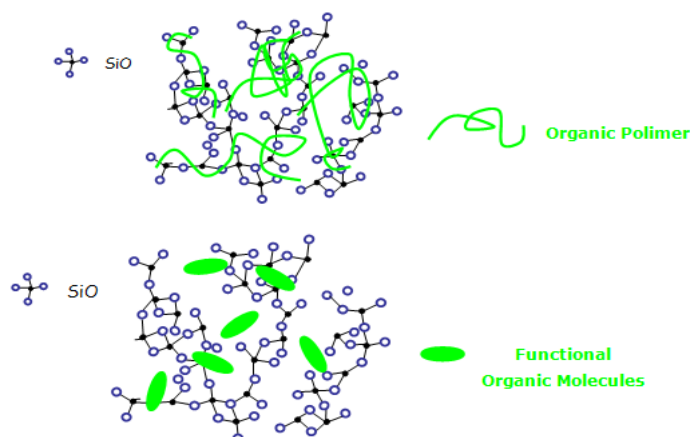


Figure 2.22 Structure of class I hybrid materials

- *Class II:* Hybrid materials where the inorganic and organic parts are chemically linked by a strong covalent or ionic-covalent bond. In sol-gel synthesis, the precursors of these systems are organically modified alkoxides  $R'_nSi(OR)_{4-n}$  where  $R'$  represent an organic functionality directly linked to the silicon atom and  $OR$  groups will be hydrolysed to achieve an inorganic network. The main feature of this bond C-Si is that it cannot be hydrolysed and the organic groups  $R'$  can have two different functions: *network modifiers* or *network formers*. If  $R$  is a simple non hydrolysable group, it will have a



network modifying effect (e.g., R containing an alkyl group or an organic dye). On the other hand, if R bears a reactive group that can polymerize (e.g., methacrylic, epoxy, vinyl or styryl groups) it will act as a network former if polymerized. This approach is no longer valid in the case of transition metals precursors. Transition metals (Ti, Ge, Zr, Hf..) are less electronegative than silicon and the M-C bond has a very high ionic character. This feature makes this link easily cleaved by water and by many nucleophilic species. In the case of transition metal, different strategies can be envisaged to overcome the hydrolytic instability problem such as: (i) the formation of stable M-O-Si-R bonds, (ii) functionalization by complexing groups. The use of complexing organic ligands L like carboxylic acids,  $\alpha$ -hydroxyacids, or  $\beta$ -diketones - with an anchoring function and a general organic group- leads to the formation of modified metallic alkoxides  $M(OR)_{m-n}(L)_n$  and opens a wide range of possibilities. Modification of the kind, structure and proportions of the organic ligand and inorganic constituents allows, in principle, a tailoring of properties.

In conclusion, the nature of the ligand organic group can greatly influence the final structure and properties of the material. It can affect the kinetics of hydrolysis-condensation reactions, give special properties like plasticity (especially if the organic group is a polymerizable functionality acting as network former) or hydrophobicity, hydrophilicity, etc. Figure 2.23 shows the structures of class II hybrid materials in which the organic group have the function of network modifier or network former. Table 2.2 reports some organo(alkoxy)silanes (acting as network modifiers or network formers) and metal alkoxides serving as precursors for sol-gel-derived (hybrid) materials.

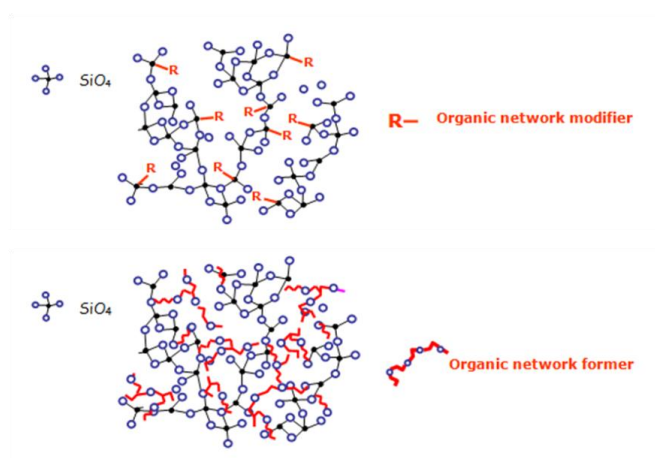


Figure 2.23 Structure of class II hybrid materials

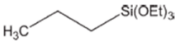
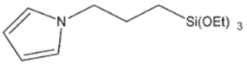
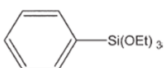
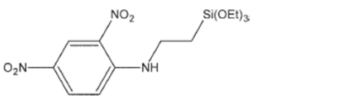
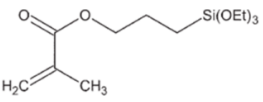
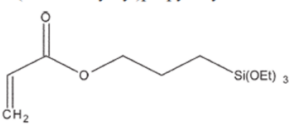
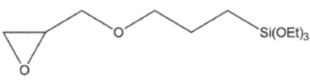
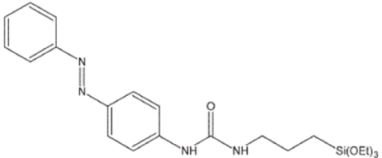
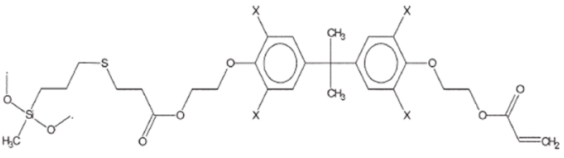
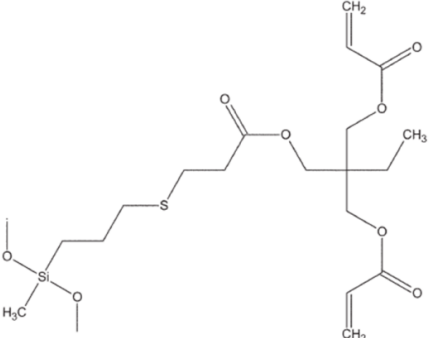
Network modifiers	Network formers
Methyltriethoxysilane $\text{H}_3\text{C}-\text{Si}(\text{OEt})_3$ Propyltriethoxysilane 	Metal alkoxides $\text{Al}(\text{OEt})_3$ , $\text{M}(\text{OEt})_4$ with $\text{M} = \text{Ti}, \text{Zr}$ <i>N</i> -(3-Triethoxysilylpropyl)pyrrole 
Phenyltriethoxysilane 	Vinyltriethoxysilane $\text{H}_2\text{C}=\text{CH}-\text{Si}(\text{OEt})_3$
3-(2,4-Dinitrophenylamino)propyltriethoxysilane 	Methacryloxypropyltriethoxysilane 
Aminopropyltriethoxysilane $\text{H}_2\text{N}-\text{CH}_2-\text{CH}_2-\text{CH}_2-\text{Si}(\text{OEt})_3$	3-(Trimethoxysilyl)propylacrylate 
Mercaptopropyltriethoxysilane $\text{HS}-\text{CH}_2-\text{CH}_2-\text{CH}_2-\text{Si}(\text{OEt})_3$	3-(Glycidoxypropyl)triethoxysilane 
4-(3-Triethoxysilylpropylureido)azobenzene 	
3-(2-Aminoethylamino)propyltriethoxysilane $\text{H}_2\text{N}-\text{CH}_2-\text{CH}_2-\text{NH}-\text{CH}_2-\text{CH}_2-\text{CH}_2-\text{Si}(\text{OEt})_3$	
3-Chloropropyltriethoxysilane $\text{Cl}-\text{CH}_2-\text{CH}_2-\text{CH}_2-\text{Si}(\text{OEt})_3$	
2-Cyanoethyltriethoxysilane $\text{N}\equiv\text{C}-\text{CH}_2-\text{CH}_2-\text{Si}(\text{OEt})_3$	
Isocyanatopropyltriethoxysilane $\text{O}=\text{N}-\text{CH}_2-\text{CH}_2-\text{CH}_2-\text{Si}(\text{OEt})_3$	

Table 2.2 Organo(alkoxy)silanes (acting as network modifiers or network formers) as precursors for sol-gel-derived (hybrid) materials. [38]

As reported, a way to synthesize hybrid materials is through the sol-gel process which allows the intimate mixing of molecular precursors at a molecular to nanometric scale. The mild conditions involved in the sol-gel synthesis allow the introduction of an organic component inside an inorganic network, offering the possibility for functional materials development. However, many parameters influence the sol-gel processes, and in turn, the properties of the final systems; a comprehensive description of sol-gel process goes beyond our intent so we point out only the main aspects.

Generally speaking, the main advantages and properties achievable from the hybrid materials through the sol-gel synthesis are:

- T processing  $< 200^{\circ}\text{C}$  to achieve a dense structure and preserving at the same time the organic part
- modulation of a great number of properties (mechanical, optical, electronic, thermal...)
- a diverse range of possible micro and nano structures obtainable in the sol. Moreover, the microstructure of gel may be controlled. Dry gels can be made with a wide range of densities, surface areas and pore sizes. This may be exploited in catalyst design, transparent insulation and in impregnation application
- good optical properties, with particular regard to the absence of light scattering and transparency
- refractive index control
- easy processability: the rheological properties of sol allow the formation of fiber, films and composites by such techniques as spinning, dip-coating, injection, impregnation or simple mixing and casting
- simple and low cost production
- easily obtainable thick films (and monoliths)
- high laser damage threshold respect to polymers

Among the listed properties, a key feature of the hybrid materials is the low temperature necessary to obtain a dense structure in spite of the inorganic glass.

#### **2.4.1. Hybrid organic-inorganic resists**

Gonsalves and co-workers [<sup>39,40</sup>] have shown that the incorporation of POSS in organic polymer backbones can enhance the contrast while not effecting the sensitivity of the resist materials, being promising for sub-100 nm lithography. Towards this end, terpolymers of polyhedral oligosilsesquioxanemethacrylate (POSS), methyl methacrylate (MMA) and tertbutylacrylate (TBA) were synthesized by a solution-polymerization method, Figure 2.24a. This resist shows a maximum contrast (23.50) and a sensitivity ( $1350 \text{ mJ/cm}^2$ ), comparable to that of standard PMMA.

POSS can also be incorporated into CA resists to improve the resist performance. As an example, Wu and co-workers [<sup>41</sup>] synthesized a POSS-containing CA resist using TBMA as deblocking component, Figure 2.24b. The incorporation of POSS units, thanks to the their

inorganic characteristics, has been found to be effective in improving RIE resistance when using  $O_2$  as plasma source.

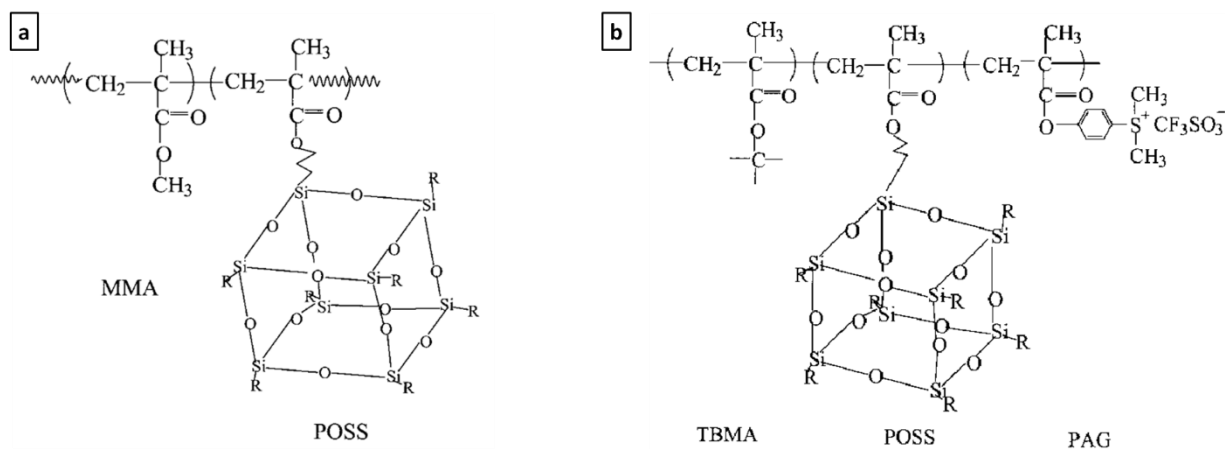


Figure 2.24 (a) Structure of POSS cage in copolymer; (b) Structure of PAG and POSS-containing CA resist.

Nanocomposites resists were also obtained incorporating 1 to 2 nm silica particles into ZEP520. [42] The addition of the silica to ZEP520 improved the resolution of the pattern writing, in fact when the pattern generator called for line widths of 40 nm, 47 nm lines and 131 nm lines were obtained in modified and unmodified ZEP520 respectively. Moreover it increased ZEP520 resistance in oxygen plasma etching, while not significantly change the sensitivity and contrast of the nanocomposite over unmodified ZEP520, Figure 2.25.

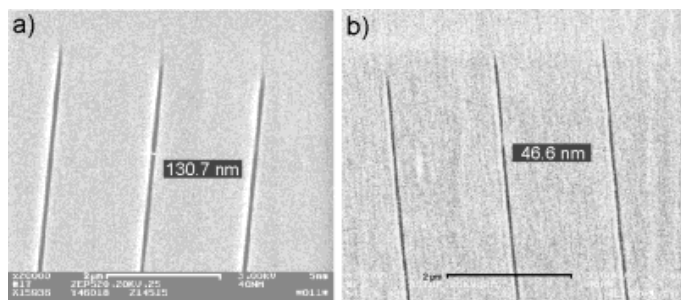


Figure 2.25 Images obtained by writing parallel lines on resists with a 40 nm diameter electron beam. a) On ZEP520 (20 keV, 400 nm film thickness and dose  $25 \mu C/cm^2$ ), b) on ZEP520 with 4 wt.-% silica particles (20 keV, 370 nm film thickness and dose  $25 \mu C/cm^2$ ).

Similarly, RIE rates in oxygen and chlorine plasmas were significantly reduced in a resists (Shipley AR3) containing 8-10 nm colloidal silica nanoparticles as compared to commercial unmodified resists [43]. Silica domains were also dispersed homogeneously in an acrylic polymer component in order to increase RIE resistance, heat resistance and compatibility with quartz substrates [44].

Moreover since HSQ is considered to be most prominent as negative e-beam resist for high resolution patterning because of its high  $T_g$ , small molecular size leading to good LER, high etching resistance but it suffers from a rather low sensitivity, as compared with chemically amplified resists, and lack of long-term chemical stability, organosilicate polymers for e-beam resist application, were synthesized starting with triethoxysilane (the precursor of HSQ) modified with bicycloheptenyl (normally called norbornene) and chloromethylphenyl groups. The organosilicate polymers exhibited significant improvements in the sensitivity and stability over those of HSQ while maintaining its high resolution capability and good LER: 15 nm lines width were fabricated at half the exposure dose required for HSQ, Figure 2.26.

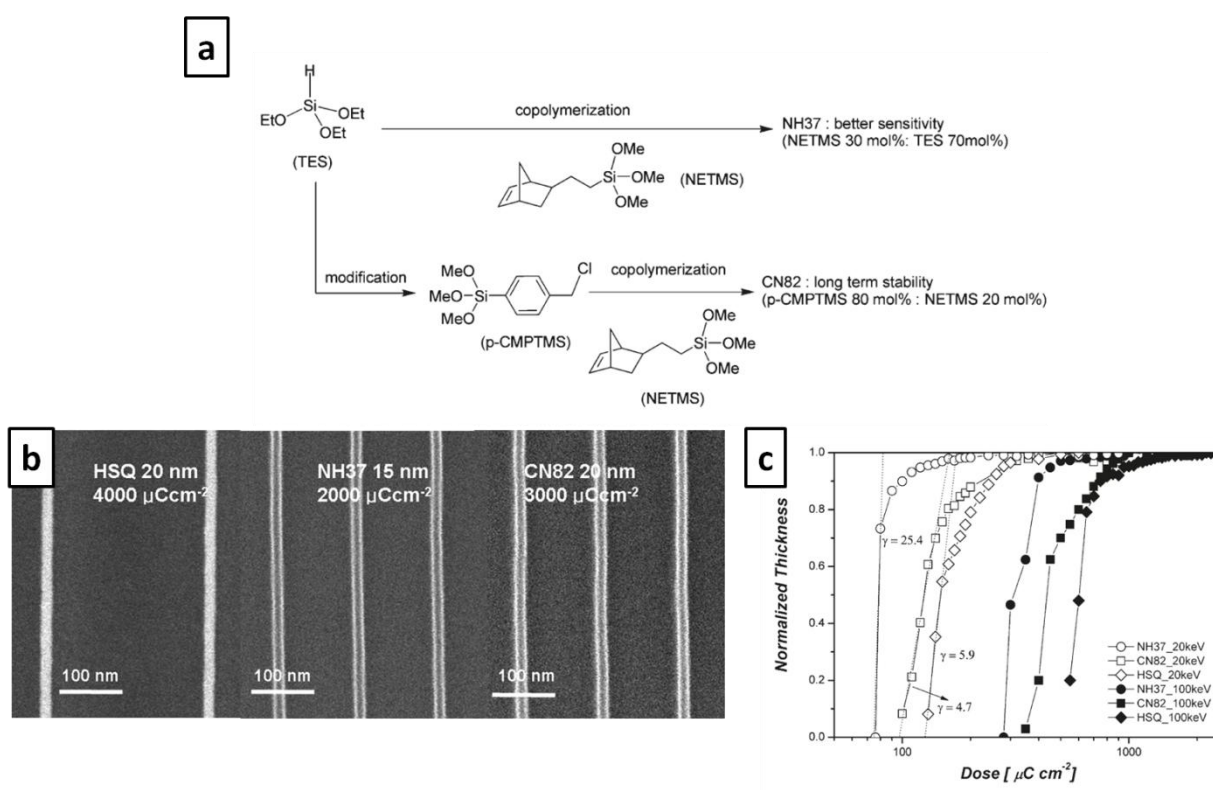


Figure 2.26 (a) Schemes for Synthesizing Organosilicate E-Beam Resists with Improved Sensitivity and Stability in Comparison to HSQ Resist; (b) high resolution line width gratings achieved with HSQ and synthesized organosilicate resists; (c) Contrast curves of HSQ and new organosilicate polymer resists upon exposure to e-beam of 20 and 100 keV, respectively, followed by development in TMAH 25 wt % solution. [43]

Alternative promising hybrid resists were also proposed: organically modified ceramic (ORMOCER<sup>®</sup>, registered trademark of Fraunhofer-Gesellschaft zur Förderung der angewandten Forschung e. V. in Germany), a Class II hybrid polymer materials synthesized by the sol-gel process. Currently, the most common way to introduce an organic group into an inorganic silica network is to use organo-alkoxysilane molecular precursors or oligomers of

general formula  $R'_n\text{Si}(\text{OR})_{4-n}$  or  $(\text{OR})_{4-n}\text{Si}-R''-\text{Si}(\text{OR})_{4-n}$  with  $n = 1,2,3$ . The general HOI synthetic process starts by building up an inorganic network through controlled hydrolysis and condensation of organically modified Si alkoxides, preserving the organic component in solid state in order to be exploited to produce the structure modification upon exposure and solubility change or thermal treatments. In fact, in most sol-gel conditions the Si-C bond remains stable towards hydrolysis and the  $R'$  group introduces focused new properties to the inorganic network (flexibility, hydrophobicity, refractive index modification, optical response, etc.). Therefore, in the subsequent lithographic step the polymerizable groups, which are fixed to the inorganic network, react with each other in a thermal or UV-initiated process. Silicon alkoxides can be modified with epoxy groups or C=C bond (such as  $\gamma$ -glycidyloxypropyl trimethoxysilane (GPTMS),  $\gamma$ -methacryloxypropyl trimethoxysilane (TMSPM) or vinyl trimethoxysilane) which upon exposure or thermal curing (with or without addition of different photo or thermal initiators) undergo cationic or radical polymerization, respectively. In this two-stage process an inorganic-organic copolymer is synthesized. The sol-gel synthesis of siloxane based hybrid organic-inorganic compounds usually involves di- or trifunctional organosilanes co-condensed with metal alkoxides, such as  $\text{Si}(\text{OR})_4$ ,  $\text{Ti}(\text{OR})_4$ ,  $\text{Zr}(\text{OR})_4$  or  $\text{Al}(\text{OR})_3$ . Trifunctional alkoxysilanes and metal alkoxides are efficient crosslinkers that usually lead after co-condensation to hybrid materials having high Young's modulus ( $E \sim 10$  GPa) and either high glass transition temperature ( $T_g > \text{RT}$ ) or no  $T_g$ .

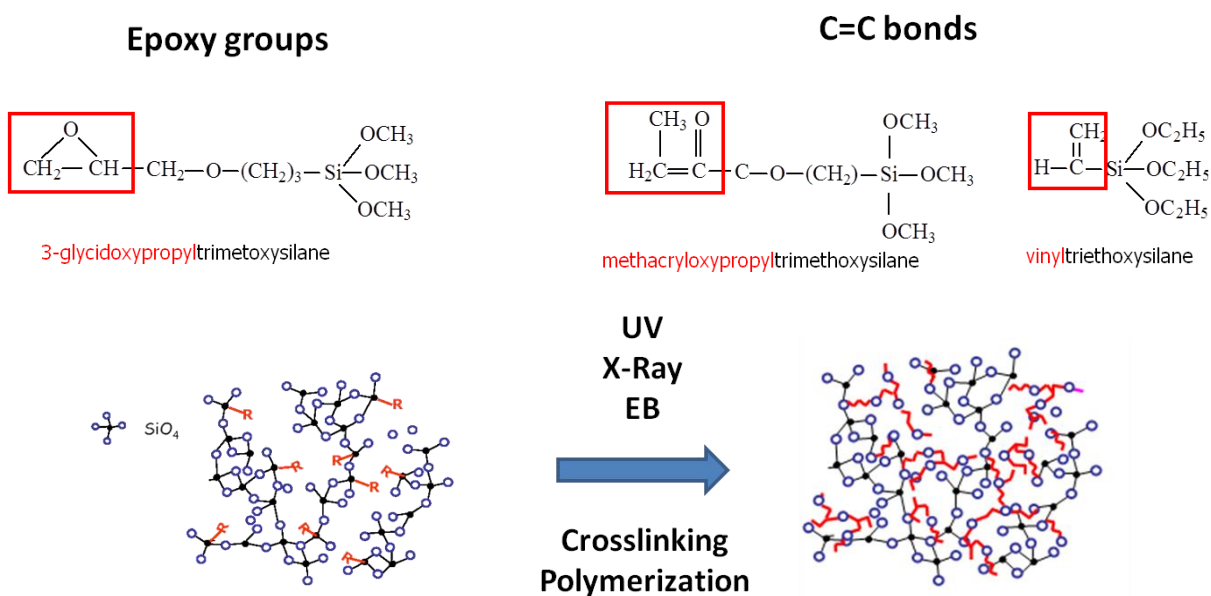


Figure 2.27  $\gamma$ -glycidyloxypropyl trimethoxysilane (GPTMS),  $\gamma$ -methacryloxypropyl trimethoxysilane (TMSPM) or vinyl trimethoxysilane as organically modified silicon alkoxides precursors for hybrid sol-gel synthesis. The figure also shows the mechanism exploited for UVL, XRL and EBL processes of hybrid materials.

ORMOCER® offer perfect media for high resolution photolithography because [38]:

- (i) the precursor oligomers of the siloxane part have a small size around 1–5 nm,
- (ii) the chemical cross-linking during mask-aligning (UV-polymerization based patterning) is strongly sterically hindered by the oligomers which cause a fast break-down of radical polymerisation avoiding parasitic reactions into the mask-shaded areas,
- (iii) the resist mechanical stability allows the build-up of very fine structures <100 nm.

Several ORMOCER® for optical applications are now licensed by Fraunhofer-ISC to the company Micro Resist Technology GmbH and they are producing them in large scale and marketing them worldwide under the names: “Ormocore”, “Ormoclad” and “Ormocomp”, Figure 2.28. As a result, besides the given industries, lots of companies from Japan and South Korea as well as from Europe (Germany, Switzerland, Sweden, and Finland) have integrated these materials mostly in micro-optical products.

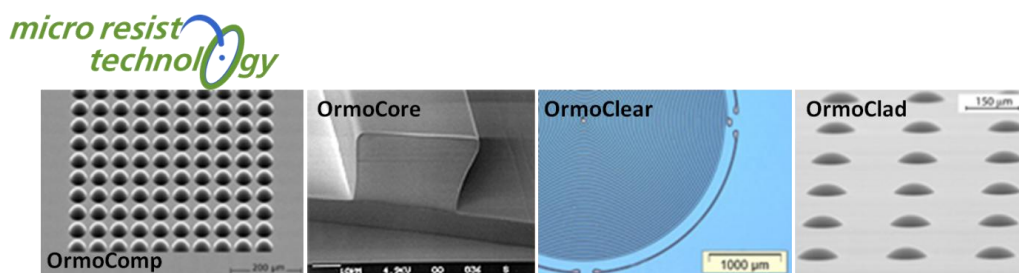


Figure 2.28 “Ormocore”, “Ormoclad”, “Ormocomp”, “Ormoclear” products sold as hybrid photoresists by Micro Resist Technology GmbH

#### 2.4.1.1. Directly patternable HOI resists

Differently from the above discussed trend using HOI materials as sacrificial resists, HOI resists have been also designed to be integral part of a devices, both overcoming the frequent inadequacy and problem of “unknown chemistry” typical of commercial resists and greatly simplifying the traditional lithographic procedure. For example, it is possible to dope the patternable film with organic dyes, nanoparticles or other organic and inorganic species; tuning the optical properties such as refractive index and resist porosity. Several HOI materials have already been reported in literature since few decades, as directly writable materials; the main part of it concerns UV sensitive HOI mainly methacrylate based, for the production of waveguides [46,47] and few other products [48,49] by using mask assisted UV lithography techniques (UVL) and UV Laser Interferential Lithography (UV-LIL). A review on HOI materials based on 3-glycidoxypropyltrimethoxysilane (GPTMS) and different



inorganic oxide precursors, in particular Si tetramethoxide (TMOS), Ge tetraethoxide (TEOG), Zr butoxide (ZrBut) and Ti propoxide (TiProp), directly patternable with UVL, UV-LIL, EBL, XRL and NIL has recently been reported by Brusatin et al. [50]. In particular, results about the investigation of the interaction between radiation and HOI materials have been presented. The great advantage is that some of the presented materials can be processed with all the lithographic methods above mentioned, without any significant modification of their main composition and synthesis procedure. Moreover, epoxy based HOI systems offer a few important properties with respect to acrylate based HOI: a higher thermal stability of un-polymerized epoxies and UV transparency, because of the cationic polymerization mechanism, higher pattern resolution achievable with EBL or XRL and limited shrinkage during polymerization typical of epoxy based HOI.

As already mentioned the organic groups R' of the silicon alkoxide can be introduced not only as network formers (R' contains a vinyl, a methacryl or an epoxy group) but also as network modifiers (Si-CH<sub>3</sub>, Si-phenyl, etc.), Figure 2.29. In the latter case no organic polymerization reaction takes place upon exposure or thermal treatment; thereby the organic modification either contributes to an organic functionalization of the inorganic network leading to functional hybrid materials or it can be degraded during the lithographic exposure process, as more recently proposed by Brusatin et al. [51,52,53,54] allowing to obtain inorganic structures at the end of the lithographic process.

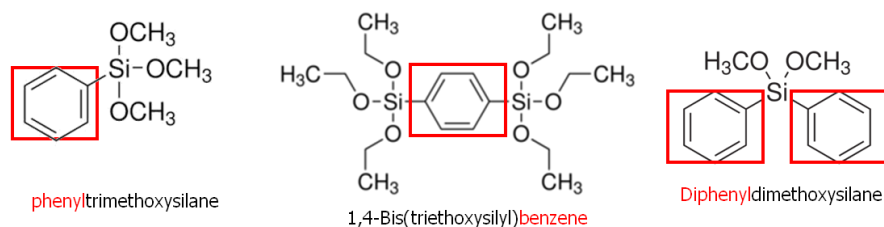


Figure 2.29 Example of silicon alkoxides where the organic component acts as network modifier

An example of no-chemically amplified *Ph*-Bridged PolySilsesquioxanes based resist has been proposed by L. Brigo et al. as a UVL, XRL and EBL resist [52,53]. For example in the case of e-beam, this resist allows to obtain high resolution patterns and presents the advantage of being patternable with a double tone behaviour depending on the PEB applied [55], Figure 2.30. The presented materials not only act as a promising silica resist that can be used a sacrificial layer but it has also been exploited as a functional porous material even coupled to gold nanoparticles for the realization of surface plasmon resonance xylene sensors [56].



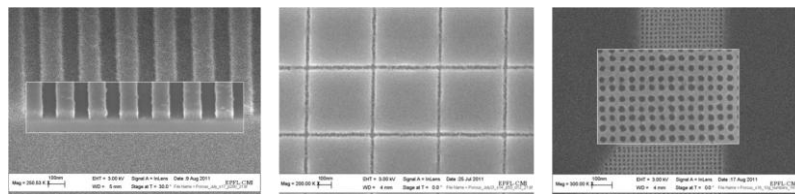


Figure 2.30 80nm L/S, 30nm isolated lines, 50 nm dots patterns obtained with the *Ph*-Bridged PolySilsesquioxanes based e-beam resist.

Another negative tone system synthesized through the sol-gel method starting from a phenyl modified silica precursor and a Zr-alkoxide has been proposed by Della Giustina et al.<sup>[54]</sup> The hybrid patternable material presented acts as a potential solid supports for the immobilization of biomolecules, allowing to realize innovative architectures for new generations of biosensors, thanks to the good mechanical properties and thermal stability, as well as resistance to microbial attack and organic solvents of Zirconia films.

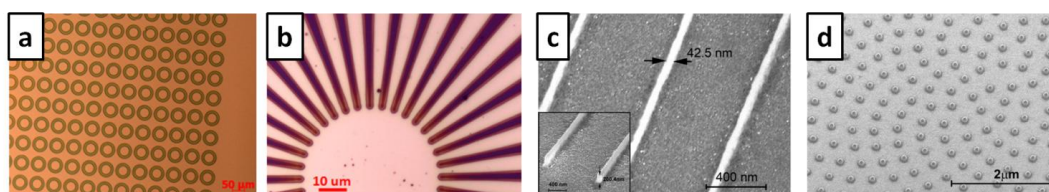


Figure 2.31 (a) and (b) Optical images of ZrO<sub>2</sub> micro structures obtained by UV lithography; (c) and (d) SEM images of ZrO<sub>2</sub> single lines (c) and aperiodic nano structure (d) obtained by EBL on film with a starting thickness of 250 nm. The ultimate single line resolution is less than 50 nm. The inset shows the SEM cross section of the isolated lines.

Another way of obtaining inorganic structures starting with hybrid resists is the one presented by M. Saifullah et al., who have synthesized different sol-gel systems starting with metal alkoxides chemically modified with  $\beta$ -diketones and  $\beta$ -ketoesters. In fact AcAc, ethylacetoacetate, EAcAc, and benzoyl acetone, BzAc, have optical absorption bands in the ultraviolet UV range, characteristic of the  $\pi - \pi^*$  transition in chelate bonds. Therefore, exposure to UV radiation results in the break down of the chelate bonds and reduces their solubility in alcohols and acidic solutions, behaving as a negative EB sensitive materials.<sup>[57,58,59,60]</sup> However the sensitivity is not an optimized parameter (for example for ZnO based resists the sensitivity is around 15 mC/cm<sup>2</sup> compared to 250  $\mu$ C/cm<sup>2</sup> of HSQ).

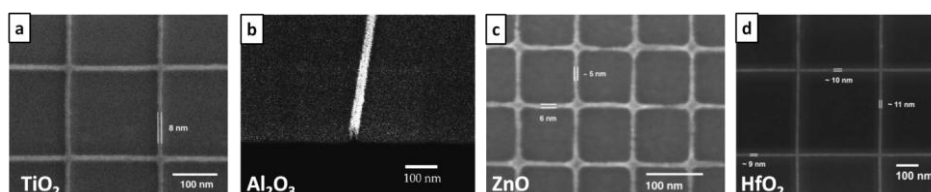


Figure 2.32 SEM images of sub-10 nm different oxides patterned using sol-gel based spin-coatable resists.

## 2.5. *NIL resists*

There is a class of resists which are not necessarily photosensitive and which are engineered and developed for nonradiation-based pattern lithography, such as thermal-nanoimprint resists. As previously mentioned in Chapter 1, nanoimprint lithography (NIL) is an alternative approach to optical lithography for obtaining feature sizes in the sub-100 nm range. Here, the resist shape is physically deformed with a mould.

Even in this case imprint materials used for NIL can be either utilized as an intermediate masking layer for the substrate or as a functional layer for a specific application. The materials used in NIL can be categorized into two main types: thermoplastic materials generally used in hot embossing lithography, and thermosetting (or curable) materials with either ultraviolet (UV) initiated precursors used in UV-NIL, or thermal initiation in the case of thermal curing imprint lithography.

Because imprint lithography makes a conformal replica of the surface relief patterns by mechanical embossing, the resist materials should be easily deformable under an applied pressure, it should have a sufficient mechanical strength as well as a good mould-releasing properties to maintain their structural integrity during the de-moulding process, it should be imprinted at modest temperature and pressure and it should present a high etch resistance to allow pattern transfer into the substrate.

Two material properties are important for the imprinting process:

- the resist material should have a Young's modulus lower than that of the mould during imprinting in order to be deformed by the mould.
- the resist material should also have a sufficiently low viscosity to complete the imprinting process within a practical time frame. In fact, according to the Stephan equation (1874), under a fixed pressure the imprinting time scales linearly with viscosity and quadratically with the pattern size.

$$v_i(t, T) = -\frac{dh}{dt} = \frac{2F \cdot h^3(t)}{\eta(T) \cdot s_0^4}$$

Traditional imprint resists are *thermoplastic materials*. During the imprint step, the resist is heated to a temperature above its glass transition temperature. At that temperature, the resist becomes a viscous liquid and can flow and, therefore, can be readily deformed into shape of the mould. This specific temperature ( $T_g$ ) is chosen because above it both requirements mentioned in the previous paragraph can be met simultaneously. In fact above  $T_g$  both the

Young's modulus and the viscosity will drop by several orders of magnitude compared to their respective values below  $T_g$ .

In practice, the suitable imprint temperature is normally chosen 70-80°C above the material's glass transition temperature ( $T_g$ ), when the viscous liquid flow state is reached and the polymer flows by chain sliding. A reduction in temperature has to be compensated by corresponding increases in imprinting pressure and time to obtain satisfactory results. Since the  $T_g$  is the onset temperature for molecular motion of polymers, factors that increase the energy required for molecular motion (e.g. intermolecular forces, inter-chain steric hindrance and bulky and stiff side groups) also increase the  $T_g$  value; those factors that decrease the energy requirements (e.g. flexible bonds and flexible side groups) decrease the  $T_g$ .

Another factor that affects the viscosity of a polymer material is the polymer's molecular weight,  $M_w$ , that determines many physical properties (e.g. glass transition temperature, mechanical properties such as stiffness, strength, viscoelasticity and viscosity). In practice, low-molecular-weight polymers can be imprinted at lower temperatures, lower pressures, or within shorter times.

Thermal NIL profits from the availability of polymers such as poly(methylmethacrylate) (PMMA) and polystyrene (PS) with a range of molecular weights  $M_w$ . These resists can be easily prepared for a range of thicknesses in a spin-coating process. PMMA can be used as NIL resist since its glass transition temperature  $T_g$  of PMMA is low enough to enable molding at temperature below 200°C, but high enough to ensure a sufficient thermal stability in etching processes.

Obviously, these materials are not optimized at all for the special requirements of the NIL process. For example one critical requirement of the candidate polymers used in imprinting based lithography is that they should provide excellent mould releasing properties during the de-moulding process and at the same time should not compromise the adhesion of the mould to the substrate. Commercially available polymer materials can hardly satisfy these seemingly contradictory requirements. Although the mould surface is treated normally with a low surface energy surfactant, when imprinting high density or high aspect ratio patterns, the imprinted polymer tends to adhere to the mould, creating pattern defects that are not acceptable for many applications. Block copolymer materials that have dual surface properties through microphase segregation can be exploited to solve this problem.

Another example of nanoimprint resist material developed to modify the fundamental surface interactions between resists and mould for defect reduction in nanoimprint patterning

replication is an acrylate type material containing 4,4,5,5,6,6,7,7,8,8,9,9,10,10,11,11,11-heptafluoro-2-hydroxyundecyl acrylate as an ultraviolet reactive fluorine surfactant [61].

In addition to the easy de-moulding, a higher dry etching resistance is highly desirable if the imprinted polymer pattern is to be used as a dry etching mask for further pattern transfer. Adding a Si-containing material in the polymer formulation could be an effective method.

Of special interest are the PDMS–organic block or graft copolymers. In contrast to PMMA, and organic polymers in general, siloxane copolymers exhibit significant differences by virtue of the highly open, flexible, and mobile Si–O–Si backbone. These include a low surface energy, low  $T_g$ , and a high thermal stability. Furthermore, it is known that these copolymers undergo a microphase segregation above their  $T_g$ s because of the unfavourable enthalpy of mixing. When cast or hot-pressed onto a high-surface-energy substrate such as silicon, glass, or metal the copolymer film forms an air/polymer interface enriched with lower-surface-energy component (PDMS block), and a polymer/substrate interface dominated by the higher-surface energy component (organic block). The dual surface character makes these copolymers excellent candidate materials for NIL: they allow easy mould–resist separation and at the same time they exhibit good adhesion to the substrate. This duality is not possible with homopolymers. Siloxane copolymers offer another advantage over homopolymers, in that they have a strongly improved etching resistance because of the high Si content and the high strength of the Si–O bond.

Moreover, *thermally curable monomers* (thermoset) are an alternative to thermoplastic materials. These liquid materials can be imprinted in a short period of time at low pressures and temperatures. PDMS-type materials are a class of thermally curable materials widely used by many research groups. A fast, thermal-curable liquid resist is based on the same hydrosilylation chemistry of siloxane polymers and consists of two principal chemical components: a vinyl-terminated PDMS polymer, a silyl-hydride-based (Si–H) dimethylsiloxane crosslinker. The high Si content in this polymer system guarantees that the resist has a high etching resistance in RIE processes. Moreover by changing the molecular weight of the precursor and the percentage of silyl-hydride groups in the crosslinker, the Young modulus of the cured material can be tuned. The short time required for curing the material and the fast crosslinking time satisfies the need for high-speed patterning in practical applications.

*UV-curable materials* have also been developed as nanoimprint resists generally composed of a mixture of monomers (or prepolymers) and a suitable photoinitiator, and often chemicals are

added which decrease the effect of radical scavengers on photo polymerization. Nanonex, MII, AMO, and Obducat offer these materials adapted to their proprietary process and tool. Micro Resist Technology GmbH presents different UV curable NIL resists, such as mr-UVCur06 and mr-UVCur21. These materials generally present low viscosity, good film quality, fast UV-curing at low UV doses, good adhesion properties, high pattern fidelity and high plasma etch resistance.

Finally, functional materials may be imprinted directly to form a layer in a chip with no need for pattern transfer into underlying materials. The successful implementation of a functional imprint material would result in significant cost reductions and increased throughput by eliminating many difficult chip fabrication processing steps. In particular *hybrid materials* have also been used as functional NIL resists, thanks to their higher mechanical and thermal stability compared to organic resist. Moreover they presents a lower elastic modulus and are more ductile than inorganics, so shaping the precursor into the mould is easier, while cracking occurs less easily during the embossing step.

## References

- <sup>1</sup> Semiconductor Lithography: Principles, Practices, and Materials, ed. by W. M. Moreau, *Plenum*, New York **1987**.
- <sup>2</sup> G. M. Wallraff, W. D. Hinsberg, *Chem. Rev.* **1999**, 99, 1801.
- <sup>3</sup> E. Reichmanis, O. Nalamasu, F. M. Houlihan, *Acc. Chem. Res.* **1999**, 32, 659.
- <sup>4</sup> K. E. Gonsalves, L. Merhari, H. Wu, Y.Hu, *Adv. Mater.* **2001**, 13.
- <sup>5</sup> C.G. Willson, *Introduction to Microlithography*, "Organic Resist Materials," ed. by L.F. Thompson, C.G. Willson, M.J. Bowden, *American Chemical Society* **1994**, 139.
- <sup>6</sup> M.J. Bowden, "The Lithographic Process: The Physics," Introduction to Microlithography, ed. L.F. Thompson, C.G. Willson, M.J. Bowden, *American Chemical Society* **1994**, 19.
- <sup>7</sup> C.A. Mack, *Microelectronics Manufacturing Technology* **1991**, 14(1), 36.
- <sup>8</sup> B. Shokouhi, J. Zhang, B. Cui, *Micro & Nano Letters* **2011**, 6, 992–994.
- <sup>9</sup> M. Yan, S. Choi, K. R. V. Subramanian, I. Adesida, *J. Vac. Sci. Technol. B* **2008**, 26(6).
- <sup>10</sup> K. Kurihara, K. Iwadate, H. Namatsu, M. Nagase, H. Takenaka, K. Murase, *Jpn. J. Appl. Phys.* **1995**, 34, 6940.
- <sup>11</sup> A. Hajiaboli, B. Cui, M. Kahrizi, V.V. Truong, *Phys Status Solidi A: Appl Mater Sci.* **2009**, 206(5), 976–979.
- <sup>12</sup> M. D. Austin, W. Zhang, H. X. Ge, D. Wasserman, S. A. Lyon, S. Y. Chou, *Nanotechnology* **2005**, 16, 1058–1061.
- <sup>13</sup> S. Ma, C. Con, M. Yavuz, B. Cui, *Nanoscale Res Lett.* **2011**, 6(1), 446.
- <sup>14</sup> R.R. Dammel, Diazonaphthoquinone-based Resists, Bellingham, WA: *SPIE Optical Engineering Press* **1993**, Vol. TT-11.
- <sup>15</sup> M. Angelopoulos, N. Patel, J. M. Shaw, N. C. Labianca, S. A. Rishton, *J. Vac. Sci. Technol. B* **1993**, 11, 2794.
- <sup>16</sup> D. M. Tanenbaum, C. W. Lo, M. Isaacson, H. G. Craighead, M. J. Rooks, K. Y. Lee, W. S. Huang, T. H. P. Chang, *Journal of Vacuum Science & Technology B* **1996**, 14, 3829.
- <sup>17</sup> P. P. Naulleau, C. Rammeloo, J. P. Cain, K. Dean, P. Denham, K. A. Goldberg, B. Hoef, B. La Fontaine, A. R. Pawloski, C. Larson, G. Wallraff, *Proc. of SPIE 6151* **2006**, 6151Y.
- <sup>18</sup> Clifford L. Henderson, from *School of Chemical & Biomolecular Engineering*, Georgia Institute of Technology
- <sup>19</sup> J. Fujita, Y. Ohnishi, Y. Ochiai, S. Matsui, *App. Phys. Lett.* **1996**, 68(9), 1297.

- 
- <sup>20</sup> J. Fujita, Y. Ohnishi, Y. Ochiai, E. Nomura, S. Matsui, *J Vac Sci Technol B* **1996**, 14, 4272.
- <sup>21</sup> T. Tada, T. Kanayama, *Jpn. J. Appl. Phys* **1996**, 35, 63.
- <sup>22</sup> A. P. G. Robinson, R. E. Palmer, T. Tada, T. Kanayama, J. A. Preece, *Appl. Phys. Lett.* **1998**, 72, 1302.
- <sup>23</sup> T. Ishii, H. Nozawa, T. Tamamura, A. Ozawa, *J. Vac. Sci. Technol. B* **1997**, 15, 2570.
- <sup>24</sup> T. Ishii, H. Nozawa, E. Kuramochi, T. Tamamura, *Mater. Res. Soc. Symp. Proc.* **2000**, 584, 103.
- <sup>25</sup> J. K. W. Yang, B. Cord, H. Duan, K. K. Berggren, J. Klingfus, S. Nam, Ki-Bum Kim, M. J. Rooks, *J Vac Sci Technol B* **2009**, 27, 2622.
- <sup>26</sup> V. Sidorkin, A. van Run, A. van Langen-Suurling, A. Grigorescu, E. van der Drift, *Microelectron Eng.* **2008**, 85, 805–809.
- <sup>27</sup> N. Clark, A. Vanderslice, R. Grove, R. R. Krchnavek, *J Vac Sci Technol B.* **2006**, 24(6), 3073–3076.
- <sup>28</sup> A. E. Grigorescu, C. W. Hagen, *Nanotechnology* **2009**, 20(29), 292001.
- <sup>29</sup> K. Ogino, J. Taniguchi, S. Satake, K. Yamamoto, Y. Ishii, K. Ishikawa, *Microelectron Eng.* **2007**, 84, 1071–1074.
- <sup>30</sup> Y. Xia, G. M. Whitesides, *Annu. Rev. Mater. Sci.* **1998**, 28, 153–84.
- <sup>31</sup> X. M. Zhao, Y. N. Xia, G. M. Whitesides, *Adv Mater* **1996**, 8, 837–40.
- <sup>32</sup> O. F. Göbel, M. Nedelcu, U. Steiner, *Adv. Funct. Mater.* **2007**, 17, 1131–1136.
- <sup>33</sup> C. R. Martin, I. A. Aksay, *J. Electroceram* **2004**, 12, 53–68.
- <sup>34</sup> C. R. Martin, I. A. Aksay, *Electroceramic-Based MEMS: Fabrication-Technology and Applications* **2005**, Chapter 15 Low-Cost Patterning of Ceramic Thin Films, Springer, 387-410.
- <sup>35</sup> Y. Masuda, *Nano/Micro-Patterning of Metal Oxide Nanocrystals* **2011**, Chapter 10 Nanocrystal, 265-292.
- <sup>36</sup> Y. Masuda, *Journal of the Ceramic Society of Japan* **2007**, 115, 101-109.
- <sup>37</sup> S. Park, T. Y. Jeon, S. Yang, *Langmuir* **2013**, 29, 9620–9625.
- <sup>38</sup> C. Sanchez, B. Julián, P. Belleville, M. Popall, *J. Mater. Chem.* **2005**, 15, 3559–3592.
- <sup>39</sup> K. E. Gonsalves, J. Wang, H. Wu, *J. Vac. Sci. Technol. B* **2000**, 18, 325.
- <sup>40</sup> K. E. Gonsalves, J. Wang, H. Wu, *Mater. Res. Soc. Symp. Proc.* **2000**, 584, 123.
- <sup>41</sup> H. Wu, Y. Hu, K. E. Gonsalves, M. J. Yacaman, *Journal of Vacuum Science & Technology B* **2001**, 19, 851.

- <sup>42</sup> K. E. Gonsalves, Y. Hu, H. Wu, L. Merhari, in *Collected Abstracts 12th Int. Conf. on Photopolymers, Society of Plastics Engineers (SPE), McAfee, NJ, Oct. 16-18, 2000*.
- <sup>43</sup> T. H. Fedynyshyn, S. P. Doran, I. Sondi, M. L. Lind, E. Matijevic, *Proc. SPIE Int. Soc. Opt. Eng. (Adv. Resist Technol. Proc.)* **2000**, 3999, 627.
- <sup>44</sup> T. Tamai, Y. Matsuura, M. Watanabe, K. Matsukawa, *Polym Sci Polym Chem* **2006**, 44, 2107.
- <sup>45</sup> J. H. Sim, S. Lee, H. Lee, R. Kasica, H. Kim, C. L. Soles, K. Kim, D. Y. Yoon, *Chem. Mater.* **2010**, 22, 3021–3023.
- <sup>46</sup> A. Moujoud, Z. Saddiki, T. Touam, S. I. Najafi, *Thin Solid Films* **2002**, 422, 161–165.
- <sup>47</sup> R. Buestrich, F. Kahlenberg, M. Popall, P. Dannberg, R. Muller-Fiedler, O. Rosch, *J Sol-gel Sci Technol* **2001**, 20, 181–186.
- <sup>48</sup> J. Jabbour, S. Calas-Etienne, M. Smahi, S. Gatti, R. Kribich, G. Pille, Y. Moreau, P. Etienne, *Appl. Surf. Sci.* **2007**, 253, 8032–8036.
- <sup>49</sup> C. Croutxe-Barghorn, C. Belon, A. Chemtob, *J Photopol Sci Technol* **2010**, 23(1), 129–134.
- <sup>50</sup> G. Brusatin, G. Della Giustina, *J Sol-Gel Sci Technol* **2011**, 60, 299–314.
- <sup>51</sup> E. Zanchetta, G. Della Giustina, G. Greci, A. Pozzato, M. Tormen, G. Brusatin, *Adv. Mater.* **2013**, 25, 6261–6265.
- <sup>52</sup> L. Brigo, G. Greci, A. Carpentiero, A. Pistore, M. Tormen, M. Guglielmi, G. Brusatin, *J Sol-Gel Sci Technol* **2011**, 60, 400–407.
- <sup>53</sup> L. Brigo, G. Greci, L. Baù, A. Carpentiero, F. Mancin, F. Romanato, M. Tormen, M. Guglielmi, G. Brusatin, *Microelectron Eng.* **2011**, 88, 1913–1916.
- <sup>54</sup> G. Della Giustina, D. Garoli, F. Romanato, G. Brusatin, *Microelectron Eng.* **2013**, 110, 436–440.
- <sup>55</sup> L. Brigo, V. Auzelyte, K. A. Lister, J. Brugger, G. Brusatin, *Nanotechnology* **2012**, 23, 325302
- <sup>56</sup> L. Brigo, M. Cittadini, L. Artiglia, G. A. Rizzi, G. Granozzi, M. Guglielmi, A. Martucci, G. Brusatin, *J. Mater. Chem. C* **2013**, 1, 4252–4260.
- <sup>57</sup> M. S. M. Saifullah, K. Kurihara, C. J. Humphreys, *J. Vac. Sci. Technol. B* **2000**, 18(6).
- <sup>58</sup> M. S. M. Saifullah, K. R. V. Subramanian, E. Tapley, Dae-Joon Kang, M. E. Welland, M. Butler, *Nano Letters* **2003**, 3-11, 1587.



<sup>59</sup> M. S.M. Saifullah, K.R.V. Subramanian, D.-J. Kang, D. Anderson, W.T.S. Huck, G.A.C. Jones, M.E. Welland, *Adv. Mater.* **2005**, 17, 1757–1761.

<sup>60</sup> M. S. M. Saifullah, M. Z. R. Khan, D. G. Hasko, E. S. P. Leong, X. L. Neo, E. T. L. Goh, D. Anderson, G. A. C. Jones, M. E. Welland, *J. Vac. Sci. Technol. B* **2010**, 28, 90.

<sup>61</sup> S. Takei, A. Sekiguchi, *Appl. Sci.* **2012**, 2, 24-34.



---

## *Chapter 3*

### *TITANIA BASED SYSTEMS*

#### *AS HIGH REFRACTIVE INDEX RESISTS*

TiO<sub>2</sub> is a chemically stable, nontoxic, biocompatible, inexpensive material with very high dielectric constant, interesting optical properties, such as low absorption in the visible and near-infrared spectral regions and fairly large refractive index among the transparent metal oxides, and photocatalytic activity upon UV exposure [1]. It is a wide-gap semiconductor, and depending on its chemical composition, it shows a large range of electrical conductivity.

In the past few decades there have been several exciting breakthroughs with respect to titanium dioxide, especially concerning the preparation, modification, and applications of TiO<sub>2</sub> nanomaterials, including TiO<sub>2</sub>-organic/inorganic nanocomposite materials, because of their specifically size-related properties. In fact, the energy band structure becomes discrete for nanometer-scale TiO<sub>2</sub>, and its photophysical, photochemical, and surface properties are quite different from those of the bulk ones due to the quantum size effect.

The first major advance was in 1972 when Fujishima and Honda discovered the phenomenon of photocatalytic splitting of water on a TiO<sub>2</sub> electrode under ultraviolet (UV) light [2]. Since then, enormous efforts have been devoted to research on TiO<sub>2</sub> material, which has led to many promising applications in areas ranging from photovoltaics and photocatalysis to photo/electrochromics and sensors.

Nowadays, TiO<sub>2</sub> powder is widely used as a white pigment in paints (51% of total production), plastic (19%), and paper (17%), which represent the major end-use sectors. Furthermore, as a result of its high refractive index, it finds important applications in antireflection coatings [3,4], (i.e. in silicon solar cells), narrow-band filters, optical waveguides [5,6,7,8,9,10,11] and photonic crystals [12,13]. Moreover, TiO<sub>2</sub> is successfully used as bio and gas sensor, due to the dependence of its electric conductivity on the ambient gas composition [14,15,16]. Due to its excellent nontoxicity and hemocompatibility with the human body, TiO<sub>2</sub> is used as a biomaterial in orthopedic and dental applications, for instance as bone substitute and reinforcing mechanical supports [17]. The catalytic activities of TiO<sub>2</sub> surface under visible

irradiation led to interesting environmental applications [<sup>18,19</sup>] such as water purification, but is also widely exploited in dye-sensitized solar cells (DSSCs) and solid-state photovoltaic solar cells [<sup>20,21,22</sup>].

In the first part of this chapter, a brief survey of the general properties and synthesis of titania based materials is presented. In the experimental part, the synthesis and characterization of TiO<sub>2</sub> based sol-gel systems as well as their application as directly patternable resists for optical and nanoimprint lithography will be described. Two basic types of materials have been addressed: in-situ and ex-situ titania materials. In the former inorganic titania NPs are formed during the synthesis of the HOI material, in the latter commercial titania NPs are added to the material already synthesized. Very interestingly, UV irradiation has been shown to be a useful tool for material modification allowing for densification strategies and organic decomposition different from heat treatment.

### 3.1. Literature background: TiO<sub>2</sub> sol-gel synthesis starting from titanium alkoxides

Titanium dioxide (TiO<sub>2</sub>), also known as titanium(IV) oxide or titania, is the naturally occurring oxide of titanium, belonging to the family of transition metal oxides. TiO<sub>2</sub> exists as three different polymorphs: anatase, rutile and brookite. Anatase and rutile, which are the main polymorphs (their key properties are summarized in Table 3.1), are in tetragonal structure while brookite is orthorhombic (Figure 3.1). In all the three TiO<sub>2</sub> structures, the stacking of the octahedra results in threefold coordinated oxygen atoms.

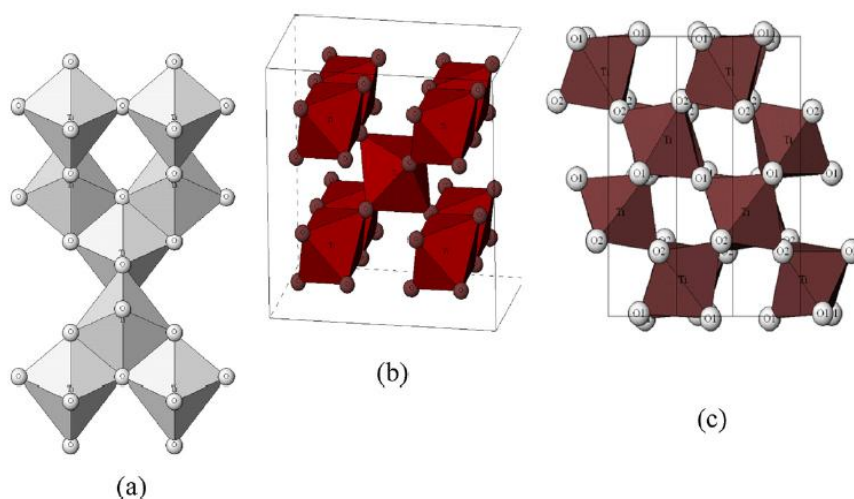


Figure 3.1 Crystalline structures of titanium dioxide (a) anatase, (b) rutile, (c) brookite [<sup>19</sup>]

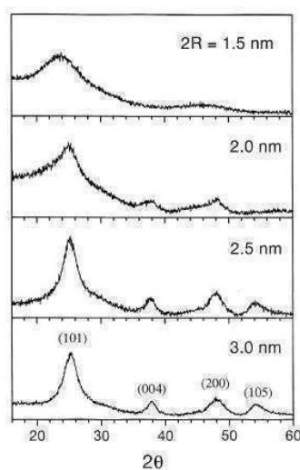
Physical and structural properties of anatase and rutile TiO<sub>2</sub>.

Property	Anatase	Rutile
Molecular weight (g/mol)	79.88	79.88
Melting point (°C)	1825	1825
Boiling point (°C)	2500–3000	2500–3000
Light absorption (nm)	<390	<415
Mohr's Hardness	5.5	6.5–7.0
Refractive index	2.55	2.75
Dielectric constant	31	114
Crystal structure	Tetragonal	Tetragonal
Lattice constants (Å)	$a = 3.78$ $c = 9.52$	$a = 4.59$ $c = 2.96$
Density (g/cm <sup>3</sup> )	3.79	4.13
Ti–O bond length (Å)	1.94 (4) 1.97 (2)	1.95 (4) 1.98 (2)

Table 3.1 Physical and structural properties of anatase and rutile TiO<sub>2</sub>

Titanium dioxide is typically an n-type semiconductor due to oxygen deficiency. The band gap is 3.2 eV for anatase, 3.0 eV for rutile, and ~3.2 eV for brookite [23].

Under ambient conditions the most thermodynamically stable form of TiO<sub>2</sub> is rutile and typically the metastable anatase and brookite transform to rutile upon calcination at temperatures exceeding ~600°C [24]. However, thermodynamic stability is particle-size dependent [25] and relative phase stability may reverse when particle sizes decrease to sufficiently low values due to surface-energy effects (surface free energy and surface stress, which depend on particle size). Rutile is the most stable phase for particles above 35 nm in size while anatase is the most stable phase for nanoparticles below 11 nm, explaining why anatase can be synthesized at ultrafine sizes. Brookite has been found to be the most stable for nanoparticles in the 11–35 nm range. Different structures can be easily distinguished through XRD diffraction analysis useful also to estimate particles size through the Scherrer formula. In Figure 3.2, XRD diffraction patterns of very small TiO<sub>2</sub> crystals whose dimensions were measured by TEM analysis [26] are shown.

Figure 3.2 XRD diffraction patterns for very small TiO<sub>2</sub> NCs [26]

Fabrication techniques of TiO<sub>2</sub> with a wide variety of properties and morphologies include both wet-chemical and vacuum-based physical techniques: Chemical Vapour Deposition, Physical Vapour Deposition, Electrodeposition, hydrothermal, solvothermal, direct oxidation of titanium metal, sonochemical, microwave, sol-gel method [<sup>27,28</sup>and ref.s therein].

In particular in this thesis the attention is focused on the preparation of TiO<sub>2</sub> high refractive index thin films. Generally titania films can be obtained through different techniques such as chemical vapour deposition CVD [<sup>29</sup>], electrodeposition [<sup>30</sup>], electron-beam gun evaporation [<sup>31</sup>], reactive sputtering [<sup>32</sup>], plasmaenhanced CVD (PECVD) [<sup>33</sup>], atomic layer deposition (ALD) [<sup>34</sup>] and sol-gel method [<sup>35,36,37,38</sup>]. Each method has its own advantages and disadvantages.

Among all these methods, *sol-gel technique* is the most interesting from our point of view since it presents the advantage of fabricating high-quality TiO<sub>2</sub> nanomaterials with high photocatalytic activities consisting of extremely dispersed clusters which can be processed and used in optical applications, especially via a simple, inexpensive (no special apparatus are required) and low-temperature solution-based process. In fact, by tailoring the chemical structure of primary precursor and carefully controlling the processing variables, nanocrystalline products with very high level of chemical purity can be achieved. Moreover nanocomposite materials [<sup>39,40</sup>] and mixed oxide hybrid films, such as titania-silica coatings [<sup>41,42,43,44</sup>], can be easily fabricated through the sol-gel method since the low temperature synthesis presents the advantage of polymerizing in-situ an organic network or introducing organic molecules and organically modified alkoxides in the mixture solution, allowing to tailor and control many properties and parameters of the final materials (for instance refractive index, rheology, porosity and material processing [<sup>45</sup>]).

The non-alkoxide route uses inorganic salts (such as nitrates, chlorides, acetates, carbonates, acetylacetonates, etc.), which requires an additional removal of the inorganic anion, while the alkoxide route (the most employed) uses metal alkoxides as starting material (Ti(*O*-Et)<sub>4</sub>, Ti(*i*-OPr)<sub>4</sub>, and Ti(*O-n*Bu)<sub>4</sub> are most commonly used, Figure 3.3). This method involves the formation of a TiO<sub>2</sub> sol or gel or precipitation by hydrolysis and polycondensation of titanium alkoxides, Ti(OR)<sub>n</sub> to form oxopolymers, which are then transformed into an oxide network.

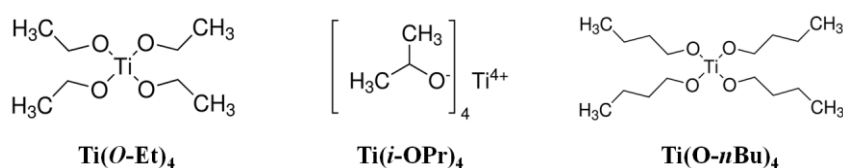
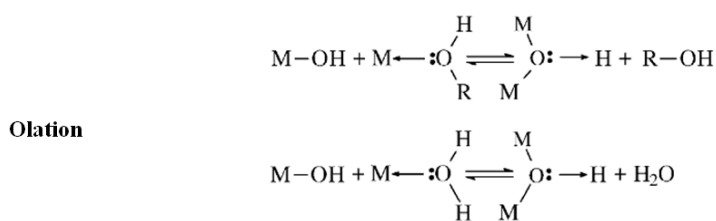
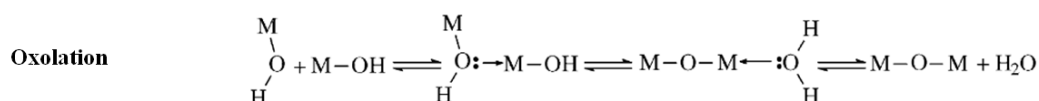
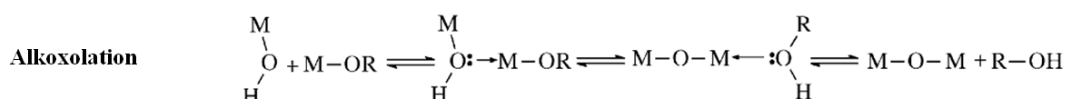


Figure 3.3 Most commonly used titanium alkoxides for sol-gel synthesis

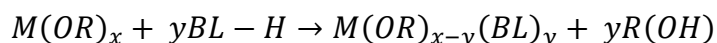
In hydrolytic syntheses, this process normally proceeds via hydrolysis step of titanium(IV) alkoxide followed by condensation, resulting in an oxide network. When Ti precursors interact with water without proper tailoring of the synthetic parameters such as pH and temperature, titanium hydroxides with a certain degree of condensation are obtained in the amorphous state. The structure of the final gel depends on the relative contribution of condensation reactions, that is alkoxolation, oxolation and ololation (below reported) because these reactions develop the three-dimensional skeletons of titania.



The amounts of water used during the gelation procedure determine the contribution of each reaction. Ti-O-Ti chains formation in the reaction mixture through alkoxolation is favored by a low content of water, low hydrolysis rates and excess of titanium alkoxide. Because each Ti is coordinated with four O atoms, three dimensional polymeric skeletons with close packing result from the development of Ti-O-Ti chains. A medium amount of water and high hydrolysis rates favour the formation of Ti(OH)<sub>4</sub> and reduce the relative contribution of alkoxolation. The excess water suppresses the development of Ti-O-Ti chains by oxolation since chemical equilibrium favours the creation of Ti-OH species. The presence of a large quantity of Ti-OH and insufficient development of three-dimensional polymeric skeletons lead to loosely packed first-order particles. For high concentration of water, polymeric Ti-O-Ti chains are developed, through the ololation reaction. Closely packed first order particles are then yielded via a three-dimensionally developed gel skeleton, generally in excess water followed by peptization in acidic condition at refluxing temperatures<sup>[46,47,48]</sup>. It is then clear that a method to control and separate titanium alkoxide hydrolysis and condensation steps consists in using acid-base catalysis: acid catalysis increases hydrolysis rates and ultimately crystalline powders are formed from fully hydrolysed precursors<sup>[49]</sup> while base catalysis is

thought to promote condensation with the result that amorphous powders are obtained containing unhydrolyzed alkoxide ligands.

It has to be pointed out that the reactivity of metal alkoxides towards water is much higher than that of silicon alkoxides because of the lower electronegativity of the metals compared to silicon and because the coordination number (c.n.) of metals is higher than their valency, which results in what is called coordination expansion. Therefore, metal alkoxides are Lewis acids, i.e. they can interact with compounds having a lone pair of electrons (Lewis bases) to achieve higher c.n.: in the case of Ti this results in compounds in which the titanium atom has a higher c.n. than 4. To obtain homogeneous titanium oxide networks for application, control of hydrolysis is then essential. In fact, while catalysts are often needed to enhance the reactivity of silicon alkoxides in sol–gel processes, chemical additives, such as diol, carboxylic acid or diketone compounds are added to moderate the reactivity of metal alkoxides in order to achieve a better control over the evolution of the microstructure [50]. Titanium alkoxides exhibit a high aggregation tendency and react vigorously with water producing ill-defined titanium-oxo/hydroxo precipitates. On the other hand, introducing chemical additives such as bidentate complexing ligands (BL), transparent titania-based sols and gels can be obtained. For example, if a metal alkoxide  $M(OR)_x$  is reacted with acetic acid or acetylacetone (BL–H), a fraction of the alkoxide groups is substituted by acetate or acetylacetonate groups, obtaining a new molecular precursor  $M(OR)_{x-y}(BL)_y$ :



The modified alkoxide exhibits a lower reactivity since the stronger bonding, multidentate ligands are less readily hydrolyzed than the remaining OR groups upon sol–gel processing. Additionally, the preferred coordination mode of these ligands can be exploited to control the evolution of the structure.

Apart from the fact that the new precursor has a different reactivity, other consequences of using complexing ligands are:

- decreased degree of crosslinking of the gel network because of the smaller proportion of hydrolyzable OR groups,
- lower connectivity of the molecular building blocks,
- change of the polarity by the organic groups (probably a similar effect on the network structure as changing the polarity of the solvent),
- hydrolysis and condensation reactions stereochemically directed by the complexing ligands.



Titanium alkoxide modification can be obtained by complexation with coordination agents that hydrolyze slower than alkoxide ligands:

- **alkoxy- and aminoalcohols:** formation of  $Ti_2(OR)_8(LH)_2$  ( $LH = ROH$  or  $RNH_2$ ) where the neutral donor ( $X = OR$  or  $NR_2$ ) group is incorporated into an alkoxo ligand (Figure 3.4). Finally the coordination of the group  $X$  to Ti stabilizes the bonding of the alkoxo ligand due to formation of a chelate ring.

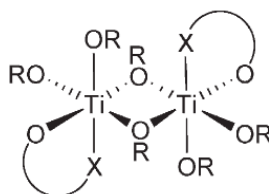


Figure 3.4 Schematic structure of  $Ti_2(OR)_6(O\cap X)_2$  ( $O\cap X =$  anionic bidentate ligand with a neutral donor group  $X$ ).

Furthermore, 2-Methoxyethanol is used as a (co-)solvent in sol-gel reactions because it is known to influence the reactivity of metal alkoxides. This is due to alkoxide exchange reactions, i.e.,  $OR$  groups are exchanged for  $OCH_2CH_2OMe$  groups [<sup>50,51</sup>]. The reactivity changes probably originate from the potential coordination of the  $OMe$  group that blocks coordination sites at the metal atom.

-  **$\beta$ -diketones,  $\beta$ -ketoesters,** whose chemical structure is reported in Figure 3.5

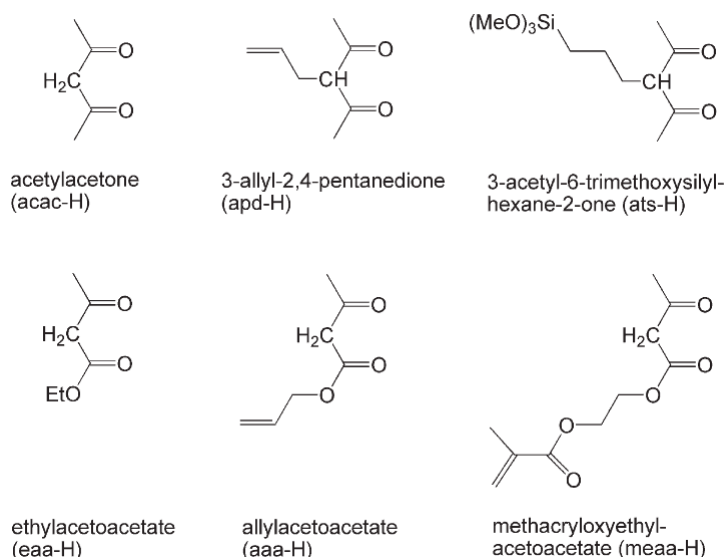


Figure 3.5  $\beta$ -diketones and  $\beta$ -ketoesters used for the chemical modification of  $Ti(OR)_4$ .

In all known structures of monomeric or dimeric titanium alkoxide derivatives, the  $\beta$ -diketonate ligands predominately form metal chelate which can cap the surface of the

structure (Figure 3.6). Substitution of OR groups by  $\beta$ -diketonate groups is restricted to disubstitution, because a higher degree of substitution would result in either a c.n. of the titanium atoms larger than 6 or in a monodentate coordination of the acac ligands.

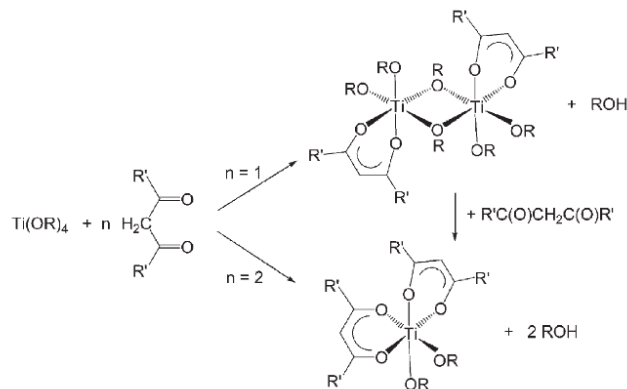


Figure 3.6 Monomeric or dimeric titanium alkoxides derivatives modified with  $\beta$ -diketonate ligands

- **carboxylic acids**, whose reaction with titanium alkoxide that generally occurs is below reported:



Carboxylate ligands have a strong tendency to bridge metal centre (Figure 3.7).

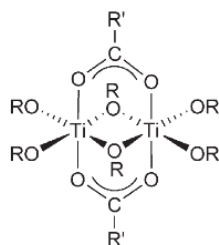


Figure 3.7 The dimeric structure of mono-substituted derivatives  $Ti(OR)_3(OOCR')$ .

- **phosphonic, phosphinic or sulfonic acids**, whose potential for varying the chemical properties of titanium alkoxides is much less investigated than the reactions of  $Ti(OR)_4$  with carboxylic acids.

After controlled hydrolysis, condensation pulls together the constitute particles or clusters of the gel into a compact mass, thus building up the metal oxide crystal. The condensation is generally accomplished by gelization and calcinations, whose temperature is especially important for removing the organic molecules from the final products and completing the crystallization to either anatase or rutile  $TiO_2$  (recent variants of the sol-gel method lowered

the crystallization temperature to less than 100°C [<sup>52,53</sup>]). However, very high calcinations temperature results in aggregation and/or phase transformation, and affects the microstructures as well as the properties of TiO<sub>2</sub> nanoparticles. It has been demonstrated that the photocatalytic activity of TiO<sub>2</sub> strongly depends on its crystal structure: anatase-phase TiO<sub>2</sub> crystallites are generally found to be more active than rutile, even if rutile phase has also been shown to be more active than anatase in few examples, such as photodecomposition of H<sub>2</sub>S and photooxidation of H<sub>2</sub>O with Fe<sup>3+</sup>. Recently, it has been found that anatase/rutile mixture (7/3) made the best photocatalyst for the oxidation of organic materials in the wastewater treatment. Thus, the microstructure of the TiO<sub>2</sub> plays crucial role in determining its photocatalytic activity [<sup>54</sup> and ref.s therein].

Another aspect that has to be considered during sol-gel film preparation is the film thickness. In fact thin film that does not crack, prepared by pure thermal decomposition of titanium alkoxides process, is only about 100-200 nm, which makes it less viable for industry use that normally requires a thickness of 500 nm to 1000 nm. During this work we faced this issue in order to produce thicker films without cracking, along with high refractive indices (higher than 1.9) and high transparency over the visible region.

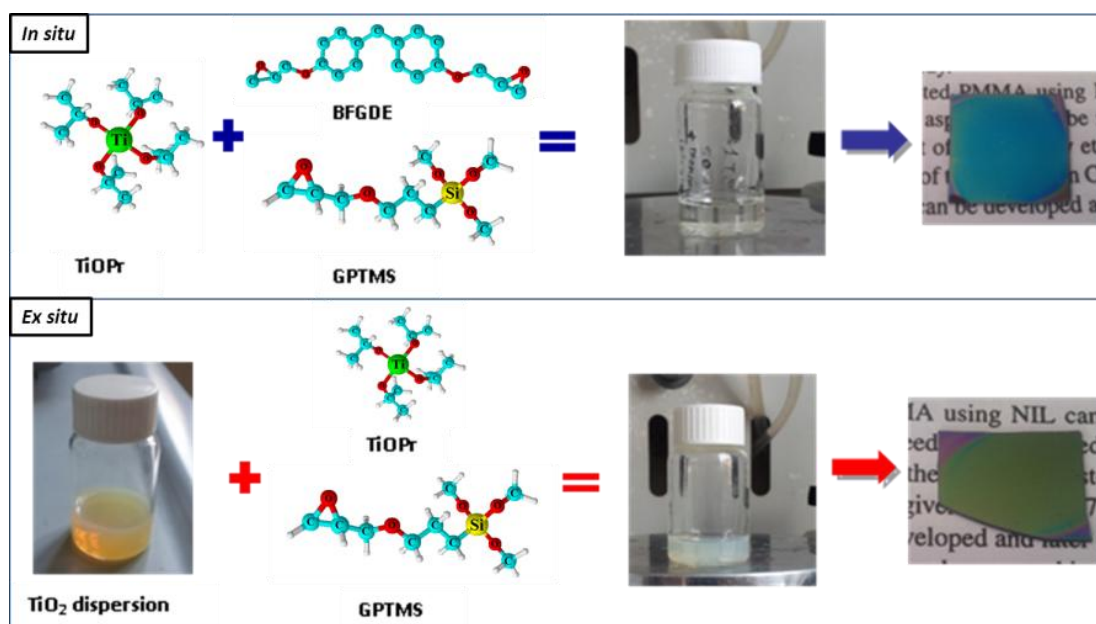
### **3.2. *Synthesis of two titania based materials: in and ex-situ***

The main methods that are usually used to fabricate organic/inorganic hybrid (HOI) materials are in-situ and ex-situ synthesis. In the first one the inorganic NPs are formed simultaneously with the synthesis of the HOI material, in the second one the NPs are added to the material already synthesized [<sup>55</sup>]. The two different titania based resists were obtained either by in-situ obtaining titania clusters starting from titanium alkoxides or by loading a silica-titania based resist with ex-situ synthesized commercial 15 nm-size anatase nanoparticles. Different silicon alkoxides or monomers were also added to improve the resists performances and material processing during lithographic processes.

The synthesis reported below are referred to the “final” recipes for ex-situ and in-situ TiO<sub>2</sub> materials. Although different recipes and titania contents were studied and modified during the study, the final recipes are the result of adjustments and changes arising from experimental evidences.

### 3.2.1. Materials and methods

Titanium(IV) isopropoxide (TiOPr, purum,  $\geq 97.0\%$ ), 3-glycidyloxypropyltrimethoxysilane GPTMS and Bis[4-(glycidyloxy)phenyl]methane BFGDE were all purchased from Aldrich and used as received. The dispersion of TiO<sub>2</sub>-Anatase in 2-Propanol (20wt%) was purchased from MKnano and it contains particles of 15 nm as stated by the supplier. DLS measurements on MKnano dispersion proved that the average diameter of the nanoparticles is  $11.4 \pm 0.4$  nm, Figure 3.8. Methoxyethanol and MEK were purchased from Aldrich and used as solvent for the resist synthesis and dilution. The two methods used in our experiments to fabricate photosensitive hybrid organic-inorganic (HOI) sol-gel based spin-on TiO<sub>2</sub> resists are named *in-situ* and *ex-situ* synthesis (Scheme 3.1).



Scheme 3.1 Alkoxides (TiOPr, GPTMS), nanoparticles (TiO<sub>2</sub> dispersion, 15nm) and organic monomer (BFGDE) used to synthesize HOI films, sol and spin coated films. The main part of *in-situ* and *ex-situ* sol composition derives from TiOPr and TiO<sub>2</sub> respectively.

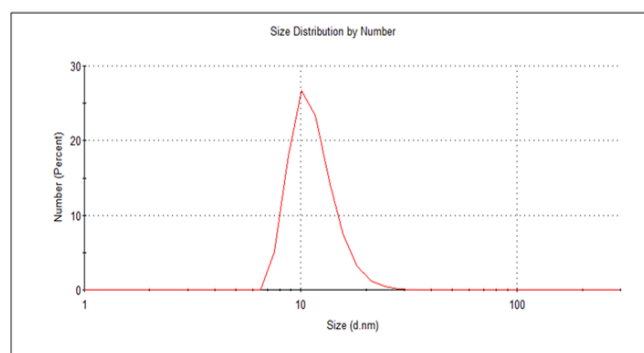


Figure 3.8 DLS measurement on MK Nano anatase NPs dispersion

### 3.2.1.1. In-situ synthesis

Titania network is formed simultaneously with the synthesis of the HOI material, by hydrolysis and condensation of TiOPr (90% mol) and minor amount of silica precursor (GPTMS). 3-glycidoxypropyltrimethoxysilane (GPTMS) is an organically modified alkoxide containing an epoxy ring. The inorganic part of the molecule is an alkoxy-silane polymerizable via hydrolysis and condensation reactions at room temperature, thus leading to a glass like material. The mild conditions under which the inorganic part of the material is prepared are compatible with the presence of the organic moiety. The epoxy group can undergo ring-opening reactions which can produce polyethylene oxide chains interconnected with the inorganic network in the final material (Class II Hybrids).

GPTMS was first hydrolyzed (molar ratio H<sub>2</sub>O:GPTMS=3:1) for one night at RT. This pre-hydrolysis step is necessary to compensate the higher reactivity of titanium alkoxides due to its Lewis acid nature, with respect to that silicon alkoxides [50]. In the second step, MeOEtOH and NaOH (0,3%M in GPTMS) were added to the GPTMS solution in this order. Separately, TiOPr was added to MeOEtOH at a 1:1 volume ratio, and the solution was stirred for about 10 minutes. As previously mentioned 2-methoxyethanol plays two different roles, acting as solvent as well as stabilizer of titanium alkoxide toward the hydrolysis reaction since it has the ability to coordinate TiOPr, decreasing its hydrolysis rate, without the need for other complexing agents or Ti precursor stabilizing additives. Too low methoxyethanol content results in sol gelation during synthesis or too fast hydrolysis of Ti precursor, obtaining a non-transparent solution. It has to be pointed out that Lewis acids such titanium, zirconium, aluminium alkoxides, in this case Ti-isopropoxide, catalyze GPTMS epoxy ring opening and its polymerisation (Figure 3.9).

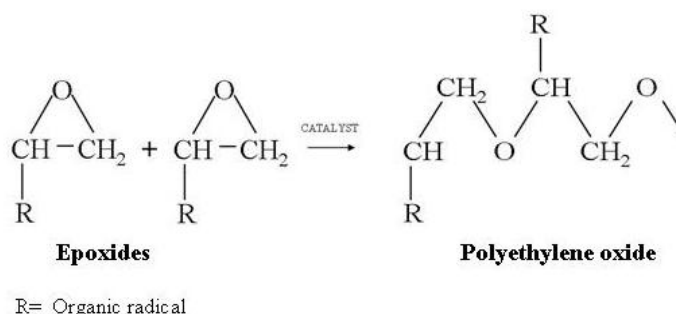


Figure 3.9 Epoxy ring polymerization and formation of polyethylene oxide

The two prepared solutions were then mixed and the monomer bisphenol F diglycidyl ether (BFDGE) (5% molar with respect to TiO<sub>2</sub> content) was added to the solution in order to decrease the hardness of the film for the imprinting process due to high TiO<sub>2</sub> content, to increase the material processing and the final films thickness. For the same purpose different monomers were tested: glycerol diglycidyl ether (GDE), glycidyl hexadecafluorononyl ether (GD16) and Zonyl<sup>®</sup> FSN 100.

monomer	PM [g/mol]	Density [g/ml]	Refractive index <i>n</i> <sub>20/D</sub>
glycerol diglycidyl ether (GDE)	204.22	1.229	1.482
glycidyl hexadecafluorononyl ether (GD16)	488.17	1.682	1.342
<sup>®</sup> Zonyl FSN 100	~950	1.35	1.395
bisphenol F diglycidyl ether (BFDGE)	312.36	1.19	1.579

Table 3.2 Different tested monomers for in-situ synthesis

However bisphenol F diglycidyl ether (BFDGE) presents several advantages over the tested monomers: it gives more stable solution and better imprinting results, it increases the contrast (that is the chemical difference) between the exposed and unexposed areas of the resist material under UV light, necessary for the optical lithography process, and finally it presents the higher refractive index among the tested monomers. The last listed property was important because the final purpose of the work was the realization of high refractive index micro- and nano- structures. Amount of monomer between 0% and 50% molar with respect to TiO<sub>2</sub> content were added to the sol in order to study their effects on the final properties of the resist and to find out the best recipe for synthesizing a titania sol that could be used both as a nanoimprint and optical lithography resist. However in the present thesis “in-situ” name without any specification refers to the sol with 5% BFDGE, the final chosen monomer content that gives a good compromise in terms of material processing and refractive index.

The synthesis was carried out in methoxyethanol solvent to obtain a final sol concentration of 100 g/l TiO<sub>2</sub> content and a molar ratio of approximately SiO<sub>2</sub>:TiO<sub>2</sub>=10:90. Finally the sol was kept under sonication for 30min and left to react under stirring for 1h at room temperature and for 2h at 80°C. The sol was filtered with a microporous membrane (0.2 µm Millipore) before use and appeared clear.

### 3.2.1.2. *Ex-situ synthesis*

Two solutions were first prepared:

- TiOPr was added to methoxyethanol, that acts both as solvent and as stabilizer of TiOPr, decreasing its hydrolysis rate,
- the dispersion of TiO<sub>2</sub>-Anatase (15 nm particles mean size) in 2-Propanol (20wt%) was loaded with 30 wt% of a previously prepared silica sol based on GPTMS, named GB, whose synthesis was previously reported in [56]. GB indicates a basic solution of GPTMS acidified with concentrated HCl 37%, obtained by GPTMS hydrolysis at 80°C for 1h with H<sub>2</sub>O and NaOH (GPTMS:H<sub>2</sub>O: NaOH=1:3:0.003), with a final concentration of silica of 220g/L. TiO<sub>2</sub> NPs dispersed in different solvent e.g. 2-isopropanol, ethylacetate, butylacetate, acetone, ethanol gives inhomogeneous and dull films full of comets.

The small amount of titanium isopropoxide (10% molar with respect to silica) was added to the sol with the aim of creating a network that traps the TiO<sub>2</sub> NPs avoiding agglomeration. Inside the sol-gel GB solution, the molecules of GPTMS are already bonded together through Si-O-Si bonds, while the chains containing the epoxy ring are not polymerized. Task of titanium isopropoxide is to catalyse the epoxy rings polymerization, building a structure that embodies the NPs. Titanium isopropoxide acts then as a catalyst while GB sol improves film quality, increases layer thickness (up to 1.5 micron thickness) and makes possible film deformation during NIL.

Both solutions were left to stir for 10min at room temperature, followed by another 10min of sonication. Then the solution containing titanium isopropoxide was poured into the GB-TiO<sub>2</sub> NPs solution and left stirring for 10min at 70°C.

The final sol was vacuum evaporated to remove solvents: 2-propanol contained in the TiO<sub>2</sub> dispersion and methoxyethanol. The evaporation step was introduced in order to obtain thick, bright and homogeneous film without cracks. It is difficult to control the evaporation rate, however, it seems that 25min are sufficient to evaporate most of the solvents, still avoiding gelation.

The evaporated solution was diluted again to obtain the final sol concentration of 90 g/l (TiO<sub>2</sub>), and a SiO<sub>2</sub>:TiO<sub>2</sub> molar ratio of 35:65. Finally the solution was centrifuged at 5000 rpm for 7 min and filtered by a microporous membrane (0.2 μm Millipore) to remove large particles and improve the resist.

### 3.2.1.3. In-situ and Ex-situ films deposition

Both sol-gel titania based solutions were spin coated at different speeds to obtain films with the desired thickness. The thickness of the spin coated films at different spin speeds (from 1000rpm to 5000rpm, Figure 3.10) was measured by profilometer. The thickness of films decreases with the spin speed and the maximum film thickness reaches values of 1.5 $\mu\text{m}$  for ex-situ and 1 $\mu\text{m}$  for in-situ sol at 1000rpm, although the film thickness might become thinner via a postbake process. As could be expected the addition of different amount of BFDGE leads to different film thickness (the values at 4000rpm are reported): higher the BFDGE content, higher the films thickness. During deposition, the solvent present inside the solution evaporates.

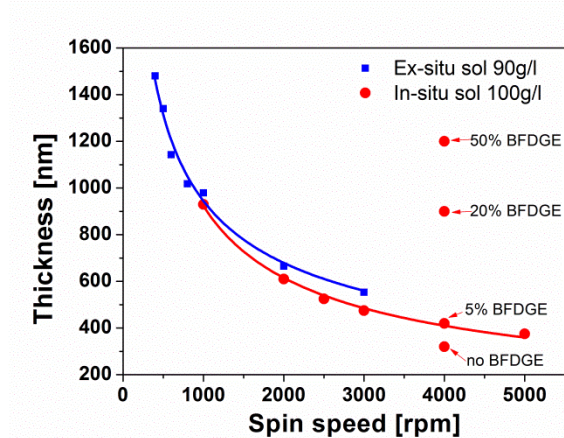


Figure 3.10 Thickness of ex-situ and in-situ (with BFDGE content between 0 and 50% mol) films vs spin speed

### 3.3. Characterization of the synthesized ex-situ and in-situ sol-gel materials

The UV-Vis absorption of the films was characterized by UV-Vis spectroscopy (JASCO V-570) in the wavelength range 200-800 nm. Fourier Transform Infrared spectroscopy (spectrometer Jasco FT-IR-620) in the range of 400-4500  $\text{cm}^{-1}$  with a resolution of  $\pm 4 \text{ cm}^{-1}$  and Rutherford Back Scattering (RBS) were performed to evaluate the composition transformations of the films deposited on silicon wafers and to examine the effects of UV irradiation and thermal treatment. Thermal analysis from RT to 1000 $^{\circ}\text{C}$  was carried out with STA409/429 Netzsch TGA instrument in order to evaluate the films composition changes during thermal treatments. Refractive index and thickness changes of the films during UV exposure and TT have been recorded by ellipsometric measurements (V-Vase J.A.Woollam Ellipsometer). The film structure and titania crystalline cluster size were investigated through



TEM (Jeol 3010 apparatus operated at 300 kV with a high resolution pole) and X-ray diffraction (XRD) using an X-ray diffractometer (Philips PW 1729) with Cu K $\alpha$  irradiation. The study of solutions rheology was conducted using AR2000ex rheometer in order to better understand the materials behaviour during imprinting tests.

Finally, the quality of the obtained imprinted and UV patterned structures was analyzed by optical microscopy, scanning electron microscopy (SEM-ESEM Quanta 200, FEI Company, Eindhoven, The Netherlands and Zeiss LEO 1550) and Atomic Force Microscopy (NT-MDT).

### 3.3.1. *UV-Vis characterization*

UV-Vis spectra of in-situ and ex-situ films deposited on quartz in the wavelength range of 200-800 nm is reported in Figure 3.11a, compared to the spectrum of the UV lamp (Hamamatsu Lightningcure LC5) with a UV power density estimated at 365nm equal about to 180mW/cm<sup>2</sup> (at 4 cm) used for film exposure and patterning. Both hybrid sol-gels show a high absorbance in the UV region below 330nm, absorbing the lower wavelength of the light emitted by the UV lamp used for exposure and patterning, while they exhibit high transparency ~92% at 630nm and at 660nm for as deposited in-situ and ex-situ films respectively

The absorption edge of the films could be estimated from the intercept of the tangents to the plots of absorbance vs wavelength. This property allows to directly obtain inorganic structures by exposing imprinted titania and to directly pattern titania films by exposing them through a quartz-Cr mask without further addition of initiators or catalyzers. The different values of the absorption edge, 318 nm (3.90 eV) and 333 nm (3.72 eV) for in-situ and ex-situ films respectively, could be due to the difference in particles size embedded in the resist films: the in-situ nanoparticles seem to be smaller than ex-situ ones, as is confirmed by XRD and TEM spectra reported in the dedicated section.

The optical bandgap of in-situ films was reduced from 3.90eV to 3.55eV after UV exposure due to organic component degradation, titania cluster growth and compaction of the film, Figure 3.11b.

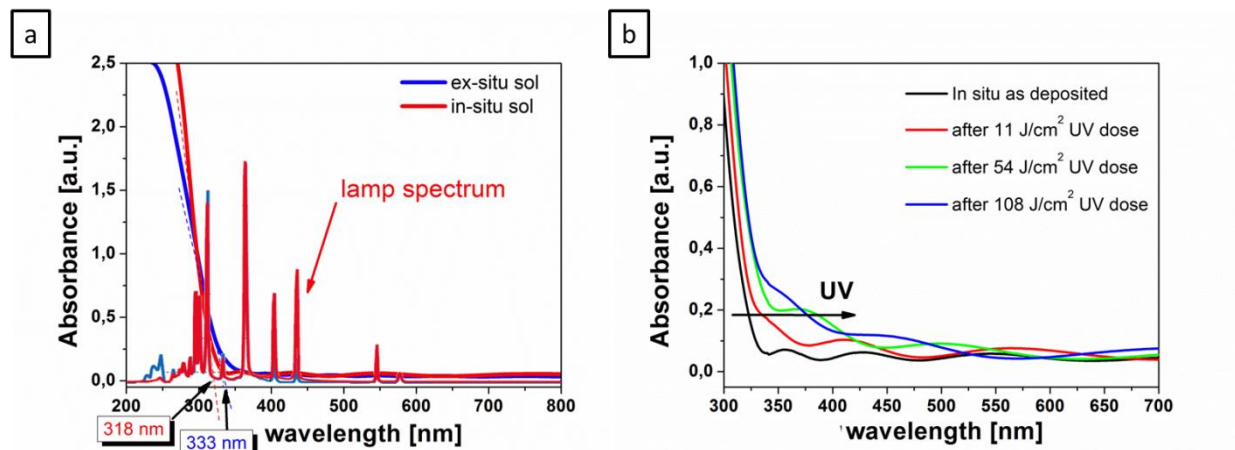


Figure 3.11 (a) Uv-Vis spectra of in-situ and ex-situ sols deposited on quartz substrates; (b) UV-Vis spectra of in-situ film deposited on quartz with increasing UV exposure doses

### 3.3.2. FTIR characterization

#### 3.3.2.1. Analysis of “as deposited” in-situ and ex-situ titania films

Figure 3.12 shows the Fourier transform infrared (FTIR) spectra of the “as deposited” ex-situ and in-situ films respectively while Table 3.3 reports the most significant absorption peaks.

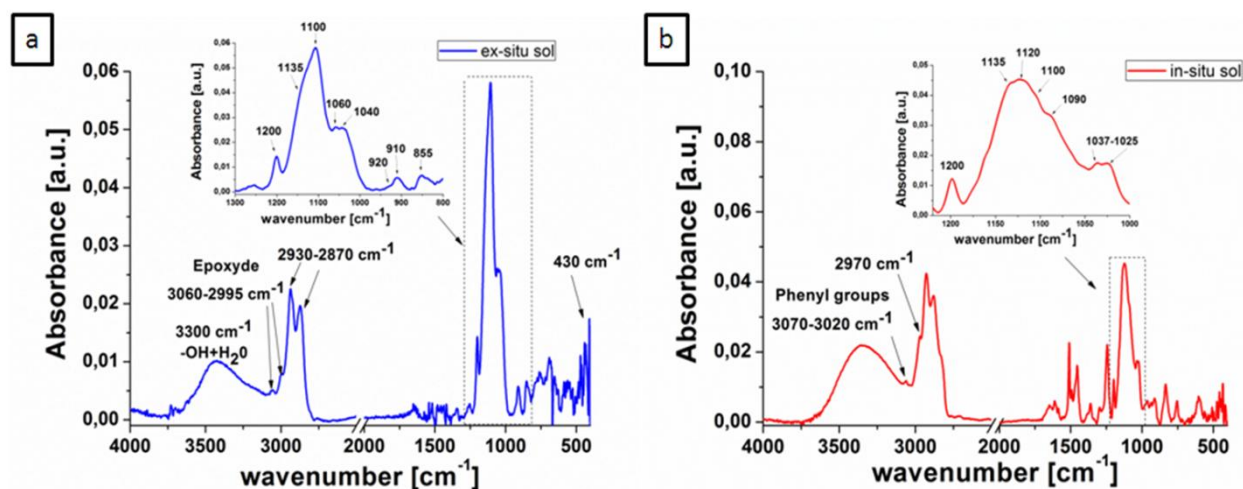


Figure 3.12 FTIR spectra of the “as deposited” ex-situ (a) and in-situ (b) films

In-situ and ex-situ FTIR spectra present the large  $\nu(\text{O-H})$  band between  $3600$  and  $3000 \text{ cm}^{-1}$  due to the absorption of the hydrolyzed precursors and the  $\nu(\text{OH})$  group of 2-MetOEtOH (the solvent used during the synthesis), that absorbs at  $3420 \text{ cm}^{-1}$ , which maybe gives his contribution on that band together with the  $\nu(\text{OH})$  of water and solvents formed during hydrolysis and condensation of precursors (methanol and isopropanol).

Both spectra show the C-H set vibrations, due to the organic component of the films, visible between  $3000$  and  $2800 \text{ cm}^{-1}$  (C-H stretching vibrations) and between  $1500$  and  $1300 \text{ cm}^{-1}$

(simple bending vibrations). In particular, we observe the asymmetric C-H stretch of the methylene groups ( $2930\text{ cm}^{-1}$ ) occurring at slightly higher frequency than symmetric vibrations ( $2855\text{ cm}^{-1}$ ), and the methylene C-H bend at  $1485\text{--}1445\text{ cm}^{-1}$ .

In the in-situ spectra two other peaks at  $2970\text{ cm}^{-1}$  and  $2830\text{ cm}^{-1}$  are present. The former is due to the stretching of the C-H bond that can be ascribed to isopropoxide species, as they are coincident with bands due to titanium isopropoxide and isopropanol [<sup>57,58</sup>], and the latter to the presence of the  $\text{-OCH}_3$  of the methoxyethanol used as the solvent for the synthesis and to some extent also to the  $\text{Si-OCH}_3$  groups (of the GPTMS) not yet reacted.

The epoxy ring in GPTMS (and in BFDGE for the in-situ sol) has four characteristic vibrational modes: ring breathing at  $1260\text{--}1240\text{ cm}^{-1}$ , antisymmetric ring stretching at  $910\text{ cm}^{-1}$  and  $855\text{--}750\text{ cm}^{-1}$ , C-H stretching at  $3060\text{--}2995\text{ cm}^{-1}$  which are clearly visible in ex-situ spectra.

Group frequency wavenumber ( $\text{cm}^{-1}$ )	Assignment
<b>3600-3000</b>	Hydroxy group, O-H stretch
<b>3070 and 3020</b>	C-H aromatic groups
<b>3060 and 2995</b>	Epoxy ring C-H stretching
<b>2970</b>	Methylene C-H stretch
<b>2930</b>	Methylene C-H asym. stretch
<b>2855</b>	Methylene C-H sym. stretch
<b>2830</b>	$\text{OCH}_3$ groups
<b>1720</b>	C=O stretch
<b>1613-1585-1510-1470</b>	Aromatic C=C-C stretch
<b>1500-1300</b>	Methylene C-H bend
<b>1360</b>	Methyl in the "iso" form
<b>1260-1240</b>	Epoxy ring breathing
<b>1200-1070</b>	- $\text{CH}_2\text{-O-CH}_2$ - sym. stretch
<b>1135-1140</b>	silica cages
<b>1150-1050</b>	Alcohol C-O stretch
<b>1100-1030</b>	silica asym. stretching vibrations (Si-O-Si)
<b>920-910</b>	Ti-O-Si stretching and Si-OH bonds
<b>910 and 855-750</b>	Epoxy ring asym. stretch
<b>458</b>	Si-O-Si rocking
<b>430</b>	Ti-O bond

Table 3.3 Most significant FTIR absorption peaks for the sols analysis

BFDGE epoxy ring absorption are still detectable at the end of in-situ synthesis, in spite of titanium high concentration, at  $3060\text{--}2995\text{ cm}^{-1}$  and  $1244\text{ cm}^{-1}$ , the former overlapped with the peaks due to the C-H solvent absorption or the C-H aromatic groups of BFDGE absorption at  $3020$  and  $3070\text{ cm}^{-1}$ . This is explained by the fact that the basic condition prevent the full ring opening, decreasing the Lewis activity of the metal alkoxide precursor.

In the in-situ spectra, other most important set of bands are the aromatic ring vibrations (para-substituted phenyl groups stretching vibrations) centred around  $1600$  and  $1500\text{ cm}^{-1}$  of the monomer BFDGE: there are aromatic C=C-C stretch bands (for the carbon-carbon bonds in the aromatic ring) at  $1613\text{--}1585\text{--}1510\text{--}1470\text{ cm}^{-1}$ .

This bands overlap with other C-H set of vibrations which occur between  $1500$  and  $1200\text{ cm}^{-1}$  (simple bending vibrations of the methylene C-H bend at  $1485\text{--}1445\text{ cm}^{-1}$  and asym/sym. bending of methyl  $\text{-CH}_3$  at  $1470\text{--}1430\text{ cm}^{-1}$ ),  $1360\text{ cm}^{-1}$  related to the methyl in the “iso” form as for isopropanol). The peak at  $1244\text{ cm}^{-1}$  is referred to the epoxy groups or generally to the C-H in plane bending.

The broad peak between  $1200\text{--}1000\text{ cm}^{-1}$  is a sum of absorptions due to stretching vibration of C-O of alcohols between  $1050$  and  $1150\text{ cm}^{-1}$  and of symmetric stretching vibration of the  $\text{CH}_2$  and  $\text{-CH}_2\text{-O-CH}_2\text{-}$  linear groups of the propylic chain of GPTMS (or the etheric groups of BFDGE for the in-situ sol) between  $1070$  and  $1200\text{ cm}^{-1}$ . All these peaks are related to the presence of the organic component in the “as coated” film [59].

The vibrational modes directly related to Si-O-Si antisymmetric stretching [60] show a complex feature, with several overlapped bands that are observed in the range  $1300\text{--}950\text{ cm}^{-1}$ . The explanation is somehow complex because of the formation of polycyclic siloxanes often observed in trifunctional organically modified alkoxides. In particular, in both solution a band around  $1060$  can be detected, that corresponds to the  $\nu_{\text{as}}$  antisymmetric stretching of the O atoms along a direction parallel to Si-Si in Si-O-Si bond  $(\text{TO}_3)$ [61] found in sixfold ring structures typical of amorphous dense silica in GB. A distinct region of interest is in the  $1100\text{--}950\text{ cm}^{-1}$  interval, in which several overlapped modes are observed. The  $1035\text{--}1060$  region is typical of open chain trisiloxane units and  $\text{T}_x(\text{OH})_y$  species. However due to the high condensation degree of GPTMS in basic synthesis this band can be assigned to extended chain structures, such as polymeric, linear, branched or ladder type structures [62]. Ladder-like structures is accompanied by a stronger absorption at  $1135\text{--}1155\text{ cm}^{-1}$ , present in both solutions that is ascribed to large strain-less cage species  $\text{T}_n$  such as  $[\text{RSiO}_{1.5}]_{8,10}$  or  $12$  silica structures ( $\text{T}_n$  denotes a cage structure with  $n\text{ SiO}_{3/2}$  groups). This absorption band indicates

that highly condensed cage species are preferentially formed during the basic synthesis process. This is in agreement with the small absorption of SiOH around  $920\text{ cm}^{-1}$  maybe overlapped with Ti–O–Si and epoxy stretching vibration [59]. The –OH band at 3600–3000 could be then mainly attributed to solvents or hydrolyzed titanium precursor, rather than hydrolyzed GPTMS. The absorption features around  $430\text{ cm}^{-1}$ , can be assigned to stretching vibration of Ti–O band overlapped with the rocking ( $458\text{ cm}^{-1}$ ) vibration modes of the Si–O–Si bonds in  $\text{SiO}_2$ .

As reported by other authors the ratio between the intensity absorption at 1135 and  $1035\text{ cm}^{-1}$  indicates a measure of the condensation state of the xerogel; a larger ratio between the two intensities suggest that more T cube-like species are formed and less polycondensed species that act as linking units between the silica cages, are formed. As could be noticed in Figure 3.13 this ratio increases during the “in-situ” synthesis, no open chains are present as siloxane condensation products and the structure is dominated by  $T_n$  ( $n = 8, 10$  and  $12$ ) cube-like species connected with short ladder-like bridging 4-member rings [63].

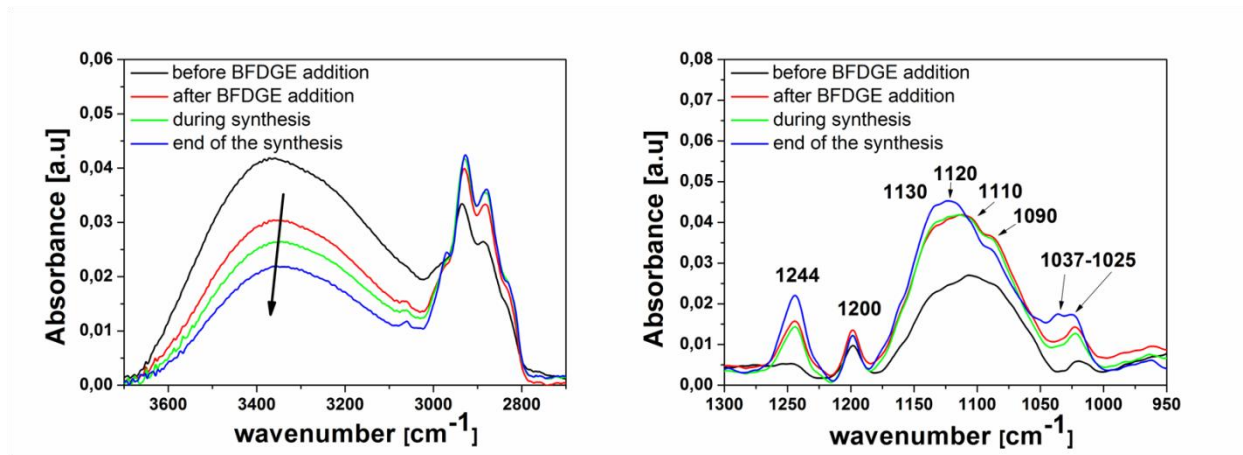


Figure 3.13 FTIR spectra of “in-situ” films at different steps during synthesis

### 3.3.2.2. FTIR and ellipsometry after high temperatures thermal treatment

FTIR spectra of ex-situ and in-situ films treated 1h at different temperatures (up to  $500^\circ\text{C}$ ) are reported in Figure 3.14 and Figure 3.15.

In both ex-situ and in-situ spectra the degradation of the organic species increase with thermal treatment temperature. The  $\text{CH}_2$  doublet absorption at  $2937$  and  $2876\text{ cm}^{-1}$ , that can be used to control the organic chain evolution, decreases continuously in in-situ films with temperature, instead in ex-situ films is almost constant up to  $300^\circ\text{C}$ , when it shows an abrupt decrease. In both in and ex-situ films this absorption completely disappears at  $300^\circ\text{C}$ . The second

representative region is the one between 1300-700  $\text{cm}^{-1}$  range. Even in this case, the intense peak at 1107  $\text{cm}^{-1}$ , related to  $\nu_{\text{AS}}(\text{C-O-C})$  bonds of the propyl chain, and the one at 1200  $\text{cm}^{-1}$  related to the symmetric stretching vibration of the  $\text{CH}_2$  groups of the propyl chain disappear after thermal treatments, in particular after 300°C, indicating a thermal decomposition of the organic components. In both films a broad absorption around 950  $\text{cm}^{-1}$  appears with TT due both to Si-OH of hydrolyzed GPTMS absorption and to Ti-O-Si vibrations and so to the bonding of silica and titania clusters. In in-situ films up to 200°C this band could be ascribed to some extent to formation of Si-OH, but with higher temperatures – OH band at 3700-2700  $\text{cm}^{-1}$  decreases because solvents evaporate and Si-OH and Ti-OH condensation reactions are promoted. In ex-situ the broad band at 3100–3600  $\text{cm}^{-1}$  due to – OH absorption becomes weaker for increasing temperatures up to 200°C due to the proceeding of the inorganic condensation, whereas it increases in intensity for higher temperatures as a consequence of water released after the combustion of organic compounds. A high absorption at 430  $\text{cm}^{-1}$  that increases with temperature is observed in both ex and in-situ films and can be attributed to stretching vibration of Ti–O ascribed to the formation and condensation of titania clusters.

In in-situ films, the other bands centred around 1600 and 1500  $\text{cm}^{-1}$  due to the aromatic ring vibrations of BFDGE (para-substituted phenyl groups stretching vibrations and bending vibrations of the methylene C-H and methyl  $-\text{CH}_3$ ) decrease with thermal treatment and totally disappear at 300°C.

Figure 3.14b and Figure 3.15b reports the plot of the thickness (left) and refractive index@632nm (right) vs thermal treatment temperature for ex-situ and in-situ films. The refractive index of ex-situ film increases with thermal treatment up to 200°C, reaching the maximum value of 1.65@632nm, while an abrupt decrease is observed at 300°C. This could be explained by the FTIR spectra (Figure 3.14a): the organics CH absorption at 2800-3000  $\text{cm}^{-1}$  is almost constant with TT up to 200°C but organics start degrading. This is confirmed by the appearance of a peak around 1725  $\text{cm}^{-1}$ , ascribed to C=O bonds which can derive from the degradation of more labile organic species such as the  $\text{CH}_2\text{--O--CH}_2$  of GPTMS. With a thermal treatment of 1h at 300°C this peaks decreases since the degraded organic component starts to be removed and a porosity is probably formed. As a consequence the refractive index decrease even if the films thickness shrinks of its 25%.

As concern the in-situ film, the refractive index increases with treatment temperature up to 2.1@632nm after 1h at 500°C. As it can be seen from FTIR spectra, between 300 and 400°C

the degradation of the organic species occurs (CH absorption decreasing at 2800-3000  $\text{cm}^{-1}$ ), with the formation of new species ( $\text{COO}^-$  at 1520 $\text{cm}^{-1}$ ), and at 400°C these degradation species are removed leaving pores inside the film and leading to a only slight increase of the refractive index between 300 and 400°C.

The higher refractive index of the in-situ films compared to the ex-situ ones even at RT could be related to the lower porosity of in-situ films due to the formation of the clusters simultaneously with the synthesis of the HOI material. The higher refractive index obtained with increasing temperature thermal treatment is confirmed by FTIR spectra that report the formation of highly condensed titania clusters (increase of Ti-O-Ti) bonded to silica clusters (increase of Si-O-Ti with temperature).

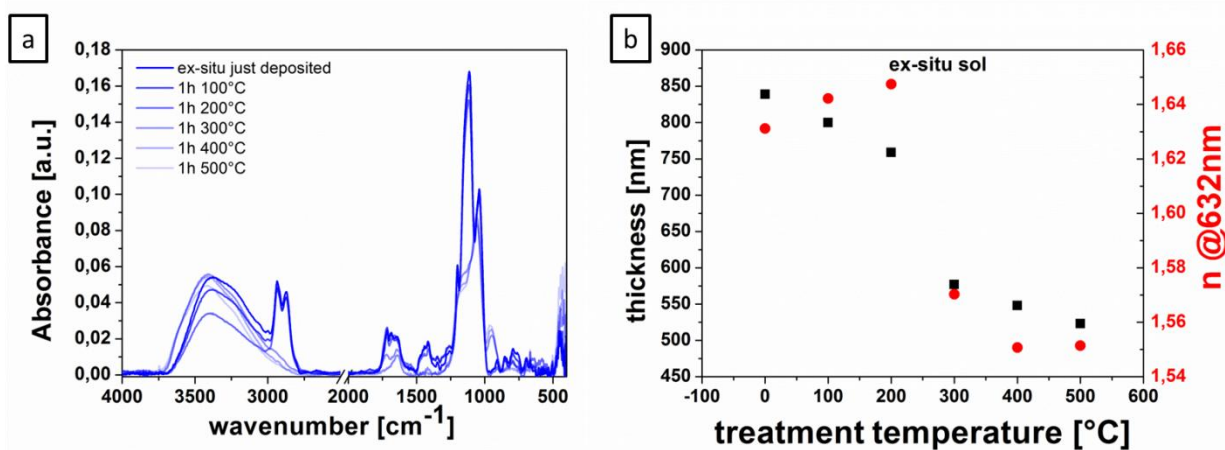


Figure 3.14 FTIR spectra of the ex-situ films after 1h thermal treatment at increasing temperatures (a) and plot of thickness and  $n@632\text{nm}$  vs treatment temperature (b)

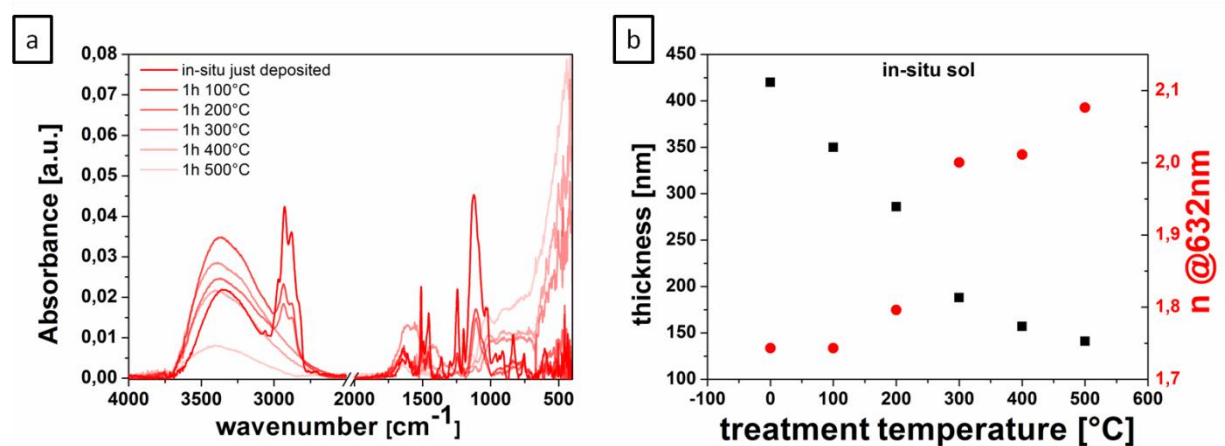
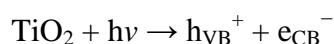


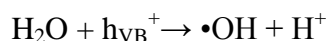
Figure 3.15 FTIR spectra of the in-situ films after 1h thermal treatment at increasing temperatures (a) and plot of thickness and  $n@632\text{nm}$  vs treatment temperature (b)

### 3.3.2.3. FTIR and ellipsometry after UV exposure

An alternative low-temperature strategy to transform films in inorganic SiO<sub>2</sub>-TiO<sub>2</sub> is the exposure to UV light, exploiting the photocatalytic titania effect since it is well-known that titania exhibits a strong oxidizing ability when exposed to UV: most aromatic and aliphatic substances are oxidized to CO<sub>2</sub> by active oxygen species that are generated at the TiO<sub>2</sub> surface [64] and some inorganic species are also oxidized to their most stable forms. In fact, in photocatalysis, the absorption of a photon of energy greater than the band gap of the semiconductor excites an electron to the conduction band (e<sub>CB</sub><sup>-</sup>) generating a positive hole in the valence band (h<sub>VB</sub><sup>+</sup>).



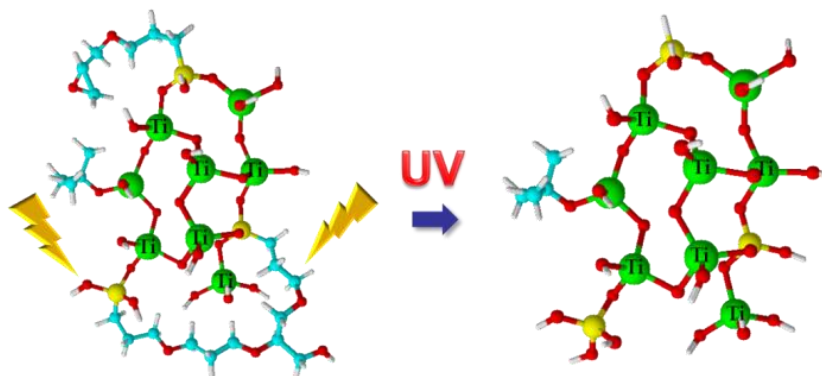
Charge carriers Ti<sup>3+</sup> and O<sup>-</sup> can recombine or alternatively can be trapped as defect sites in the TiO<sub>2</sub> lattice and initiate redox reactions in the presence of organic molecules. Positive holes photogenerated on TiO<sub>2</sub> can oxidize OH<sup>-</sup> or absorbed water to produce •OH radicals, which subsequently oxidize organic species producing mineral salts, CO<sub>2</sub> and H<sub>2</sub>O.



Molecular oxygen adsorbed on the titania particle traps electrons in the conduction band and reduces to form superoxide radical anion (O<sub>2</sub><sup>•-</sup>) that may further react with H<sup>+</sup> to generate hydroperoxyl radical (•OOH) and further electrochemical reduction yields H<sub>2</sub>O<sub>2</sub>. These reactive oxygen species may also contribute to the oxidative pathways such as the degradation of organics.

Therefore, when in and ex-situ titania films are irradiated with a light of energy higher than the energy gap of the active material, absorbing the incident radiation (for in-situ and ex-situ 3.90 and 3.72 eV, respectively), the organic component reacts with oxygen resulting in the production of carbon dioxide, water and mineral acids. Here presented titania materials efficiently absorb the light wavelength <330nm emitted by the lamp used for exposure and patterning, allowing to obtain inorganic structures when exposing imprinted films, or to directly pattern films by UV exposure without further addition of initiators or catalysts (Scheme 3.2).





Scheme 3.2 Photocatalytic effect of titania under UV irradiation

Therefore, the UV exposure induces analogous effect of thermal treatment concerning the organic component decomposition, as it is confirmed by a decreased absorption of organic  $\text{CH}_2$  groups at  $2937$  and  $2876\text{ cm}^{-1}$  and C-O-C absorption at  $1100\text{ cm}^{-1}$  in the FTIR spectra of both UV exposed ex-situ and in-situ sols (Figure 3.16a and Figure 3.17a). The disappearance of the asymmetric and symmetric C-H stretch could be achieved after an exposure of  $43\text{ J/cm}^2$  and  $108\text{ J/cm}^2$  for ex-situ and in-situ films respectively. This confirms that the removal of the organic component in ex-situ system is easier with respect to the in-situ one, because of the anatase crystalline structure of the former, in fact as already mentioned the photocatalytic activity of  $\text{TiO}_2$  strongly depends on its crystalline structure.

As it was for thermally treated films, in the ex-situ spectra the appearance of a small peak around  $1725\text{ cm}^{-1}$  can be observed in the film irradiated after  $11\text{ J/cm}^2$  exposure dose. This is a typical IR absorption region of C=O bonds which can derive from the degradation of more labile organic species such as the  $\text{CH}_2\text{-O-CH}_2$  bond of the etheric group in the propylic chain of GPTMS or surfactants/dispersants used in the commercial dispersion. Further proofs of this effect are the corresponding decreasing of the absorption at  $1100\text{ cm}^{-1}$  due to the C-O bond of the ether group and the increase at  $3400$  and  $1640\text{ cm}^{-1}$  of absorption of water molecules through an H bond with C=O groups, that are known to be very hydrophilic. An exposure dose of  $65\text{ J/cm}^2$  leads to the formation of Ti-O-Si bonds whose asymmetric stretching is around  $950\text{ cm}^{-1}$ .

The peak at  $1725\text{ cm}^{-1}$  decrease after irradiation with  $65\text{ J/cm}^2$  dose: this fact is probably due to the removal of such organic species which become more volatile and leave pores inside the film (as it was for the  $300^\circ\text{C}$  thermal treatment). This observation is confirmed by the plot of the refractive index vs UV dose of Figure 3.16b: after UV dose of  $65\text{ J/cm}^2$  the refractive index of ex-situ films decrease even if the film shrinks, confirming that the porosity increases

due to the disappearance of the volatile organic species. The ex-situ maximum refractive index obtained is  $\sim 1.65@632\text{nm}$  after  $43\text{ J/cm}^2$  UV exposure dose. The same maximum value was obtained with a thermal treatment of  $200^\circ\text{C}$ : UV exposure and TT have seem to have comparable effects on titania ex-situ films.

In the in-situ FTIR spectra the degradation of the organic species occurs in the same way with UV exposure: the two band at  $2930\text{ cm}^{-1}$  and  $2870\text{ cm}^{-1}$  due to  $-\text{CH}_2-$  asymmetric and symmetric stretching respectively, the band at  $1200\text{ cm}^{-1}$  attributed to the skeleton vibration of  $-\text{CH}_2-$  groups of the GPTMS chain, the main band at  $1100\text{ cm}^{-1}$  related to C-O-C bonds of the propylic chain, simple bending vibrations between  $1500$  and  $1300\text{ cm}^{-1}$ , due to the organic component of the films, decrease with UV exposure dose and completely disappear after a dose of  $108\text{ J/cm}^2$ . The organic set of bands of aromatic ring vibrations (para-substituted phenyl groups stretching vibrations) at  $1613$ - $1585$ - $1510$ - $1470\text{ cm}^{-1}$  decrease as well. Two other peaks at  $2970\text{ cm}^{-1}$  and  $2830\text{ cm}^{-1}$  present in the “as deposited” film, due to C-H bond, ascribed to isopropoxide species in titanium alkoxides precursor and  $-\text{OCH}_3$  of the methoxyethanol or  $\text{Si-OCH}_3$  groups not yet reacted, respectively, disappear with UV irradiation since an important effect of the exposure is the promotion of hydrolysis and condensation sol-gel reactions as well as solvents evaporation. The important role of UV in the photodegradation of organic component is further confirmed by the increase of the large  $\nu(\text{O-H})$  band between  $3600$  and  $3000\text{ cm}^{-1}$  and of the absorption at  $1640\text{ cm}^{-1}$  due to the production of molecular water. The condensation of Ti-O-Si network is visible in the increase of the  $950\text{ cm}^{-1}$  broad band absorption. With exposure the absorption of new species, such as  $\text{COO}^-$  at  $1570\text{ cm}^{-1}$ , can be detected and starts decreasing after irradiation with  $108\text{ J/cm}^2$ . At  $108\text{ J/cm}^2$  these degradation species start to be removed and a porosity is probably formed.

As a consequence, the refractive index increases until  $86\text{ J/cm}^2$  UV exposure dose reaching values of  $1.8@632\text{nm}$  and then decreases but the films thickness doesn't change, see Figure 3.17 which reports the plot of the in-situ thickness (left) and refractive index@ $632\text{nm}$  (right) vs UV dose. It is then clear that organic degradation occurring after UV exposure leads to the possibility of producing almost inorganic features at room temperature, with the same refractive index of  $200^\circ\text{C}$  thermal treatment.

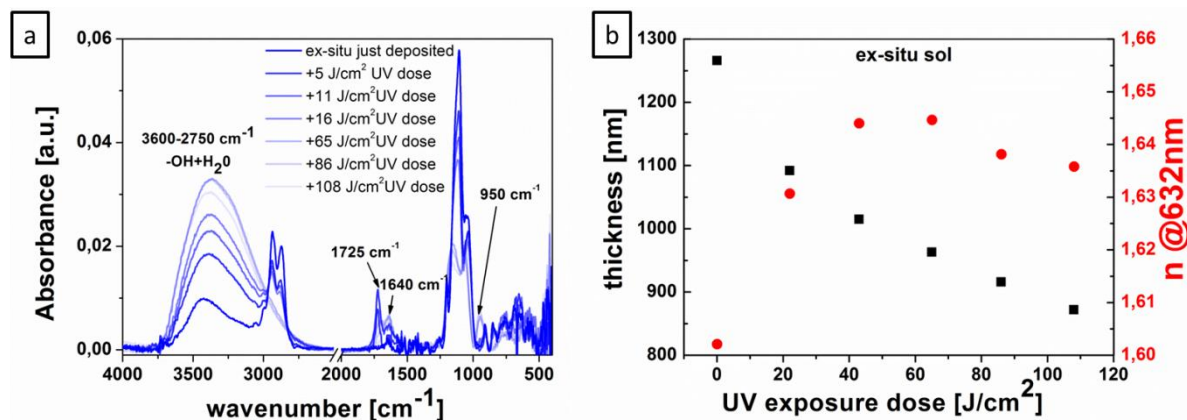


Figure 3.16 FTIR spectra of the ex-situ films after UV exposure (a) and plot of thickness and  $n@632\text{nm}$  vs UV exposure dose (b)

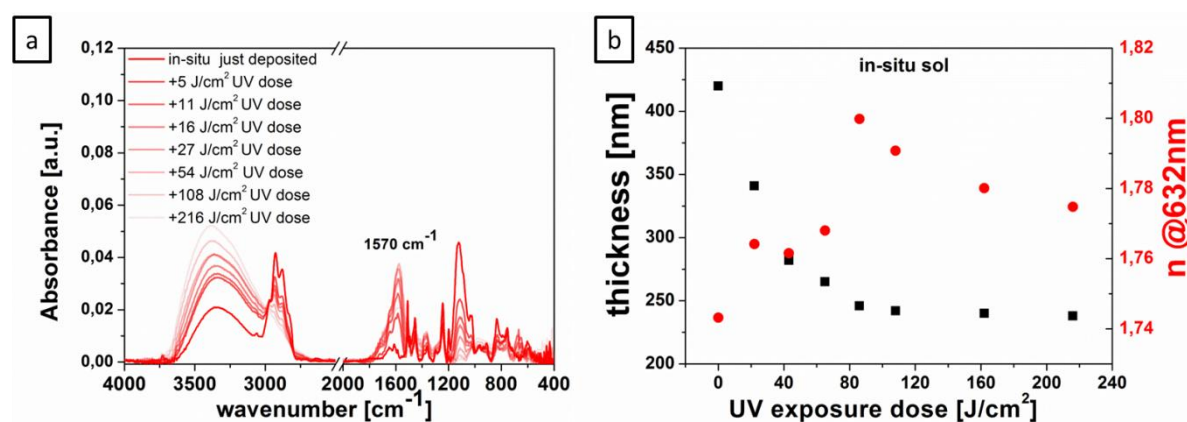


Figure 3.17 FTIR spectra of the in-situ films after UV exposure (a) and plot of thickness and  $n@632\text{nm}$  vs UV exposure dose (b)

Subtracting the  $-\text{OH}$  and  $\text{H}_2\text{O}$  contribution to the absorption of the band between 3020 and 2780  $\text{cm}^{-1}$  in both thermal and UV treated samples FTIR spectra, we can estimate only the organic absorption in such region, used to control the organic chain degradation during thermal treatment or UV exposure. Integrating the obtained curves in this wavenumber range, it is then possible to plot the organic % still present in the films as a function of thermal treatment temperature or UV dose (Figure 3.18). The degradation of the organic component is completed with a thermal treatment of 300-400°C for both ex-situ and in-situ films. If we compare this result with the refractive index reported in Figure 3.14 and Figure 3.15, we can conclude that with a TT at 300°C ex-situ film are almost completely inorganic and porous, confirmed by the low refractive index. Higher temperatures don't lead to a significant refractive index increase, maybe because ex-situ films are composed of already dense nanoparticles. On the other hand, in-situ film become inorganic with a TT of 300°C but it continuously become more dense with TT temperature up to 500°C. As it regards UV

treatment, the UV dose needed to obtain a completely inorganic film is around  $65 \text{ J/cm}^2$  for ex-situ films and  $216 \text{ J/cm}^2$  for in-situ films, confirming that these doses removes all the organic from the already dense structure leaving porosity.

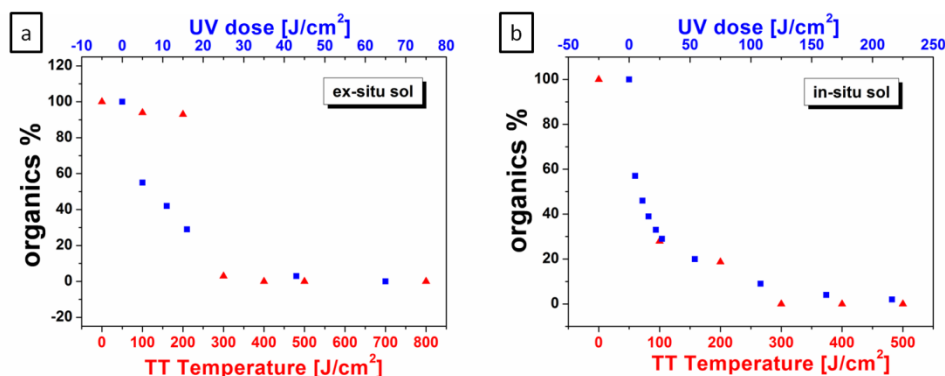


Figure 3.18 Plot of % of organic component after thermal treatment and UV exposure: ex-situ (a) and in-situ films (b)

### 3.3.3. Rutherford back scattering RBS

Rutherford backscattering (RBS), a spectrometric analytical technique used to determine the structure and composition of materials by measuring the backscattering of a beam of high energy ions impinging on a sample, of in-situ and ex-situ films was measured with  $4\text{He}^+ 2 \text{ MeV}$  beam at AN2000 accelerator. Table 3.4 reports the samples measured.

	sample	treatment	Starting thickness [nm]	Thickness after treatments[nm]
Ti- in-situ	Ti- 1	30min 80°C	368	368
	Ti-2	30min 80°C+1h300C	368	185
	Ti-3	30min 80°C+1h500C	368	129
	Ti-4	30min 80°C+1h800C	368	118
	Ti-5	30min 80°C+15J/cm <sup>2</sup>	368	276
	Ti-6	30min 80°C+43J/cm <sup>2</sup>	368	287
	Ti-7	30min 80°C+86J/cm <sup>2</sup>	368	253
	Ti-8	30min 80°C+108J/cm <sup>2</sup>	368	215
Ti- ex-situ	Ti-9	30min 80°C	467	467
	Ti-10	30min 80°C+1h300C	467	306
	Ti-11	30min 80°C+1h500C	467	266
	Ti-12	30min 80°C+1h800C	467	238
	Ti-13	30min 80°C+15J/cm <sup>2</sup>	467	328
	Ti-14	30min 80°C+43J/cm <sup>2</sup>	467	274
	Ti-15	30min 80°C+86J/cm <sup>2</sup>	467	252
	Ti-16	30min 80°C+108J/cm <sup>2</sup>	467	250

Table 3.4 Ti-in-situ and Ti-ex-situ samples for RBS analysis

The RBS analysis showed that a thermal treatment of in-situ films leads to an homogeneous C removal through the sample thickness, while with the UV exposure the C is first removed from the surface, showing a gradual concentration of C through the film thickness. On the other hand, both UV and thermal treatment of ex-situ films showed an homogeneous removal of C through film thickness. The effect of TT and UV exposure on in-situ and ex-situ films is reported in Figure 3.19, in terms of concentration of elements in the analyzed films: Carbon, Oxygen, Silicon, Titanium. It seems that a TT of 300°C is not sufficient for the removal of all the C content in all the in-situ films and that a TT at 500°C is needed. It has to be pointed out that the C concentration still revealed in ex-situ films even after TT at 500°C is probably due to the fact that C can be trapped in the matrix and difficult to be completely removed. For in-situ samples TT are more effective for C removal than the maximum UV dose measured (it is possible that a higher UV dose is needed, as confirmed by FTIR), while for ex-situ TT is comparable to UV treatment.

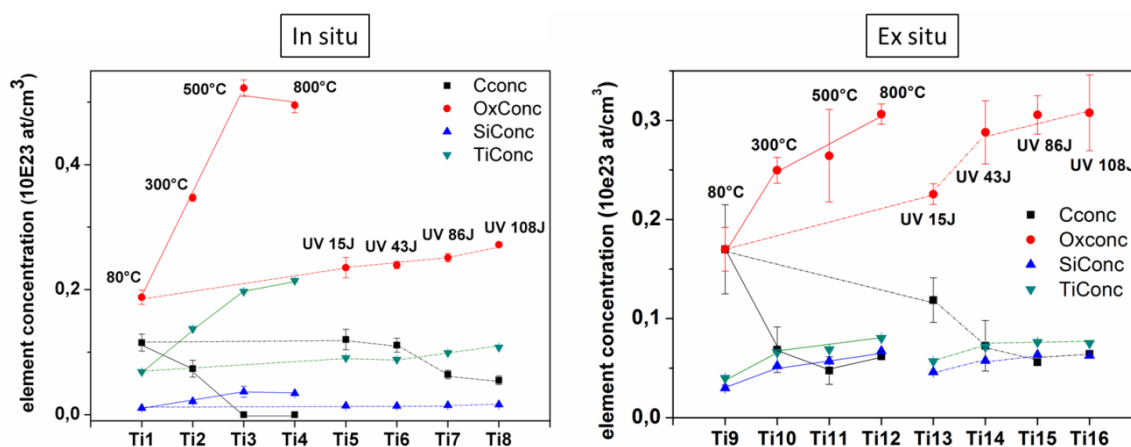


Figure 3.19 atomic concentration of Ti-in-situ and Ti-ex situ measured with RBS

### 3.3.4. DTA/TGA and DSC

Thermal analysis (STA409/429 Netzsch) were performed on the powder of the two systems (both sols were dried for one night at 60°C). Even if the microstructure of a powder can be quite different from the one of a film it could give an idea about the process which might similarly happen in the films. The heating rate was 5°/min in flowing air from RT to 1000°C (Figure 3.20).

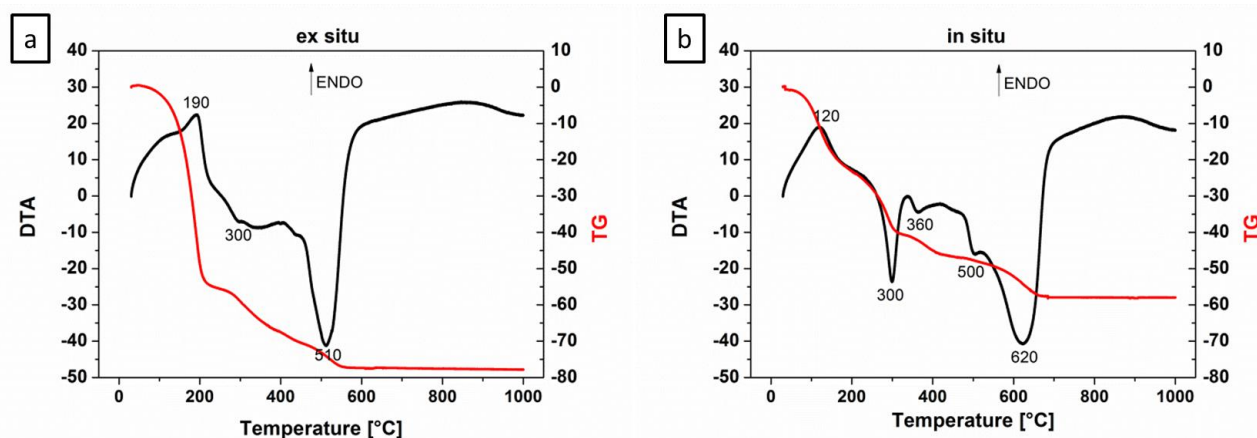


Figure 3.20 DTA and TG thermal analysis of ex-situ (a) and in-situ (b) systems

The TG analysis shows a very different thermal behaviour of the two systems. Below 200°C and 100°C respectively for ex-situ and in-situ systems the weight loss is considered to be due to the evaporation of water formed during condensation and the volatilization of the residual organic solvents. Between 200°C and 500°C the weight loss can be attributed to the carbonization or the combustion (oxidation) of organic compounds (loss of carbon, hydrogen and oxygen) with the formation of H<sub>2</sub>O and CO<sub>2</sub> molecules which are quickly released at any temperature above ca. 200°C as well as the promotion of condensation reactions and the sudden removal of the solvent formed [65]. In fact exothermic peaks at 300 °C and 300°C-360°C in ex-situ and in-situ respectively can be ascribed to organics combustion accompanied by amorphous titania phase transformation to anatase around 500°C. The total weight loss observed in ex-situ system is higher than that of in-situ powder: it is possible that the organic component (such as surfactants, dispersants) used in the MK Nano titania commercial dispersion is higher in % than the one used in in-situ synthesis.

### 3.3.5. Rheology of in-situ and ex-situ films

As previously mentioned in the resist synthesis section, the in-situ and ex-situ resists compositions were optimized after preliminary NIL tests; these tests showed the need of an organically modified silicon alkoxide, 3-glycidoxypropyltrimethoxysilane GPTMS, for both materials and a further organic modification for in-situ resist, the organic monomer BFGDE. Both GPTMS and BFGDE were added in minor amount (<20%) to tailor the rheology of the film during the imprinting process and reduce shrinkage during pattern and UV curing. In

fact, if the BFGDE monomer hadn't been added in-situ films couldn't be patterned without cracks formation, obtaining shallow structures, while ex-situ films could be easily patterned by NIL if the only GPTMS had been added.

As expected, both in-situ and ex-situ titania sols show a general increase of viscosity with temperature with a slight decrease around 80°C only for ex-situ just before the rapid increase at higher temperatures (Figure 3.21). It has to be pointed out that the viscosity values of the two sols are very different, more than one order of magnitude, although low with respect to characteristic values of thermoplastic resists at typical imprinting temperatures.

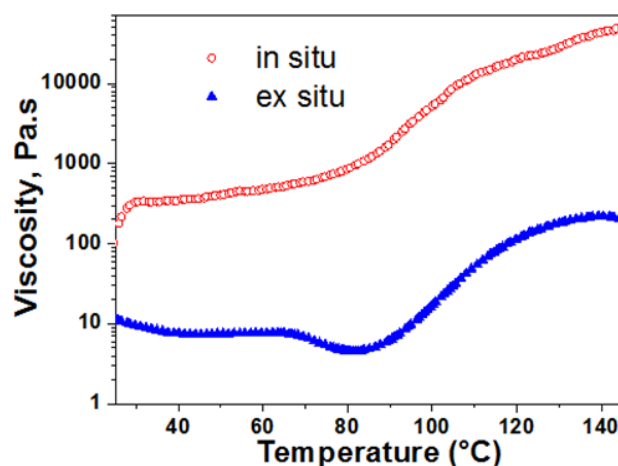


Figure 3.21 Viscosity measurements of in-situ and ex-situ sols on 500 $\mu$ m films

However, it has to be considered that the viscosity measurement was made on a thick sol film (around 500  $\mu$ m) from which the solvent has only partially evaporated, while film used for imprinting was up to 1  $\mu$ m thick. Moreover during deposition of the films by spin coating the main part of the solvent evaporated without necessity of any drying step. Therefore the absolute value of the viscosity of the films used for imprinting tests can be reasonably much higher with respect to the values reported in Figure 3.21, probably approaching those typical of thermoplastic polymers at usual imprinting temperatures. It follows that only the viscosity trends and not the absolute values of Figure 3.21 represent the rheological behaviour of the sols.

The most striking feature of Figure 3.21 is the slow but continuous increase of viscosity versus temperature shown by in-situ sol. This fact indicates that crosslinking reactions occur just after the film deposition at room temperature and continue at increasing temperature, accelerating their kinetics between 80 and 100°C. However, the network formation is not

completed even for  $T > 140^\circ\text{C}$ , because viscosity is trending upwards at the end of the measure.

On the contrary, ex-situ film shows a constant viscosity until the temperature reaches  $70^\circ\text{C}$ , slightly decreasing at  $80^\circ\text{C}$ , followed by a rapid growth and stabilization at  $T > 80-90^\circ\text{C}$ . At these temperatures crosslinking reactions become very effective, probably inducing a totally hardening at temperature around  $140^\circ\text{C}$ .

These different behaviour can be explained by analysing the sol composition: in-situ is a sol rich in pre polymerized Titanium(IV) isopropoxide TiOPr, that undergoes to continuous crosslinking reactions with temperature while the negligible concentration of silicon and titanium alkoxides in ex-situ sol prevents hardening of the network and requires higher temperatures in order to crosslink the alkoxides around anatase nanoparticles. These differences would justify also the lower viscosity of ex-situ sol, that consists of low viscosity anatase nanoparticles dispersion with minor amount of pre polymerized TiOPr.

### ***3.3.6. Crystalline structures of ex-situ and in-situ films after UV and thermal treatments: XRD and TEM characterization***

XRD is essential in the determination of the crystal structure and the crystallinity, and in the estimate of the crystal grain size. The XRD patterns of films UV and thermally treated are shown in Figure 3.22. It can be observed that all the ex-situ spectra present anatase phase ( $2\theta = 25.5^\circ/48.2^\circ/37.8/55^\circ$ ) just after the synthesis., thus confirming that the  $\text{TiO}_2$  NPs dispersion used for ex-situ really consists in anatase nanoparticles. Concerning in-situ  $\text{TiO}_2$  no diffraction peaks were observed for the as deposited and  $108 \text{ J/cm}^2$  UV exposed films, indicating their amorphous structure. The anatase phase can be obtained only by annealing in-situ films at  $500^\circ\text{C}$  for 1h.

It is well-known that the anatase titania phase shows the highest photoactivity rather than brookite or rutile, instead amorphous titania generally exhibits negligible photocatalytic activity: in fact, it is commonly accepted that amorphous metal oxides contain high concentrations of defects that will invariably function as rapid electron–hole recombination centres to render them inactive [<sup>66-67-68</sup>]. However, although in-situ films are supposed to be totally amorphous from XRD analysis, they display a relevant photocatalytic effect: this is explained by TEM analysis that revealed the presence of a crystalline phase made of small and rare crystals undetectable by XRD in in-situ sol.



TEM analysis of the in-situ films after  $500^{\circ}\text{C}$  and  $44 \text{ J/cm}^2$  UV exposure dose is shown in Figure 3.23. After UV the occasional presence of crystalline phases dispersed in an amorphous background was detected and identified from diffraction analysis as anatase and rutilo. The annealing at  $500^{\circ}\text{C}$  leads to anatase crystals formation.

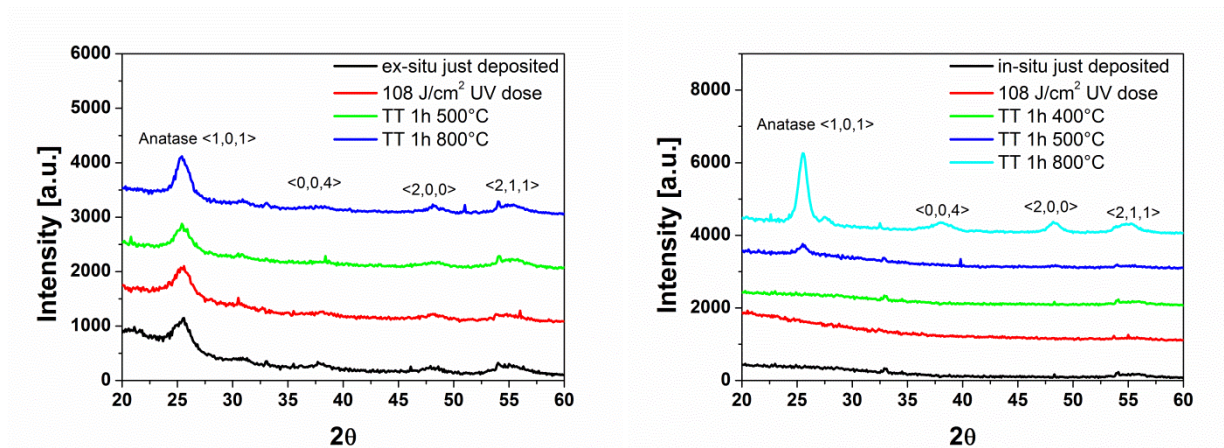


Figure 3.22 XRD spectra of ex-situ and in-situ films just deposited and after UV exposure and TT.

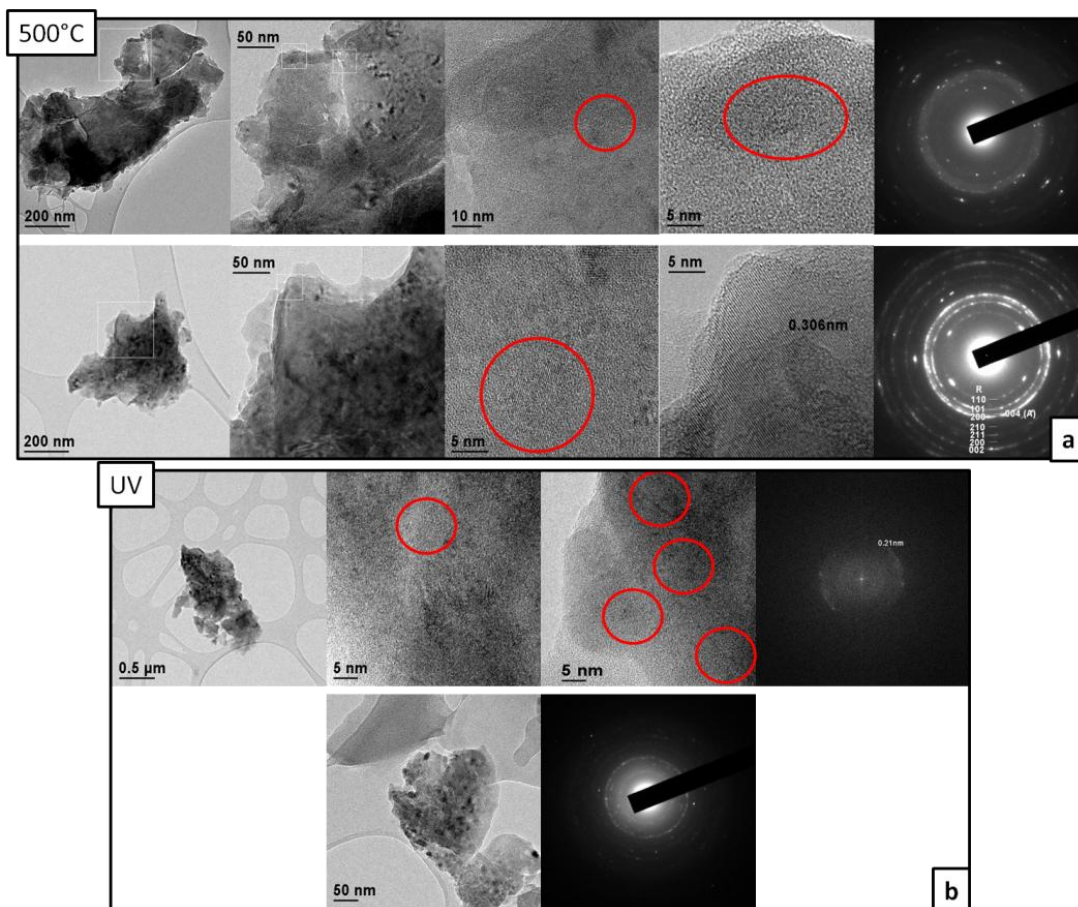


Figure 3.23 TEM images of: (a) an in-situ particle of anatase after annealing at  $500^{\circ}\text{C}$ , and (b) an in-situ particle of rutile (up) and anatase (bottom) after UV exposure dose together with the diffraction images

According to the Scherrer equation

$$D = \frac{K\lambda}{\beta \cos \theta}$$

where  $K$  is a dimensionless constant,  $2\theta$  is the diffraction angle,  $\lambda$  is the wavelength of the X-ray radiation, and  $\beta$  is the full width at half-maximum (fwhm) of the diffraction peak. Crystallite size is determined by measuring the broadening of a particular peak in a diffraction pattern associated with a particular planar reflection from within the crystal unit cell. It is inversely related to the fwhm of an individual peak: the narrower the peak, the larger the crystallite size. The periodicity of the individual crystallite domains reinforces the diffraction of the X-ray beam, resulting in a tall narrow peak. If the crystals are randomly arranged or have low degrees of periodicity, the result is a broader peak. This is normally the case for nanomaterial assemblies. Thus, it is apparent that the fwhm of the diffraction peak is related to the size of the nanomaterials.

The average crystallite size (Table 3.5) is calculated from the XRD line broadening using the reported Scherrer equation with  $k=0.9$  (assuming that the crystallites are spherical),  $\lambda=1.54178\text{\AA}$  and  $\beta$  calculated at  $25.5^\circ$ . The average crystallite size of titania dispersion is  $\sim 5\text{nm}$ , smaller than the NPs size declared ( $15\text{nm}$ ) from the supplier which are maybe aggregates. The crystallite size increases of  $1\text{-}1.5\text{ nm}$  for both UV and thermally treated samples. The average crystallite size of in-situ samples annealed at  $500^\circ\text{C}$  is  $\sim 5\text{ nm}$ . Bigger crystallites can be achieved with annealing at  $800^\circ\text{C}$  both for ex-situ and in-situ samples which show crystallites of  $\sim 6$  and  $\sim 8\text{ nm}$ , respectively. Experiments with in-situ sol without the silica modification (GPTMS) annealed at  $500^\circ\text{C}$  exhibits anatase crystals of  $15\text{ nm}$  size, highlighting the inhibition created by silica on titania crystals growth.

sample	Crystallite size [nm]
Anatase NPS dispersion	4.85
Ex-situ just deposited	4.79
Ex-situ after $108\text{ J/cm}^2$ UV exposure dose	5.58
Ex-situ annealed at $500^\circ\text{C}$ 1h	5.62
Ex-situ annealed at $800^\circ\text{C}$ 1h	6.47
In-situ annealed at $500^\circ\text{C}$ 1h	4.77
In-situ annealed at $800^\circ\text{C}$ 1h	8.32
In-situ (without GPTMS) annealed at $500^\circ\text{C}$ 1h	15.01

Table 3.5 Average crystallite size of in-situ and ex-situ samples annealed or UV exposed calculated from Sherrer formula

### 3.4. *From micro- to nano- lithography*

Micro- or nano-scale patterned titania improves or derives new properties (e.g. different surface wettability [69]) and enlarge titania applications (e.g. waveguides, cell growth substrate, microlasers, photonic crystals, antireflective coatings, etching masks) [70,71,72,73,74,75,76,77,78,79,80] with respect to bulk TiO<sub>2</sub>.

Conventionally, the traditional lithographic process consists in the sputtering of TiO<sub>2</sub> onto a pre-patterned organic resist which is then removed by the lift-off process [74,81,82] or using different material templates, leaving titania structures [83,84,85,86,87,88]. However, generally, lift-off process causes degradation of performance, is more time-consuming, increases waste and energy consumption, and makes the process complicated. Furthermore it does not work well when thick films (some hundred nm) of titania or complex patterns are desired. Attempts to patterns titanium dioxide simplifying the traditional complex lift-off process were made using resist pattern as a mold, as reported by Ozawa and Yao [89] on the fabrication of micro patterns titanium dioxide by synthesis reaction from aqueous solution or by Wu et al. on spin coating surfactant-templated TiO<sub>2</sub> precursor solution onto electron-beam (EB) lithographically prepared resist moulds [90]. Also three-dimensional titania patterns were produced, by Cuisin et al., Wathuthanthri et al. and Park et al., using the sol-gel filling technique in resist templates prepared by X-ray lithography [86] or two-beam interferometer [87,91]. Masuda et al [85,92,93] and Sukenik's group [94,95] obtained micropatterned TiO<sub>2</sub> by depositing titania from aqueous solution onto photopatterned self-assembled monolayer (SAM) films. All these examples achieve titania structures by means of a sacrificial photosensitive material patterned before titania deposition from wet chemistry and so acting as template, then eliminated through high temperatures thermal treatment. Anyway, this procedure, even though simpler than traditional complex lift off process, consists in some different steps, requires the use of another material, the photoresists, and limits the usable substrates due to the calcination step. For this reasons researchers are putting many efforts on finding out direct, fast, economical and easy ways to obtain completely inorganic titanium oxide features without the need for a multi-step process, often degrading resolutions and pattern quality, and standard photoresists, not always compatible with the inorganic film solution. One way to do this is synthesizing titania-based materials which, thanks to their photosensitivity, are directly patternable with different lithographic processes: optical lithography, electron beam lithography [96,97], interference lithography [98,99], AFM nanolithography [100], two-photons lithography [101], electrohydrodynamic patterning [102],

laser writing [<sup>103</sup>], micromoulding in capillaries method [<sup>104</sup>], nanosphere lithography [<sup>105</sup>], Particle Replication In Non-wetting Templates (PRINT) [<sup>106</sup>], ink-jet printing technology [<sup>107</sup>], step-and-flash imprint lithography [<sup>108</sup>] and nanoimprint lithography (NIL).

Among the reported techniques, in this thesis work the attention was focused on the direct patterning of in-situ and ex-situ sol-gel-based spin-coatable TiO<sub>2</sub> resists by optical lithography and thermal micro and nanolithography (T-NIL), obtaining high refractive index (over 2@632nm) micro- and nano- patterned features with smallest sizes of 50 nm and up to 630 nm deep. The strategy, with respect to commonly prepared titania resist obtained by adding photopolymerizable organically modified metal alkoxide, consisted in the exploitation of the photocatalytic effect of titania under UV irradiation that brings to a completely inorganic titania patterned area, without the need for high T annealing, allowing to obtain titania structures on every kind of substrates.

### **3.5. UV lithography**

Among various patterning methods, photolithography is one of the most convenient, because it can transfer an entire pattern from a photomask to a film through a single step process. Furthermore, UV photolithography is one of the most used and consolidated micro-patterning technique and many of the equipment required, such as the UV photomasks and lamps, are readily available.

In literature, photolithography have been used to direct pattern organically modified titania sol-gel films by adding organically modified silicon alkoxides [<sup>109</sup>] and methacrylic monomers [<sup>110</sup>] that undergo polymerization when exposed to UV, or organic additives such as chelate rings (i.e.  $\beta$ -diketones) which decompose upon UV irradiation [<sup>111,112</sup>]. However, in the former the organic component is maintained at the end of the lithographic process, while the latter requires a following calcination step to fully transform the features to inorganic or to densify exposed structures.

Herein, we have focused our research to the direct achievement of completely inorganic titania micro-patterning by a one-step photolithography and using spin-on resists from wet chemistry, exploiting their photocatalytic activity under UV irradiation, without the need for high temperatures thermal treatments and bringing to inorganic titania micro-structures on every kind of substrates.

As reported in paragraph 3.3.2.3, small crystalline  $\text{TiO}_2$  clusters allow the generation of oxygen radicals that can oxidize and decompose most organic compounds. This well-known effect, here allowed by the titania film structure, was exploited to convert the HOI to inorganic  $\text{TiO}_2$  in the exposed areas, and therefore to direct pattern the film by optical lithography.

Optical lithography process parameters were optimized (in collaboration with *Micro Resist Technology MRT, Berlin*) using films of in-situ and ex-situ systems spin coated at 4000rpm 30s. In-situ titania films presented the advantage of giving either negative or positive patterns of the mask used since exposed and unexposed parts, depending only on the lithographic process parameters, were differently soluble in acidic solutions (Figure 3.24).

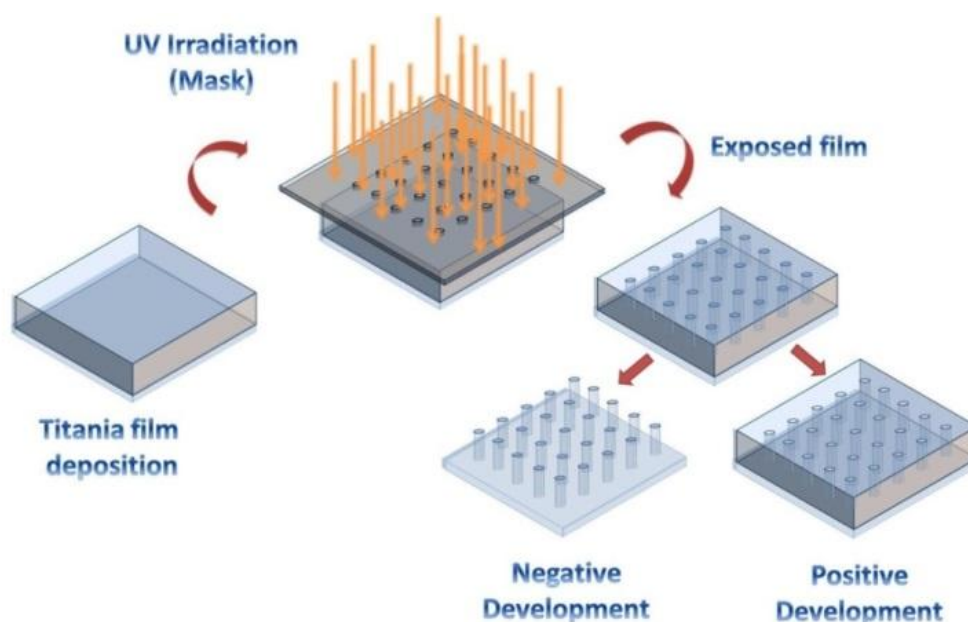


Figure 3.24 Scheme of the photolithographic process: titania films could be directly patterned by UV exposure showing positive and negative tone depending on the process parameters and development

After a dose matrix the optimized dose has been determined to be 1.25 and 150  $\text{J}/\text{cm}^2$  for in-situ negative and positive tone, respectively, and 90  $\text{J}/\text{cm}^2$  dose for ex-situ films. The positive tone of in-situ system requires a PAB (post application bake) of 30min at 80°C, while the in-situ negative tone and ex-situ positive tone need a PEB (post exposure bake) of 30s at 80°C and 5min at 70°C, respectively. Development was carried out for 15s in HCl 1N, 1 minute in HCl 37% and 1'10" in KOH 1N for negative and positive un-situ and positive ex-situ, respectively.



In Figure 3.25 optical and SEM images of a titania structures obtained by negative and positive in-situ tone process and positive ex-situ are reported. The in-situ patterns show that a resolution  $<2\mu\text{m}$  can be achieved.

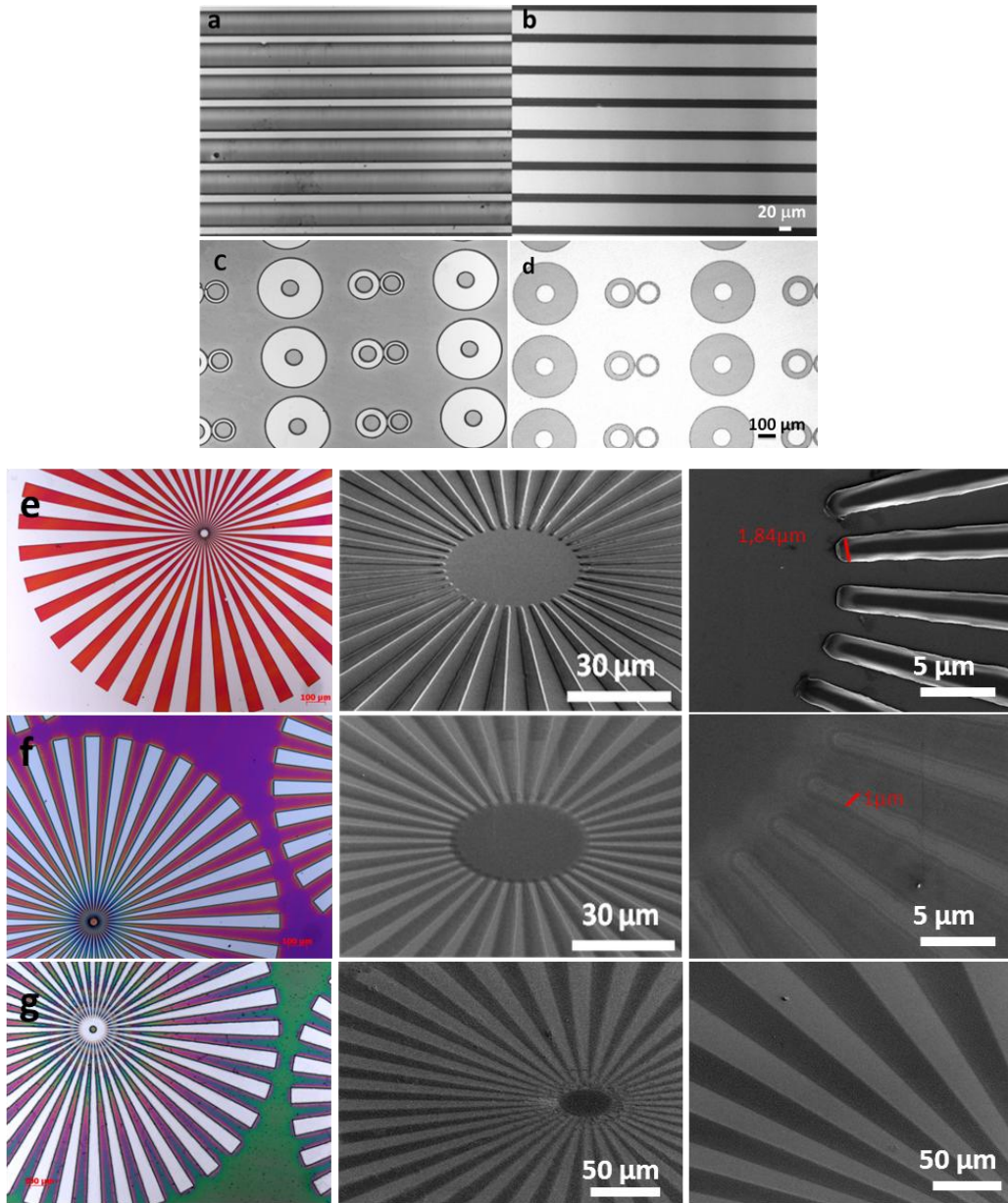


Figure 3.25 Optical and SEM images of in-situ resist positive (a,c,f) and negative (b,d,e) tone and ex-situ positive tone (g)

Figure 3.26 shows the contrast curve of in-situ (positive and negative) and ex-situ (positive) systems, i.e. the normalized developed film thickness as a function of UV dose. The resolution of a resist depends on its contrast  $\gamma$ , the higher the contrast the higher the resolution.

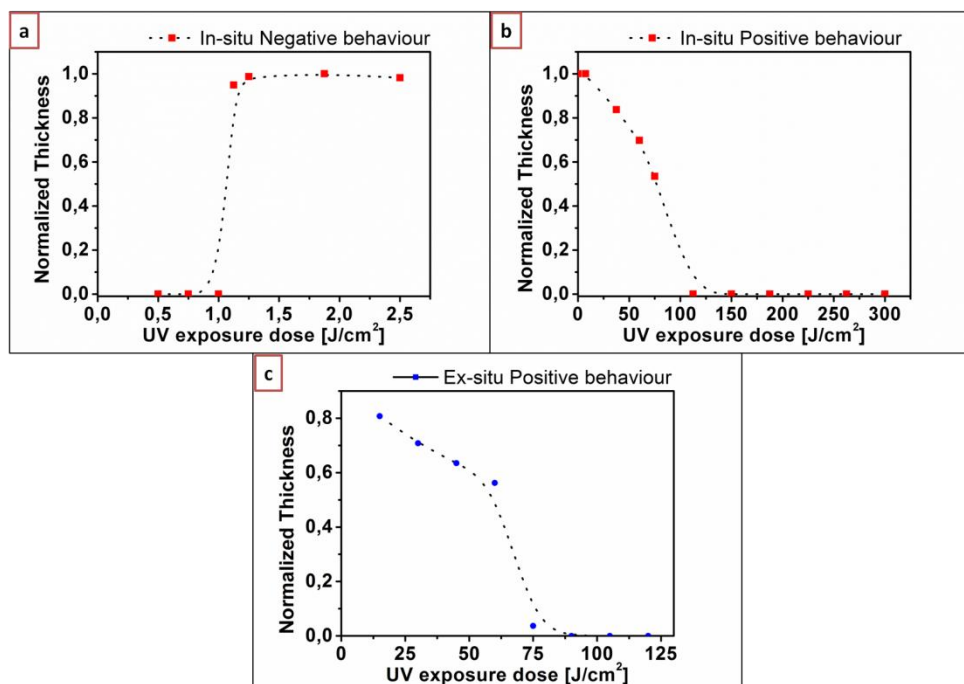


Figure 3.26 contrast curve of in-situ negative (a) and positive (b) tone and of ex-situ positive tone (c)

The contrast value is calculated for positive and negative resist as:

$$\gamma_P = \left( \log \left( \frac{d_c}{d_o} \right) \right)^{-1}$$

$$\gamma_N = \left( \log \left( \frac{d_o}{d_i} \right) \right)^{-1}$$

where  $d_c$  is the dose to clear all resist and  $d_o$  is the extrapolated dose at which the film thickness remain unaltered. For negative resist,  $d_o$  and  $d_i$  are likewise defined.

In particular, the calculated contrasts are here reported:

$$\gamma_{in\ situ\ N} = \left( \log \left( \frac{d_o}{d_i} \right) \right)^{-1} = \left( \log \left( \frac{1.13}{1} \right) \right)^{-1} = 19$$

$$\gamma_{in\ situ\ P} = \left( \log \left( \frac{d_c}{d_o} \right) \right)^{-1} = \left( \log \left( \frac{126}{34} \right) \right)^{-1} = 1.7$$

$$\gamma_{ex\ situ\ P} = \left( \log \left( \frac{d_c}{d_o} \right) \right)^{-1} = \left( \log \left( \frac{87}{38} \right) \right)^{-1} = 2.8$$

The in-situ negative tone contrast is very high, if compared with common organic resists, whose typical values are around 2-3: the unexposed parts in fact don't wear thin during development but suddenly crack and are removed by the developer. In particular, for titania resist  $d_i$  is the dose required for the exposed material to remain, although not totally, when developed. The photocatalytic effect starts to be effective and the exposed areas start changing the composition to inorganic. Besides the contrast value, many other parameters have a great relevance in the pattern outcome. The optimization of exposure dose plays an essential role for the quality of the final structures. However, the development step is a key point in the pattern generation and many parameters, such as the pre and post-exposure thermal treatments (time, temperature), the solvent used to remove the wanted areas together with time and temperature used during the development step have to be carefully selected to obtain good pattern profiles, on the base of structural changes observed in the film. Other influencing factors are the adhesion between the hybrid film and the substrate and the dry step as well. Figure 3.27 shows some examples of initial direct patterning problems: definition of the pattern edges before and after optimization of the in-situ negative tone process.

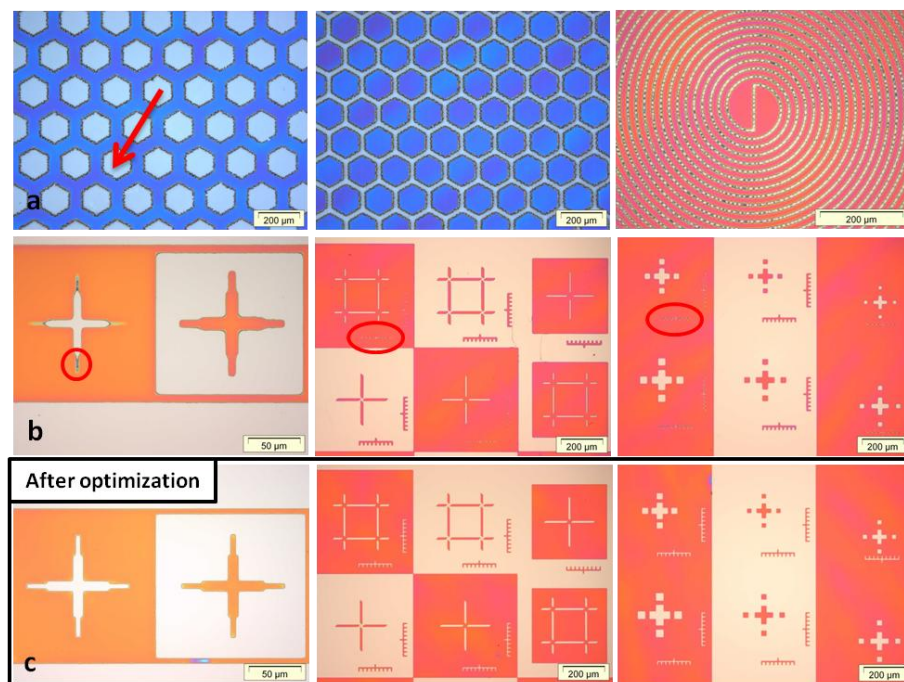


Figure 3.27 Examples of initial direct patterning problems: too high exposure dose (a) and optimization of postbake (b and c).

In particular, Figure 3.27a highlights the effects of a wrong exposure dose: the structures are overexposed and the unexposed parts near the edges are not removed. A strict control of the exposure is necessary to avoid that an unwanted organic-degradation due to photocatalytic



effect of titania occurs in the not irradiated zones. In fact with a lower exposure dose better edges were obtained as could be seen from Figure 3.27b, even if the pattern is still not fully developed (see red circles). Figure 3.27 b and c underline that the post-exposure bake enhances the development of the unexposed areas, i.e. the contrast between the exposed and unexposed areas (in Figure 3.27b the exposed samples were treated for 30s at 80°C). After the optimization of the lithographic process (spinning/ pre-baking/ exposure dose/ post-baking/ development), the spatial resolution of the micrometric structures was below 1 $\mu\text{m}$  (see Figure 3.25).

As expected from contrast calculation, the in-situ negative resist shows a better resolution and quality of the patterns obtained, together with a higher refractive index with respect to ex-situ system (see Figure 3.16 and Figure 3.17). Examples of the patterns obtained are reported in Figure 3.28, Figure 3.29 and Figure 3.30. However, if a certain application would require anatase features the ex-situ resist could be exploited to obtain anatase structures without the need for further UV exposure or thermal treatment. The real advantages of this approach are that significant parameters such as refractive index and crystallinity can be tailored during the material synthesis: with a single lithographic step the device is ready without any further etching process, undoubtedly simplifying devices fabrication.

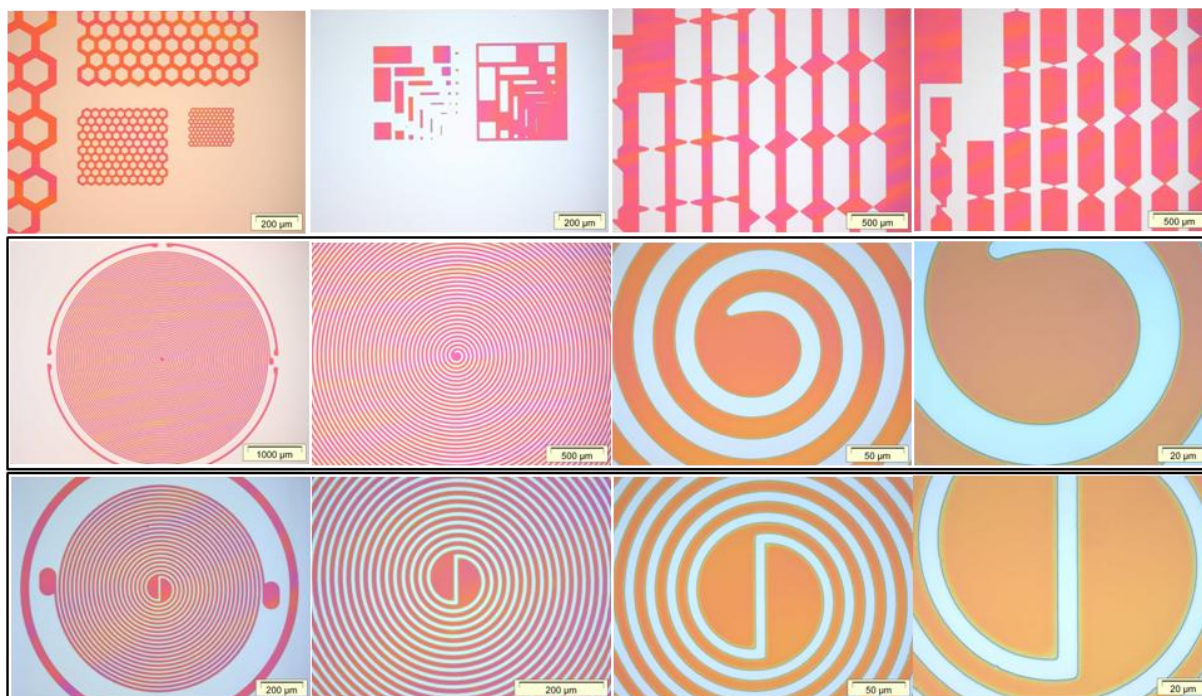


Figure 3.28 Examples of the patterns obtained with in-situ negative tone process

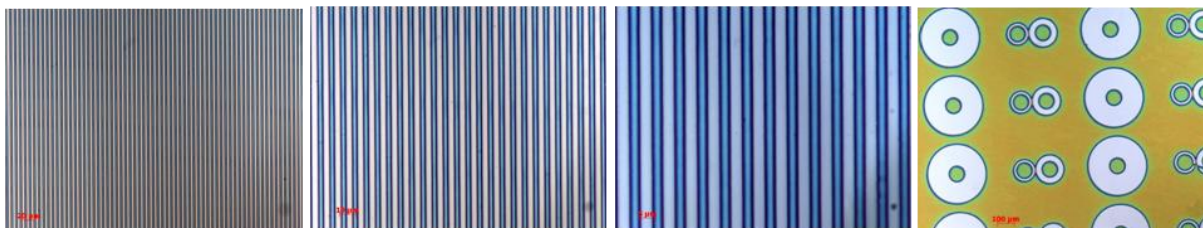


Figure 3.29 Examples of the patterns obtained with in-situ positive tone process

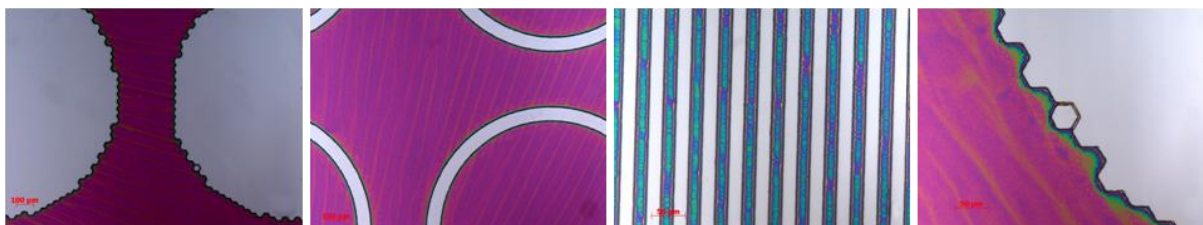


Figure 3.30 Examples of the patterns obtained with ex-situ positive tone process

### 3.5.1. Chemical understanding of the double tone processes of in-situ system

As previously mentioned the resist tone depends only on the lithographic process parameters that confers the different tone to the material. The importance of the process parameters were studied through the FTIR characterization of the films after each step of photolithography, both for positive and negative tone, to confer the wanted tone to the resists. The FTIR spectra reported in Figure 3.31 refer to the optimized negative (a) and positive (b) tone lithographic process.

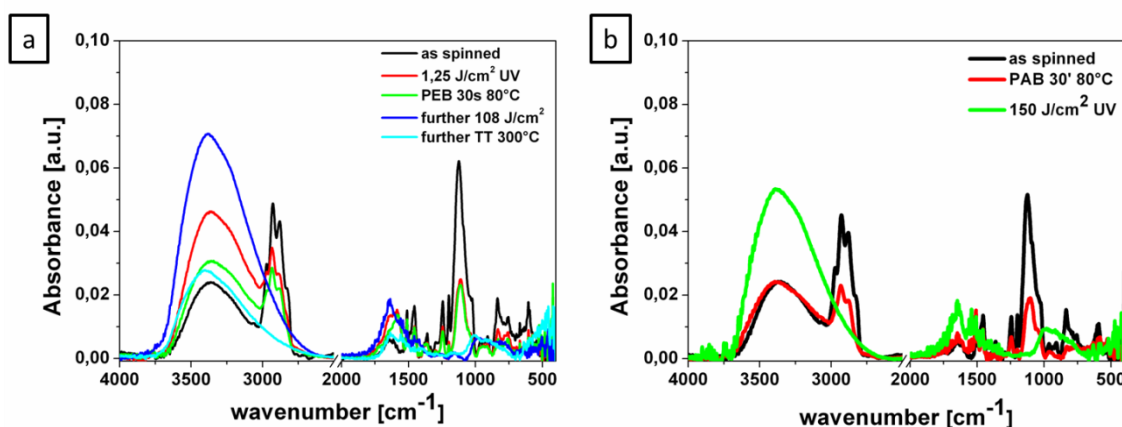


Figure 3.31 FTIR of titania films after each step of the in-situ “negative tone”(a) and “positive tone” (b) process

Experiments showed that a *negative resist behaviour* is displayed by film exposed to 1.25 J/cm<sup>2</sup> UV dose just after spin coating. The exposure leads to the evaporation of methoxyethanol, partial degradation of BFDGE and promotion of alkoxides hydrolysis. In fact, asymmetric and symmetric C-H stretch absorption of the methylene groups (2930 cm<sup>-1</sup>-

2855  $\text{cm}^{-1}$  and at 1485–1445  $\text{cm}^{-1}$ ) and C-O-C absorption of the ether group at 1100  $\text{cm}^{-1}$  decrease while  $\nu(\text{O-H})$  band between 3600 and 3000  $\text{cm}^{-1}$  increases and a band between 1650–1560  $\text{cm}^{-1}$  (water and  $\text{COO}^-$  as a consequence of photocatalytic reactions) is gradually detected. The further PEB for 30s at 80°C on a hotplate, completes the sol-gel reactions activated by UV exposure, thus increasing the contrast between exposed and unexposed parts of the film, essential for a high contrast. Moreover, PEB partially evaporates the water formed during photocatalytic reactions (1640  $\text{cm}^{-1}$ ) leading to condensation and  $\text{-OH}$  absorption decreasing.

Instead, a prebake (post application bake, PAB) at 40°C is necessary to observe *positive tone behaviour*; however the development is slow and even the unexposed part wears thin during the wet etching. Increasing the prebake temperature the development time decreases and the unexposed part seems not wearing thin, also showing good pattern edges. A prebake of 30 minutes at 80°C promotes the evaporation of the solvent used for the synthesis (methoxyethanol) as well as the reactions of hydrolysis and condensation: 2970  $\text{cm}^{-1}$  peak due to the stretching of the C-H bond of isopropoxide species and 2830  $\text{cm}^{-1}$  peak ascribed to  $\text{-OCH}_3$  of the methoxyethanol (as well as 1100  $\text{cm}^{-1}$  peak) and  $\text{Si-OCH}_3$  groups (of the GPTMS) disappear but the  $\text{-OH}$  band doesn't change. With further UV exposure (150  $\text{J}/\text{cm}^2$ ) almost all the organic components are removed, thanks to the photocatalytic effect of titania when UV exposed: all the peaks related to  $\text{-CH}$  bond vibrations and C-O-C absorption of the ether group at 1100  $\text{cm}^{-1}$  of methoxyethanol and of BFDGE disappear. At the same time the exposed areas become more hydrophilic: the increase of  $\text{-OH}$  band between 3600 and 3000  $\text{cm}^{-1}$ , a band at 960  $\text{cm}^{-1}$  ascribed to  $\text{Si-OH}$  and water peak intensity (1640  $\text{cm}^{-1}$ ) indicate the hydrolysis progress. Finally, Ti-O-Si asymmetric stretching around 950  $\text{cm}^{-1}$  increases with exposure.

A closer examination of development process is shown in Figure 3.32 that reports the comparison between exposed and unexposed areas of titania films during negative and positive tone development in HCl 1N and HCl 37%, respectively.

Regarding the negative process, the acidic development solution enters more easily in the uncondensed network containing more organic components: the decrease of the C-O-C peak at 1100  $\text{cm}^{-1}$  and the increase of the peaks related to  $\text{-OH}$  and absorbed water (1640  $\text{cm}^{-1}$ ) is in fact more evident in the unexposed part partially developed than in the exposed ones.

As it concerns the positive process, a porosity seems to form for films exposed to UV doses exceeding 86  $\text{J}/\text{cm}^2$ , as previously discussed referring to Figure 3.17.

Moreover overexposed titania areas shows  $-OH$  formation due to promoted hydrolysis, underlying the hydrophilicity. The same explanation can be in fact attributed to ex-situ films positive behaviour:  $90J/cm^2$  UV exposure dose required for patterning are necessary for porosity formation in the inorganic features, allowing the development to enter the exposed areas (Figure 3.16).

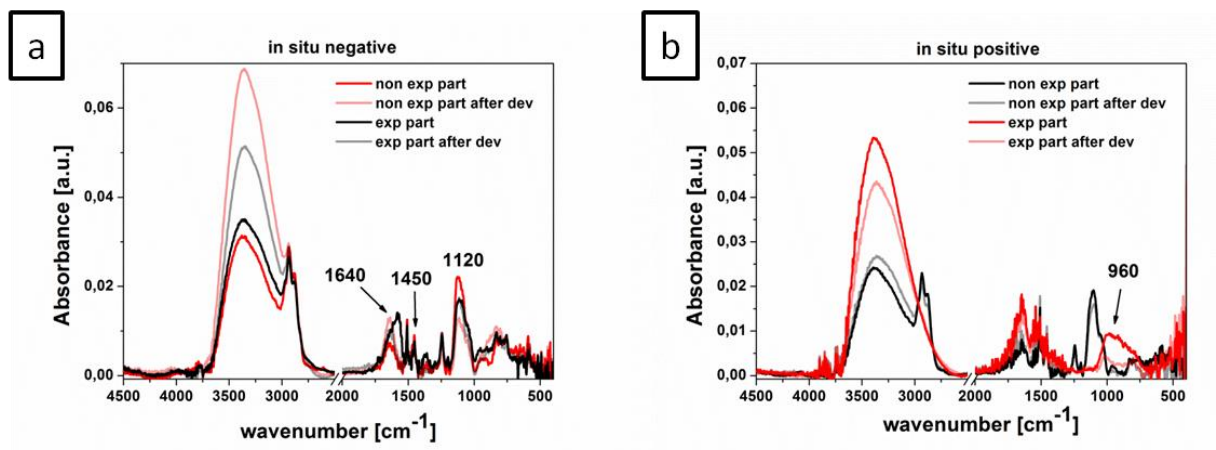


Figure 3.32 FTIR of exposed and unexposed parts of titania film partially developed in HCl 1N (a: negative tone) and HCl 37% (b: positive tone)

Figure 3.33 reports the SEM images of negative and positive tone titania gratings with  $3\mu m$  line width obtained after development and the evolution of the same ones after further UV exposure and thermal treatment for 1h at  $500^{\circ}C$ . With UV it was possible to obtain an almost complete inorganic pattern and the formation of some rutile crystallites in an amorphous background, with TT to achieve the best refractive index ( $2.1@632nm$ ) and a crystalline anatase phase, as already reported. The inset figures refer to the 3D profile obtained with AFM.

As it concerns the negative in-situ tone we observed a 16 % and 33% lateral shrinkage and 20 % and 50% of vertical shrinkage for UV and TT, respectively. The positive tone showed no lateral shrinkage after TT and a 8% after UV and a 16 % and 40% vertical shrinkage is observed after UV and TT treatment, respectively. The resist synthesis and process, in particular the in-situ positive tone, offer then a great advantage if no distortion of the pattern is required. Furthermore the UV treatment could be used as a valid alternative to high temperature thermal treatment in order to obtain inorganic structures with low shrinkage with respect to mask features.

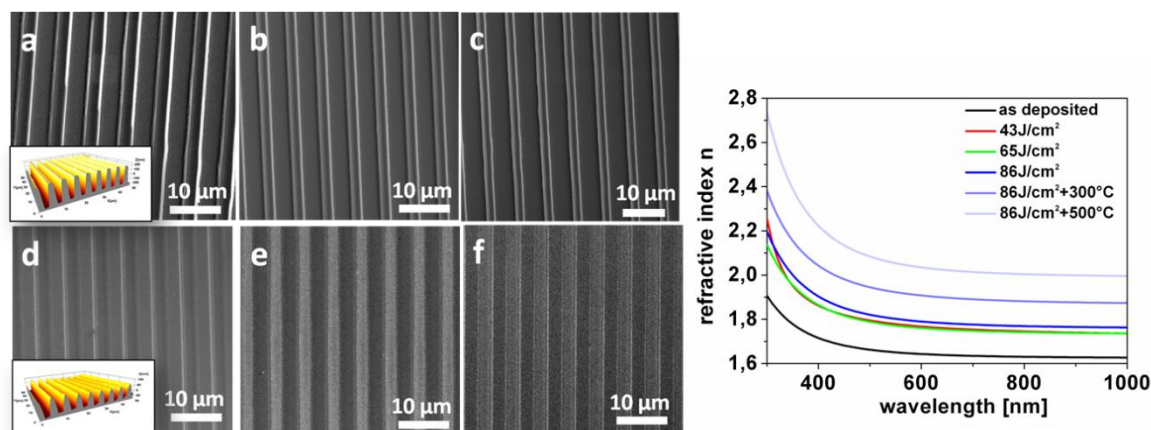


Figure 3.33 SEM images of “negative” (a,b,c) and “positive” (d,e,f) tone titania gratings with  $3\mu\text{m}$  lines after development (a,d) and further UV exposure (b,e) or thermal treatment at  $500^\circ\text{C}$  (c,f) in order to obtain completely inorganic structures. On the right: the refractive index of exposed and further treated at  $300^\circ\text{C}$  and  $500^\circ\text{C}$  samples.

### 3.6. Nanoimprint lithography

Recently many efforts have been done even to use nanoimprint (NIL) as a direct patterning method, since it possess a potential industrial impact in the production of optical micro- and nano- systems, enabling low-cost, high throughput and high resolution. However it has been hardly ever used with inorganic films, especially titania [108,113, 114,115]. The few examples in literature of direct imprint of inorganic  $\text{TiO}_2$  systems reveals that few major challenges have to be faced when working with titania sol-gel compounds. In fact sol-gel precursors have high surface energy and cause mould release problems, the solvent or organic moieties (chelating or coordinating agents) that helps to ‘soften’ the material get generally trapped in the imprinted structures and sol-gel materials do not have a workable softening point since they generally exhibit a thermosetting behaviour. The outcome of NIL using sol-gel materials is characterized by pattern depths generally limited by cracks, incomplete filling of the mould, high vertical and lateral shrinkage after imprint and following thermal treatment. Soft lithography [116] can eventually help to overcome these problems since PDMS [117,118] and PFPE [119] soft moulds have low surface energies and a permeable nature that absorbs the sol-gel solvent used. However this technique presents mould deformation problems, in particular when sub- 100-nm features are desired, high shrinkages, and shallow structures are usually obtained [120].

In summary, inorganic titania patterned films obtained either by thermal (T-NIL) or UV assisted (UV-NIL) imprint lithography suffer the following limits: 1) only shallow, less than



100 nm [<sup>121,122</sup>], can be obtained, 2) films with low titania content can be patterned [<sup>23,123,124</sup>], 3) high shrinkages occur during process (up to 75%) [<sup>125,126,108</sup>] and 4) refractive index up to 1.98@632nm [<sup>127</sup>] only after annealing at 500°C can be achieved.

The purpose of this thesis work was to overcome these limitations by patterning TiO<sub>2</sub> in-situ and ex-situ films using T-NIL and subsequent UV exposure (Figure 3.34), producing almost inorganic micro- and nano- structures up to 630 nm deep with lateral shrinkage close to 0 after UV or thermal treatment.

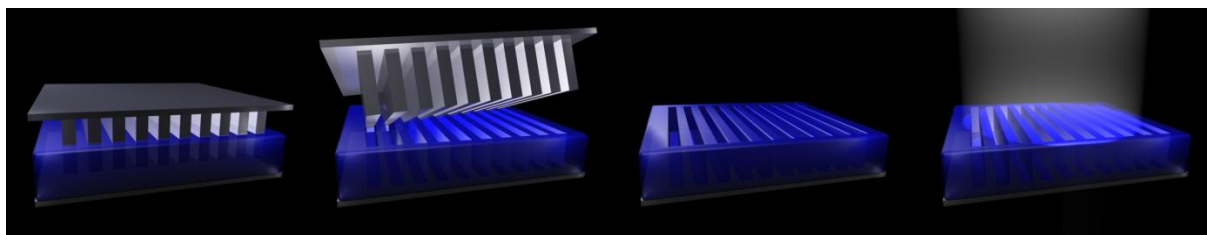


Figure 3.34 Scheme of the patterning process: micro- or nano-imprint lithography and UV exposure of the patterned titania to obtain completely inorganic features with high refractive index

### 3.6.1. FTIR and ellipsometric characterization of nanoimprint process

In-situ and ex-situ composition evolution during imprinting tests was monitored by FTIR analysis. FTIR spectra (Figure 3.35) of as deposited films show doublets at 2930 and 2870 cm<sup>-1</sup> ( $\nu_{as}(\text{CH}_2)$  and  $\nu_s(\text{CH}_2)$ , respectively) and peaks between 1150 cm<sup>-1</sup> and 1030 cm<sup>-1</sup> due in part to residual solvents present into the films (methoxyethanol in both sols and MEK and propanol in ex-situ) and residual alkoxides species (TiOPr and GPTMS). MEK is also well visible in spectrum of as deposited ex-situ film between 1470 and 1370 cm<sup>-1</sup> (Methyl C-H asym./sym. Bend).

All these absorptions decrease largely after treatment at 70°C, indicating that solvent evaporation and residual alkoxy reaction (hydrolysis) would play the major role during imprinting process at this or higher temperatures.

Figure 3.35c shows the area of the absorption of the band integrated between 3020 and 2780 cm<sup>-1</sup>, after subtraction of -OH absorption, of films as deposited and cured at different temperatures used during imprinting experiments. As it can be seen, the main part of organic (55%) is removed during curing at 70°C, reasonably due to solvent evaporation. The decrease of organic content with curing at higher temperature is limited at about 15% in in-situ, mainly imputable to residual alkoxy reaction (hydrolysis) and secondary to residual solvent evaporation, and around 0% for ex-situ. In fact, ex-situ contains a negligible amount of

residual alkoxides with respect to in-situ, where the presence of pre polymerized Ti-isopropoxyde is dominant.

The reduction of alcoholic solvents content in films upon thermal treatment (methoxyethanol in both sols and propanol or MEK in ex-situ) is confirmed by the decreasing of OH absorption at  $3400\text{ cm}^{-1}$ , particularly evident in ex-situ after curing at  $70^\circ\text{C}$  and that can be correlated to the sharp increase of viscosity around  $70\text{-}80^\circ\text{C}$  visible in Figure 3.21. In-situ films show a gradual -OH absorption reduction during curing, easily due to condensation progress and solvent evaporation which hide a possible -OH formation from the residual alkoxy species hydrolysis; this trend explains the slow but continuous increase of viscosity versus temperature shown by in-situ sol, as already observed.

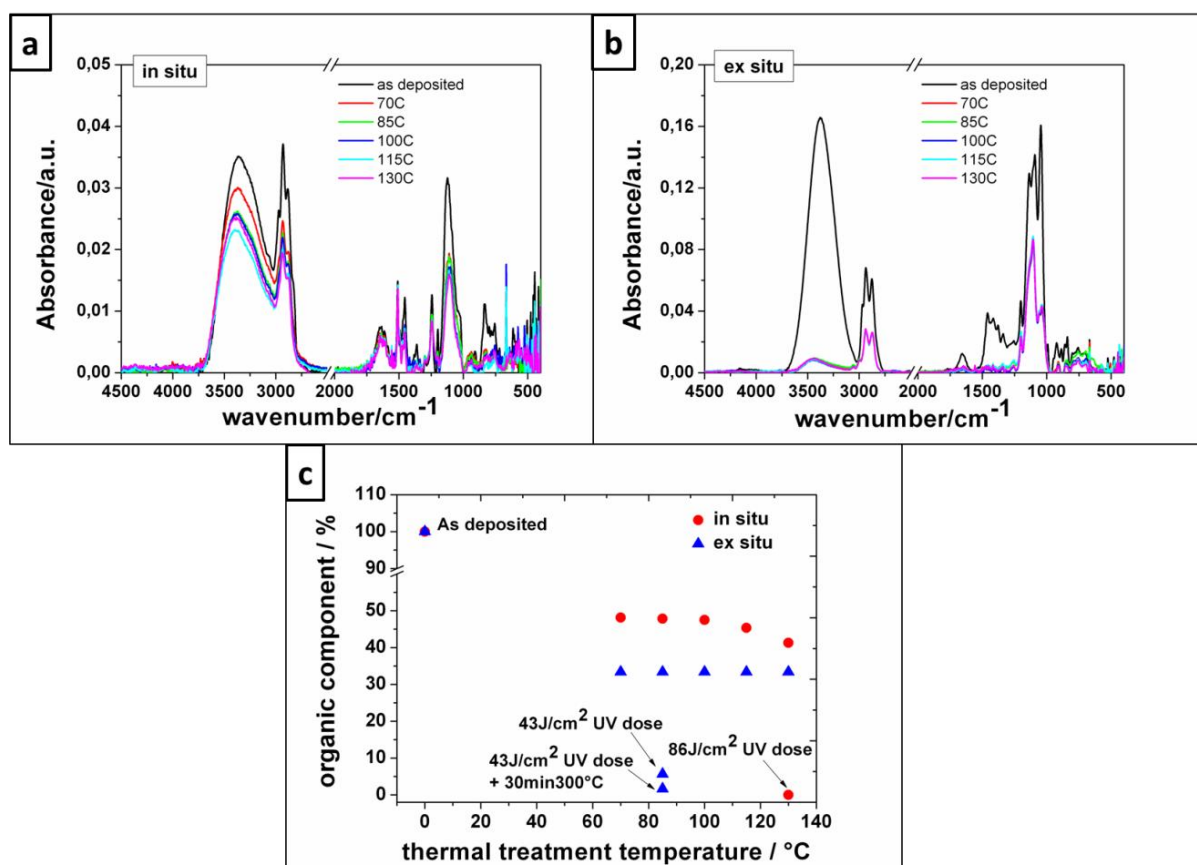


Figure 3.35 FTIR spectra of in-situ (a) and ex-situ (b) films treated at different temperatures used during imprint experiments and (c) residual organic component of the films calculated from the areas of FTIR bands absorption of (a) and (b), together with the areas from FTIR spectra after UV and TT at  $300^\circ\text{C}$ , integrated between  $3020$  and  $2780\text{ cm}^{-1}$ .

As previously discussed, the distinctive feature of these  $\text{TiO}_2$  based resists is the possibility to convert patterned structures into inorganic oxide by UV curing, determined from the photoactivity of  $\text{TiO}_2$  network that locally induce the degradation of organic species present in the material under UV illumination. If needed, with a post exposure thermal treatment at

300°C, a further densification of the structure can be achieved. This transformation has the further distinguishing feature of maintaining, within certain limits discussed later, shape and dimension of the imprinted structures, differently from the results reported in literature until now on inorganic patterned structures [126,128].

Refractive index and thickness measurements of the above discussed un-patterned films are reported in Figure 3.36c and d.

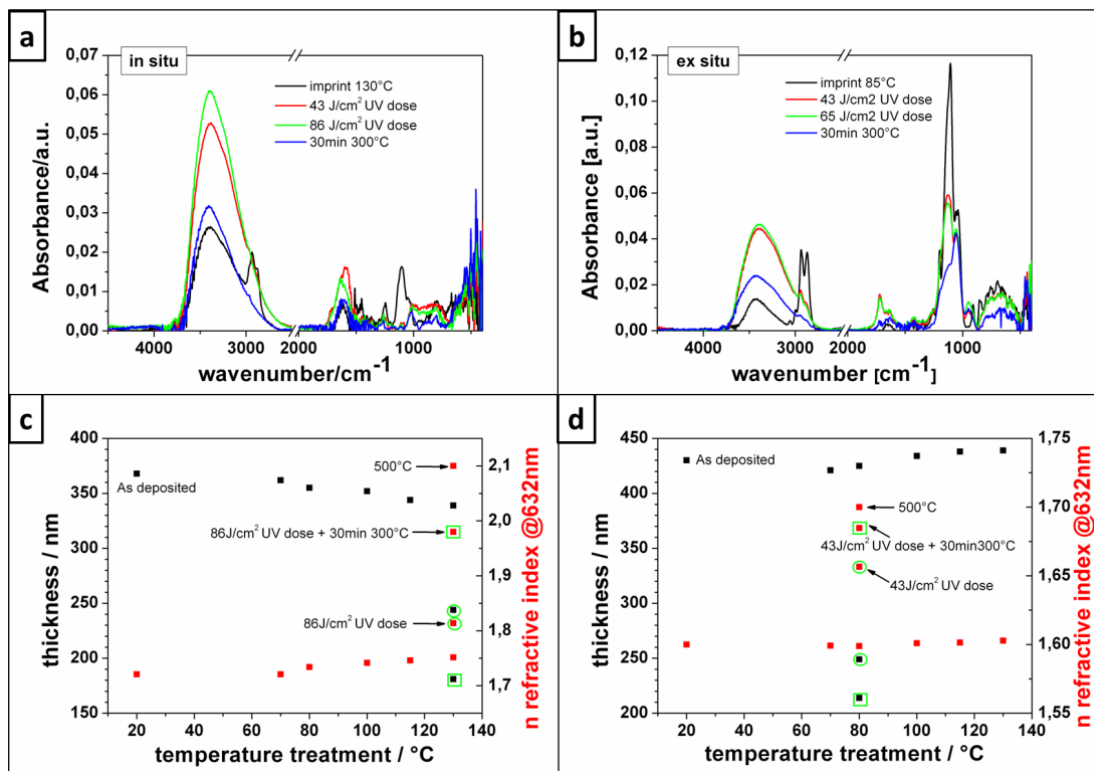


Figure 3.36 a and b) FTIR spectra of the films treated at the imprinting temperature, then exposed to UV and further cured at 300°C. c and d) Thickness and refractive index of ex situ (d) and in situ films (c) cured at different temperatures. Circled and squared off points refers to data of films exposed and then treated at 300°C after curing at imprinting temperature, respectively.

Only in-situ films thickness shows an almost linear decrease accompanied by a slight refractive index growth, while ex-situ refractive index and thickness remain constant with thermal treatment. A comparison between in-situ and ex-situ thickness change shows that the shrinkage of in-situ films after treatment at 130 °C is lower than 8%, while ex-situ doesn't contract. At this temperature the organic component (apart from solvent) is still present in both films (see Figure 3.35c) but the densification of in-situ is more effective, as confirmed by refractive index of films treated at 130°C: 1.75 and 1.60 for in-situ and ex-situ respectively. Moreover, even if in ex-situ the presence of anatase nanoparticles should further contribute to



increase the film refractive index, a poor compaction efficiency of the nanoparticles clearly takes place with a consequent high final porosity of the film.

A 28 and 40% shrinkage, for in-situ and ex-situ respectively, is observed after UV exposure of films cured at the selected imprinting temperatures (130°C for in-situ and 80°C for ex-situ), accompanied by a refractive index rise up to 1.81 and 1.66@632nm respectively. After curing at 300°C the irradiated films, refractive index values close to 2 and 1.7@632nm and 50% shrinkages are measured. Eventually, a refractive index up to 2.1@632nm could be reached with a thermal treatment at 500°C for in-situ. This suggests that depending on the requirement of the application, patterned films could be produced with a designed refractive index.

However, these refractive index values compared with those of both amorphous and crystalline dense TiO<sub>2</sub> of 2.49621 reported by the Handbook of Optics [<sup>129</sup>], suggest that the films are still quite porous even taking into consideration the presence of silica phase of about 10 and 30% for in-situ and ex-situ respectively, that limits the achievement of the maximum n value. The porosity of in-situ films reasonably arise from the removal of volatile organic species degraded under UV and from the presence of not condensed TiOH bonds, while in ex-situ it is the result of spaces between dense anatase nanoparticles that don't sinter at these low temperatures.

### 3.6.2. *Nanoimprint lithography of in-situ and ex-situ films*

The synthesized HOI titania films up to 1.5 μm were spin coated at different speeds depending on the wanted thickness (and on the stamp depths) and imprinted at temperatures ranging from room temperature (RT) to 130°C with pressures between 20-40 MPa. Stamp materials, silicon (purchased from Silicon materials) and Ormostamp® (Micro Resist Technology) possessing multi micro- to nano- metric features pattern and features depth from 150 to 730 nm were used. The anti-sticking layer was obtained using 1H,1H,2H,2H-Perfluorooctyl-trichlorosilane 97% (Aldrich). The imprint process was optimized both by fine-tuning of resists synthesis, adding BFDGE and a certain amount of silica modification (GB) during in-situ and ex-situ synthesis respectively, and by controlling process parameters (film thickness, pressure, time, temperature), in order to avoid cracks and shallow structures, Figure 3.37.

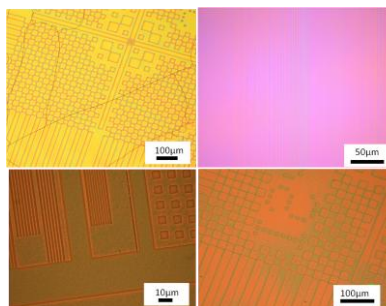


Figure 3.37 Examples of problems during imprint process (cracks or shallow structures) for in-situ films without BFDGE (upper) and ex-situ (lower) resists

It is then clear that a right balance between temperature, time and pressure are necessary during NIL, otherwise final structures depth, lower than the stamp features used, due to incomplete filling caused by premature or insufficient crosslinking of the film during imprinting, are obtained.

In particular, the presence of highly reactive precursors that tend to crosslink instead of soften with temperature, contrary to thermoplastic resists, forces to limit time (at a certain temperature) or temperature used during imprinting, to avoid premature crosslink of the sol and incomplete filling of the structures. On the other hand, once cavities are filled, it is necessary to crosslink the resist to maintain the structures shape after pressure removal.

As discussed in paragraph 3.3.5, it is reasonable that the slow hardening of in-situ films allows them to be imprinted in a range of temperatures from RT to the highest tested (130°C), preserving the soft texture. Therefore, imprints for time long enough and/or at high temperatures are reasonably required to harden the structures and to avoid the emptying of the cavities during demoulding. On the contrary, ex-situ films should be imprinted just after deposition i.e. in presence of residual solvent, otherwise the premature crosslinking and hardening prevent a complete cavities filling.

These expectations are confirmed by NIL of Figure 3.38a where three different nanostructures with sizes ranging from 50 nm to 1.5 µm size and with depth up to 510 nm are shown: 1 µm in-situ films were imprinted at temperatures ranging from 80 to 130 °C. The network hardening is reached in 20 min at 100-130°C with a pressure of 30 MPa as confirmed by the crack-free flat profile of the structures. In the case of stamp with deep cavities the difference between stamp depth and AFM profile of the structures is 30%: in fact with a 730nm stamp depth, lines of 510 nm high are obtained, Figure 3.38b. Therefore, a partial, even if low, contribution of an incomplete filling of the structures has to be considered, since the shrinkage of in-situ flat films after treatment at 100 °C is lower than 5%, as shown in Figure 3.36.

Figure 3.38a also shows SEM micrographs of 1  $\mu\text{m}$  imprinted ex-situ film. With this system a more stringent compromise between solvent evaporation with temperature and time to crosslink has to be found to obtain a good imprint. In fact, the best imprint results were achieved at room temperature with a long imprinting time of several hours, during which the sol can flow within the structures but requires long time to crosslink or in shorter time at temperature not higher than 80°C.

The conditions that gave best results, in terms of structures sharpness and uniformity of filling, were 10 min at 80°C and RT for several hours. Structures depth up to 630 nm have been produced with stamp cavities depth of 730 nm. Figure 3.38b shows the AFM image and profile of 630nm height imprinted lines: the measured difference between stamp depth and AFM profile of the structures is 15%, probably due to incomplete filling of cavities rather than shrinkage, negligible in flat ex-situ films as already shown in Figure 3.36.

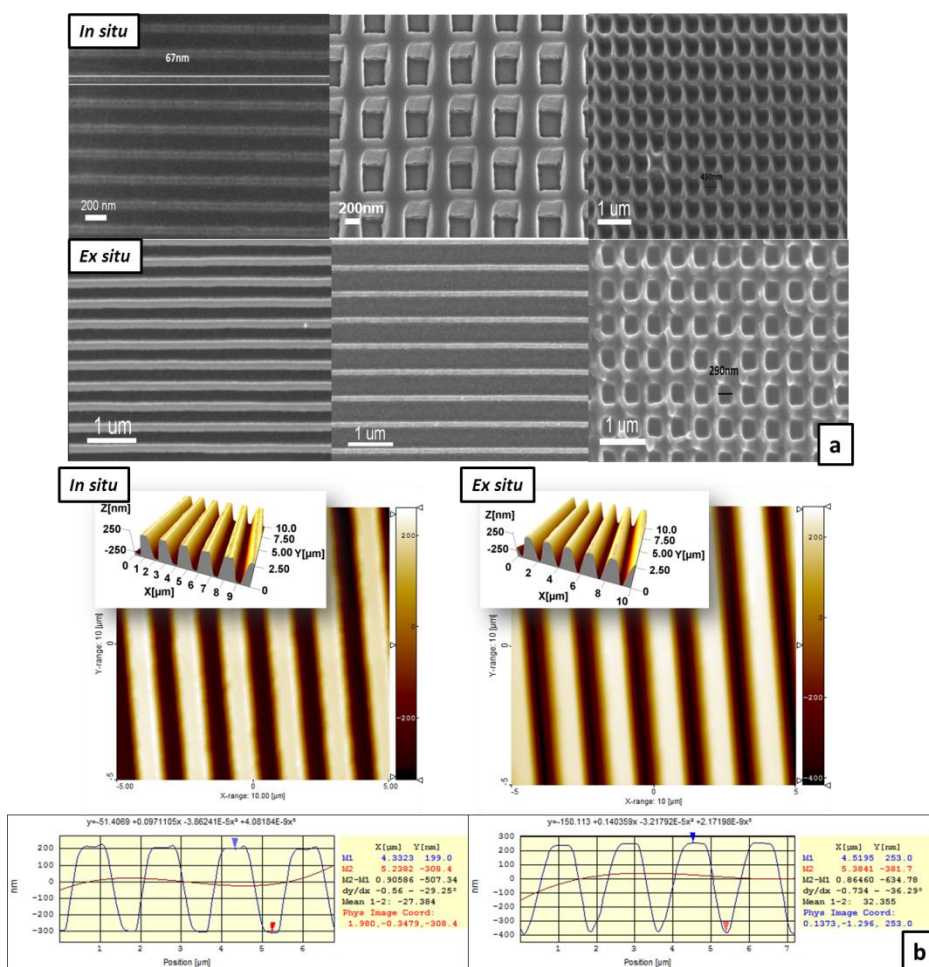


Figure 3.38 a) SEM micrographs of  $\text{TiO}_2$  *in-situ* patterns obtained with stamp depth of 180nm (left), 360 nm (centre) and 700 nm (right); and *ex-situ* patterns: lines with stamp depth of 160nm imprinted at 80°C for 10 min with a pressure of 40MPa (left) or at room temperature for 24h with the same pressure (centre); pattern with a 700 nm depth stamp at room temperature for 24h with a pressure of 40MPa (right); b) AFM images and depth profile of  $\text{TiO}_2$  *in-situ* (left) and *ex-situ* (right) imprinted structure with a 730 nm depth stamp

After imprinting patterned surfaces were exposed to UV with the minimum dose needed to eliminate organic component and to transform the film in an inorganic material; the exposure is expected to lead to a further vertical and eventually lateral shrinkage, based on data of Figure 3.36. However, the shrinkage exhibited by in-situ films is very low, as demonstrated by the AFM images of Figure 3.39, corresponding to the same grating of Figure 3.38b but after UV exposure.

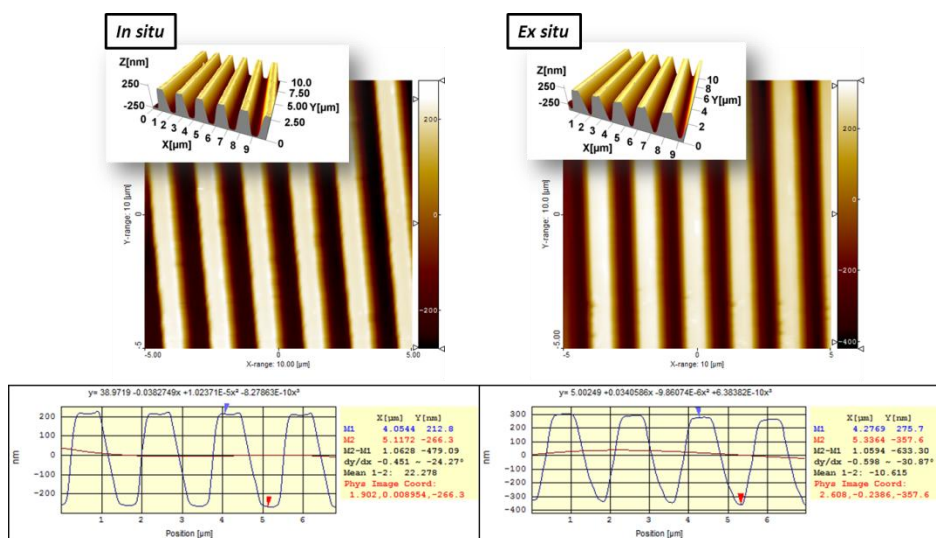


Figure 3.39 AFM images of  $\text{TiO}_2$  *in-situ* imprinted with a 730 nm depth stamp exposed for 8 min ( $86 \text{ J/cm}^2$ ) to UV radiation (left);  $\text{TiO}_2$  *ex-situ* imprinted with a 730 nm depth stamp and then exposed for 4 min ( $43 \text{ J/cm}^2$ ) to UV radiation (right)

The lateral profile of simple gratings (period  $1.5 \mu\text{m}$  and stamp depth 730 nm) reveals that the mean height of the gratings changes from 510 nm after imprinting to 479 nm with a resulting vertical shrinkage around 7%, much lower than a value of 28% measured on flat films treated at  $130^\circ\text{C}$  and then exposed to the same dose, as shown in Figure 3.36.

This effect is also more evident in *ex-situ* films, that don't undergo to vertical shrinkage after irradiation, as shown by the gratings of Figure 3.39, which corresponds to the grating of Figure 3.38b after UV exposure. In fact the measured shrinkage of flat *ex-situ* films after curing at  $80^\circ\text{C}$  and UV exposure at the same dose was around 40%, as shown in Figure 3.36. Moreover, it is noteworthy that both in *in-situ* and in *ex-situ* the relatively low vertical shrinkage is not accompanied by a lateral shrinkage and all the deformation necessary to compensate the degradation of the organic part of the film is probably "absorbed" by vertical shrinkage. This behaviour represents an important advantage because simplify the prediction of the final geometry of the structures: only vertical shrinkage has to be considered during the design of the initial thickness. This behaviour can be due to simultaneous application of

pressure and temperature during imprinting process: it could be reasonable that the thermal step carried out during imprinting is more effective towards the compaction of the film than pure thermal treatment at the same temperature, thanks to the applied pressure. The following UV treatment would have an effect only on the organic degradation and not on a further shrinkage. The lack of shrinkage would also help to maintain the shape and quality of the pattern after UV exposure and no cracks were observed at the end of the process.

An example of possible application of patterned titania is reported in Figure 3.40. As it can be seen from UV-Vis spectra reported, imprinted films with hexagonal array nanostructures (depth 140nm and 300nm period) are effective as antireflective coating compared to flat titania films.

**Ni Master:** hexagonal array nanostructures.

Depth: 140 nm – period: 300 nm along the X' and Y' directions

**Titania patterned with dense nanostructures:  
AR coating are obtained**

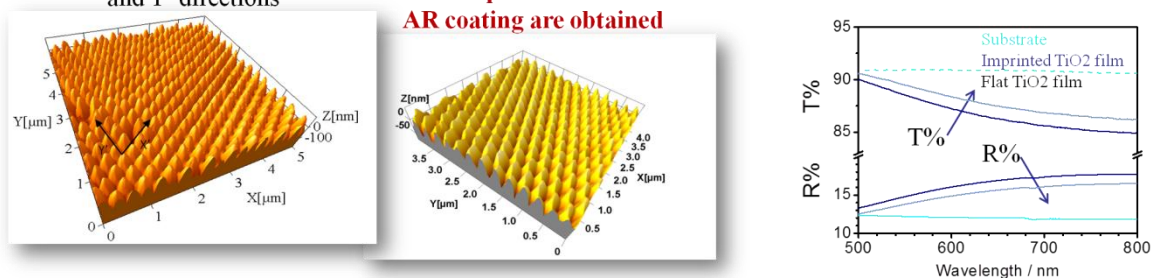


Figure 3.40 AFM images of master with hexagonal array nanostructures and of imprinted titania film. On the right: UV-Vis spectra of flat and imprinted titania shows the antireflective properties of imprinted titania.

In conclusion,  $\text{TiO}_2$  was patterned in a one-step process starting from hybrid organic-inorganic (HOI) based sol-gel systems with up to 90% titania. Large area inorganic titania micro and nanoscale patterns were fabricated directly through photolithography and nanoimprint lithography without need for transfer processes. The novelty of both fabrication approaches lies in the exploitation of titania photocatalytic character, responsible of the structural change of the film when exposed to UV light (during the lithographic process for photolithography and after pattern realization with thermal NIL), which enables to realize high refractive index (up to 1.8@632nm for in-situ and 1.64@632nm for ex-situ) inorganic and partially crystalline structures, without the need for high temperature treatments. Noticeable, in-situ system revealed a high versatility when used as optical lithography resist since it shows both positive and negative tone with lithographic contrast up to 19, simply changing the process parameters.

## References

- <sup>1</sup> D. P. Macwan, Pragnesh N. Dave, Shalini Chaturvedi, *J Mater Sci* **2011**, 46, 3669–3686.
- <sup>2</sup> A. Fujishima, K. Honda, *Nature* **1972**, 37, 238.
- <sup>3</sup> M. Langlet, M. Burgos, C. Coutier, C. Jimenez, C. Morant, M. Manso, *Journal of Sol-Gel Science and Technology* **2001**, 22, 139–150.
- <sup>4</sup> J. Barbé, A. Francis Thomson, E. Wang, K. McIntosh, K. Catchpole, *Prog. Photovolt: Res. Appl.* **2012**, 20, 143–148.
- <sup>5</sup> A. W. Harris, B. P. Ludden, D. C. W. Blaikley, *Vacuum* **1992**, 43(1–2), 143–147.
- <sup>6</sup> W. Que, Y. Zhou, Y.L. Lam, Y.C. Chan, C.H. Kam, *Appl. Phys. A* **2001**, 73, 171–176.
- <sup>7</sup> Z. Jiwei, Y. Tao, Z. Liangying, Y. Xia, *Ceramics International* **1999**, 25, 667–670.
- <sup>8</sup> R. Deb Roy, D. Sil, S. Jana, P. K. Biswas, S. K. Bhadra, *Photonic Sensors* **2012**, 2, 81–91.
- <sup>9</sup> X. Orignac, H. C. Vasconcelos, X. M. Du, R.M. Almeida, *J Sol Gel Sci Technol.* **1997**, 8(1–3), 243–248.
- <sup>10</sup> M. Yoshida, P. N. Prasad, *Chem. Mater.* **1996**, 8, 235–241.
- <sup>11</sup> U. Diebold, *Appl. Phys. A* **2003**, 76, 681–687.
- <sup>12</sup> X. Wang, M. Fujimaki, K. Awazu, *Optics Express* **2005**, 13, 1486–1497.
- <sup>13</sup> A. S. Sinitskii, V. V. Abramova, Y. D. Tretyakov, *Mendeleev Commun.* **2007**, 17, 1–3.
- <sup>14</sup> Y. Lixia, L. Shenglian, C. Qingyun, Y. Shouzhuo, *Chinese Sci Bull* **2010**, 55.
- <sup>15</sup> H. Tang, K. Prasad, R. Sanjinés, F. Lévy, *Sens Actuators B Chem.* **1995**, 26(1–3), 71–75.
- <sup>16</sup> L. Gao, Q. Li, Z. Song, J. Wang, *Sens Actuators B Chem.* **2000**, 71(3), 179–183.
- <sup>17</sup> E. Palin, H. Liu, T. J Webster, *Nanotechnology* **2005**, 16, 1828–1835.
- <sup>18</sup> A. Fujishima, T. N. Rao, D. A. Tryk, *J. Photochem. Photobiol. C* **2000**, 1, 1–21.
- <sup>19</sup> M. Pelaeza, N. T. Nolanb, S. C. Pillai b, M. K. Seeryc, P. Falarasd, A. G. Kontosd, P. S.M. Dunlope, J. W.J. Hamiltone, J.A. Byrne, K. O’Sheaf, M. H. Entezarig, D. D. Dionysioua, *Applied Catalysis B: Environmental* **2012**, 125, 331–349.
- <sup>20</sup> T. Yamaguchi, N. Tobe, D. Matsumoto, T. Nagai, H. Arakawa, *Solar Energy Materials & Solar Cells* **2010**, 94, 812–816
- <sup>21</sup> S. Ito, T. N. Murakami, P. Comte, P. Liska, C. Grätzel, M. K. Nazeeruddin, M. Grätzel, *Thin Solid Films* **2008**, 516, 4613–4619
- <sup>22</sup> S. S. Williams, M. J. Hampton, V. Gowrishankar, I-K. Ding, J. L. Templeton, E. T. Samulski, J. M. DeSimone, M. D. McGehee, *Chem. Mater.* **2008**, 20 (16), 5229–5234.

- 
- <sup>23</sup> M. Koelsch, S. Cassaignon, C.T. Thanh Minh, J.-F. Guillemoles, J.-P. Jolivet, *Thin Solid Films* **2004**, 451, 86–92
- <sup>24</sup> Y. Hu, H.-L. Tsai, C.-L. Huangk, *European Ceramic Society* **2003**, 23, 691–696.
- <sup>25</sup> H. Zhang, J.F. Banfield, *J. Phys. Chem. B* **2000**, 104, 3481\_3487.
- <sup>26</sup> S. Monticone, R. Tufeu, A.V. Kanaev, E. Scolan, C. Sanchez, *Applied Surface Science* **2000**, 162, 565 .
- <sup>27</sup> X. Chen, S. S. Mao, *Chem. Rev.* **2007**, 107, 2891-2959.
- <sup>28</sup> A. N. Banerjee, *Nanotechnology, Science and Applications* **2011**, 4, 35–65.
- <sup>29</sup> V.M. Gun'ko, A.G. Dyachenko, M.V. Borysenko, J. Skubiszewska-Zieba, R. Leboda, *Adsorption* **2002**, 8, 59–70.
- <sup>30</sup> C. Natarajan, G. Nogami *J. Electrochem. Soc.* **1996**, 143(5), 1547-1550.
- <sup>31</sup> T. Chen, C. Luo, D. Wang, Y. Xiong, *Physics Procedia* **2011**, 18, 136–142.
- <sup>32</sup> P. K. Dutta, M. Frank , G. W. Hunter, M. George, *Sensors and Actuators B* **2005**, 106, 810–815.
- <sup>33</sup> J. Kowalski, A. Sobczyk-Guzenda, H. Szymanowski, M. Gazicki-Lipman, *Journal of Achievements in materials and manufacturing engineering* **2009**, 37.
- <sup>34</sup> B.A. Latella, G. Triani, Z. Zhang, K.T. Short, J.R. Bartlett, M. Ignat, *Thin Solid Films* **2007**, 515, 3138–3145.
- <sup>35</sup> K. Jiang, A. Zakutayev, J. Stowers, M. D. Anderson, J. Tate, D. H. McIntyre, D. C. Johnson, D. A. Keszler, *Solid State Sciences* **2009**, 11, 1692–1699.
- <sup>36</sup> R.S. Sonawane, S.G. Hegde, M.K. Dongare, *Materials Chemistry and Physics* **2002**, 77, 744–750.
- <sup>37</sup> S. Phadke, J. D. Sorge, S. Hachtmann, D. P. Birnie, *Thin Solid Films* **2010**, 518, 5467–5470.
- <sup>38</sup> N. Negishi, K. Takeuchi, T. Ibusuki, *Journal Of Sol-Gel Science And Technology* **1998**, 13, 691–694.
- <sup>39</sup> J. Zhang, F. H. J. Maurer, M. Yang, *J.Phys.Chem.C* **2011**, 115, 10431–10441.
- <sup>40</sup> C. Lu, Z. Cui, C. Guan, J. Guan, B. Yang, J. Shen, *Macromol. Mater. Eng.* **2003**, 288.
- <sup>41</sup> F. Wang, Z. Luo, S. Qing, Q. Qiu, R. Li, *Journal of Alloys and Compounds* **2009**, 486, 521–526.
- <sup>42</sup> M. Houmard, D. Riassetto, F. Roussel, A. Bourgeois, G. Berthomé, J.C. Joud, M. Langlet, *Surface Science* **2008**, 602, 3364–3374.

- <sup>43</sup> L. Lee, W. Chen, *Chem. Mater.* **2001**, 13, 1137-1142
- <sup>44</sup> S. Karataş, C. Kızılkaya, N. Kayaman-Apohan, A. Güngör, *Progress in Organic Coatings* **2007**, 60, 140-147.
- <sup>45</sup> B. Schwenger, L. Wang, J. S. Swensen, A. B. Padmaperuma, G. Silverman, R. Korotkov, D. J. Gaspar, *Langmuir* **2012**, 28, 10072-10081.
- <sup>46</sup> Y. Bessekhoud, D. Robert, J. V. Weber, *J. Photochem. Photobiol.A* **2003**, 157, 47.
- <sup>47</sup> B. L. Bischoff, M. A. Anderson, *Chem. Mater.* **1995**, 7, 1772-1778.
- <sup>48</sup> S. Sahni, S. Bhaskar Reddy, B.S. Murty, *Materials Science and Engineering A* **2007**, 452-453, 758-762.
- <sup>49</sup> S. Mahshid, M. Sasani Ghamsari, M. Askari, N. Afshar, S. Lahuti, *Semiconductor Physics, Quantum Electronics & Optoelectronics* **2006**, 9, 65-68.
- <sup>50</sup> U. Schubert, *J. Mater. Chem.* **2005**, 15, 3701-3715.
- <sup>51</sup> M. Pathak, R. Bohra, R. C. Mehrotra, I.-P. Lorenz, H. Piotrowski, *Transition Met. Chem.* **2003**, 28, 187.
- <sup>52</sup> N. Uekawa, J. Kajiwara, K. Kakegawa, Y. Sasaki, *Journal of Colloid and Interface Science* **2002**, 250, 285-290.
- <sup>53</sup> N. M. Tuan, N. T. Nha, N. H. Tuyen, *Journal of Physics: Conference Series* **2009**, 187, 012040.
- <sup>54</sup> C. Su, B.-Y. Hong, C.-M. Tseng, *Catalysis Today* **2004**, 96, 119-126.
- <sup>55</sup> B. Liu, S. Tang, Y. Yu, S. Lin, *Colloids and Surfaces A: Physicochemical and Engineering Aspects* **2011**, 377, 138-143.
- <sup>56</sup> G. Brusatin, G. Della Giustina, F. Romanato, G. Guglielmi, *Nanotechnology* **2008**, 19, 175306.
- <sup>57</sup> P.F. Rossi, G. Busca, V. Lorenzelli, O. Saur and J.C. Lavalley, *Langmuir* **1987**, 3, 52.
- <sup>58</sup> C. Martin, I. Martin, V. Rives, B. Grzybowska, I. Gressel, *Spectrochimica Acta Part A* **1996**, 52, 733-740.
- <sup>59</sup> S. Gardin, R.a Signorini, A. Pistore, G. Della Giustina, G. Brusatin, M. Guglielmi, R. Bozio, *J. Phys. Chem. C* **2010**, 114, 7646-7652.
- <sup>60</sup> P. Innocenzi, *J.Non-Cryst.Solids* **2003**, 316, 309-319.
- <sup>61</sup> F. L. Galeener, *Phys. Rev.* **1979**, B19, 4292.
- <sup>62</sup> J. F. Brown, L. H. Vogt, *J. Am. Chem. Soc.* **1965**, 4313-4317.
- <sup>63</sup> B. Orel, R. Jese, A. Vilcnik, U. L. Stangar, *J. Sol-Gel Sci. Techn.* **2005**, 34, 251-265.



- 
- <sup>64</sup> T. Tatsuma, W. Kubo, A. Fujishima, *Langmuir* **2002**, 18, 9632-9634
- <sup>65</sup> W. Que, Y. Zhou, Y. L. Lam, Y. C. Chan, H.T. Tan, T.H. Tan, C.H. Kam, *Journal of Electronic Materials* **2000**, 29.
- <sup>66</sup> B. Ohtani, Y. Ogawa, S. Nishimoto, *J. Phys. Chem. B* **1997**, 101, 3746-3752.
- <sup>67</sup> H. D. Jang, S. Kim, S. Kim, *Journal of Nanoparticle Research* **2001**, 3, 141-147.
- <sup>68</sup> Z. Zhang, P. A. Maggard, *Journal of Photochemistry and Photobiology A: Chemistry* **2007**, 186, 8-13.
- <sup>69</sup> F.J. Jing, L. Wang, R.K.Y. Fu, Y.X. Leng, J.Y. Chen, N. Huang, Paul K. Chu, *Surface & Coatings Technology* **2007**, 201, 6874-6877.
- <sup>70</sup> X. Le Guével, C. Palazzesi, P. Proposito, G. Della Giustina, G. Brusatin, *J. Mater. Chem.* **2008**, 18, 3556-3562.
- <sup>71</sup> R. Vogel, P. Meredith, I.Kartini, M. Harvey, J. D. Riches, A. Bishop, N. Heckenberg, M. Trau, H. Rubinsztein-Dunlop, *Chem. Phys. Chem.* **2003**, 4, 595 - 603.
- <sup>72</sup> X. Wang, M. Fujimaki, and K. Awazu, *Optics Express* **2005**, 13, 1486-1497.
- <sup>73</sup> C. Won Chung, I. Chung, *J. Vac. Sci. Technol. A* **2000**, 18.3.
- <sup>74</sup> N. Ozawa, H. Yabe, T. Yao, *J. Am. Ceram. Soc.* **2003**, 86 (11), 1976-78.
- <sup>75</sup> P. Yang, M. Yang, S. Zou, J. Xie, W. Yang, *J. Am. Chem. Soc.* **2007**, 129, 1541-1552.
- <sup>76</sup> F.J. Jing, L. Wang, R.K.Y. Fu, Y.X. Leng, J.Y. Chen, N. Huang, Paul K. Chu, *Surface & Coatings Technology* **2007**, 201, 6874-6877.
- <sup>77</sup> P. Yang, M. Yang, S. Zou, J. Xie, W. Yang, *J. Am. Chem. Soc.* **2007**, 129, 1541-1552.
- <sup>78</sup> J. P. Lee, M. M. Sung, *J. Am. Chem. Soc.* **2004**, 126, 28-29.
- <sup>79</sup> H. Haick, Y. Paz Dark, *Chem. Phys. Chem.* **2003**, 4, 617- 620.
- <sup>80</sup> X. Zhang, M. Jin, Z. Liu, D. A. Tryk, S. Nishimoto, T. Murakami, A. Fujishima, *J. Phys. Chem. C* **2007**, 111, 14521-14529.
- <sup>81</sup> L. Francioso, P. Siciliano, *Nanotechnology* **2006**, 17, 3761-3767.
- <sup>82</sup> L. Francioso, A.M. Taurino, A. Forleo, P. Siciliano, *Sens. Actuators B Chem.* **2008**, 130, 70-76.
- <sup>83</sup> D. Xia, Y. Jiang, X. He, S. R. J. Brueck, *Applied Physics Letters* **2010**, 97, 223106.
- <sup>84</sup> P. Yang, M. Yang, S. Zou, J. Xie, W. Yang, *J. Am. Chem. Soc.* **2007**, 129, 1541-1552.
- <sup>85</sup> Y. Masuda, T. Sugiyama, H. Lin, W.S. Seo, K. Koumoto, *Thin Solid Films* **2001**, 382, 153-157.

- <sup>86</sup> C. Cuisin, A. Chelnokov, J.-M. Lourtioz, D. Decanini, Y. Chen, *J. Vac. Sci. Technol. B* **2000**, 18, 3505.
- <sup>87</sup> I. Wathuthanthri, Y. Liu, K. Du, W. Xu, C. Choi, *Adv. Funct. Mater.* **2013**, 23, 608–618.
- <sup>88</sup> M.S. Sander, M.J. Côté, W. Gu, B.M. Kile, C.P. Tripp, *Advanced Materials* **2004**, 16, 2052–2057.
- <sup>89</sup> N. Ozawa, T. Yao, *Solid State Ionics* **2002**, 151, 79–87.
- <sup>90</sup> C. Wu, T. Aoki, M. Kuwabara, *Nanotechnology* **2004**, 15, 1886–1889.
- <sup>91</sup> Sung-Gyu Park, Tae Yoon Jeon, Seung-Man Yang, *Langmuir* **2013**, 29, 9620–9625.
- <sup>92</sup> Y. Masuda, W. S. Seo, K. Koumoto *Langmuir* **2001**, 17, 4876–4880.
- <sup>93</sup> Y. Masuda, N. Saito, R. Hoffmann, M. R. De Guire, K. Koumoto, *Advanced Materials* **2003**, 4, 461–467.
- <sup>94</sup> H. Shin, R. J. Collins, M. De Guire, R. A. H. Heuer, C. N. Sukenik, *J. Mater. Res.* **1995**, 10 (3), 692.
- <sup>95</sup> R. J. Collins, H. Shin, M. R. DeGuire, A. H. Heuer, C. N. Sukenik, *Appl. Phys. Lett.* **1996**, 69, 860.
- <sup>96</sup> M. S. M. Saifullah, K. R. V. Subramanian, E. Tapley, D. J. Kang, M. E. Welland, M. Butler, *Nano Lett.* **2003**, 3, 1587–1591.
- <sup>97</sup> B. Liu, S. Ho, *Journal of The Electrochemical Society* **2008**, 155, 57–60.
- <sup>98</sup> A. Shishido, I. B. Diviliansky, I. C. Khoo, T. S. Mayer, S. Nishimura, G. L. Egan, Thomas E. Mallouk, *Appl. Phys. Lett.* **2001**, 79.
- <sup>99</sup> H. Segawa, S. Matsuo, H. Misawa, *Appl. Phys. A* **2004**, 79, 407–409.
- <sup>100</sup> B. Garipcan, J. Winters, J. S. Atchison, M. D. Cathell, J. D. Schiffman, O. D. Leaffer, S. S. Nonnenmann, C. L. Schauer, E. Piskin, B. Nabet, J. E. Spanier, *Langmuir* **2008**, 24, 8944–8949.
- <sup>101</sup> S. Passinger, M. S. M. Saifullah, C. Reinhardt, K. R. V. Subramanian, Boris N. Chichkov, M. E. Welland, *Adv. Mater.* **2007**, 19, 1218–1221.
- <sup>102</sup> N. E. Voicu, M. S. M. Saifullah, K. R. V. Subramanian, M. E. Welland, U. Steiner, *Soft Matter* **2007**, 3, 554–557.
- <sup>103</sup> S. Pelli, G. C. Righini, A. Scaglione, M. Guglielmi, A. Martucci, *Optical Materials* **1996**, 5, 119–126.
- <sup>104</sup> S. U. Khan, J. E ten Elshof, *Sci. Technol. Adv. Mater.* **2012**, 13, 025002.
- <sup>105</sup> H. A. Bullen, S. J. Garret, *Nano Lett.* **2002**, 2.

- <sup>106</sup> M. J. Hampton, S. S. Williams, Z. Zhou, J. Nunes, D. Ko, J. L. Templeton, E. T. Samulski, J. M. DeSimone, *Adv. Mater.* **2008**, 20, 2667–2673.
- <sup>107</sup> D. Kuscer, G. Stavber, G. Trefalt, M. Kosec, *J Am Ceram Soc* **2012**, 95 [2], 487–493.
- <sup>108</sup> R. Ganesan, J. Dumond, M. S. M. Saifullah, S. Lim, H. Hussain, Hong Yee Low, *ACS Nano*, **2012**, 6 (2), 1494–1502.
- <sup>109</sup> X. Luo, C. Zha, B. Luther-Davies, *Optical Materials* **2005**, 27, 1461–1466.
- <sup>110</sup> H. Segawa, K. Tateishi, Y. Arai, K. Yoshida, H. Kaji, *Thin Solid Films* **2004**, 466, 48 – 53.
- <sup>111</sup> H. Segawa, S. Adachi, Y. Arai, K. Yoshida, *J. Am. Ceram. Soc.* **2003**, 86 (5), 761–64.
- <sup>112</sup> T. Imao, D. Hazama, N. Noma, S. Ito, *Journal of the ceramic society of Japan* **2006**, 114(3) 238-240.
- <sup>113</sup> J. Guo, *Advanced Materials* **2007**, 19, 4, 495 – 513-
- <sup>114</sup> Y. Chou, P. Krauss, P. Renstrom, *Science* **1996**, 272, 5258, 85-87.
- <sup>115</sup> B. Bhushan, Cap. 8 Nanoimprint Lithography, *Springer Handbook Of Nanotechnology* **2007**.
- <sup>116</sup> O. F. Göbel, M. Nedelcu, U. Steiner, *Adv. Funct. Mater.* **2007**, 17, 1131–1136.
- <sup>117</sup> K. Yoon, K. Yang, H. Lee, *Thin Solid Films* **2009**, 518, 126–129.
- <sup>118</sup> K. Yoon, K. Yang, H. Lee, H. Kim, *J. Vac. Sci. Technol. B* **2009**, 27.
- <sup>119</sup> S. S. Williams, M. J. Hampton, V. Gowrishankar, I-K. Ding, J. L. Templeton, E. T. Samulski, J. M. DeSimone, M. D. McGehee, *Chem. Mater.* **2008**, 20 (16), 5229–5234.
- <sup>120</sup> Woo-S. Kim, K. B. Yoon, B.-S. Bae, *J. Mater. Chem.* **2005**, 15, 4535–4539.
- <sup>121</sup> H.Ho Park, D. Choi, X. Zhang, S. Jeon, S. Park, S. Lee, S. Kim, K. Kim, J. Choi, J. Lee, D. K. Yun, K. Jo. Lee, H. Park, R. H. Hill, J. Jeong, *J. Mater. Chem.* **2010**, 20, 1921–1926.
- <sup>122</sup> H. Park, X. Zhang, S. Lee, D. Jeong, S. Lee, K. Kim, D. Choi, J. Choi, J. Lee, E. Lee, H. Kwan Kang, H. Park, R. H. Hill, J. Jeong, *Microelectronic Engineering* **2011**, 88, 923–928.
- <sup>123</sup> C. Wu, S. L. Hsu, *J. Phys. Chem. C* **2010**, 114, 2179–2183.
- <sup>124</sup> B. K. Lee, L. Hong, H. Y. Lee, D. Kim, T. Kawai, *Langmuir* **2009**, 25(19), 11768–11776.
- <sup>125</sup> M. Li, H. Tan, L. Chen, J. Wang, S. Y. Chou, *J. Vac. Sci. Technol. B* **2003**, 21.2.
- <sup>126</sup> S. H. Lim, M S M Saifullah, H. Hussain, W. W. Loh, H. Y. Low, *Nanotechnology* **2010**, 21, 285303.
- <sup>127</sup> V.K. Parashar, A. Styah, E.Cuche, C.Depeursinge, M.A.M. Gijs, The 12th International Conference on Solid State Senson, Actuators and Mbmsystems, Boston, *June 8-12, 2003*.

---

<sup>128</sup> R. Ganesan, S. H. Lim, M. S. M. Saifullah, H. Hussain, J. X. Q. Kwok, R. L. X. Tse, H. A. P. Bob, H. Y. Lowa, *J. Mater. Chem.* **2011**, 21, 4484-4492.

<sup>129</sup> *Handbook of Optics*, McGraw-Hill, Vol. 4, **2009**.

---

## *Chapter 4*

### *HIGH SELECTIVE ETCHING MASKS: ALUMINA BASED RESIST*

It is uncommon that materials that need to be incorporated into micro- or nano-device architectures may be structured directly by lithography. More often in the traditional lithographic process the functional material is structured indirectly, first by patterning a sacrificial material - the resist - and then by a pattern transfer step by which the functional material inherits the pattern of the sacrificial layer on top. The structured device could be the final output of the fabrication process, or it could be an intermediate product further used as a template for the fabrication of many replicas, like e.g. in NanoImprint Lithography (NIL) or Injection moulding technology.

Therefore, pattern transfer is often one critical step toward the fabrication of micro or nano features starting from the 2D resist lay-out. The resists' properties are in particular extremely relevant to the outcome of the nanofabrication. They need to be optimized both for the specific lithographic technology adopted and for the subsequent process of pattern transfer, typically obtained by dry etching. Dry etching takes advantage of modern ICP reactors able to provide high etching rate on silicon or its compounds with almost vertical walls. The actual quality of the obtained structures is related not only to the performances of ICP reactor, but depends strongly on the characteristic of the mask material used (i.e. selectivity toward the substrate in the chosen plasma chemistry) and on the aspect ratio requested. Thereby, there is a growing demands on developing high resolution, high selectivity mask for dry etching processes, which could be easily removed after the pattern transfer, leaving the substrate patterned with high quality nano-structures.

With a few exceptions, for which it is desirable that the resist is etched simultaneously to the functional material (e.g. for the transfer of three-dimensional structures by proportional etching, [1,2]), the resist should remain ideally unaffected during the entire plasma etching process so that the dimensional control on the structures is not compromised. High selectivity

of the resist towards the functional material during etching process is desirable also in applications in which high-aspect-ratio structures need to be achieved.

Insufficient selectivity leads to significant degradation of the mask pattern during the etching, resulting in sloped sidewalls, line edge roughness and limitations on the achievable structures' depth. Increasing resists thickness may partially compensate the effects of erosion, potentially introducing different types of side-effects such as a limitation of the lateral resolution or, in the case of high aspect ratio structures, pattern collapse during development and drying, as reported in paragraph 1.1.2. Although commercial resists offer the simplicity of a single process step, they generally exhibit poor dry etching selectivity, as they are usually carbon-based materials. Inductively Coupled Plasma (ICP) cryogenic reactive ion etching, a process assisted by cryo-cooling, or Bosch process (alternating passivation and etching steps) are known for being able to enhance the process selectivity using photoresists compared to the standard Reactive Ion Etching (RIE), but are complicated by the need of low temperatures or a discontinuous process, and hence advanced and sophisticated processing equipment. [<sup>3-4-5-6</sup>] In order to overcome this problem, inorganic mask, mainly metals such as chrome (Cr) and nickel (Ni), are often introduced as a patterned intermediate layer, via the process of lift-off. The enhanced etch selectivity towards the functional material has, even in this case, the drawback of increasing the number of patterning steps and is not fully reliable and thus avoided in industrial applications. [<sup>7,8,9</sup>]

A slightly simplified method have been obtained by means of a two-step developing process: after a partial development a ~4 nm thin metal film is deposited on the nanopatterned resist which is then fully developed. [<sup>10</sup>] This method allowed an enhancement in the aspect ratio of the resist features but is still too complex.

Recent studies are focusing on aluminum oxide based resists, since alumina in fluorine-containing plasmas leads to the formation of non-volatile compounds (AlF<sub>3</sub> for instance sublimates at ca. 1250 °C) and therefore etch extremely slowly, and is easily removable by wet etching.

First attempts on using alumina as a promising material mask for silicon etching were carried out by means of porous anodic aluminum oxide mask [<sup>11,12,13,14,15,16</sup>]. The great advantage of using alumina mask was confirmed in a first study that demonstrated a selectivity of 68:1 for the etching of silicon vs. an alumina mask deposited by reactive magnetron sputtering of aluminum in a mixed argon and oxygen process gas, enabling the fabrication of dense arrays

of nanopillars with smooth and steep sidewalls. However, also in this case the process included the additional step of alumina lift-off. [17]

An example of a fabrication process using alumina as an intermediate hard mask to improve organic resist performance is presented in [18]: a soft azopolymer mask is directly patterned by interferential lithography without the need of development step and used as mask for transferring the structures to the 5nm alumina layer and silicon. However even if the use of azobenzene-functionalized polymers as resist decreases patterning process steps, it needs alumina to improve the selectivity.

A different approach is proposed in [19] by using a fullerene-based spin-on-carbon intermediate hardmask to transfer the pattern, that led the authors to achieve aspect ratio in excess of 11:1, though with imperfect control on the slope of the sidewalls.

In [20] the authors demonstrated a method to enhance the etch resistance of polymethyl methacrylate (PMMA) by alternately infiltrating it with vapours of Trimethyl aluminum and water and in-situ synthesis of alumina, according to Atomic Layer Deposition (ALD) technology. Fine (sub-20 nm) and dense PMMA lines, reinforced by the incorporation of alumina, were successfully transferred into silicon with amplification of their aspect-ratio. Again, the process still appears too complex and costly to be considered a practical solution in micro- or nano- fabrication.

The need for directly patternable spin-on hard masks which already possess the proper dry etching resistance with respect to silicon is then increasing. Suitable modifications to improve the properties of high resolution electron-beam resists have also been reported: chemical amplification (molecular structure or chemical composition modification) and doping with 1-3nm metal nanoparticles of positive and negative tone resists (PMMA, ma-N, ZEP..) have been proposed: the former still presents the problems typical of organic resist, the latter has a better dry etching resistance (generally in between the commercial resist and the metal used) but still lower than silicon. [21,22]

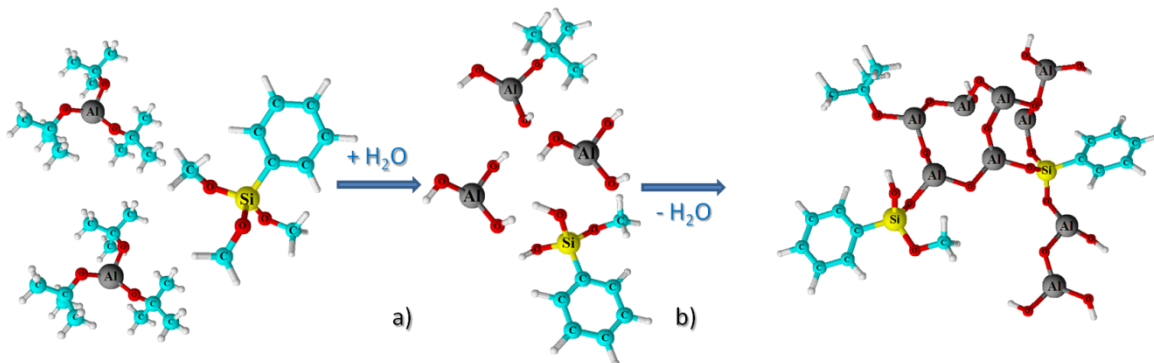
We first obtained a high etch resistance resist based on a hybrid organic-inorganic (HOI) system loaded with 80% of boehmite nano-particles ( $\text{Al}_2\text{O}_3/\text{AlO}(\text{OH})$ ). [23,24,25,26,27] Dry etching selectivity for silicon in excess of 60:1 (comparable to metallic mask in the same etching conditions) was obtained with this system in a set of tests involving deep X-ray Lithography (XRL) and a fluorine-based RIE-ICP etcher. However, the surface and line edge roughness of the pattern were far from optimal due to the size of the nano-particles filled-in. A similar strategy was followed by Brewer Science Inc., which studied the effect of

incorporating metal oxide ( $\text{HfO}_2$ ,  $\text{ZrO}_2$ ,  $\text{ZnO}$ , and  $\text{TiZrO}_2$ ) nanocrystal into polymer-based spin-on hard mask coatings. [28]

These last encouraging results justify the use of mostly inorganic resist directly patternable with high resolutions, as in the case of titania based resist or HSQ, both showing selectivity up to 10 with respect to InP or Si respectively; however, a high temperature treatment is needed to decrease the etch rate. [29,30]

The urgent demand of spin-on materials ready for direct patterning and behaving as etching mask is confirmed by the recent patent by EKC Technology Inc., in which a metal-organic precursor is transformed by radiation in imaged etching mask; however, no commercial product with similar characteristics is available yet. [31]

In this chapter, a spin-on alumina-based resist with outstanding etching properties is presented. The advantage of that it is spin coated from a sol whose main part consists of an alumina precursor, which after deposition reaches an adequate condensation degree transforming into an alumina-like organically modified film (Scheme 4.1), without the need to be loaded with a solid fraction (nanoparticles, nanocrystals), as it was for the first alumina based material previously synthesized for the same purpose [27].



Scheme 4.1 Hydrolysis (a) and condensation (b) reactions of metal-organic precursors with formation of organically modified partially condensed Aluminum Oxide network. The structure represents that of the spin coated film before exposure.

Therefore, the new resist combines the exceptional properties of alumina as etching mask with the ease of deposition and patterning process typical of organic resists avoiding the need for complex synthesis or post-processing, with the further advantage of being patternable by several lithographic techniques (UV, X-ray, Electron Beam, and Nanoimprint Lithography). It exhibits excellent performances both in term of lateral resolution achievable and etch resistance in fluorine-based dry etching processes [32].



### 4.1. Alumina resist synthesis

Different recipes to obtain an homogeneous and stable alumina-based resist were studied and optimized during the study, the final recipes are the result of adjustments and changes arising from experimental evidences.

The 80% alumina based resist was synthesized by the sol-gel method starting with aluminum-tri-sec-butoxide (97%, Aldrich) and trimethoxyphenylsilane ( $\geq 95.0\%$ , Aldrich). The aluminum-tri-sec-butoxide was left stirring with acetic acid in the volume ratio of 1:0.05, in methoxyethanol. A variation of the synthesis could be carried out without acetic acid addition. After 1h the 20% molar ratio phenylsilane was added, and the solution was left stirring at 80°C.

Silicon substrates were spin-coated at different speed with the sol diluted in methoxyethanol to easily adjust film thicknesses in the 30 nm - 1  $\mu\text{m}$  range (examples of spin curve are reported in Figure 4.1). As deposited films were baked 5 min @ 100 C in order to remove the residual solvent and promote sol-gel reactions.

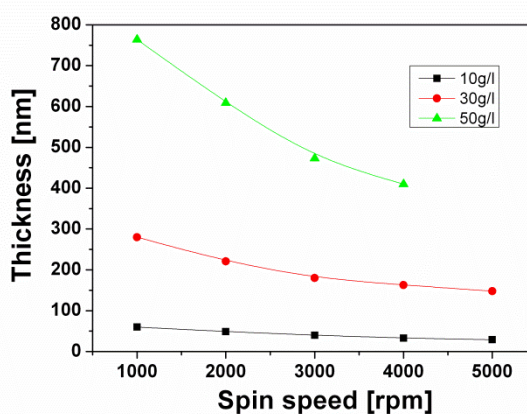


Figure 4.1 Alumina-based resist thickness vs Spin speed

### 4.2. Characterization

The UV absorption and the composition transformations of the films when exposed to UV or X-rays were characterized through UV-Vis spectroscopy (JASCO V-570) and Fourier Transform Infrared spectroscopy (spectrometer Jasco FT-IR-620) with a resolution of  $\pm 4 \text{ cm}^{-1}$ , respectively. The changes occurring in the films in terms of composition and crystalline clusters were evaluated with STA409/429 Netzsch TGA instrument and X-ray diffraction (XRD) using an X-ray diffractometer (Philips PW 1729) with Cu  $K\alpha$  irradiation. Refractive index and thickness changes of the films during UV exposure and TT have been recorded by

ellipsometric measurements (V-Vase J.A.Woollam Ellipsometer). The UV exposure, X-ray and Electron beam lithography were performed with an UV lamp (Hamamatsu Lightningcure LC5), a soft X-ray source at LILIT beam line of Elettra Synchrotron (Trieste, Italy) and EBL (Leo 1540xb column Gemini), respectively. Pattern transfer in Si substrate was then obtained in an ICP dry etcher reactor (SPTS Technologies, Newport UK) with fluorine-based chemistry. Pattern structures were analyzed by optical microscopy and SEM scanning electron microscopy (Zeiss Supra40 SEM Carl Zeiss SMT, Cambridge, UK).

#### 4.2.1. Characterization of the as deposited alumina-based resist

The UV-Vis spectra of alumina resist deposited on quartz in the wavelength range 200-800 nm is reported in Figure 4.2. The resist is transparent for wavelengths exceeding 280nm while it exhibits a  $\lambda_{\max}$ , that corresponds to the energy required for the promotion of electrons from the highest occupied molecular orbital (HOMO) to the lowest unoccupied molecular orbital (LUMO), around 263nm. In fact benzene compound primary bands are generally detected at 184 and 202 nm and a secondary fine structure band at 255 nm. Substituents on the benzene ring (as for the organically modified silica precursor) cause shifts of various peaks to higher wavelengths but, unlike dienes and unsaturated ketones, the effects of various substituents on the benzene ring are not predictable.

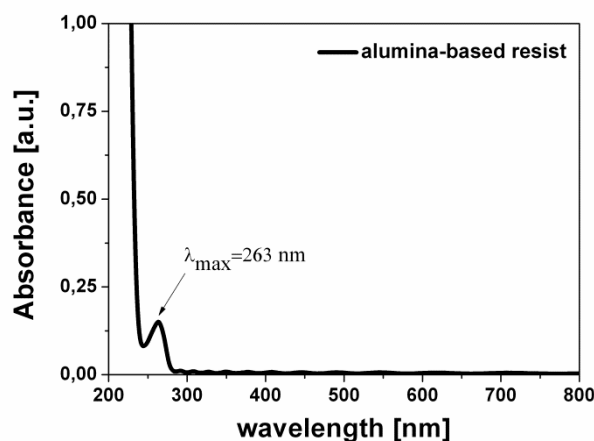


Figure 4.2 UV-Vis spectra of the as deposited alumina resist

The FTIR spectra of the two precursors of the alumina sol-gel solution and of acetic acid are reported in Figure 4.3a.

The *trimethoxyphenylsilane* presents the characteristic CH stretching vibrations of the aromatic ring at 3070-3050-3027-3005  $\text{cm}^{-1}$  as well as at 1590 and 1488-1460  $\text{cm}^{-1}$ . The silicon-phenyl bond presents a multiplicity of absorptions: 1430, 1125-1118 (generally the 1120 is split into a double when two phenyls are attached to Si), weaker peaks at 1032-1000  $\text{cm}^{-1}$  and the strong characteristic peaks at 760-740-719-703  $\text{cm}^{-1}$ . Peaks at 2838-1187-1080  $\text{cm}^{-1}$  are related to the hydrolysable Si-OCH<sub>3</sub> bond. Other peaks at 2970-2940 and 913 are due to the C-H aliphatic stretching vibrations.

The *Aluminum-tri-sec-butoxide* presents the asym/sym stretching CH<sub>3</sub> and CH<sub>2</sub> at 1965-2876  $\text{cm}^{-1}$  and 2931-2843  $\text{cm}^{-1}$  respectively. The CH bending absorption is visible at 1460 and 720  $\text{cm}^{-1}$ . The iso-methyl group absorbs at 1376  $\text{cm}^{-1}$ . *Acetic acid* significant absorption peaks are related to C=O at 1759-1715-1415-1295  $\text{cm}^{-1}$ , CH<sub>3</sub> rocking at 2940-1430-1362  $\text{cm}^{-1}$ , C-C stretching at 1110-1056  $\text{cm}^{-1}$  and C-H stretching modes, out of plane bending and in plane bending at 2630-2688  $\text{cm}^{-1}$ , 890-951  $\text{cm}^{-1}$ , 1362-1250  $\text{cm}^{-1}$  respectively.

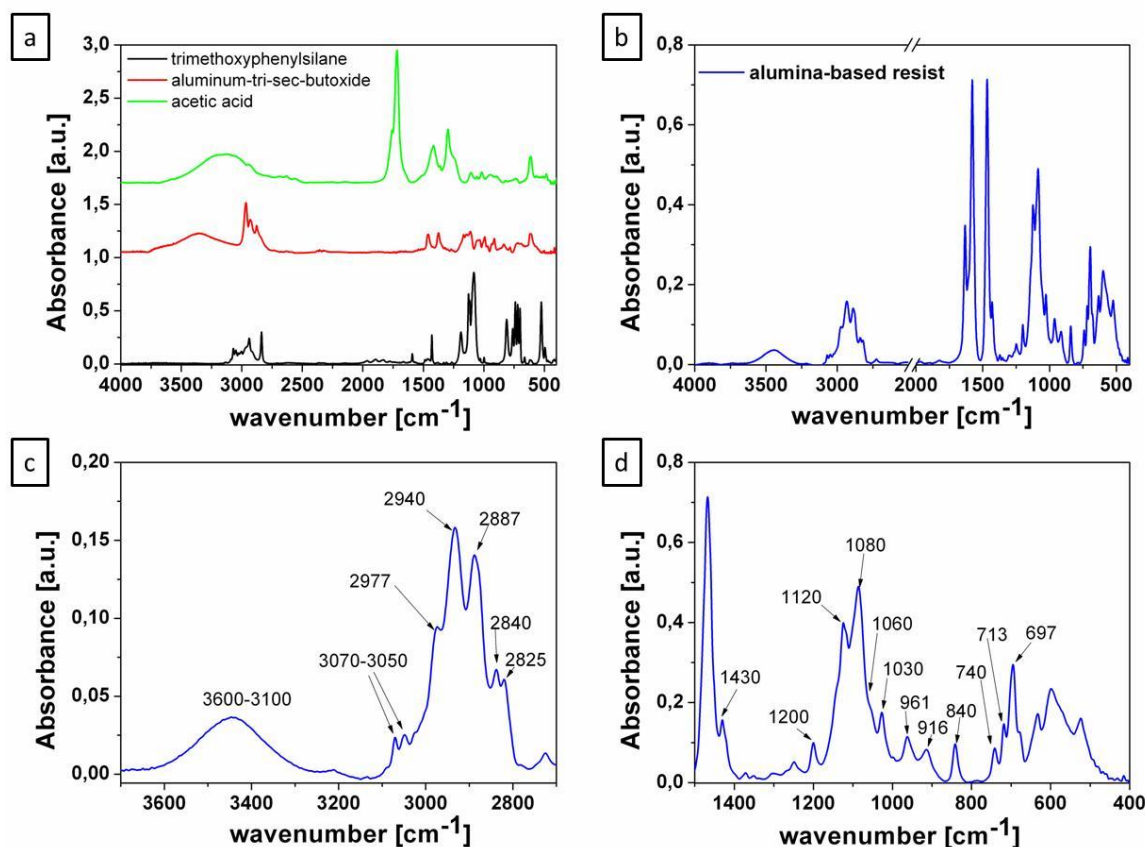


Figure 4.3 FTIR spectra of the synthesis precursors (a) and of the final alumina-based resist (b); zooms of alumina system FTIR spectra (c,d)

The alumina-resist FTIR spectra (Figure 4.3b, c and d) shows the CH stretching vibrations of the aromatic ring at 3070 and 3050  $\text{cm}^{-1}$  as well as the silicon-phenyl bond absorption at

1430, 740, 713, 697  $\text{cm}^{-1}$  and at 1120, 1028 overlapped with the Si-O-Si (1120-1080-1028  $\text{cm}^{-1}$ ) and Al-O-Al broad absorption (between 1000 and 500  $\text{cm}^{-1}$ , in particular the 1060  $\text{cm}^{-1}$  peak) of the partially condensed inorganic network. Peaks at 2977-2887  $\text{cm}^{-1}$  and at 2940-2840  $\text{cm}^{-1}$  are due to the asym/sym stretching vibrations of  $\text{CH}_3$  and  $\text{CH}_2$  respectively. The solvent still present in the as deposited film shows absorptions features at 2825 and 1200  $\text{cm}^{-1}$  ( $-\text{OCH}_3$  bond). The Si-OH and Al-OH bond of the hydrolyzed silica and alumina precursor absorbs at 961-916-840  $\text{cm}^{-1}$ . Table 4.1 reports the significant peaks assignments.

Group	Group frequency wavenumber ( $\text{cm}^{-1}$ )
Phenyl	3070-3050-1430
$\text{CH}_3$	2977-2887 asym/sym stretch
$\text{CH}_2$	2940-2840 asym/sym stretch
$-\text{OCH}_3$	2825-1200
Acetic acid	1631-1580-1468 chelant acetic acid
Si-Ph	1430-1120-1028-740-713-697
Si-OH	961-916-840
Si-O-Si	1120-1088-1028

Table 4.1 Significant alumina-resist FTIR peaks assignments

#### 4.2.2. Characterization of the thermally treated alumina-based resist

When thermally treated alumina films show an amorphous structure: no crystals formation can be detected with X-ray diffraction measurements after annealing at 500 and 800°C, Figure 4.4a. Thermal analysis (STA409/429 Netzsch) on the sol dried for one night at 60°C was performed with an heating rate of 5°C/min in flowing air from room temperature to 1000°C, Figure 4.4b.

The TG analysis shows two main region of weight loss: until 200°C, the loss is due to water evaporation and remaining organic solvent volatilization (methoxyethanol and butanol), at higher temperature it derives from the thermal decomposition (carbonization or oxidation) of the organic component present in the matrix. Beyond 550°C, the weight loss is negligible, indicating a complete degradation of the organic group. In accordance with TG, DTA reveals a first endothermic peak around 105°C attributed to the loss of water and solvent. The peak around 300°C and 400°C are due to the combustion of  $-\text{OC}_4\text{H}_9$  and  $-\text{OCH}_3$  groups.

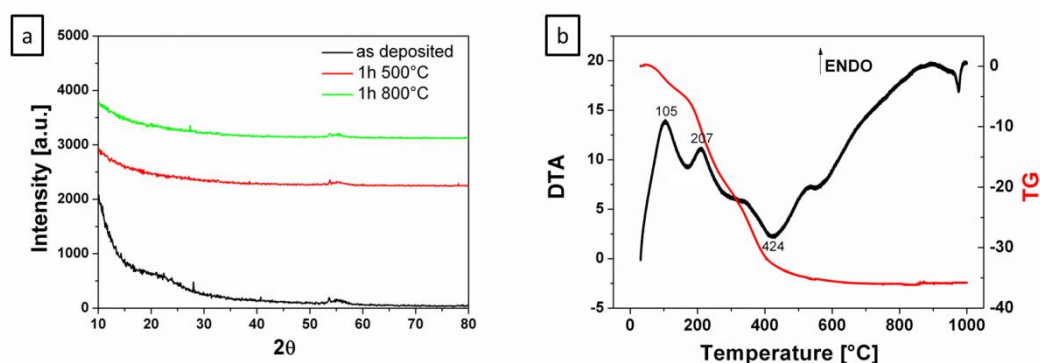


Figure 4.4 (a) XRD of alumina films after annealing at 500 and 800°C; (b) DTA/TG analysis of alumina dried sol from RT up to 1000°C

### 4.2.3. Characterization of the alumina-based resist exposed to UV or X-rays

The UV-Vis spectra of the alumina-based resist compared to the spectrum of the UV lamp (250nm-enhanced type Xe-Hg Hamamatsu Lightningcure LC5) used for film exposure and patterning shows that the resist absorbs the lower emission bands of the UV lamp used (Figure 4.5a). When exposed to UV light the peak related to substituted-benzene ( $\lambda_{\max}=263$  nm) decreases (Figure 4.5b). This behaviour is ascribed to phenyls degradation and photolysis upon UV exposure.

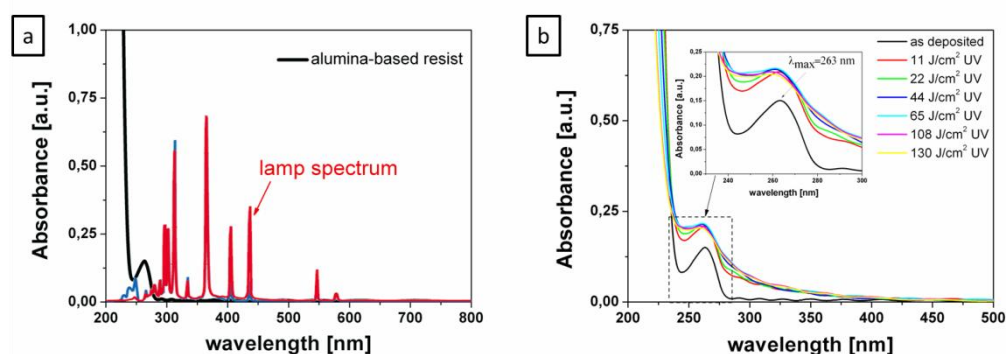


Figure 4.5 (a) UV-Vis spectra of the as deposited alumina resist compared to the UV lamp spectrum; (b) UV-Vis spectra of alumina film after exposure at increasing UV doses

The chemical-physical processes responsible for the sensitivity to radiation of this HOI resist can be easily investigated through FTIR analysis of non-irradiated and UV or X-rays exposed large areas of alumina films deposited on silicon. UV and X-ray exposures were performed with the UV lamp (Hamamatsu Lightningcure LC5) and the soft X-ray source (energy window of 1-4 keV, mostly suited for high resolution patterning) at LILIT beam line of Elettra Synchrotron (Trieste, Italy), respectively [33,34]. The search for the optimal dose for

lithography was obtained by a dose matrix up to  $108 \text{ J/cm}^2$  and scans between 1 and  $20 \text{ J/cm}^2$  in a series of “blank exposures” (i.e. without any mask) with UV and X-rays, respectively. The exposure of the spin-coated films both to UV light and X-rays modifies the film degrading the organic component of the system and condensing the inorganic network, as it could be seen in the FTIR spectra reported in Figure 4.6.

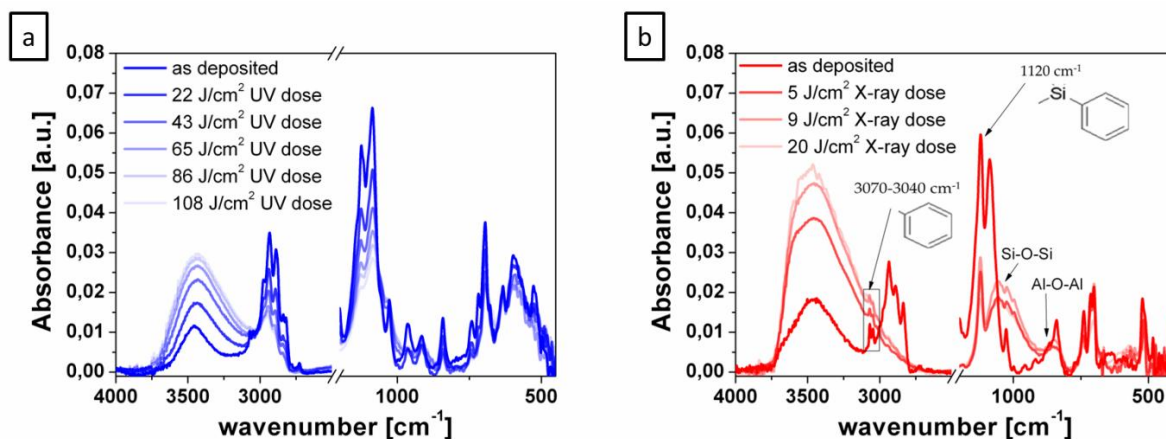


Figure 4.6 FTIR spectra of the alumina-based HOI system films before and after increasing exposure to UV (a) and X-rays (b)

As expected, the degradation of the aromatic rings proceed with irradiation, clearly indicated by the relative intensity reduction of the absorbance peaks at  $3070\text{--}3040 \text{ cm}^{-1}$  due to the aromatic C–H stretching vibration in the diphenyl silica precursor and the absorption at  $1120 \text{ cm}^{-1}$  ascribed to the stretching of phenyl–silicon bond. A further effect is the changing in the region between  $2830$  and  $2970 \text{ cm}^{-1}$ ; these absorption bands are assigned to the aliphatic C–H symmetric and asymmetric stretching vibrations in the Si and Al alkoxides highlighting the presence of a large amount of unreacted species (methoxy and butoxy groups) in the unexposed film. The interaction with UV and soft X-ray promotes the hydrolysis reaction as confirmed by the increment of the -OH absorption band, centred at  $3400 \text{ cm}^{-1}$  with increasing dose and the decrease of the peaks related to the alkoxide groups, already at the minimal investigated doses. The overall outcome is the complete removal of the organic component with a progression in the cross-linking of the inorganic network [35] This is confirmed by the Si-O-Si ( $1100\text{--}1030 \text{ cm}^{-1}$ ) and Al-O-Al (broad band between  $1000$  and  $500 \text{ cm}^{-1}$ ) absorption visible in the spectrum of the alumina-based resist films after exposure. [36,37]

The densification of the film upon UV exposure is also confirmed by the increase of the refractive index of the film with increasing UV exposure doses (Figure 4.7). The PEB of 2 min at  $120^\circ\text{C}$  (that will be chosen as the best PEB during the lithographic process

optimization, see paragraph 4.3.1) further promotes the film densification (through condensation).

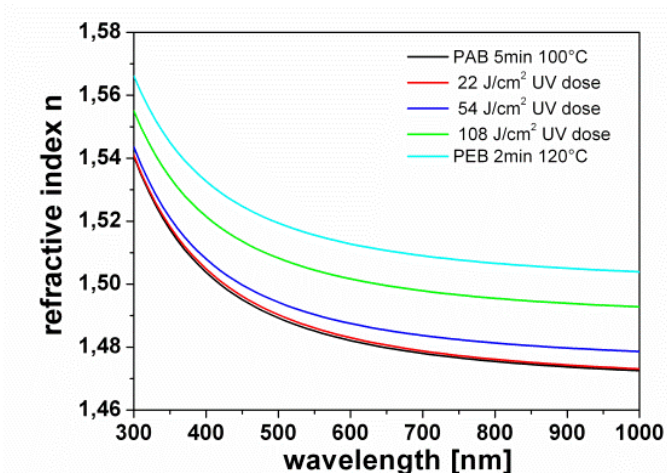


Figure 4.7 Refractive index of the alumina film after PAB of 5min at 100°C, increasing UV exposure doses and PEB of 2min at 120°C

### 4.3. UV lithography

Exploiting the effects of UV exposure on alumina-based films, i.e. the removal of the organic component with a progression in the cross-linking of an inorganic network, the use of UV light through a mask allows to directly pattern the sol-gel films. A peculiarity, not shared by any of the known commercial resist generally used as sacrificial layer and which may prove interesting for special applications, is that its formulation behaves either as a positive or as a negative tone resist depending on the solvent used for the development (Figure 4.8). This resist gives then the possibility of etching the silicon both obtaining the same structures or the negative of the UV mask (or X-ray mask).

The different behaviour depends on the developer chemistry, which are simply Buffered Oxide Etching (BOE) and Hydrochloric acid (1N) diluted 1:25 in volume in Isopropyl alcohol for the positive and negative tone, respectively. In fact the former is a good etchant for inorganic network and affects directly the exposed areas of the resist whereas the latter is active when the phenyl groups are present, as it is in the unexposed zones. The optimized dose has been determined to be around 30J/cm<sup>2</sup> and 108J/cm<sup>2</sup> for negative and positive tone respectively. It has to be pointed out that the entire process involves not only the exposure step of the resist but also a post application bake (PAB) of 5min at 100°C and a post exposure bake (PEB) of 2min at 120°C. The explanation of the choice of these parameters will be given in the next paragraph.



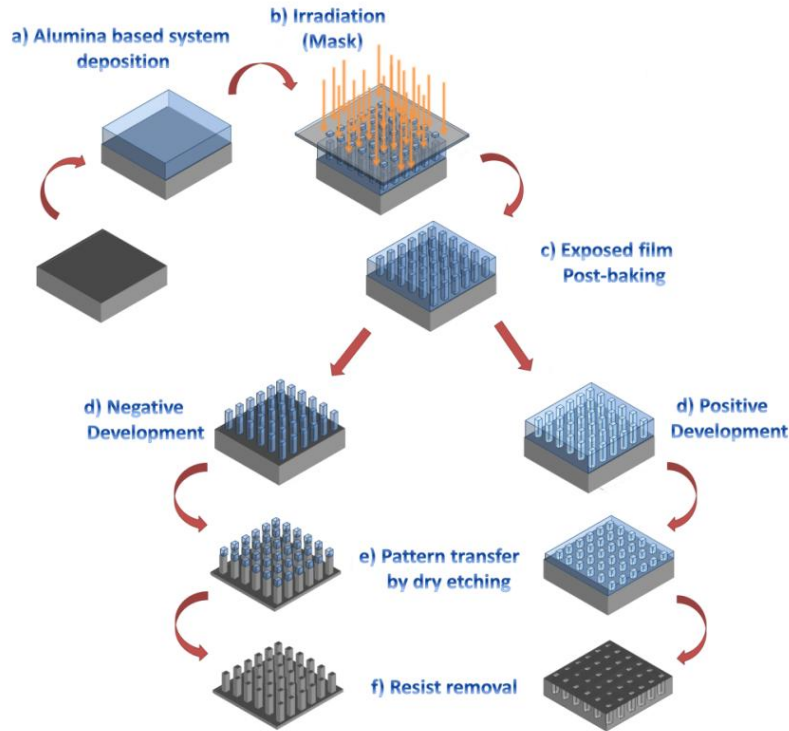


Figure 4.8 Scheme of the lithographic and pattern transfer processes using the alumina-based organic-inorganic hybrid system. After post-exposure annealing (c) the film can be developed either as a positive (right) or as a negative (left) tone resist (d) depending on the solvent used for the development.

The contrast curve, i.e. film thickness of the exposed and unexposed areas of the film for positive and negative tone respectively, normalized to initial thickness, as a function of UV dose, is reported in Figure 4.9. As already discussed, the higher the contrast  $\gamma$  the higher the pattern definition: as it was for the titania system, the negative tone shows a higher contrast even for alumina resist.

$$\gamma_N = \left( \log \left( \frac{d_o}{d_i} \right) \right)^{-1} = \left( \log \left( \frac{33.6}{21} \right) \right)^{-1} = 4.9$$

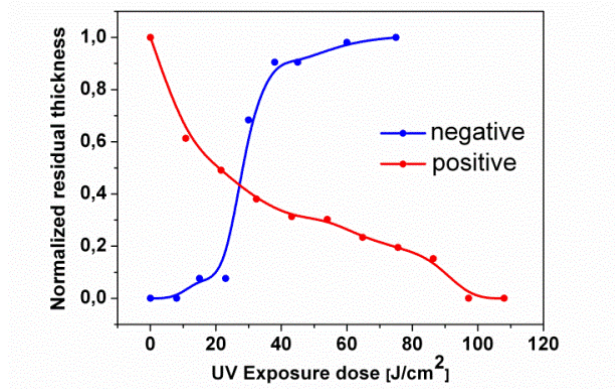


Figure 4.9 Contrast curve of the positive and negative alumina UV-resist tone



The obtained negative contrast is comparable with the one of commercial resists, whose typical contrasts are 2 to 5 for novolak- based positive resists and HSQ resist.

In Figure 4.10 optical images confirming the double tone behaviour of the resist are reported.

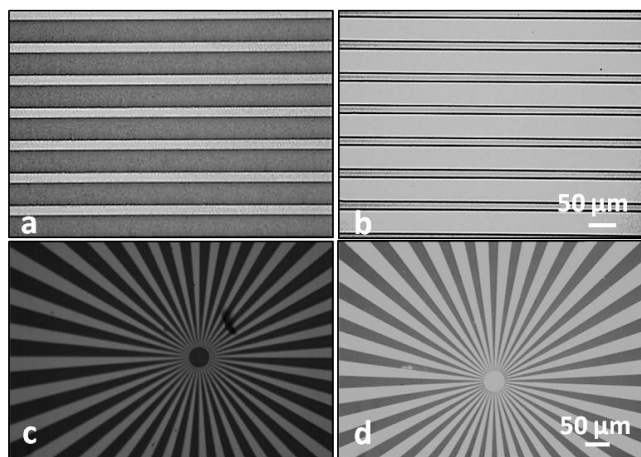


Figure 4.10 Optical images of positive (a,c) and negative (b,d) tone patterns obtained by UV lithography

The resist contrast is a function of the entire resist process, bake temperature and time, developer normality and time, adhesion between the hybrid film and the substrate, dry step, and not just the resist itself. In the next section an explanation of the chemical modification occurring during the entire optical lithography process is reported.

#### 4.3.1. Chemical modification of alumina system during lithographic process

The resistance to plasma etching of the alumina-based system is related to the degree of condensation achieved at the end of the patterning step and the chemical composition of the film. The upper limit would be set by a film of the same thickness fully composed of dense alumina. As already discussed, the presence of the organic component can be exploited as selection mechanism in the development of the pattern: the exposed part is expected to lose part of the organic content and proceed towards condensation of the inorganic component through hydrolysis. The different organic content of exposed/not exposed part is the reason why, taking the negative tone as example, an organic etcher, such as HCl, preferentially removes the parts of the film richer in organic moieties. In order to increase the contrast of the system, the difference in organic content between exposed and not exposed part needs then to be maximized.

To better understand the transformations of the alumina resist during the entire lithographic process, FTIR spectra of a 500nm sample film spin coated on silicon, after bake and exposure are reported in figure (Figure 4.11).

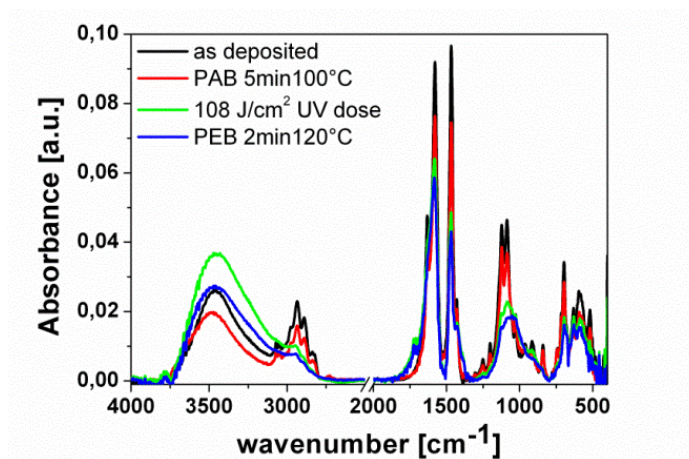


Figure 4.11 FTIR spectra of the alumina resist films after bake and exposure

The FTIR spectra of the as deposited film as already been discussed in paragraph 4.2.

*After the PAB* of 5min at 100°C all the peaks of the “as deposited” spectra decrease, mainly due to solvents evaporation. In particular the decrease of the –OH band at 3700-2800 cm<sup>-1</sup> could be ascribed to evaporation of the methoxyethanol, the solvent used for the synthesis.

*After the exposure* of the alumina film, as the absorption of the aliphatic C-H symmetric and asymmetric stretching (2830 ÷ 2970 cm<sup>-1</sup>) and of the Si-OCH<sub>3</sub> (2830-1200 cm<sup>-1</sup> and between 1200-1000 cm<sup>-1</sup>) decreases, the OH absorption band centred at 3400 cm<sup>-1</sup> increases, confirming the promotion of hydrolysis reactions of the residual alkoxide groups of the films. The aromatic rings in the phenyl silica precursor are degraded with UV exposure since the peaks at 3070-3040 cm<sup>-1</sup> due to the aromatic C-H stretching vibration and at 1120-740-713-700 cm<sup>-1</sup> ascribed to the stretching of phenyl-silicon bond are no more detectable in the exposed films. The absorption between 1300 and 1000 cm<sup>-1</sup> decrease due to the degradation of the Si-phenyl bond as well, and the absorption of the Si-O-Si (1080-1028 cm<sup>-1</sup>) and Al-O-Al (1060 cm<sup>-1</sup> peak) is still and more clearly detectable, confirming the inorganic condensation.

*The post exposure bake* is then necessary to further promote the condensation reaction of the inorganic network since the OH band of the hydrolyzed alkoxides decreases after bake. The post exposure bake is a key step of the process since the condensation process is also promoted by heat treatment, depending on both temperature and time of application. Thus, we

studied more deeply by IR spectroscopy the variations of chemical composition of the system during different post exposure bake temperatures, in order to optimize the baking conditions in this respect and understand which bake would have brought to obtain the best contrast of the resist.

Samples were prepared by spin coating the alumina-based resist on bare silicon and applying a pre-bake for 5 min at 100 °C degrees. This first step was maintained unaltered for the all the experimental studies. The effects generated by post-exposure bake were studied in 6 conditions changing the PEB temperature: 100-120-140-160-180-200 °C. Half of each sample was exposed to UV at an energy dose of 30 J/cm<sup>2</sup>, the optimized dose for the negative tone process. IR spectra were then collected on half-exposed samples (1x1 cm<sup>2</sup>) before and after PEB applied (Figure 4.12). The bold lines referred to the post exposure treated samples (blue to the unexposed, red to the exposed) while the more transparent ones to the same samples without PEB (same colours). If we look at the spectra collected, we can see that peaks of Al and Si alkoxides (2830-2970 cm<sup>-1</sup>) diminish also at the lower temperature of 100 °C, highlighting that even a mild post exposure bake promotes hydrolysis of the precursors in the unexposed part and condensation (hydrolysis was already produced by exposure) in the exposed one (see the opposite behaviour of the -OH broad band at 3600-3000 cm<sup>-1</sup>). The greater difference between unexposed and exposed areas is registered for 120 °C, where the difference between bold blue and red line is more evident and inorganic network condensation, through hydrolysis, in the exposed areas is more effective. At higher temperature, from 140 °C and above, this mechanism is induced also in unexposed areas: the two bold blue and red lines show the same trend and at 160°C alkoxides are no more detectable (2830-2970 cm<sup>-1</sup>) while the Al-O-Al and Si-O-Si absorption is more evident even in the unexposed part. A small evaporation of acetic acid (peaks in the range 1400-1700 cm<sup>-1</sup>), whose boiling point is 118°C, is recorded at lower temperatures (100 and 120 °C), while higher temperatures are effective for the evaporation of all the organic component. Nevertheless, the behaviour in this part of the spectra follow the same trends, both in unexposed and exposed areas, thus it is not a mechanism to be exploited for increasing the chemical differences between the two areas.

Phenyl peaks (3070 e 3040 cm<sup>-1</sup>) seem to be at most only slightly affected by PEB conditions. The overall trends emerging from our FTIR study is, nevertheless, that in the experimental conditions, phenyl groups follow the same behaviour both in exposed and un-exposed areas

after PEB, while alkoxides hydrolysis and condensation show a viable selecting mechanism with different applied temperatures.

In conclusion, the exploitation of hydrolysis as the main mechanism for inorganic condensation, which brings to a chemical difference between exposed and un-exposed areas, is better achieved for 120 °C PEB treatment.

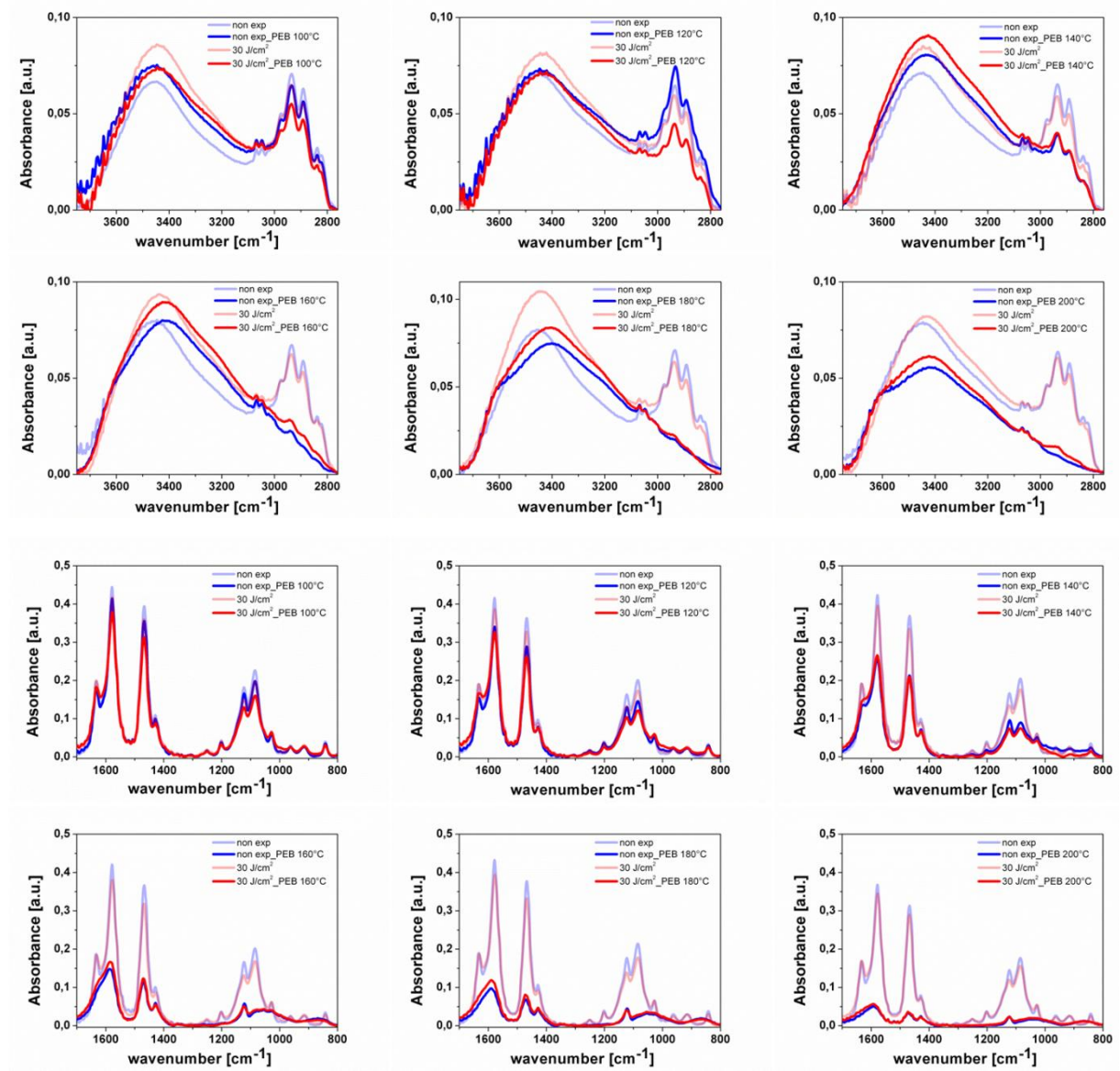


Figure 4.12 Study of the optimized post exposure bake temperature: FTIR spectra of alumina-based resist on Si after pre-bake of 5' at 100 °C (“non exp”) and after exposure to UV light (“30 J/cm<sup>2</sup>”), compared with the same samples before and after post exposure bakes at different temperatures (between 100 and 200°C)

#### 4.3.2. Chemical understanding of the double tone processes of alumina system

The explanation of the double tone behaviour of the resist in different developer solution could be found in the FTIR spectra reported in Figure 4.13.

The samples were prepared by spin coating the alumina-based resist on silicon and exposing half part of them, following the procedure for the positive and negative tone process. The FTIR spectra of the samples was collected in the exposed and unexposed areas before and after partial development in BOE (positive tone, blue lines) and diluted HCl (negative tone, red lines), in order to better understand which are the mechanisms that lead to the different behaviour and the resist components that are leached during development.

The BOE solution used for positive development removes most of the inorganic (silica+alumina) exposed areas of the films: peaks around  $1100\text{-}1000\text{ cm}^{-1}$  related to silica network decrease, according to the well-known fact that BOE is a wet etchant for silica. However BOE also acts as an etcher for the organic components of the film different from the aromatic rings, which are mainly present in the unexposed parts linked to the partially reacted silica precursor: all the peaks related to the aliphatic component of the unexposed areas decrease. The BOE solution acts then in the irradiated areas both for the presence of silica network as well as for the absence of phenyl compounds. This behaviour also explains the low contrast observed for the positive tone of the resist: the BOE doesn't act only in the exposed areas even if it displays a different behaviour in the exposed and unexposed areas.

In the case of negative development (diluted HCl) the exposed part spectra doesn't change during development, which confirms the best contrast of the negative tone, while all the organic peaks included the ones related to the phenyls decrease in the unexposed areas. In conclusion the different tone behaviour is related to the selective removal of either the inorganic network as well as to the presence/absence of the phenyl groups.

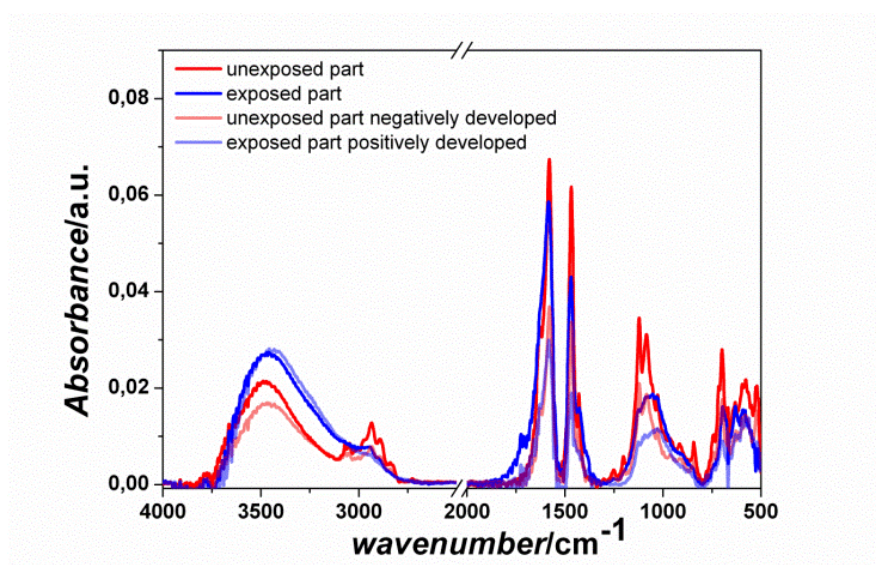


Figure 4.13 FTIR spectra of the exposed and unexposed areas of the resist before and after development in diluted BOE or HCl solution for negative and positive tone respectively.



#### 4.4. X-rays lithography

As reported in paragraph 4.2.3, exposure to X-ray has approximately the same chemical effects as UV light on alumina-resist: the cross-linking of an inorganic network increases with X-ray exposure while the organic content diminishes. In the investigated energy range, doses of  $9 \text{ J/cm}^2$  result in the full degradation of whole organic part, thus giving an approximate evaluation of the correct dose for X-ray lithography. Even in the case of X-ray lithography, the structural and chemical difference between exposed and unexposed areas of the film led to the possibility of pattern the resist both positively and negatively, as demonstrated by SEM images of Figure 4.14. The changing parameter of the process is again the development: MF319 diluted 1:10 in DI H<sub>2</sub>O and HCl 1N diluted 1:25 in DI H<sub>2</sub>O for positive and negative tone, respectively [38].

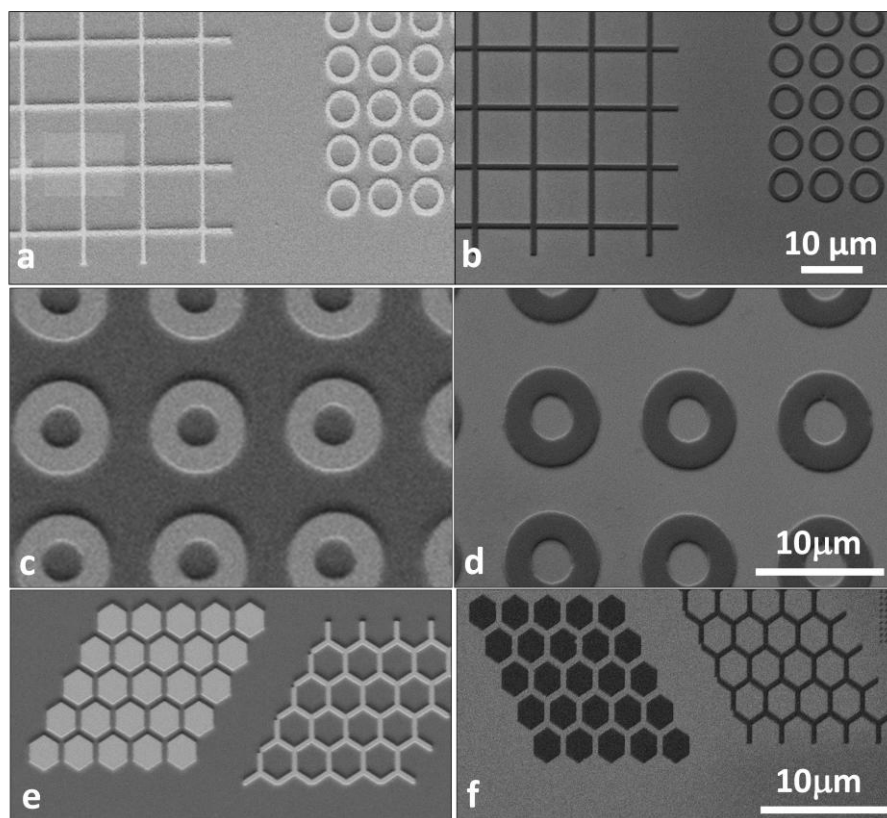


Figure 4.14 Positive (a, c, e) and negative (b, d, f) patterns of the mask obtained by X-ray lithography

In the case of negative tone, the best exposure dose arisen from FTIR results was also confirmed by the obtained contrast curve, shown in Figure 4.15: the residual thickness of the alumina resist after development (normalized to 30 nm) is presented as a function of the applied exposure dose. Samples of 200 nm thickness (spin coated from a 30g/l solution at

4000rpm for 30s) exposed to dose of  $9 \text{ J/cm}^2$  were developed in HCl 0.025 N for a total time of 5 min; the samples were then rinsed in DI water and dried in nitrogen stream.

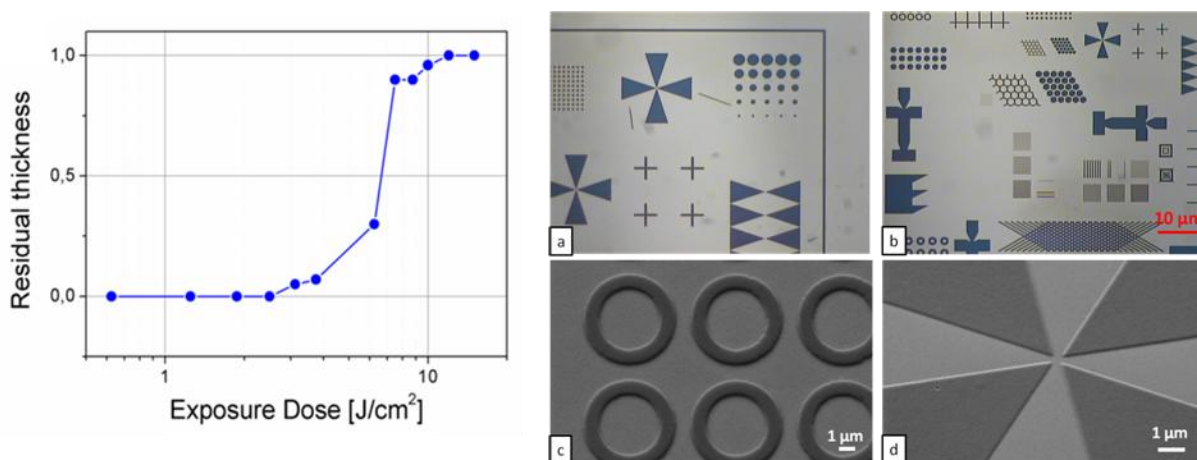


Figure 4.15 Contrast curve of the negative alumina resist used for X-ray lithography; on the right: 100x (a) and 50x (b) optical microscope images of the XRL results achieved exposing the films to  $10 \text{ J/cm}^2$  dose and developed for 5 minutes; SEM images of the same samples (c,d)

Figure 4.15a and b shows some optical images of the lithographed structures. Examples of the same structures investigated by SEM are reported in Figure 4.15c and d.

Patterns with sub-micron resolution were successfully obtained. SEM inspection (Figure 4.16) of the features in comparison with the used mask showed very good agreement of CD.

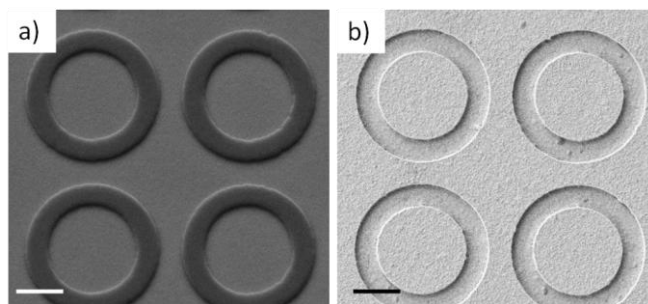


Figure 4.16 a) features obtained in the alumina resist after exposure at  $9 \text{ J/cm}^2$  and development; b) image of the same features as in a), on the used mask for X-ray lithography. Scale bars are  $2 \mu\text{m}$  wide.

### 4.5. EBL

In order to explore the ultimate resolution capability of the alumina system EB lithography was performed and EBL parameters were optimized, taking advantage of knowledge achieved with optical and X-rays lithography.

#### 4.5.1. First lithographic results

First EBL experiments on 200 nm thick films were conducted with an acceleration voltage of 30 keV and energy doses ranging from 100 to 1500  $\mu\text{C}/\text{cm}^2$ , with a current of 20 pA and a pixel size of 5 nm. The deposited film was first treated for 5 min at 100 °C before exposure. The pattern was generated with the Elphy Quantum CAD tool and written by an Elphy pattern generator. Examples of dose matrixes are reported in Figure 4.17.

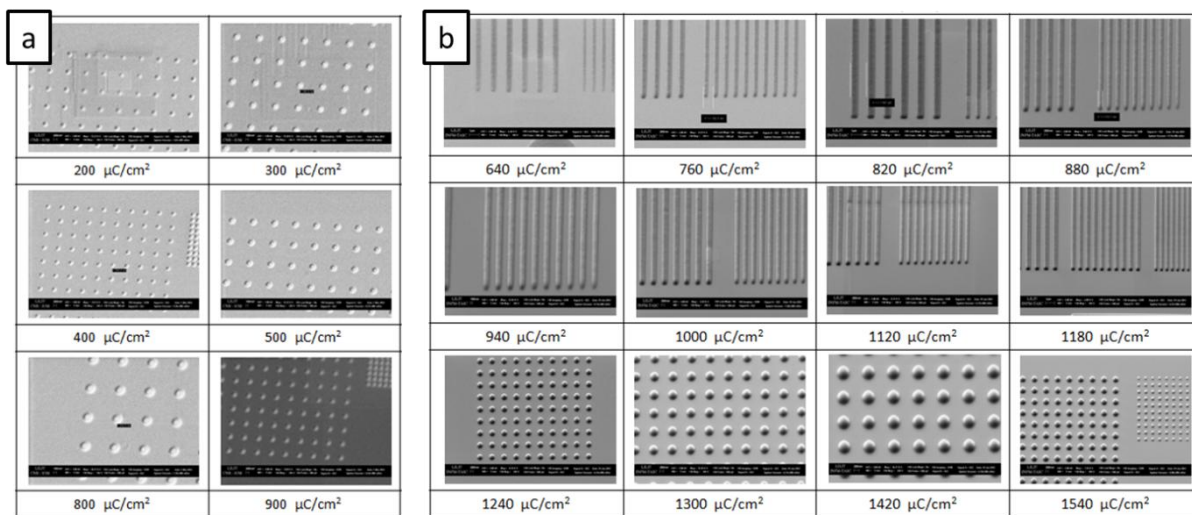


Figure 4.17 Positive and negative tone dose matrix after EBL with electron beam at acceleration voltage of 30 keV

Even after exposure to electron beam the resist exhibits a double tone behaviour (Figure 4.18) if the suitable development is used. The best results were obtained with an exposure dose of 600-800  $\mu\text{C}/\text{cm}^2$ , and developing the system in HCl 1N diluted 1:30 in IPA and BOE diluted 1:20 in DI H<sub>2</sub>O, for negative and positive tone respectively.

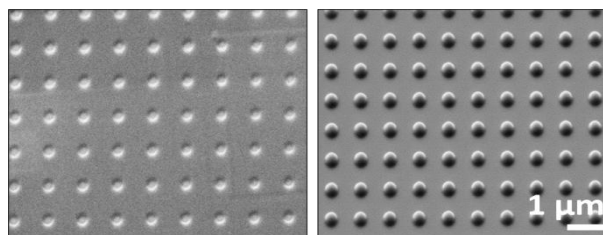


Figure 4.18 Positive (left) and negative (right) patterns obtained on alumina resist with EBL at acceleration voltage of 30keV



Optimization of the EBL process was carried out together with optical lithography improvements, confirming the results already discussed for the UV lithography: PEB was again found to increase the chemical selectivity for the developing step, examples are reported in Figure 4.19. Applying a PEB of 120°C instead of 100°C allows obtaining features with better resolution and edges.

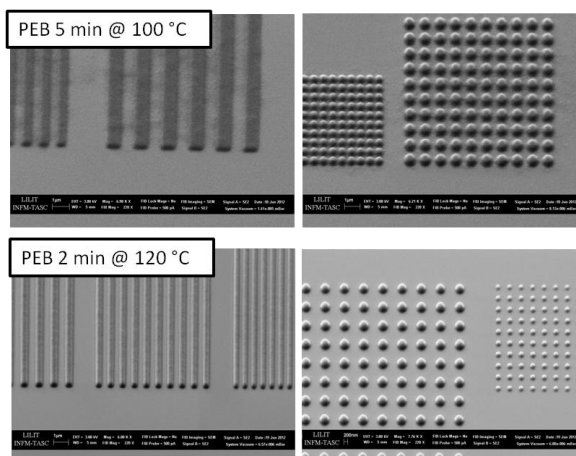


Figure 4.19 Example of optimization of the process: PEB at 120°C allows to obtain the best contrast when the resist is exposed to electron beam

#### 4.5.2. *Casino*® simulations

In order to find out the ultimate resolution of the resist, *Casino*® simulations were used to evaluate the expected performances of the new resist depending on film thickness and acceleration energy for the electrons. The CASINO acronym has been derived from the words "monte CARlo SIMulation of electroN trajectory in sOLids". It is a Monte Carlo simulation program of electron trajectory in solid specially designed for low beam interaction in a bulk and thin foil. It is specifically designed for low energy beam interaction and can be used to generate many of the recorded signals (X-rays and backscattered electrons) in a scanning electron microscope.

Interaction between incoming electron beam and alumina resist was simulated using the following materials atomic composition: Al 12%, Si 3%, C 33%, H 33%, O 19%.

Since the new sol-gel studied was intended to work as EBL resist for pattern transfer processes, with possible applications in the generation of high aspect ratio, high resolution NIL masters, our primary interest was to test the performances of the material when used on bulk silicon substrate.

Therefore, a sol-gel layer of 200 nm thickness on silicon substrate, obtained by spin-coating at 4000 rpm an alumina system with 30 g/l solid concentration, was firstly simulated. These are also the usual conditions used for X-ray lithography (see paragraph 4.4), and the thickness used for the first EB exposure (see paragraph 4.5.1).

In Figure 4.20 the resulting spatial distributions of absorbed energy (the best conditions of Casino®) are reported, for energy of the impinging electron beam ranging from 5 to 30 keV, step 5 keV.

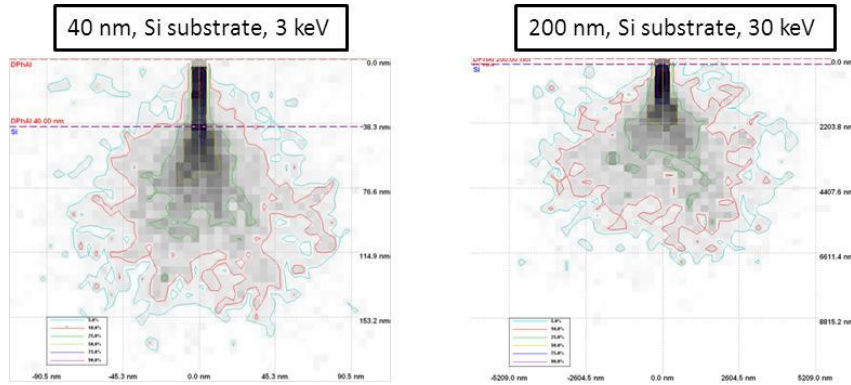


Figure 4.20 Casino® simulations on 40 nm and 200 nm alumina film coated on Si substrate (i.e. a normal wafer) for energy of the impinging electron beam ranging from 3 to 30 keV

Alumina film thickness and used substrate		
	40nm	200nm
E [keV]	silicon	silicon
1	NA	/
2	NA	/
3	13	/
4	19	/
5	27	NA
10	/	98
15	/	158
20	/	270
25	/	540
30	/	520

Table 4.2 Evaluation of line resolution of 40 nm and 200 nm alumina film coated on Si substrate (i.e. a normal wafer) for energy of the impinging electron beam ranging from 1 to 30 keV

In order to compare the simulated results, the line resolution has been evaluated (Table 4.2). This has been determined by the part of the resist volume where 50% of the energy is

absorbed, that is line-contour on the graphs in Figure 4.20 yellow in colour. The selection of one specific boundary in the volume of the system has to be accounted to the selectivity of the applied development step. In other words, chemical etching mechanism and variations of the chemical constitution of the system induced by exposure and PEB determine the contrast achievable by a specific development recipe. As a first evaluation, we started with the hypothesis that we would be able to select from regions where 50% of energy is absorbed and volume where this value is lower.

For a sol-gel thickness of 200 nm initially simulated, the best resolution achievable (around 100nm)) would have been obtained with energy of 10 keV. Lower beam energies, would not allow to expose completely the resist, while energies higher than 30 keV could be expected to provide increasing resolution. However, since our EBL system is not able to work at higher energies than 30 keV, this direction was not further explored. On the other hand, using a thin film of 40 nm the best expected resolution was in the range 10-20 nm achievable, according to our simulations, with 3-4 keV beam energy.

### 4.5.3. *Optimized lithographic results*

Samples for lithography were prepared according to the protocol optimized with FTIR measurements for UV and X-ray lithography, assuming that EBL would have produced the same results. In fact, micro-FTIR was also carried out but no changes in the film response were detected, probably due to the low signal.

As previously reported, the results of the simulations show how the highest resolution on silicon substrate would be achievable by using a thin film, while for UV and X-rays lithography we always used thicker films. Further proof of the validity of software simulations can be found in Figure 4.21 where a 200 nm thick film was exposed to EB at 5keV acceleration voltage: the proximity is too high and so not good edges could be achieved.

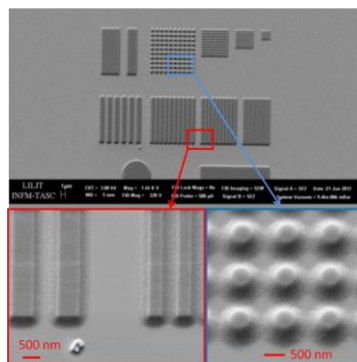


Figure 4.21 EBL on 200nm thick alumina film with an EB at 5keV acceleration voltage

The request for lower solid concentration in the starting solution poses a new question about the quality of the film after spin coating. To obtain film as thin as 30-40 nm, we used a solution diluted to 10 g/l. Spin coating at 4000 rpm in a normal clean room environment (i.e. with RH content of 50-60 %) produced films affected by pits with a mean size of ~190 nm, calculated as the mean size over 110 measures, see Figure 4.22a). This pits introduced unacceptable discontinuity in the patterned structures (Figure 4.22b). In thicker films, they would possibly still affect the quality of the film, but in most cases without generating totally uncovered substrate's areas. We found that a solution to this problem was to perform the spin coating on a glove box with very low humidity content, as shown in Figure 4.22c and Figure 4.22d. The obtained film shows a much smaller pits formation, with mean size  $\ll$  100 nm and practically never exposing the underneath substrate. The better quality of the film is clearly discernible in the obtained pattern (Figure 4.22d).

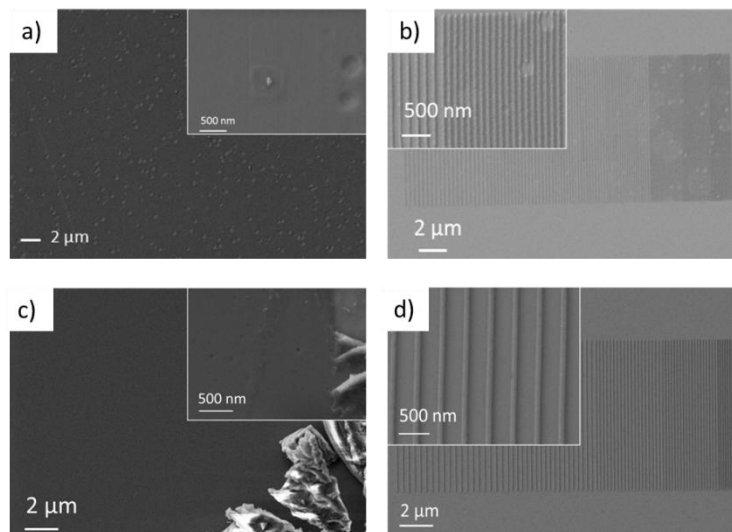


Figure 4.22 Pits formation on 40 nm film (solution of 10g/l) spin coated at 4000 rpm in a normal clean room environment (i.e. with RH content of 50-60 %) (a, b), and spin coating on a glove box with very low humidity content (c, d)

The set of simulation performed with Casino® software suggest that we could achieve the best resolution working with a beam acceleration of 3 keV. We concentrated thus in optimizing the EBL step in this conditions, and after a dose matrix experiment, we could get our best results with a dose of 200-250  $\mu\text{C}/\text{cm}^2$ . After exposure, a PEB of 2min at 120°C on a hotplate was necessary to improve the contrast and the development was done in HCl 1N diluted in IPA at 1:100 ratio. Developer and IPA rinser were maintained at 4 °C during the process. Finally the films were dried with nitrogen blow. It has to be pointed out that the EBL was optimized at the ultimate resolution only with the negative tone, since experimental

evidences showed that the negative process presented the higher contrast (as it was for UVL and XRL).

Lines with different resolution and pitch were obtained, but still proximity effects limited the pattern density achievable: for resolution down to 50 nm, gratings with 50% duty cycle were possible, while for the 20 nm lines it was not possible to get better than 20% duty cycle (i.e. lines with 20 nm width and 100 nm pitch). Examples of these results are shown in Figure 4.23.

With the optimized parameters (EB acceleration voltage and post-bake conditions) features down to 10 nm were achieved; Even if with commercial resists (i.e HSQ) the achievable resolution is below 10 nm the combination of outstanding selectivity and resolution remains a distinctive feature of the presented material.

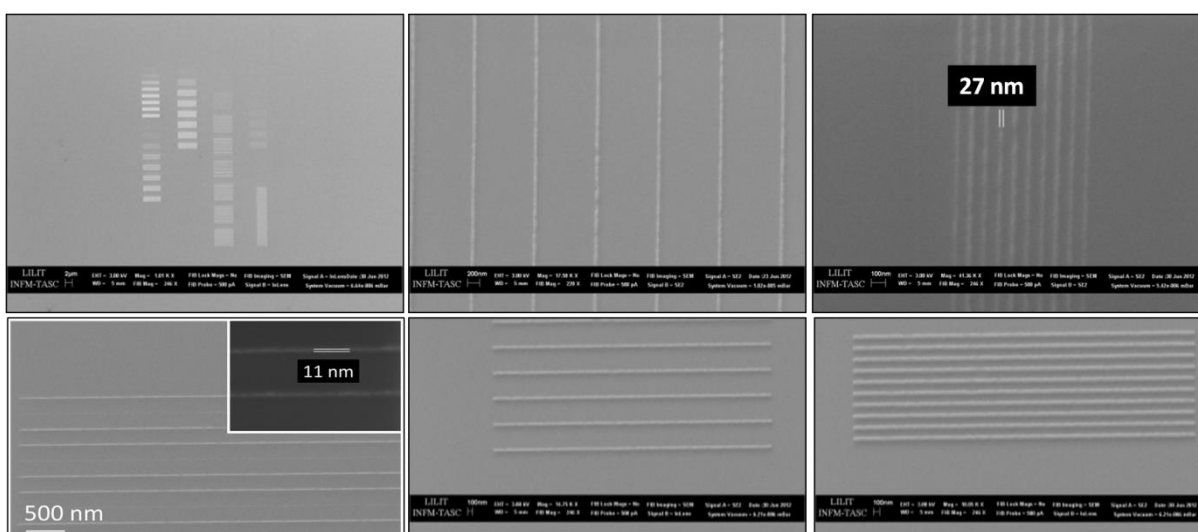


Figure 4.23 Lines down to ~10 nm width with different pitches successfully written by EB in 40 nm thick alumina film on silicon

#### 4.6. Nanoimprint lithography

Proofs of the possibility of using this alumina system as a NIL resist are here reported, though the process hasn't been completely optimized yet. The underlying idea was to further decrease the patterning steps, and all the problems related to the wet development, and the overall cost of the process, still guaranteeing good structures resolutions. Imprinting tests were performed with a hot press (P/O Weber). After first process optimization experiments, it was possible to imprint the material with low residual layer (up to 30 nm) at room temperature (21 °C) for 5 minutes applying a pressure of 500 bar (Figure 4.24).

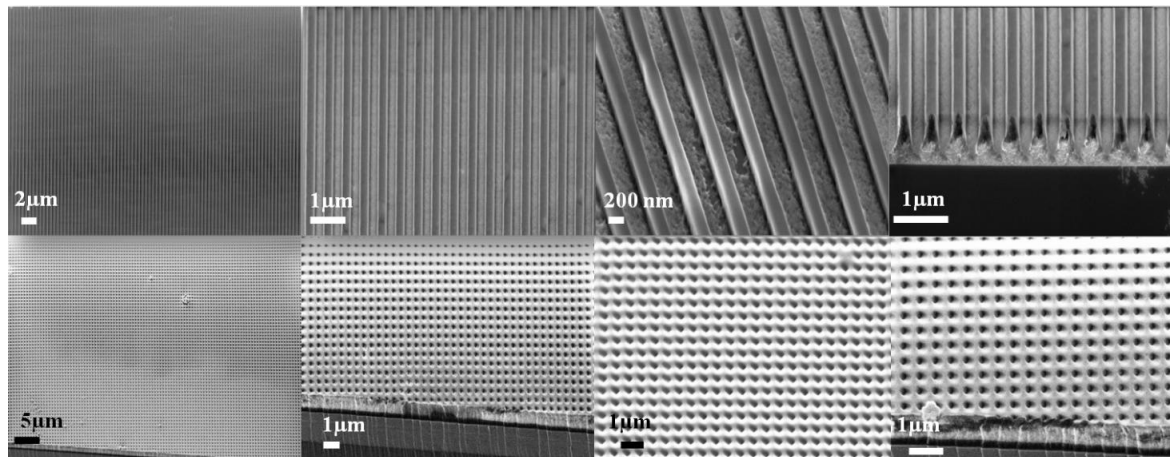


Figure 4.24 Lines and holes down to 200 nm obtained with NIL

#### 4.7. Etching resistance tests

The technological interest of such resist is due to the extremely high selectivity shown by alumina (with respect to silicon) in fluorine-based dry etching processes. In fact, as already reported in the introduction of the chapter, alumina has many advantages over commercial resists: in fluorine-containing plasmas leads to the formation of non-volatile compounds ( $\text{AlF}_3$  for instance sublimates at ca. 1250 °C) and therefore etch extremely slowly, and is easily removable by wet etching after pattern transfer. The great achievement, with respect to metallic mask or other hard intermediate mask that need other resists and complicate lithographic processes in order to be patterned, was that this alumina resist can be directly patterned. The obtained lithographed structures were in fact directly used as hard etch-mask in a pattern transfer processes in Si substrate (Figure 4.25) in an ICP dry etcher reactor (SPTS Technologies, Newport UK) with fluorine-based chemistry.

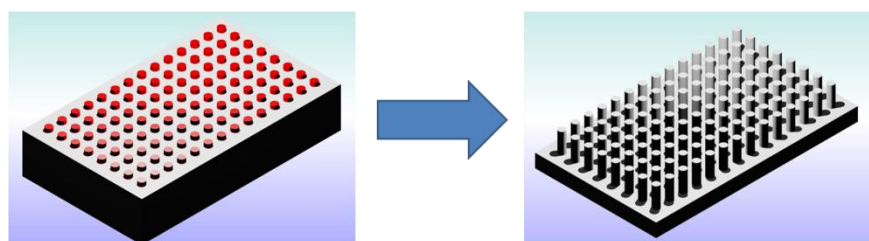


Figure 4.25 Pattern transfer on silicon using alumina structures as etching mask

The continuous etching process was obtained with 400 W RF power applied to the coil and 20 W applied to the platen, a plasma generated with the mixture of  $\text{SF}_6$ ,  $\text{C}_4\text{F}_8$  and Ar (un-

switched) gases with flux of 60, 30, 10 sccm, respectively, at a pressure of 8.0 mT, with a resulting bias of 90 V (Table 4.3). The overall etching process was finally concluded with a 10-15s of oxygen process for 10s as the one reported in Table 4.4.

<b>Coil</b>	Platen	Pressure	SF <sub>6</sub>	C <sub>4</sub> F <sub>8</sub>	Ar	Bias	Etch Rate
<b>Power (W)</b>	Power (W)	(mT)	(sccm)	(sccm)	(sccm)	(V)	nm(sec)
<b>400</b>	20	8	30	60	10	95	≈ 3

Table 4.3 ICP process used for the etching of silicon

This process was developed in TASC laboratory in Trieste as a standard anisotropic process for silicon etching, with a resulting etching rate of 170 nm/min [<sup>39</sup>]. With these process parameters, the etch rate of alumina was 2.67 nm/min.

It has to be pointed out that in the case of NIL structures the residual layer was previously removed with an oxygen process able to take away the organic part of the resist and then an Argon process in charge of removing the inorganic one.

<b>Gas</b>	Coil	Platen	Pressure	Flow	Bias	time (sec)
	Power (W)	Power (W)	(mT)	(sccm)	(V)	
<b>O<sub>2</sub></b>	200	10	4	40	38	30
<b>Ar</b>	400	30	4	30	40	30

Table 4.4 Plasma process for removing the residual layer in the NIL structures.

Sub-micrometer resolution features structures were etched down to a depth of 3 μm (depending only on the time of the etching process), with only 30 nm thick resist masks, resulting in a selectivity of 100:1. Examples of the structures obtained using UV, X-ray, EB and NIL patterns as etching masks for silicon are shown in Figure 4.26.

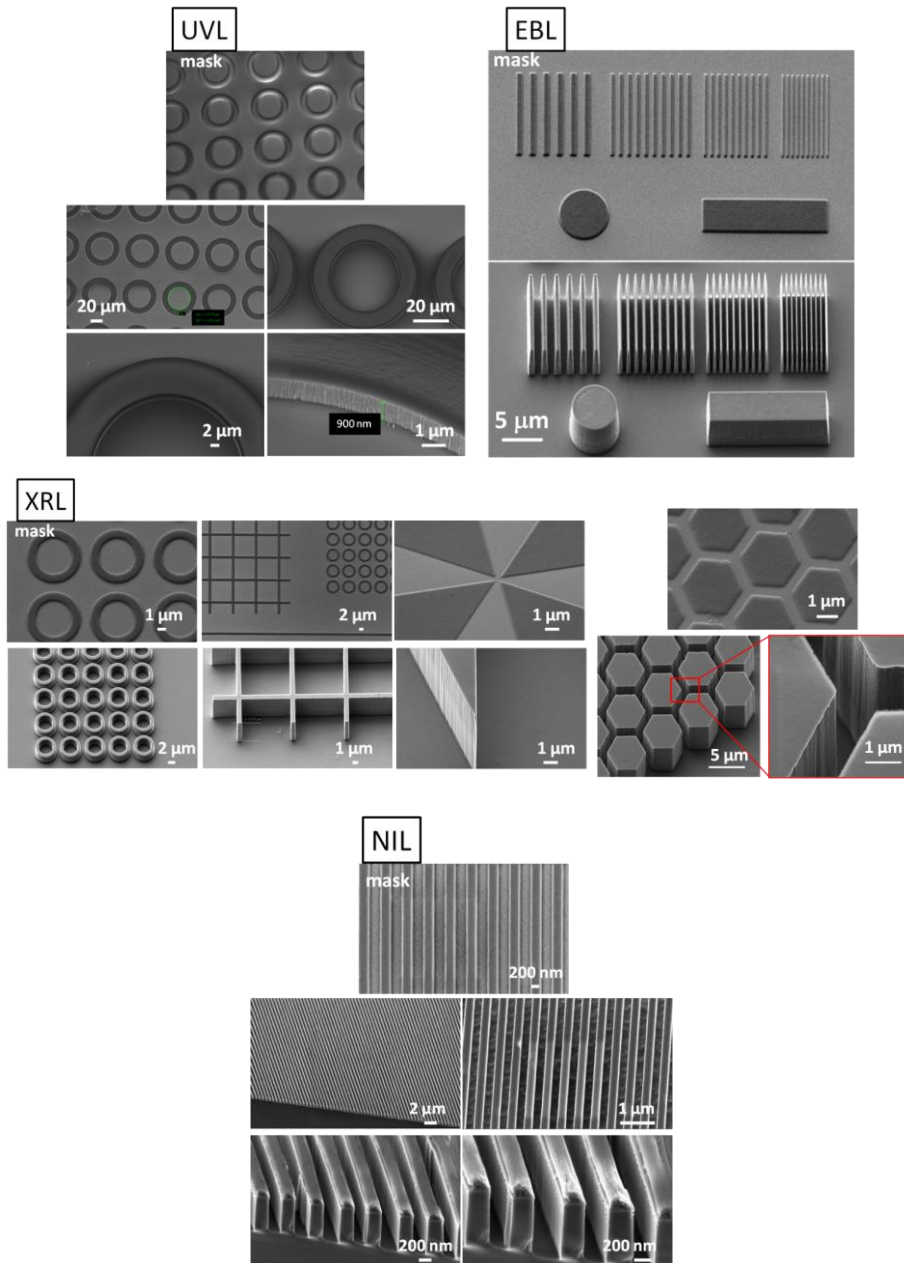


Figure 4.26 UV, EBL, XRL, NIL alumina patterns used as etching mask for silicon (the upper part correspond to the mask, the lower part to the etched silicon structures using the same mask)

Figure 4.27 demonstrates that the negative tone of the resist is more effective for obtaining a good hard mask for etching: this is mainly due to the higher condensation degree of the exposed parts of the resist with respect to unexposed ones as well to the higher contrast of the negative process. Lower contrast result in “silicon grass” formation due part of the resist remained in the exposed parts that were supposed to be leached away during positive development.



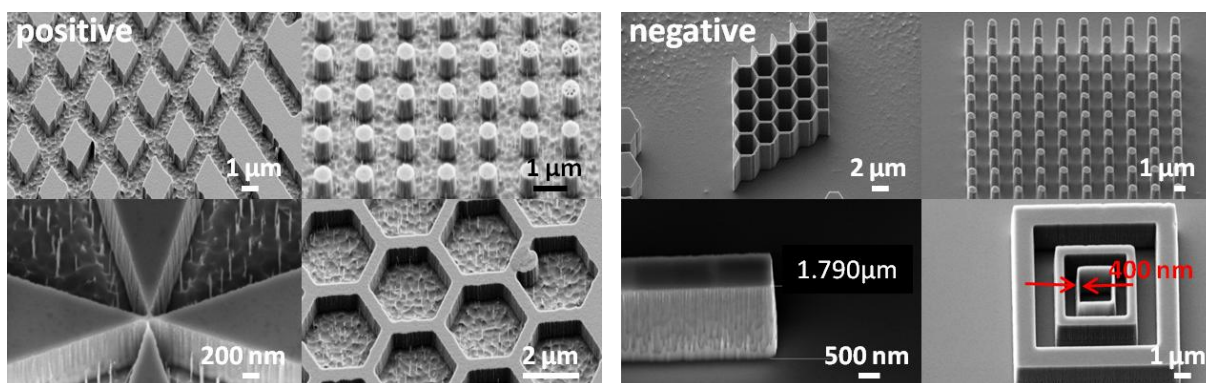


Figure 4.27 Silicon etched structures obtained with the positive and negative tone of alumina resist

As previously demonstrated, the ultimate achievable resolution can be obtained by electron beam lithography (EBL). The same etching process applied for the 40 nm resist layer and high resolution pattern, allowed us to produce line gratings with a thickness of 200-240 nm, reaching an aspect ratio for the highest resolution of about 10. Given the dimension of the starting structures, under-etching and local erosion of the mask produced by heavy ions (like Ar) starting from the edges is to be accounted, thus higher performances couldn't be achieved, even if the chemical composition of the resist and the resistance of alumina-like compound subjected to fluorine-based plasma would suggest otherwise.

In Figure 4.28 SEM images of the obtained high resolution structures after the plasma etching are reported.

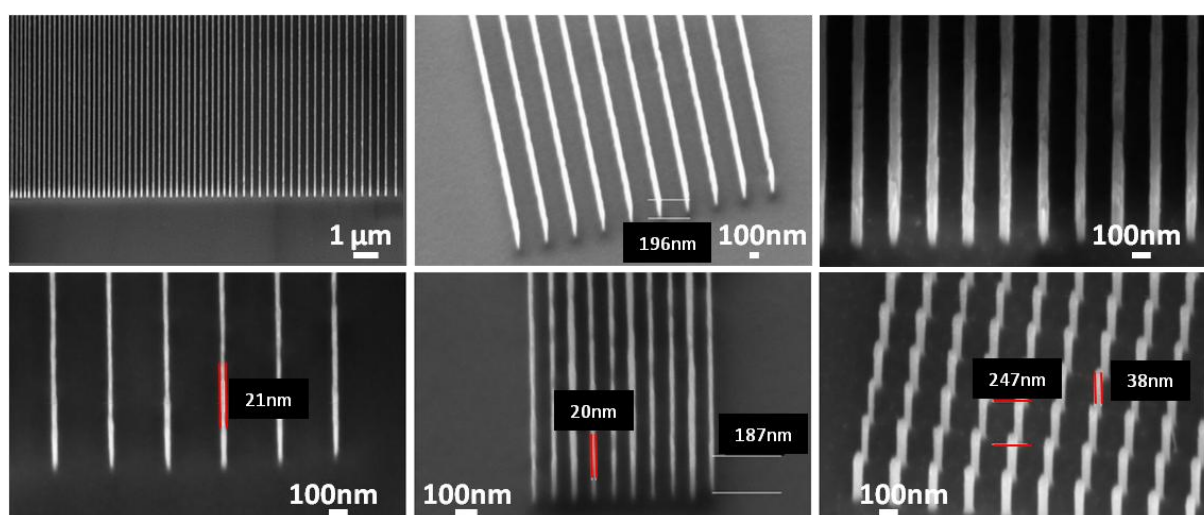


Figure 4.28 SEM images of etched silicon structures using EBL alumina mask with the ultimate resolution achievable

In conclusion, this new spin on metal-organic resist is then unique since it presents a combination of worthwhile properties: a simple processability typical of polymeric resists,

direct patternability with various radiations (UV, X-rays or EB) and NIL, mild post-exposure treatment requirement, positive or negative tone development and outstanding selectivity during etching of silicon. In particular, silicon nanostructures could be etched in a fluorine based non cryo-cooled continuous plasma etching process ICP with selectivity exceeding 100:1 with respect to the resist and deliberately avoiding the use of techniques such as the Bosch process or cryogenic plasma etching. In the same etching conditions HSQ hard masks present a selectivity up to 6:1, while this measured outstanding selectivity of 100:1, herein reported, is comparable with the selectivity achievable with metallic masks, yet avoiding the steps, cost and risk of vacuum deposition of metal and subsequent lift-off in organic solvents. [<sup>40</sup>] Furthermore, for the present sol formulation, no high-temperature annealing step was required, as generally used in other protocols, to obtain a completely inorganic etch resistant patterns.

## References

- <sup>1</sup> G. Nakagawa, K. Miura, M. Makiuchi, M. Yano, *Opt. Eng.* **1994**, 33, 3547.
- <sup>2</sup> J. Lee, D. Lee, Y. Baek, *Opt. Commun.* **2013**, 289, 69.
- <sup>3</sup> Ü. Sökmen, M. Balke, A. Stranz, S. Fündling, E. Peiner, H.-H. Wehmann, A. Waag, *Proc. SPIE*, **2009**, 7362, 736213.
- <sup>4</sup> Ü. Sökmen, A. Stranz, S. Fündling, S. Merzsch, R. Neumann, H.-H. Wehmann, E. Peiner, A. Waag, *Microsyst. Technol.* **2010**, 16, 863.
- <sup>5</sup> M. J. Walker, in *Proc. SPIE*, **2001**, 4407, 89.
- <sup>6</sup> Z. Liu, Y. Wu, B. Harteneck, D. Olynick, *Nanotechnology* **2013**, 24, 015305.
- <sup>7</sup> M. Serry, M. Ibrahim, S. Sedky, 2012 IEEE 25th International Conference on Micro Electro Mechanical Systems (MEMS) **2012**, 321.
- <sup>8</sup> Semiconductor Technologies, InTech, ed. by Jan Grym, **2010**.
- <sup>9</sup> K.-M Lim, S. Gupta, C. Ropp, E. Waks, *Microelectron. Eng.* **2011**, 88, 994.
- <sup>10</sup> B. Y. Zong, P. Ho, G. C. Han, G. M. Chow, J. S. Chen, *J. Micromech. Microeng.* **2013**, 23, 035038.
- <sup>11</sup> Y. Kanamori, K. Hane, H. Sai, H. Yugami, *Appl. Phys. Lett.* **2001**, 78 (2), 142–143.
- <sup>12</sup> D. Crouse, Y.H. Lo, A. E. Miller, and M. Crouse, *Appl. Phys. Lett.* **2000**, 76 (1), 49–51.
- <sup>13</sup> A. N. Belov, *Semiconductors* **2008**, 42 (13), 1519–1521.
- <sup>14</sup> A. N. Belov, Yu. A. Demidov, M. G. Putrya, A. A. Golishnikov, A. A. Vasilyev, *Semiconductors* **2009**, 43 (13), 1660–1662.
- <sup>15</sup> A. N. Belov, S. A. Gavrilov, Yu. A. Demidov, V. I. Shevyakov, *Nanotechnologies In Russia* **2011**, 6, 11–12.
- <sup>16</sup> V. Gianneta, A. Olziersky, A. G. Nassiopoulou, *Nanoscale Research Letters* **2013**, 8:71.
- <sup>17</sup> M. D. Henry, S. Walavalkar, A. Homyk, A. Scherer, *Nanotechnology* **2009**, 20, 255305.
- <sup>18</sup> A. Kravchenko, A. Shevchenko, V. Ovchinnikov, A. Priimagi, M. Kaivola, *Adv. Mater.* **2011**, 23, 4174.
- <sup>19</sup> A. Frommhold, J. Manyam, R.E. Palmer, A.P.G. Robinson, *Microelectron. Eng.* **2012**, 98, 552.
- <sup>20</sup> Y. Tseng, A. U. Mane, J. W. Elam, S. B. Darling, *Adv. Mater.* **2012**, 24, 2608.
- <sup>21</sup> Z. Cui, *Micro-Nanofabrication Technologies and Applications*, Higher Education Press, Springer, **2005**.

- <sup>22</sup> B. Zong, G. Han, Y. Zheng, L. An, T. Liu, K. Li, J. Qiu, Z. Guo, P. Luo, H. Wang, B. Liu, *Adv. Funct. Mater.* **2009**, 19, 1437.
- <sup>23</sup> G. Brusatin, G. Della Giustina, F. Romanato, M. Guglielmi, *Nanotechnology* **2008**, 19, 175306.
- <sup>24</sup> G. Brusatin, G. Della Giustina, *J. Sol-Gel Sci. Technol.* **2011**, 60, 299.
- <sup>25</sup> E. Zanchetta, V. Auzelyte, J. Brugger, A. V. Savegnago, G. Della Giustina, G. Brusatin, *Microelectron. Eng.* **2012**, 98, 176.
- <sup>26</sup> L. Brigo, V. Auzelyte, K. A. Lister, J. Brugger, G. Brusatin, *Nanotechnology* **2012**, 23, 325302.
- <sup>27</sup> G. Greci, G. Della Giustina, A. Pozzato, G. Brusatin, M. Tormen, *Microelectron. Eng.*, **2011**, 88, 1964.
- <sup>28</sup> M. Ann Hockey, Q. Lin, E. Calderas, in *Proc. SPIE* **2012**, 8456, 84560Q.
- <sup>29</sup> B. Liu, S T Ho, *J. Electrochem. Soc.* **2008**, 155, 57.
- <sup>30</sup> L. O'Faolain, M. V. Kotlyar, N. Tripathi, R. Wilson, T. F. Krauss, *J. Vac. Sci. Technol. B* **2006**, 24, 336.
- <sup>31</sup> D. J. Maloney, W. M. Lee, P. J. Roman, M. A. Fury, R. H. Hill Method of making electronic materials US 6,566,276 B2, **2003**.
- <sup>32</sup> E. Zanchetta, G. Della Giustina, G. Greci, A. Pozzato, M. Tormen, G. Brusatin, *Adv. Mater.* **2013**, 25, 6261–6265
- <sup>33</sup> E. Di Fabrizio, A. Nucara, M. Gentili, R. Cingolani, *Rev. Sci. Instrum.* **1999**, 70, 1605.
- <sup>34</sup> F. Romanato, E. Di Fabrizio, L. Vaccari, M. Altissimo, D. Cojoc, L. Businaro, S. Cabrini, *Microelectron. Eng.* **2001**, 57, 101.
- <sup>35</sup> J. Coates, Interpretation of infrared spectra, a practical approach, in *Encyclopedia of Analytical Chemistry* R.A. Meyers (Ed.), **2000**, John Wiley & Sons Ltd, Chichester, 10815.
- <sup>36</sup> A. Roy Chowdhuri, C.G. Takoudis, *Thin Solid Films* **2004**, 446, 155.
- <sup>37</sup> T. M. H. Costa, M. R. Gallas, E. V. Benvenuti, J. A. H. da Jornada, *J. Phys. Chem. B* **1999**, 103, 4278.
- <sup>38</sup> G. Greci, G. Della Giustina, A. Pozzato, E. Zanchetta, M. Tormen, G. Brusatin, *Microelectron. Eng.* **2012**, 98, 134–137.
- <sup>39</sup> A. Pozzato, G. Greci, G. Birarda, M. Tormen, *Microelectron. Eng.* **2011**, 88, 2096-2099.
- <sup>40</sup> G. Greci, A. Pozzato, A. Carpentiero, E. Sovernigo, M. Tormen, *Microelectron. Eng.* **2011**, 88, 2552.

---

## *Chapter 5*

# **ZIRCONIA BASED MATERIALS FOR ADAPTIVE OPTICS AND STEM CELLS DIFFERENTIATION DEVICES**

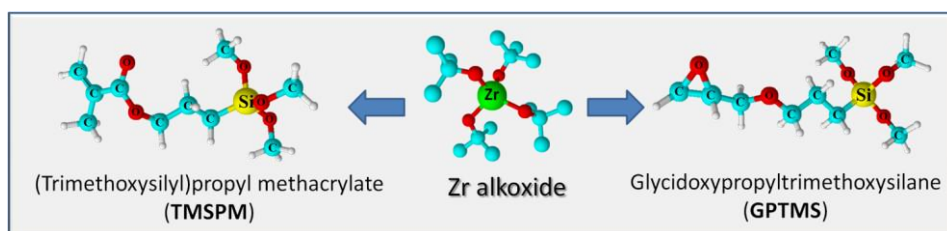
The development of different new miniaturized devices in the fields of optics, electronics, ionics, mechanics, energy, environment, biology and medicine has considerably increased the demand of materials with advanced functional and structural properties. As reported in Chapter 2, an important class of advanced materials, sol-gel Hybrid Organic–Inorganic (HOI) systems, are well suited for such applications due to their high degree of flexibility to design their physical (high transparency, thermal stability, refractive index,..) and chemical properties (composition, hydrophobicity, hydrophilicity,..), directed to the application. These sol-gel hybrid materials combine the qualities of organic molecules or polymers (flexibility, versatility) and the physical properties of a glass (refractive index, transparency, thermal and mechanical resistance), which can be adjusted by incorporating other metal alkoxides (Ti, Zr, Al, etc.). In fact, among the many attractive features displayed by sol-gel route, the process versatility in terms of synthesis and final composition is very important, thanks to the wide range of available precursors on the market that allow to develop an incredible number of possible materials. Organically modified precursors (the most employed are Glycidoxypropyltrimethoxysilane and (Trimethoxysilyl)propyl methacrylate) allow to produce composite materials with the organic and inorganic components intimately mixed at a molecular scale thanks to the covalent C-Si bonds that remains stable under the synthesis conditions; while the addition of tetrafunctional alkoxides, such as silicon or metal alkoxides, both increases the reticulation degree and consequently the material mechanical properties (such as scratch, abrasion, plasma etching resistance) and confers particular characteristics to the final materials, i.e. to modulate the refractive index.

Moreover, in addition to the high versatility in terms of chemical and physical properties and shaping, hybrid materials present the paramount advantage of facilitating both integration and

miniaturization since they can be directly writable by different lithographic techniques, generally thanks to the engineered organic component. In fact, besides the right material composition, the other fundamental aspect for the realization of the final device is the patterning process.

### 5.1. *Synthesis and characterization of two Zr- based materials: photosensitive and thermosetting resists*

In this chapter we focus the attention on the synthesis by the sol-gel process and patterning of new hybrid Zr-based systems, organically modified with 3-glycidoxypropyltrimethoxysilane (GPTMS) and 3-(Trimethoxysilyl)propyl methacrylate (TMSPM), see Scheme 5.1, trying to deepen the relation between the final structure and process parameters. GPTMS and TMSPM are organically modified alkoxydes containing an epoxy ring and a double bond C=C, respectively. The inorganic part of the molecule is an alkoxy-silane polymerizable via hydrolysis and condensation reactions, thus leading to a glass like material. The mild conditions under which the inorganic part of the material is prepared are compatible with the presence of the organic moiety.



Scheme 5.1 Precursors used for the synthesis of Zr-based patternable Hybrid sol-gel materials

UV absorption of Zr-based films was investigated with UV-Vis spectroscopy (JASCO V-570) in the wavelength range 200-800 nm. Fourier Transform Infrared spectroscopy (spectrometer Jasco FT-IR-620) in the range of 400–4500  $\text{cm}^{-1}$  with a resolution of  $\pm 4 \text{ cm}^{-1}$ , thermal analysis with STA409/429 Netzsch TGA instrument and ellipsometric measurements (V-Vase J.A.Woollam Ellipsometer) were performed to evaluate films composition and structural changes upon UV irradiation and thermal treatment. Finally, the quality of the patterns obtained with UVL or NIL were analyzed by optical microscopy, scanning electron microscopy (Quanta<sup>TM</sup> 450) and Atomic Force Microscopy (NT-MDT).

### 5.1.1. Synthesis of GZ system

GPTMS is hydrolysed at room temperature in acidic condition with molar ratios  $\text{H}_2\text{O}:\text{HCl}$  (1N):GPTMS=1.5:0.005:1 for 1h. In a separate holder Zirconium(IV) butoxide ( $\text{Zr}(\text{But})_4$ ) is added to 2-Methoxyethanol and the solution is stirred for about 15 minutes. The two solutions are then mixed with a molar ratio of GPTMS:Zr=80%-20% (Figure 5.1) and 2-Methoxyethanol is added to reach the desired concentration (150 or 100 g/l  $\text{SiO}_2+\text{ZrO}_2$ ). The final sol is left to react under reflux at  $80^\circ\text{C}$  for 1h30min. Large particles in the mixture solution are finally removed by a microporous filter (0.2  $\mu\text{m}$  Millipore).

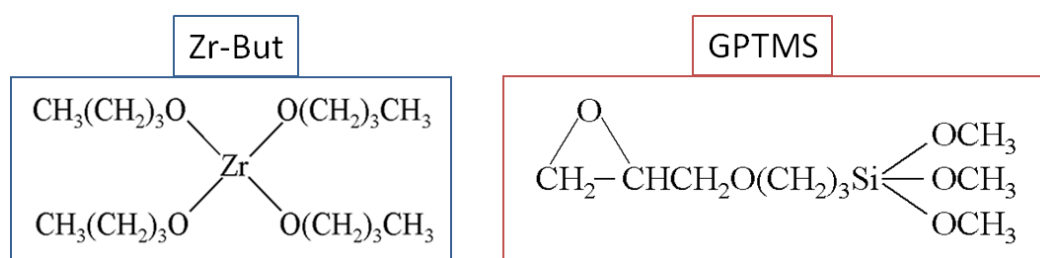


Figure 5.1  $\text{Zr}(\text{But})_4$  and 3-Glycidoxypropyltrimethoxysilane molecular formula

Hybrid films, with desired thickness, have been deposited by spin coating on silicon wafer (100). The thickness of the films plotted as a function of the spin coating speed is reported in Figure 5.2a and the UV-Vis spectra shows that the GZ film presents a low absorbance in the UV region below 300 nm, with high transmission coefficients even for films of 100  $\mu\text{m}$  or more, not common for most of the commercial resists [1], Figure 5.2b.

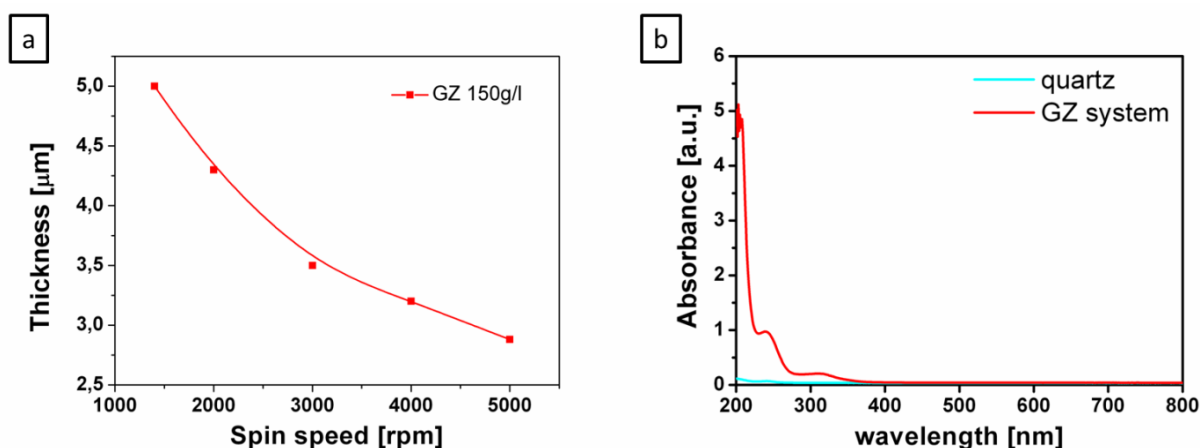


Figure 5.2 (a) Spin speed curve of GZ 150 g/l; (b) UV-Vis spectra of the GZ film

### 5.1.2. GZ characterization

#### 5.1.2.1. FTIR analysis of as deposited GZ system

GZ 150g/l of 3.5  $\mu\text{m}$  thickness was spin coated on cleaned silicon at 3000rpm for 30s in order to collect the FTIR spectra, Figure 5.3.

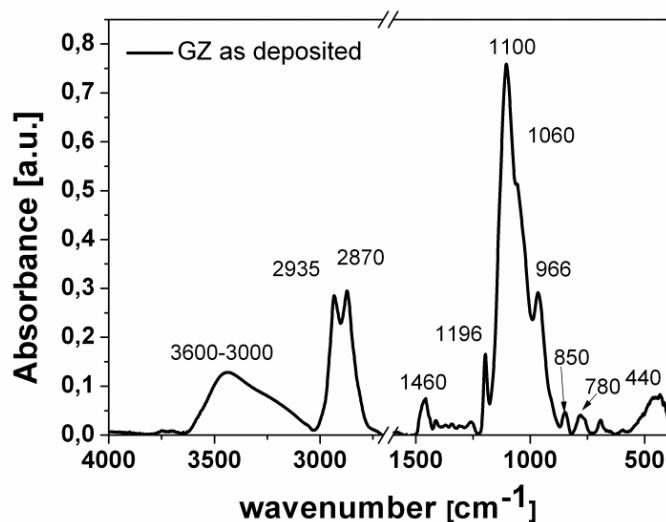


Figure 5.3 FTIR spectra of GZ 150g/l spin coated on silicon at 3000rpm30s

The large  $\nu(\text{O-H})$  band between 3600 and 3000  $\text{cm}^{-1}$  due to the absorption of the hydrolyzed precursors and in particular of 2-MetOEtOH that absorbs at 3420  $\text{cm}^{-1}$  is clearly visible at the end of the synthesis. The two main bands around 2935 and 2870  $\text{cm}^{-1}$  are attributed to  $\text{CH}_2$  anti-symmetric ( $\text{CH}_2, \nu_{\text{asym}}$ ) and  $\text{CH}_2$  symmetric stretching ( $\text{CH}_2, \nu_{\text{sym}}$ ), respectively, while the peak at 1460  $\text{cm}^{-1}$  is assigned to  $\text{CH}_2$  bend absorption.

The Si-OH stretching and Si-O-Zr hetero-linkages band at 966  $\text{cm}^{-1}$  can be detected. The band at around 1100-1060  $\text{cm}^{-1}$  and, in particular, the shoulder at 1060  $\text{cm}^{-1}$  correspond to the  $\nu_{\text{as}}$  antisymmetric stretching of the O atoms along a direction parallel to Si-Si in Si-O-Si bond of open chain trisiloxane units  $\text{T}_x(\text{OH})_y$  species structures, typical of amorphous dense silica with the linear species absorbing at 1032  $\text{cm}^{-1}$ . Silica LO vibration mode is detectable at 1100–1170  $\text{cm}^{-1}$ . Symmetric stretching ( $\text{TO}_2$ ) and rocking modes are observed around 800 and 450  $\text{cm}^{-1}$ , respectively. The last one is overlapped with the absorption of Si-O-Zr around 440  $\text{cm}^{-1}$ . The band at 1100  $\text{cm}^{-1}$  overlaps with the one ascribed to -C-O-C- sym. stretch of GPTMS chain around 1200-1100  $\text{cm}^{-1}$ .



The four characteristic vibrational modes attributed to the epoxy ring in GPTMS are: 1260-1240  $\text{cm}^{-1}$  (ring breathing), 910-810  $\text{cm}^{-1}$  (antisymmetric ring stretching), and 3060-2995  $\text{cm}^{-1}$  due to C-H stretching. The antisymmetric ring stretching mode (910  $\text{cm}^{-1}$ ) is generally chosen in epoxy resins to evaluate ring opening in hybrid materials. Concerning the epoxy ring, several reactions can take place leading to monomeric, oligomeric and polymeric ether structures, diols, metal esters and even to double bonds, aldehydes and ketone. As reported by Hoebbel *et al.* [2] that have performed a systematic quantitative study about the reactions between GPTMS and different metal alkoxides ( $\text{Si}(\text{OEt})_4$ ,  $\text{Sn}(\text{O}^t\text{Bu})_4$ ,  $\text{Zr}(\text{O}^n\text{Bu})_4$ ,  $\text{Al}(\text{O}^s\text{Bu})_3$ ,  $\text{Al}(\text{OEtO}^t\text{Bu})_3$ ,  $\text{Ti}(\text{OEt})_4$ ,  $\text{Ta}(\text{OEt})_5$ ), a small amount (even 1 mole%) of Zr-, Al-, Ta- and Sn-alkoxides already activates the ring-opening in 24 h hybrid sols, while a 10% content of these precursors leads to the almost complete ring opening in 24h at 25°C and to a complete ring-opening in hybrid gels after thermal treatment (7h at 130°C), Figure 5.4.

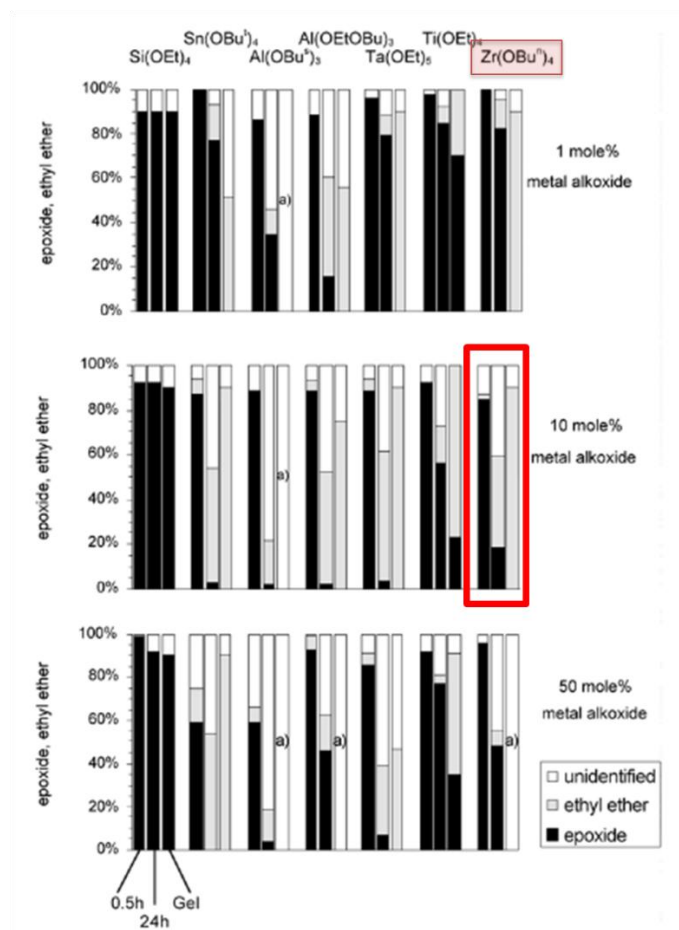


Figure 5.4 Amount of epoxy rings and ethyl ether groups in hybrid sols after 0.5 h and 24 h reaction time at room temperature and in corresponding gels of the systems ( $\text{H}_2\text{O}/\text{GPTMS}=1,5$ ) with different metal alkoxide molar concentration (1, 10, 50%). The 20% Zr-precursor content is highlighted in red.

Zr-precursor then acts as a Lewis acid for the opening of the epoxy rings: all the absorptions related to epoxides are not detectable at the end of the synthesis at 80°C, only a slight absorption is visible at 850 and 910 cm<sup>-1</sup>. The latter can be detected as a shallow shoulder overlapped with Si-OH and Si-O-Zr absorption. Ring-opening reactions can produce polyethylene oxide chains interconnected with the inorganic network in the final material (Class II Hybrids), Figure 5.5.

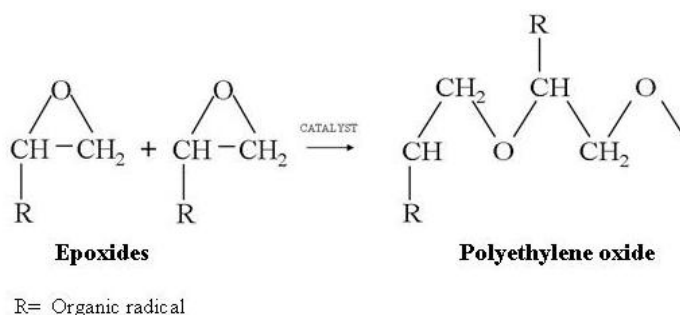


Figure 5.5 Epoxy ring polymerization and formation of polyethylene oxide

Even water in acidic condition or in alcoholic solvent, as in the case of the GZ synthesis, can trigger epoxy ring opening (in particular after 24h at 25°C) because of the formation of diols or methyl ether groups at the end of the organic chains, Figure 5.6.

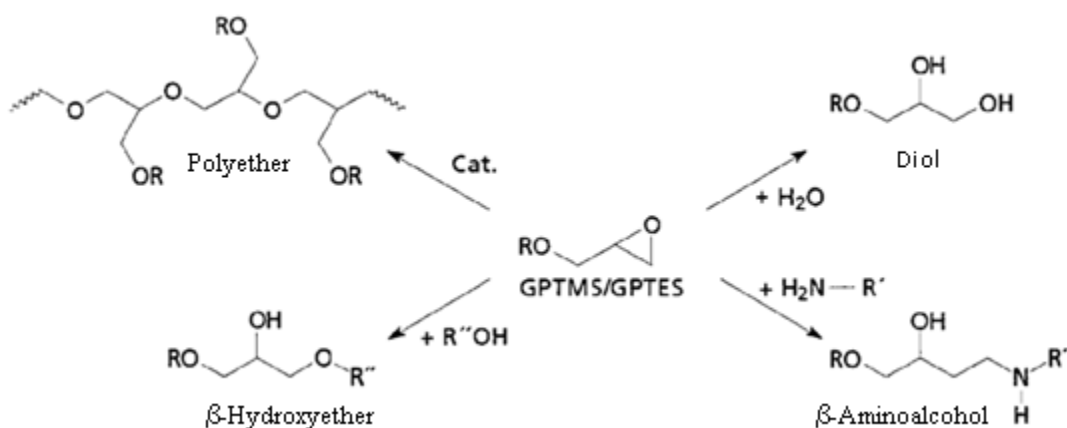


Figure 5.6 Scheme of some possible reactions of epoxy group present in the GPTMS [3]

This feature allows obtaining a final material with good properties, such as a high homogeneity degree at molecular level, a great scratch and abrasion resistance [4], synthesis of non-porous systems and with very low optical losses [5]. For these reasons, hybrid GPTMS based systems find applications in a wide range of fields such as contact lenses [6],

antifogging, photochromic, antireflective and coloured layers on glass [7,8], corrosion preventing coatings, photographic films, waveguides [9,10], optical limiters [11] and matrices for optically active molecules or nanoparticles [12,13].

### 5.1.2.2. Characterization of thermally treated GZ system

Hydrolysis and condensation reactions of GZ films are promoted by thermal treatment. In fact, as it can be depicted from Figure 5.7, reporting the FTIR spectra of GZ films at increasing TT temperatures (up to 200°C for 30min), the  $\nu(\text{O-H})$  band between 3600 and 3000  $\text{cm}^{-1}$  and the Si-OH stretching peak at 966  $\text{cm}^{-1}$  decrease with temperature.

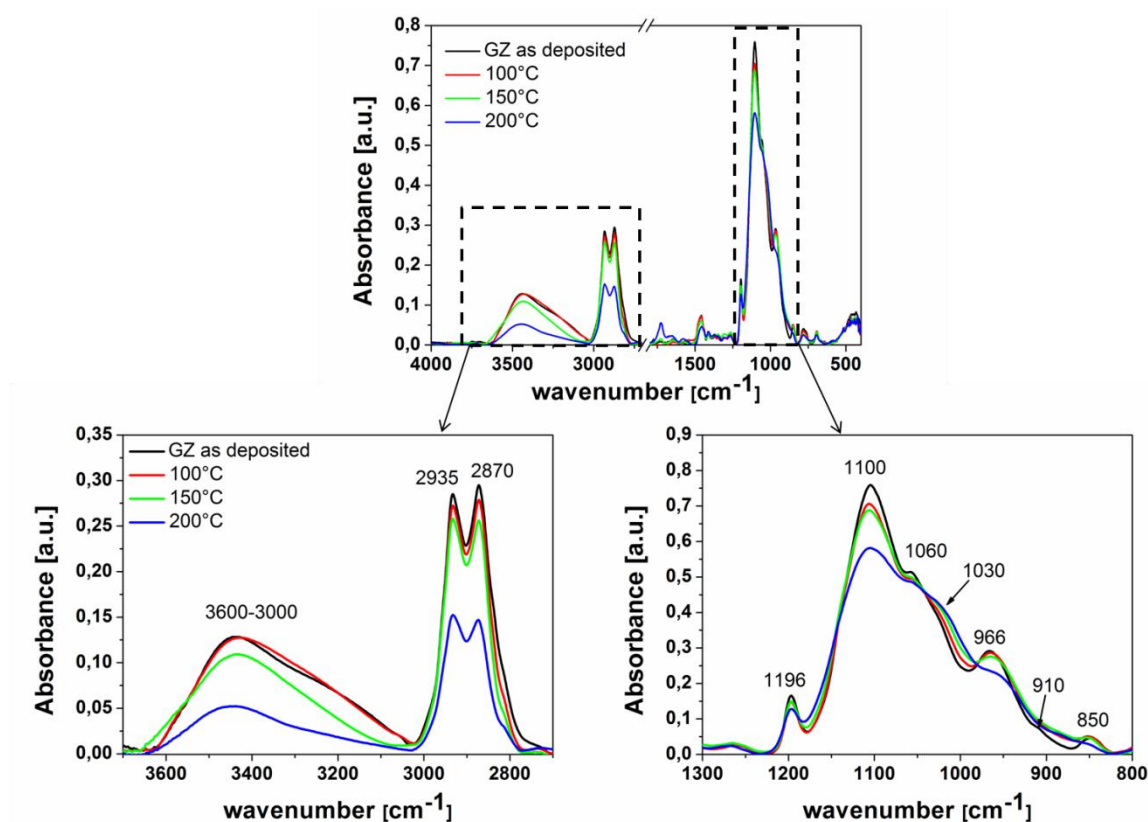


Figure 5.7 FTIR spectra of GZ 150g/l spin coated on silicon at 3000rpm30s at increasing thermal treatment temperatures

The peak at 1060  $\text{cm}^{-1}$  typical of trisiloxane structures with a lower crosslinking degree, that mainly contributes to the formation of the silica network with linear species, decreases with TT temperature due to inorganic network crosslinking. In fact at the same time the shoulder at 1030  $\text{cm}^{-1}$  due to Si-O-Si bonds in condensed polymeric, branched structures increases. Since the ratio between the intensity absorption at 1100 and 1030  $\text{cm}^{-1}$  decreases, polycondensed

silica species are formed, indicating a progression in the crosslinking and a densification of the coating with temperature.

Ellipsometric measurements confirm the condensation-densification of films and a decrease of porosity with thermal treatment: the refractive index (Figure 5.8a) increases with thermal treatment temperatures (higher than 100°C) and at the same time the thickness of films decreases (Figure 5.8b).

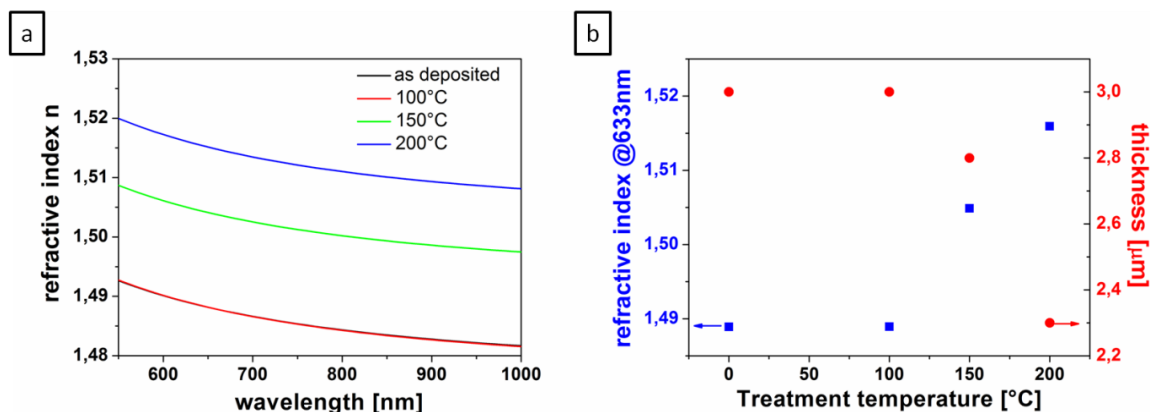


Figure 5.8 (a) ellipsometric measurements on GZ films at increasing thermal treatment temperatures; (b) refractive index @633nm and thickness of GZ films as a function of thermal treatment temperature

The thermal analyses (see Figure 5.9) on GZ powder display a continuous weight loss until 600°C. In the first region until 250°C, there is a first endothermic peak characteristic of water and solvent evaporation, but also of condensation reaction progress, confirming the FTIR analysis. Around 300 °C, an abrupt weight loss occurs due to the degradation of the organic groups. Finally at temperatures above 550°C, there is an evolution of network formation accompanied by the evaporation of the water produced by the dehydroxylation and/or condensation reaction and further combustion of the remaining organic compounds.

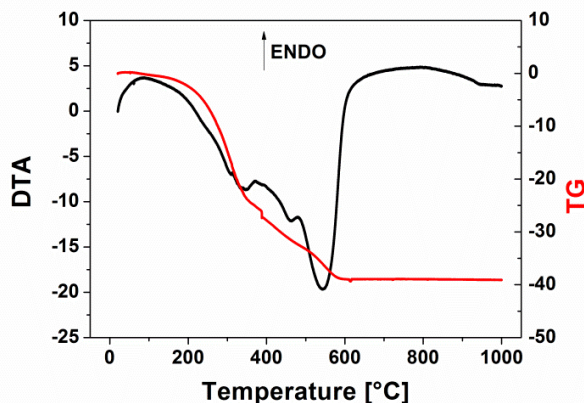


Figure 5.9 Thermal analysis (TG and DTA) of GZ powder in flowing air

### 5.1.3. Synthesis of TMSPM-Zr system

3-(Trimethoxysilyl)propyl methacrylate (TMSPM) is hydrolysed in acidic conditions for 1 h at room temperature. The molar ratios are TMSPM:H<sub>2</sub>O:HCl=1:3:0.01. Zr-butoxide (Zr(OBut)<sub>4</sub>) and Metacrylic acid (MAA) are separately left stirring for five minutes, Figure 5.10. The two solutions are mixed together, and put under stirring for one hour. The molar ratios between the precursors are TMSPM:Zr(OBut)<sub>4</sub>:MAA=1:0.5:1; THF is added to reach the desired concentration (110 or 80 g/l SiO<sub>2</sub>+ZrO<sub>2</sub>). The sol is finally filtrated through a 0.2 µm filter in order to get a better film quality after spin coating.

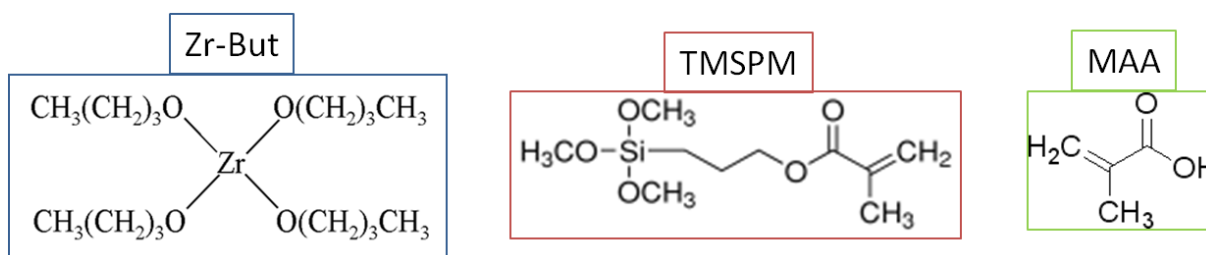


Figure 5.10 TMSPM-Zr precursors chemical formula

The UV photopolymerization can be induced and enhanced by the addition of photoinitiators, which may be classified into two main categories related to their mechanism of free radical formation: photocleavage or photofragmentation (e.g. aryl ketones), and hydrogen abstraction (e.g. benzo-phenone, thioxanthone). The photoinitiator chosen for this study was 2-Benzyl-2-dimethylamino-1-(4-morpholinophenyl)-butanone-1 (Ciba® IRGACURE® 369) at concentrations of 1% with respect to the number of acrylic units of TMSPM. This photoinitiator was eventually added to the sol in order to speed up the photopolymerization, Figure 5.11.

IRGACURE 369 is a highly efficient UV curing agent which is used to initiate the photopolymerization of chemically prepolymers -e.g. acrylates- in combination with mono-or multifunctional monomers. We chose Irgacure 369 among other photoinitiators (Irgacure 184, Irgacure 907, Isopropyl-9H-thioxanthen-9-one IT9) because it enhances the absorption of TMSPM-Zr films around 360 nm, which corresponds to the highest emission line of the UV lamp (Hamamatsu Lightningcure LC5) used for film exposure and patterning, Figure 5.11

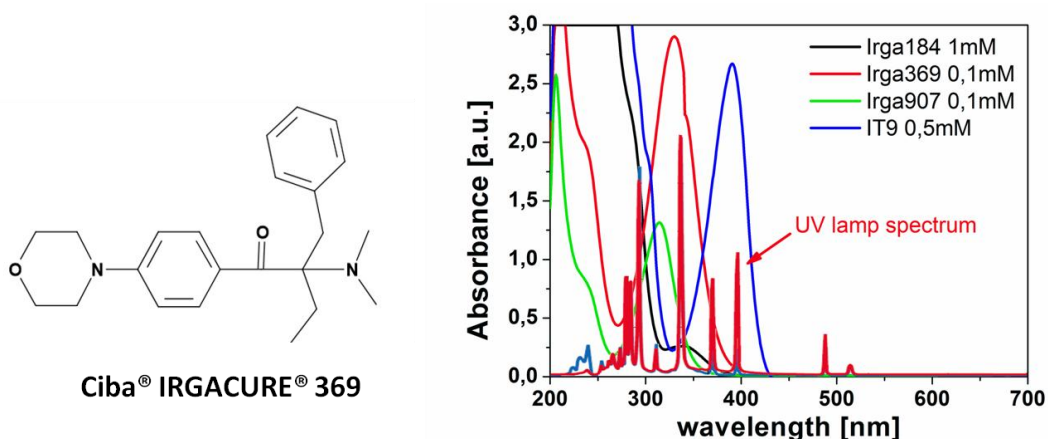


Figure 5.11 2-Benzyl-2-dimethylamino-1-(4-morpholinophenyl)-butanone-1 (Ciba® IRGACURE® 369); on the right: UV-Vis spectra of different photoinitiators: Irgacure 184, 369, 907 and Isopropyl-9H-thioxanthen-9-one IT9

The sol was then spin-coated for 10s on cleaned silicon, quartz and steel substrates at different dilution and spin coating speeds in order to get the final wanted film thickness, Figure 5.12.

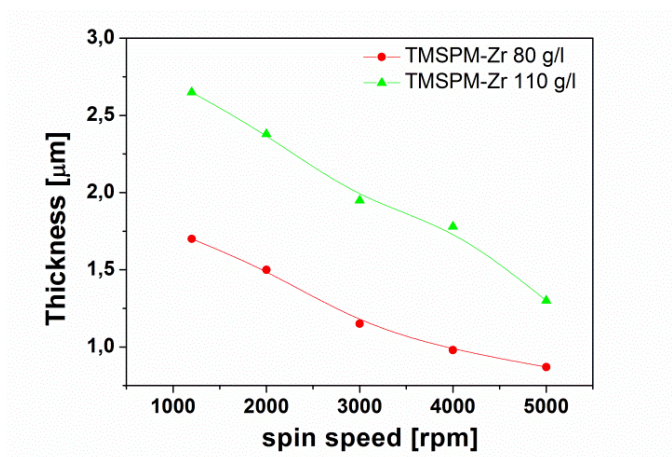


Figure 5.12 Spin speed curve of TMSPM-Zr at different dilution with THF

#### 5.1.4. TMSPM-Zr characterization

##### 5.1.4.1. FTIR analysis

Films of TMSPM-Zr 110 g/l deposited on silicon by spin coating at 5000rpm30s (1.3 μm thickness) were characterized by FTIR spectroscopy in order to analyze the chemical changing in the system during exposure to UV. The FTIR spectra of the “as deposited” film before exposure is reported in Figure 5.13 and the most significant absorption peaks are reported in Table 5.1.

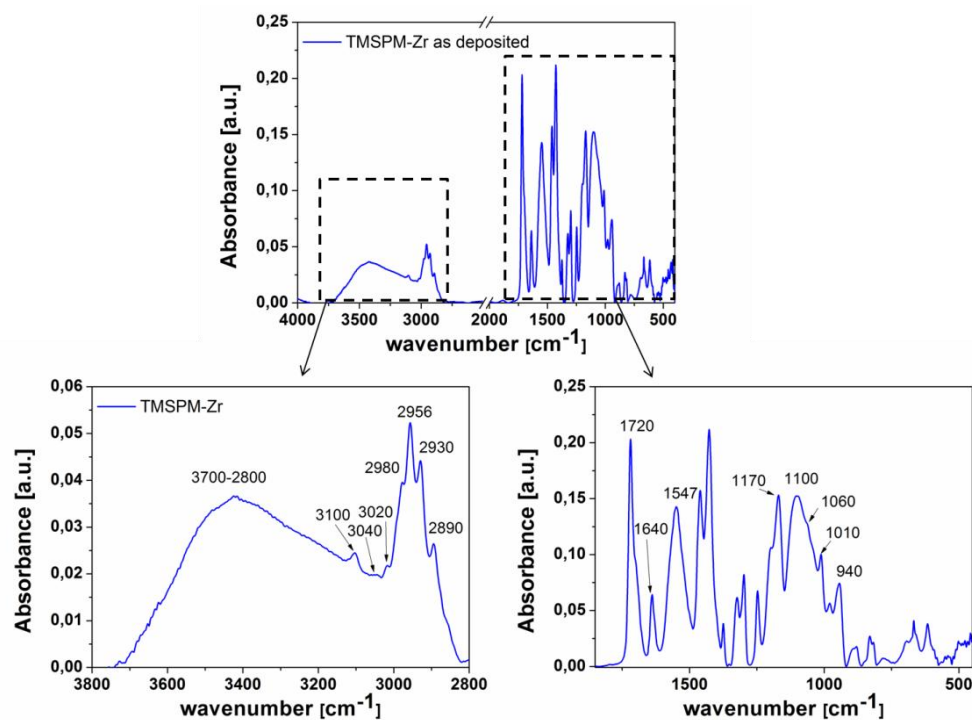


Figure 5.13 FTIR spectra of TMSPM-Zr 110g/l film spin coated on silicon at 5000rpm for 30s

Group frequency wavenumber ( $\text{cm}^{-1}$ )	Assignment
3600-3000	Hydroxy group, O-H stretch
3100-3040-3020	C-H vnyil stretch
2980-2960	$\text{CH}_2$ stretch (THF)
2956-2890	$\text{CH}_3$ asym/sym stretch
2930-2860	$\text{CH}_2$ asym/sym stretch
1720	C=O stretch
1640	C=C
1547	$\text{COO}^-$
1460-1377	$\text{CH}_3$ asym/sym stretch and $\text{CH}_2$ bend
1425-1324-1300	vinyl C-H in-plane bend
band 1350-1260	-OH in-plane bend
1170-1050	- C-O-C- sym. stretch and alcohol C-O stretch
1060	- C-O-C- oxyrane (THF)
1100-1000	silica stretching vibrations (Si-O-Si)
983-880	vinyl C-H out-of-plane bend
950-810	Si-OH
1000-950	Si-O-Zr
880	C-O-C oxyrane (THF)

Table 5.1 Most significant FTIR absorption peaksof TMSPM-Zr

The large  $\nu(\text{O-H})$  band between  $3600$  and  $3000\text{ cm}^{-1}$  and  $1350\text{--}1260\text{ cm}^{-1}$  are due to the absorption of the hydrolyzed precursors and of solvents formed during hydrolysis and condensation of precursors (methanol and butanol). The peaks at  $3100\text{--}3040\text{--}3020\text{--}1425\text{--}1324\text{--}1300$  and  $983\text{--}880\text{ cm}^{-1}$  are assigned to the in-plane and out-of-plane bend absorptions of vinyl C-H stretch, respectively. The peaks at  $2980\text{--}2960\text{ cm}^{-1}$  are related to the stretch of  $\text{CH}_2$  of THF.  $\text{CH}_3$  asym/sym stretch is detected at  $2956\text{--}2890\text{ cm}^{-1}$ , as well as the peaks at  $1460\text{--}1377\text{ cm}^{-1}$ , while  $\text{CH}_2$  asym/sym stretch is clearly visible at  $2930\text{--}2860\text{ cm}^{-1}$ . The stretching of the C=O bond of MAA and TMSPM is detectable at  $1720\text{ cm}^{-1}$ . The C=C double bond, necessary for the polymerization of the zirconia-based system, is present both in TMSPM and in MAA spectra at  $1640\text{ cm}^{-1}$ . The peaks at  $1547\text{ cm}^{-1}$  is ascribed to the  $\text{COO}^-$  band in a salt formed through the reaction between Zr precursor and MAA [14]. The absorption at  $1170\text{--}1050\text{ cm}^{-1}$  is assigned to the TMSPM -C-O-C- sym. stretch and alcohol C-O stretch, while the -C-O-C- bond of the oxirane ring of THF is detectable at  $1060$  and  $880\text{ cm}^{-1}$ . These absorptions overlap with Si-O-Si stretching vibrations between  $1170$  and  $1000\text{ cm}^{-1}$ : TO mode at  $1010\text{--}1060\text{ cm}^{-1}$  and LO mode at  $1100\text{--}1170\text{ cm}^{-1}$ , the latter related to the free-volume or porosity of the coatings. The other two bands at  $895\text{--}900\text{ cm}^{-1}$  and  $950\text{--}979\text{ cm}^{-1}$  have been assigned to Si-O-Zr bonds [15]. The peak centred at  $\sim 950\text{ cm}^{-1}$  can be assigned both to Si-OH groups (Si-OH stretching mode) and to Si-O-Zr bonds, due to the starting of condensation of the inorganic part of the system.

#### 5.1.4.2. UV curing of the hybrid acrylate system

Radical photopolymerization reactions are normally initiated by one or several photoinitiators that are added to the reactive mixture of acrylate monomers and oligomers. The photoinitiator and the concentration at which it is used determine the polymerization rate and the thickness of the layer that can be polymerized. The basic principle of any photoinitiator consists of two main steps: (1) absorption of the incident photons associated with an electronic excitation of the initiator molecule and (2) generation of initiating species from the excited states with a high yield. For an efficient exploitation of the UV light, the absorption spectrum of the photoinitiator has to match the emission spectrum of the UV source used. The most common light source in UV curing is the mercury arc lamp. Consequently, most initiators are tuned to its spectrum. In contrast, most photocurable oligomer resins, for example, acrylates, do not or only weakly absorb in this spectral region. The use of lamp with intense, short-wavelength emission (e.g., Xe-Hg lamp enhanced-type, which exhibits emission below  $300\text{nm}$ ) opens up



a different possibility for the initiation of the photopolymerization of acrylates without photoinitiators addition. Like most other organic compounds, acrylates strongly absorb radiation with a wavelength shorter than about 220–260 nm, as in the case of TMSPM-Zr whose absorption edge is 260nm. Therefore, acrylate molecules can be directly excited when they are exposed to short-wavelength UV radiation emitted by Hamamatsu Lightningcure LC5 with a Xe-Hg enhanced-type spectrum emission that was used for TMPSM-Zr films exposure and patterning. Examples of acrylates polymerization upon exposure to UV light with a wavelength of 222 nm are reported in Figure 5.14: the double bonds decrease without photoinitiator addition [16].

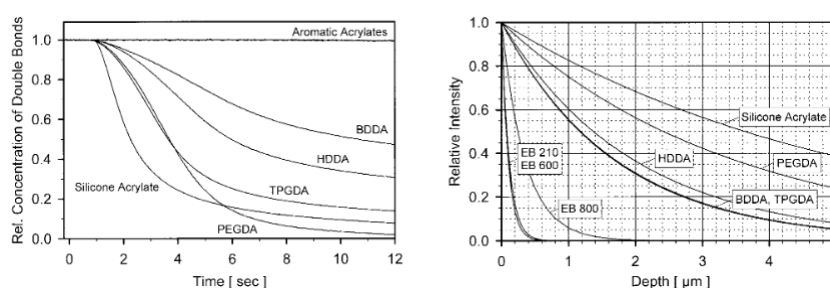


Figure 5.14 (left) Photopolymerization of various acrylates without photoinitiator by irradiation at 222nm; (right) Penetration of UV light with a wavelength of 222nm into various acrylates [16].

UV-Vis spectra of TMSPM-Zr 110g/l deposited on quartz at 2000 rpm for 30s shows that without the addition of Irgacure 369 the sol absorbs the lower wavelengths emitted by the Xe-Hg lamp 250 nm enhanced type (in Figure 5.15 the lower wavelengths are highlighted in the dashed frame). On the other hand, to ensure and widen the usability and versatility of the developed resist, allowing photopolymerization of films even with Mercury lamps, Irgacure 369 photoinitiator can be added to TMSPM-Zr sol. As it can be seen in Figure 5.15 a peak at 356 nm can be detected when few percentages of photoinitiator (molar with respect to the TMSPM double bonds) were added to the sol.

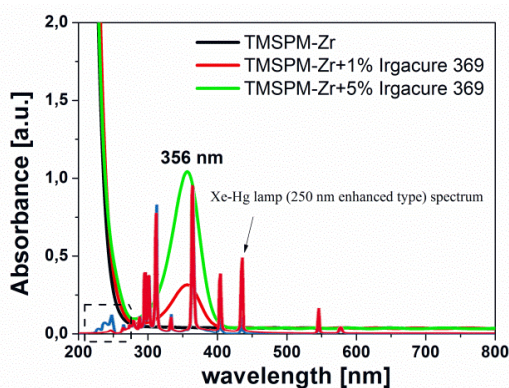


Figure 5.15 UV-Vis spectra of TMSPM-Zr deposited on quartz at 2000rpm30s, with or without the addition of Irgacure 369

The chemical changes that occur when TMSPM-Zr films without photoinitiator are exposed to Xe-Hg UV light and further TT at 100°C were analyzed with FTIR spectroscopy, see Figure 5.16. With UV irradiation, the intensity of the band due to C=C at around 1640  $\text{cm}^{-1}$  decreases, as well as all the other peaks related to the vinyl C-H stretch (3100-3040-3020  $\text{cm}^{-1}$ ), in-plane bend (1425-1324-1300  $\text{cm}^{-1}$ ), out-of-plane bend (983-880  $\text{cm}^{-1}$ ). This shows that UV irradiation leads to depletion of C=C bonds, indicating that polymerization occurred in TMSPM and MAA. The  $\text{COO}^-$  band at around 1550  $\text{cm}^{-1}$  shifts to higher wavenumbers in the UV-irradiated and TT samples, and the intensity of the band becomes smaller: polymerization must induce to different coordination states of  $\text{COO}^-$ . The decrease of LO Si-O-Si peaks indicates the densification of the coating with the subsequent lowering of porosity for increasing UV exposure and further TT, while the TO absorption remains almost constant. The absorption around 950  $\text{cm}^{-1}$  decreases mainly for Si-OH condensation after UV and thermal treatment. The other peaks between 1460 and 1260  $\text{cm}^{-1}$  decrease with UV exposure and TT due to the evaporation of alcohol formed during condensation.

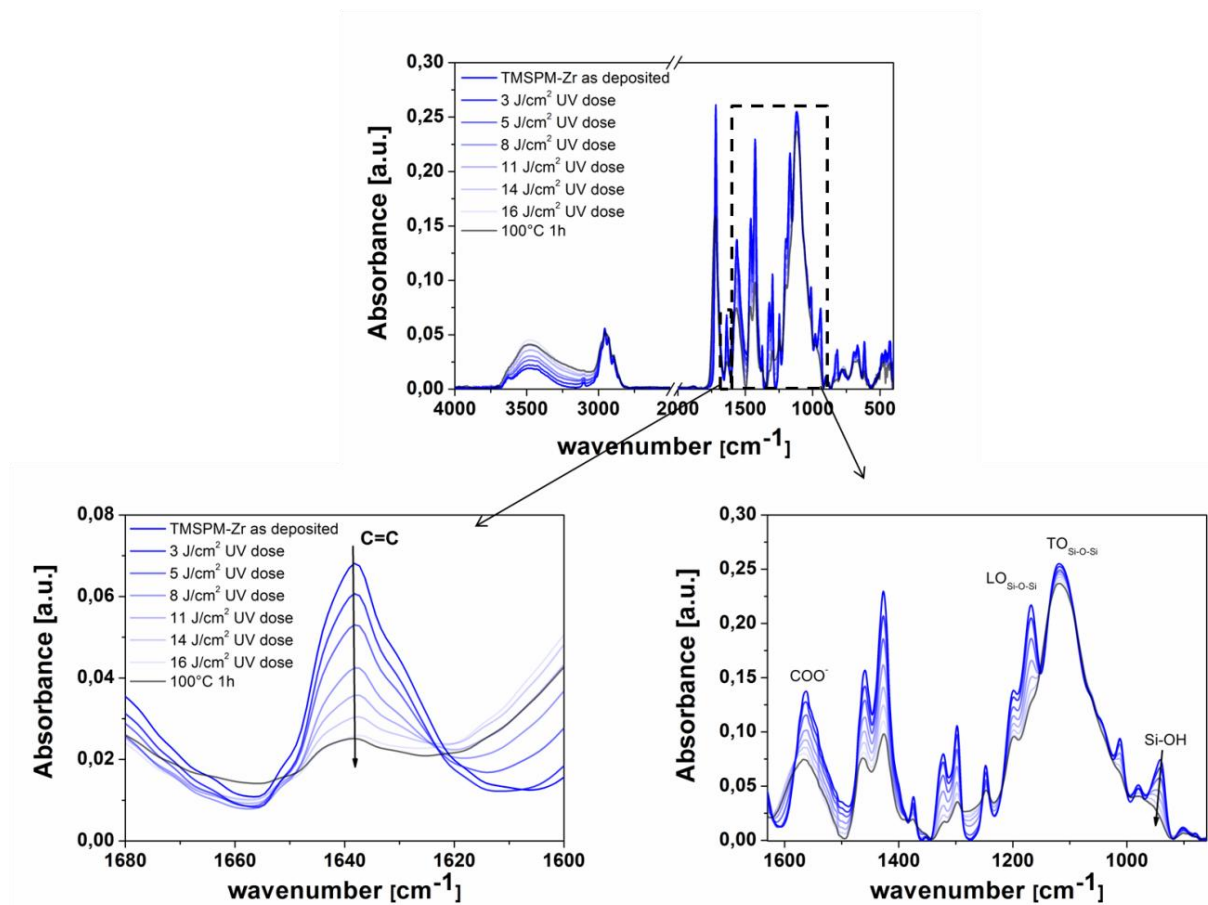


Figure 5.16 FTIR spectra of TMSPM-Zr films with increasing UV exposures

As previously mentioned, a photoinitiator can be added to the coating solution in order to initiate and accelerate the photo-polymerization or to widen the possible UV lamps used for patterning. The trend of the peak at  $1640\text{ cm}^{-1}$  in Figure 5.17 confirms in fact that C=C photopolymerization is more effective with the addition of Irgacure 369 with respect to TMSPM-Zr film without photoinitiator when exposed to the same UV dose. Therefore, we used Irgacure 369 photoinitiator (1 mol % with respect to C=C in TMSPM) when thick films had to be photo-polymerized with a shorter UV exposure to ensure a better resolution (see paragraph 5.3.1).

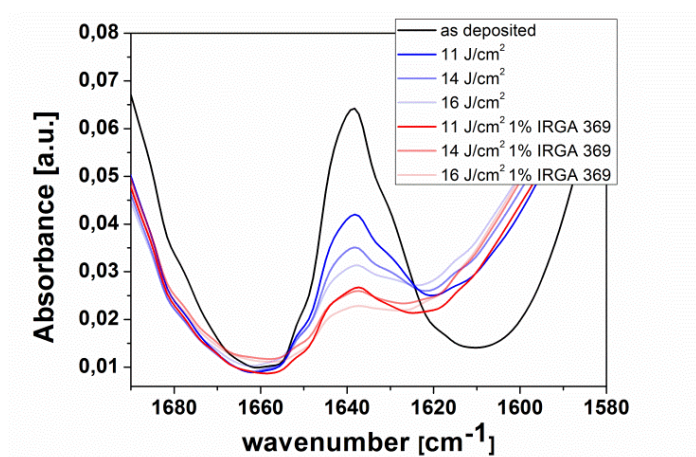
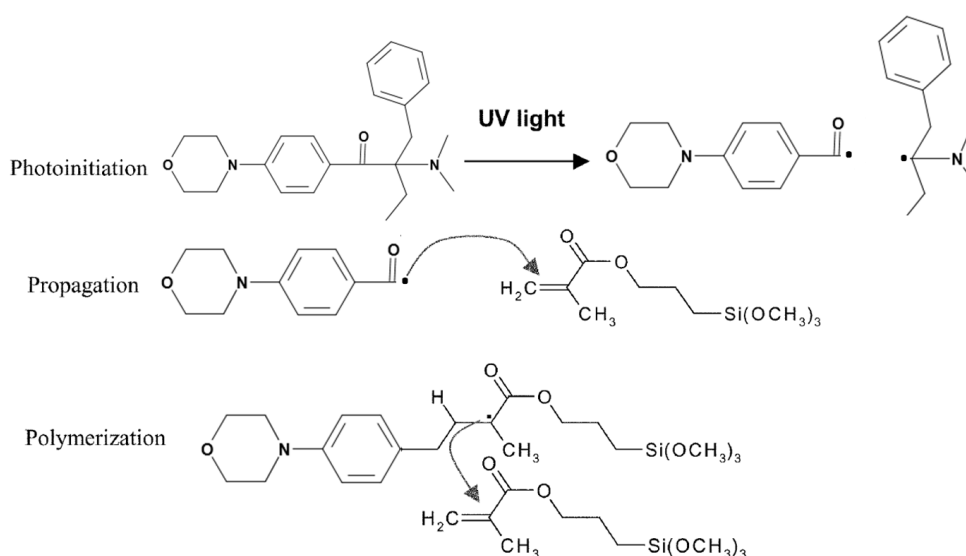


Figure 5.17 Comparison of the C=C photo-polymerization without photoinitiator (blue lines) and with the addition of Irgacure 369 1% molar with respect to TMSPM (red lines)

The photopolymerization process with the addition of Irgacure 369 is reported in Scheme 5.2.  $\alpha$ -Amino-alkylphenones undergo a rapid photocleavage reaction that generates the highly reactive free radicals needed to initiate the polymerization process.



Scheme 5.2 Photopolymerization process of TMSPM with the addition of Irgacure 369

Free radicals are readily produced upon UV irradiation of aromatic carbonyl compounds by homolytic cleavage of C-C bonds. The benzoyl radical was shown to be the major initiating species, while the other radical fragment may also contribute to the initiation. Acrylates are known to be among the most reactive monomers polymerizing by a free radical mechanism. This feature, together with the remarkable chemical, optical and mechanical properties of the polymers obtained, account for the great commercial success of acrylate-based UV-curable resins.

A further proof of the densification of the hybrid film with UV exposure ( $16 \text{ J/cm}^2$ ) and further thermal treatment at  $100^\circ\text{C}$  was obtained through ellipsometric measurements: the refractive index of a 800 nm-thick film increases, Figure 5.18.

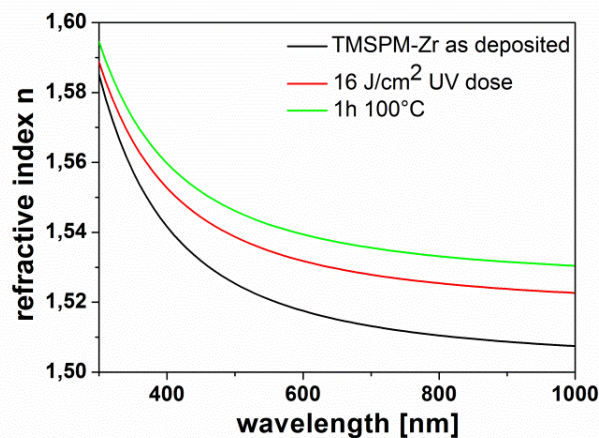


Figure 5.18 Refractive index of 800 nm-thick TMSPM-Zr film as deposited, after  $16 \text{ J/cm}^2$  UV dose and 1h TT at  $100^\circ\text{C}$

## 5.2. Adaptive optics devices: fabrication and tests

### 5.2.1. Introduction

The generation and utilization of High Harmonics (HHs) has emerged in the last two decades as a new field of nonlinear optics with very attractive characteristics. High-order harmonic generation (HHG), a nonlinear optical process in which the frequency of laser light is converted into its integer multiples, is driven by the interaction between a very intense ultrashort laser pulse and a gas jet. HHG is widely recognized as an effective way to realize coherent, brilliant, ultrashort table-top sources in the extreme ultraviolet (XUV or EUV; wavelength spectral range between 10-100 nm) and soft x-ray regions (1-10 nm) and/or X-ray radiation ( $< 1 \text{ nm}$ ) that can be exploited for time-resolved spectroscopy of matter with sub-femtosecond resolution [17,18,19,20,21,22] Laser-driven HHG uses acceleration of electrons on time-scales that are of the order of an optical cycle of the laser field. Currently this technique

gives rise to the shortest flashes of light ever generated in a laboratory which are typically of the order of a few hundreds of attoseconds ( $1 \text{ as} = 10^{-18} \text{ s}$  [23]).

The HH spectrum is described as a sequence of peaks corresponding to the odd harmonics of the fundamental laser wavelength with an intensity distribution characterized by a plateau, where the harmonic intensity is nearly constant over many orders and whose extension is related to the pulse intensity, and a sharp cutoff (see Figure 5.19).

The maximal harmonic photon energy  $E_c$  is given by the cutoff law (Krause et al., 1992),

$$E_c = I_p + 3.17U_p$$

where  $I_p$  is the ionization potential of the target atom, and  $U_p [\text{eV}] = E_{20}/4\omega_{20} = 9.337 \times 10^{-14} I [\text{W}/\text{cm}^2] (\lambda[\mu\text{m}])^2$  the ponderomotive energy, with  $E_0$ ,  $I$  and  $\lambda$  being the strength, intensity and wavelength of the driving field, respectively.

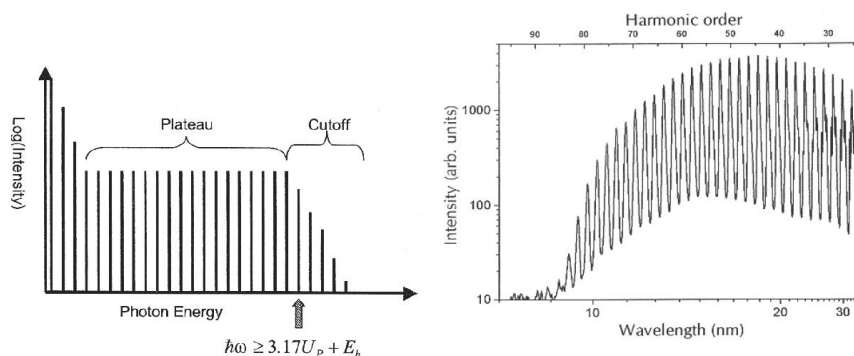


Figure 5.19 left: simplified HHG spectrum; right: Experimental HHG spectrum obtained with He gas and with a laser impulse  $\tau_p=25\text{fs}$  and  $I_0=600 \text{ TW}/\text{cm}^2$

Due to the nature of the process, HHs generation represents a powerful tool for temporal resolved measurements with sub-femtosecond resolution.[24,25,26]

In fact, several applications require the use of single harmonics which have to be extracted within the broad HH spectrum to obtain an ultrafast pulse at a suitable XUV wavelength to be scanned in a given range [27]. Due to their high repetition rate operation, tunability and high coherence degree, High-order harmonics can be used in material sciences, life sciences and detection technology

For some spectroscopic application the spectral selection of a single harmonic is required and should be accomplished by a suitable monochromator able to preserve the shortest temporal duration allowed by the selected spectral bandwidth of the XUV radiation. Although multilayer mirrors can be used to select one harmonic order, the contrast ratio of reflectivity is sometimes poor. On the other hand, a grating monochromator gives high spectral purity of the

selected radiation, but it introduces a stretch of the pulse duration due to the pulse-front tilt. This effect may compromise the ultrafast time resolution and high peak intensity when HHs are selected through a single-grating monochromator.

Therefore, the monochromator should also maintain the duration of the XUV pulse as short as in the generation process, to preserve the temporal resolution and the peak power. In case of using diffraction gratings to perform the spectral selection of HHs, the major mechanism that alters the pulse duration is the diffraction itself, since it gives rise to a difference in the lengths of the optical paths of the rays, Figure 5.20.<sup>[28]</sup>

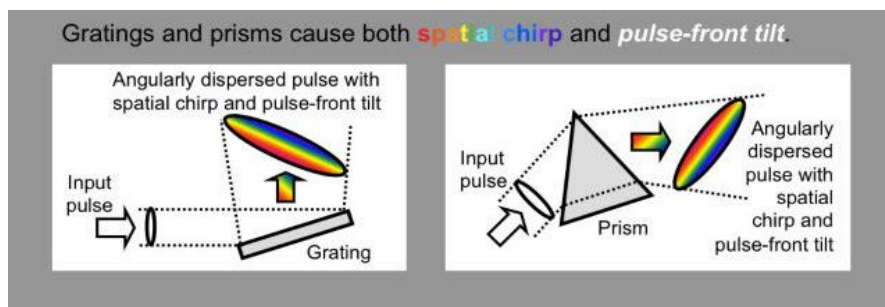


Figure 5.20 Difference in the lengths of the optical paths of the rays caused by diffraction using a diffraction grating and a prism

Indeed, if  $N$  grooves are illuminated by radiation at wavelength  $\lambda$ , the path difference  $\Delta_{OP}$  is  $Nm\lambda$  where  $m$  is the diffracted order:

$$\Delta_{OP} = Nm\lambda$$

This effect is negligible in the picoseconds or longer time scale, but may be dramatic in the femtosecond scale. As an example, let us consider a 200 gr/mm grating illuminated by radiation at 30 nm over a length of 20 mm; the total number of grooves involved in the diffraction is 4000, corresponding to a maximum delay in the first order of 120  $\mu\text{m}$ , i.e. 400 fs. Nevertheless, it is possible to design grating monochromators that do not alter the temporal duration of the ultrafast pulse by using two gratings in a subtractive configuration to compensate for the temporal and spectral dispersion. From the point of view of the ray paths, there are two conditions which the design of a monochromator must comply:

1) the differences in the path lengths of the rays at the same wavelength but with different entrance directions that are given by the first grating must be compensated by the second one, and



2) the rays at different wavelengths within the spectrum of the pulse have to be focused on the same point, i.e. the global spectral dispersion has to be zero.

Both these conditions are satisfied by the so called *time-delay compensated monochromator* (TDCM) [<sup>29,30</sup>] where two equal toroidal gratings are mounted in the classical diffraction scheme with opposite diffraction orders: the first one acts as a traditional single grating monochromator with an exit slit that performs the spectral selection of a single harmonic order, the second one is designed to compensate the temporal and spectral stretching introduced by the first grating. [<sup>31</sup>] The spectral selection is performed by a slit placed in the intermediate focal point between the gratings, Figure 5.21. This design has been proved to be very effective for the spectral selection of HHs with a temporal response as short as 10 fs. [<sup>32,33</sup>]

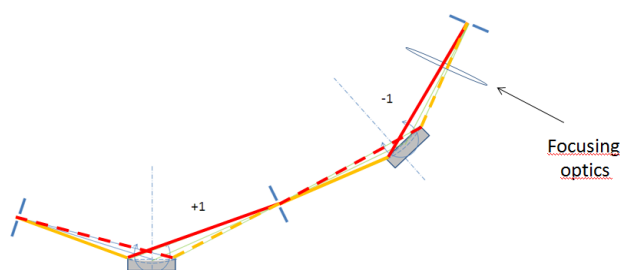


Figure 5.21 Scheme of a time-delay compensated monochromator (TDCM)

The wavelength scan is obtained by rotating each of the gratings around an axis passing through the grating vertex and parallel to the grooves. The optical design is based on the well-known Rowland geometry: [<sup>34</sup>] Source, grating and focal point lie on a circle tangent to the grating vertex and have the diameter equal to the grating radius, Figure 5.22.

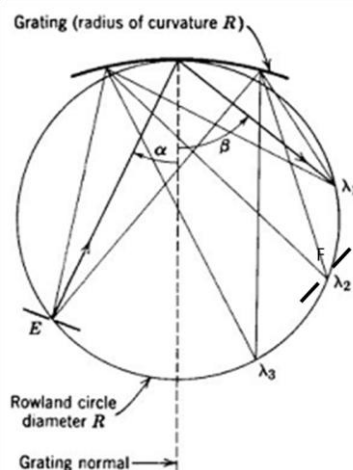


Figure 5.22 The Rowland geometry: source, grating and focal point lie on a circle tangent to the grating vertex

If we suppose having a slit F that allows to select a specific wavelength  $\lambda_1$  (as in Figure 5.22), in order to focalize  $\lambda_2$  or  $\lambda_3$  in F it is necessary to rotate the grating and change its radius of curvature. However, this operation is not possible with fixed-curvature gratings since it would be necessary to rotate and shift the grating in order to select the wanted wavelength. In fact, when the grating rotates, so does the Rowland circle, then the geometry requires that the rotation is coupled to a suitable variation of the entrance and exit arms. When the grating has a large radius, as the case of grazing-incidence operation in the XUV, this translation is not negligible at all, since it can range from several to tens of centimetres. The operation with variable entrance and exit arms is mechanically complex and often not allowed, since it is not possible to move the source or the exit focal point. It is normally avoided by adopting an included angle as low as to make the required translation negligible, for example using a toroidal-grating monochromator operating at a moderate grazing incidence [29,31].

In order to overcome these problems we propose to use a deformable grating to realize a grazing-incidence monochromator operated in the near-Rowland geometry with fixed entrance and exit arms, as it will be presented in the next paragraph. The main application of this device is the realization of double-grating monochromators for ultrafast pulses in the XUV region.

### 5.2.2. *Deformable gratings*

Deformable mirrors (DMs) are devices in which the shape of a reflective surface can be changed acting on an appropriate control parameter, usually a voltage or a current.[35] They can be realized with many technologies, e.g. piezoelectric,[36] electrostatic,[37] photo-controlled,[38] electro-magnetic.[39] DMs have found applications in many research fields such as for example: astronomy,[40] microscopy,[41] ophthalmology [42], laser focalization and shaping [43,44,45], telecommunication [46,47], optical displays [48] and in the visible to synchrotron radiation beamlines in the soft X-rays [49,50].

We propose to use an active deformable grating to realize a TDCM grazing-incidence monochromator operated in the near-Rowland geometry. The main advantage of using a deformable grating with respect to a conventional fixed one is the freedom to choose the included angle that matches at best the operation in the spectral interval of interest (e.g. the diffraction efficiency and/or the resolution) while maintaining fixed entrance and exit arms. In fact to maintain the system in the best focusing condition while scanning the wavelength, the deformable diffraction grating not only rotates but also changes its radius of curvature, as



shown in Figure 5.23. Furthermore, it is possible to use different geometries, e.g. different lengths of the entrance/exit arms to achieve different resolutions, without changing the gratings, that are normally the most expensive components of the monochromator. Therefore, the realization of active gratings to realize a TDCM has the following advantages: just two optical components, easiness of alignment, high efficiency, spectral tunability in a broad spectral range keeping fixed the source point and the output point.

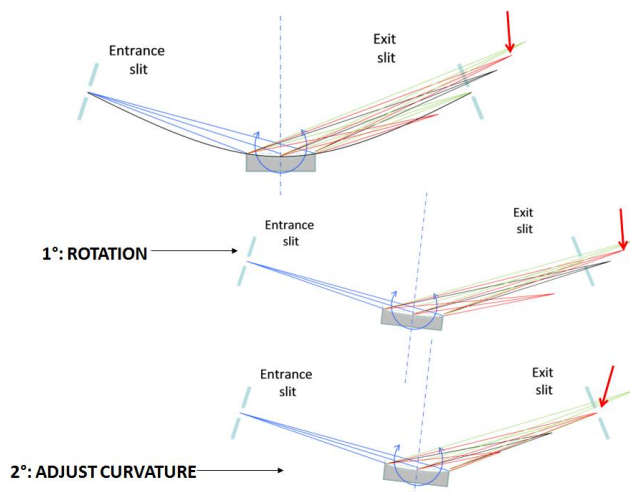


Figure 5.23 Deformable Diffraction Grating can focus the signal transmission on the exit slit thanks to the possibility to rotate and to change its radius of curvature

In collaboration with *CNR-IFN, Photonics and Nanotechnologies Institute, LUXOR Laboratory of Padova*, we overcame fixed-curvature grating problems fabricating directly patterned diffraction gratings on deformable substrates in order to realize a grazing-incidence double-grating monochromator for ultrafast pulses in the XUV region, particularly for the spectral selection of high-order laser harmonics (HHs), Figure 5.24.

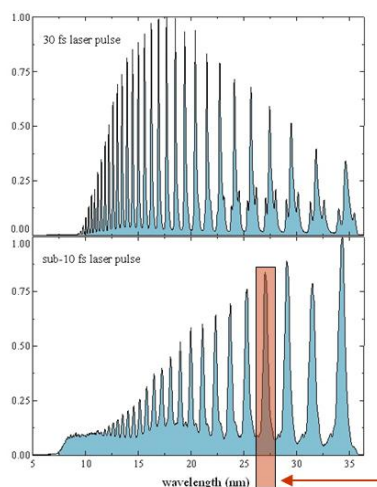


Figure 5.24 Grazing-incidence double-grating monochromator for ultrafast pulses in the XUV region has been realized for the spectral selection of high-order laser harmonics (HHs)

Both the directly patternable  $\text{ZrO}_2\text{-SiO}_2$  hybrid organic-inorganic materials were used to realize gratings on deformable substrates using the resist material itself as final patterned film, instead of using etch transfer techniques. In fact the developed systems possess greater thermal, mechanical and chemical stability respect to conventional polymeric resists, enabling their use in high-vacuum as well as other hard environmental conditions.

The first studies were conducted using a device consisting of a bimorph deformable mirror on the top of which a diffraction grating with digital profile was realized by UV lithography with TMSPM-Zr system. The final monochromator for ultrafast pulses in the XUV region was realized by fabricating a blazed grating on a deformable mirror through nanoimprint lithography using GZ system. Therefore, the advantage of this technology is to provide gratings with high optical quality, robust, compatible with any coating deposition and realized with only vacuum-compatible materials, that can be directly patterned on the final deformable mirror in one-step through UV or NIL.

The gratings are voltage-controlled devices, where the voltage that is applied to the piezo-actuator controls the radius of curvature of the spherical surface: a passive substrate is glued to a piezoelectric (PZT) disc which can change its radius of curvature according to the voltage that is applied to its electrodes, Figure 5.25. [<sup>51</sup>]

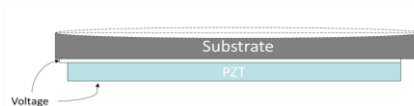


Figure 5.25 Bimorph deformable mirror

Since the operation in the XUV requires the use of the grating in high-vacuum conditions and a suitable and rather complex experimental setup, we first demonstrate the effectiveness of our design testing an active digital diffraction grating designed for the visible and near infrared spectral region at 400-850 nm wavelength range and operating in air. In a second experiment we demonstrated the compensation of the optical paths using a femtosecond Titanium Sapphire laser source ( $\lambda=800\text{nm}$ ). Hereafter we realized a blazed-grating monochromator to work in the XUV spectral region.

This is the outline of the following section:

- Demonstration of the active grating focusing capabilities using a digital deformable grating
- Demonstration of the time-delay compensated monochromator (TDCM) using a near IR ultrafast laser
- Realization of the final blazed grating device working in the XUV

### 5.2.3. Digital grating

The active diffraction grating is based on the unimorph deformable-optics technology. Specifically for the digital grating, the unimorph deformable mirror consisted in a pyrex glass substrate glued to the piezoelectric (PZT) disc. As previously discussed, the expansion of the PZT disc against the passive substrate generates a spherical change in the surface shape. The gratings were realized by photolithography of the spin-coated TMSPM-Zr film on the top of the reflective face of a spherical 0.8-mm-thick BK7 glass with a radius of curvature of 1340 mm. The curvature was concave for any applied voltage from 0 to 400 V, being the radius 1340 mm at 0 V and almost infinite at 400 V (i.e., flat surface). For applied voltages above 400 V, the grating became convex, being the radius  $-1300$  mm at 800 V. The curvature of the substrate was chosen to fulfil the specifications of the grazing-incidence monochromator that requires a variation of the radius from 2800 mm to 4200 mm. In such a way, the voltage that was applied to the grating does not exceed 400 V. The grating layout is shown in Figure 5.23a while Figure 5.23b shows the grating deformation when the applied voltage is smaller, equal, or greater than the critical voltage  $V_c$  (the value at which the grating surface becomes flat).

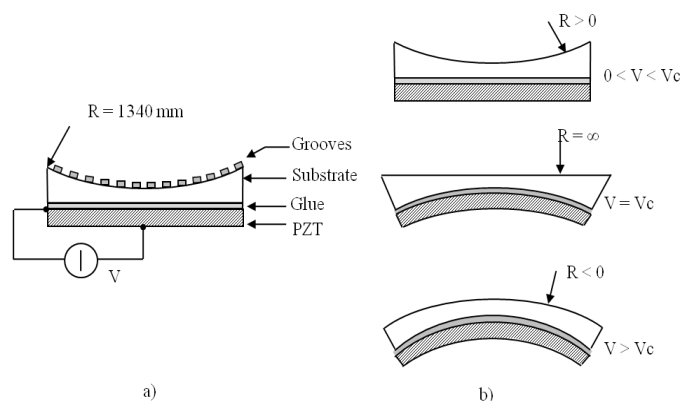


Figure 5.26 a) Adaptive grating layout, the voltage is applied to the piezoelectric disc. b) Grating shape change accordingly to the applied voltage:  $V_c$  indicates the critical voltage at which the grating surface becomes flat.

The digital groove profile and the depth of the rulings were designed to optimize the diffraction efficiency in the 400–900 nm spectral range. The optimized geometry was: groove density of 25 g/mm with  $\sim 1$   $\mu\text{m}$  height on an area of 15 mm in diameter.

In order to obtain structures of 1  $\mu\text{m}$  height the TMSPM-Zr solution was first diluted to 80g/l and then spin-coated on the cleaned bulk at 5000 rpm for 10s to reach the desired thickness. The photopolymerization process on the hybrid film was induced by UV radiation (Hamamatsu LC6 lamp) through a mask reporting the required pattern. The radiation intensity

on the sample was  $0.18 \text{ W/cm}^2$  and the film was exposed for 90s, corresponding to a total exposure dose of  $16 \text{ J/cm}^2$ . The unexposed material was removed by immersion in acetone for  $\sim 10 \text{ s}$  and then rinsed in water and ethanol, Figure 5.27. Figure 5.27 also reports the optical image and the profile of the grating obtained using a profilometer: the desired groove frequency of  $25 \text{ g/mm}$  was obtained and the groove depth was  $1 \mu\text{m}$ .

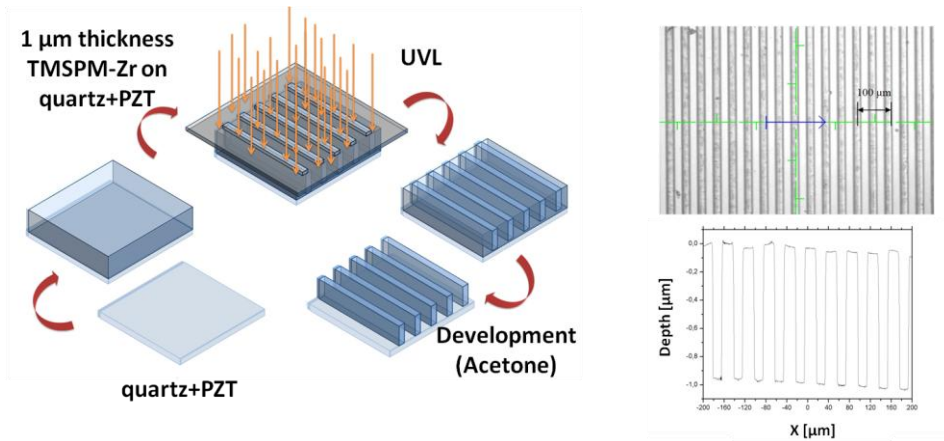


Figure 5.27 Scheme of the photolithographic process on the TMSPM-Zr system deposited on a piezoelectric-glass substrate. Right: optical image of the patterned film and grating profile sample along the direction orthogonal to the grooves; the scan length is  $450 \mu\text{m}$ . Both the digital profile and the desired grooves depth are obtained.

The proper glass bulk deformation, as a function of the applied voltage, was tested measuring the peak-to-valley (PTV) of the optical surface using a Zygo® interferometer.

The measurements have been performed in the range  $370\text{--}460 \text{ V}$ , i.e. in an interval around  $V_c$ , where the bulk deformation is directly measurable with the interferometer without any additional optics. The results are shown in Figure 5.28. The points are well fitted by a linear interpolation, as foreseen from the theory.<sup>[35]</sup> Once the PTV is known, the radius  $R$  can be obtained as  $R = (\Phi/2)^2/(2\text{PTV})$ , where  $\Phi$  is the grating diameter.

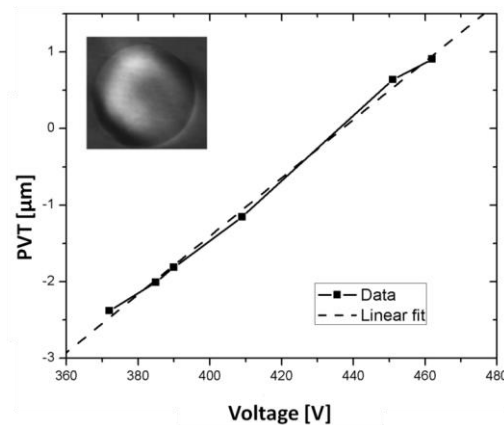


Figure 5.28 Grating PTV plotted as a function of the applied voltage. The dots represent the experimental points. The linear correlation coefficient is 0.99607, confirming a proper behaviour of the deformation. The inset shows the interferogram of the deformable mirror in its flat position with a deviation from flat of  $0.278 \mu\text{m}$  and  $0.062 \mu\text{m}$  rms.

The optical characterization procedure was based on the monitoring of the focusing capabilities of the deformable grating. The experimental setup is sketched in Figure 5.29. A laser source was focused on a pin-hole to generate a point-like source. The grating was placed at a distance  $p$  from the source and it focused the diffracted beam at a distance  $q$ . Both  $p$  and  $q$  were kept fixed during the wavelength scanning. The grating was operated at fixed constant deviation angle  $k = \alpha + \beta$ , where  $\alpha$  and  $\beta$  are, respectively, the incidence and diffraction angles. The wavelength scan was performed by rotating the grating following the grating equation  $\sin\alpha - \sin\beta = m\lambda\sigma$  that for constant deviation angle is written as:

$$\alpha = \frac{k}{2} + \text{asin}\left[\frac{m\lambda\sigma}{2\cos(k/2)}\right]$$

where  $\lambda$  is the wavelength,  $\sigma$  the groove density and  $m$  the diffracted order ( $m = \pm 1$ ). The diffraction angle  $\beta = k - \alpha$  is lower than  $\alpha$  for  $m = +1$  (internal spectrum) and higher than  $\alpha$  for  $m = -1$  (external spectrum).

Let us fix as zero rotation the position of the grating in the zero order, i.e. when the grating is operated as a mirror:  $\alpha = \beta = k/2$ . The grating rotation  $\delta$  at the wavelength  $\lambda$  is expressed as:

$$\delta = \text{asin}\left[\frac{m\lambda\sigma}{2\cos(k/2)}\right]$$

where the rotation is assumed to be positive for the internal spectrum ( $\alpha > \beta$ ) and negative for the external one ( $\alpha < \beta$ ).

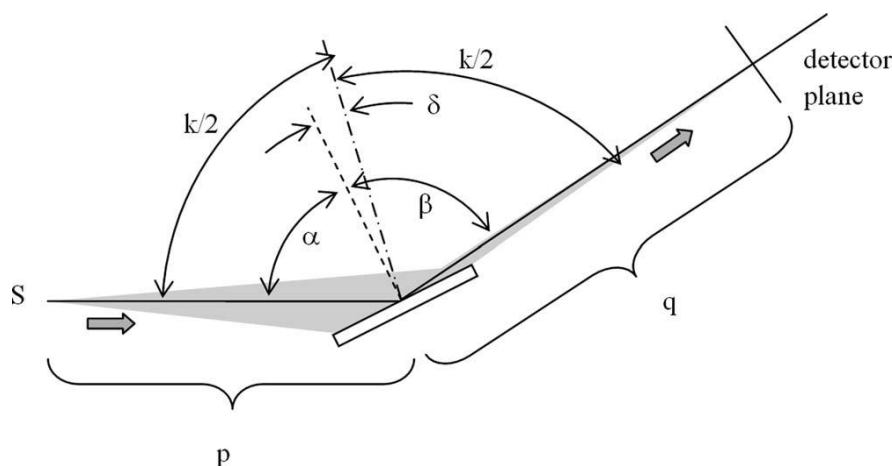


Figure 5.29 Set-up used for the optical characterization of the deformable grating. S is the source;  $p$  and  $q$  are respectively the entrance and exit arms;  $k$  is the total deviation angle;  $\alpha$  and  $\beta$  are respectively the incidence and diffracted angles. The operation in the external order, that is  $\beta > \alpha$ , is shown in the figure.

The grating radius  $R$  has to be adjusted for any wavelength to cancel the term giving the spectral defocusing [<sup>52</sup>]:

$$R = (\cos \alpha + \cos \beta) \left( \frac{\cos^2 \alpha}{p} + \frac{\cos^2 \beta}{q} \right)^{-1}.$$

The spectral resolution  $\Delta\lambda$  can be obtained from the size of the source  $S$ , as the spectral extension of its image on the output plane, which is  $S_{\text{out}} = S (q \cos\alpha) / (p \cos\beta)$ , where both the magnification ( $q/p$ ) and the anamorphic ( $\cos\alpha/\cos\beta$ ) factors have been taken into account and all the aberrations have been neglected. Taking into account the plate scale factor  $\Delta\lambda/\Delta l = \cos\beta/(\sigma q)$ ,  $\Delta\lambda$  is finally calculated as:

$$\Delta\lambda = S \frac{\cos \alpha}{\sigma p}$$

The experimental parameters to test the deformable grating in the 500-850 nm wavelength range have been chosen to be:  $k = 165$  degrees,  $p = 500$  mm and  $q = 600$  mm. The variation of the radius to maintain the spectral focus with fixed entrance and exit arms is shown in Figure 5.30 for the internal and external spectra and the zero order.

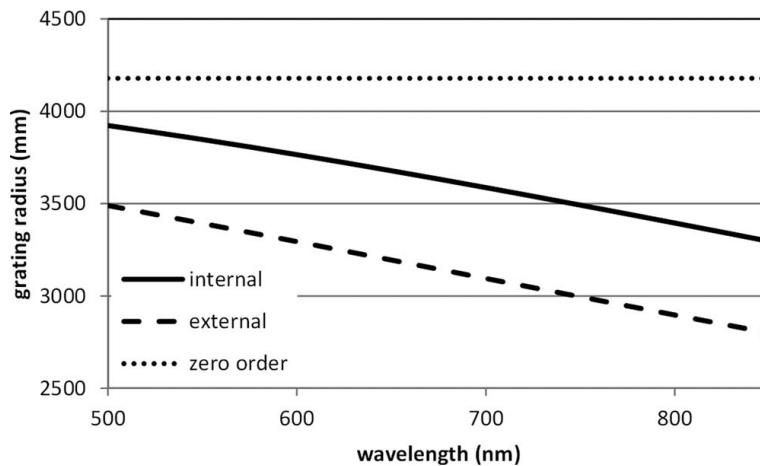


Figure 5.30 Variation of the grating radius to keep the monochromator on-focus in the 500–850 nm wavelength range. The parameters used for the calculations are:  $p = 500$  mm,  $q = 600$  mm,  $\sigma = 25$  g/mm,  $k = 165^\circ$ .

The device has been characterized at three wavelengths: 543 nm, 633 nm, and 850 nm. The results at 633 nm are presented in detail in Figure 5.31 that shows the images on the focal plane at different applied voltages for the zero order, the internal, and the external diffracted orders.

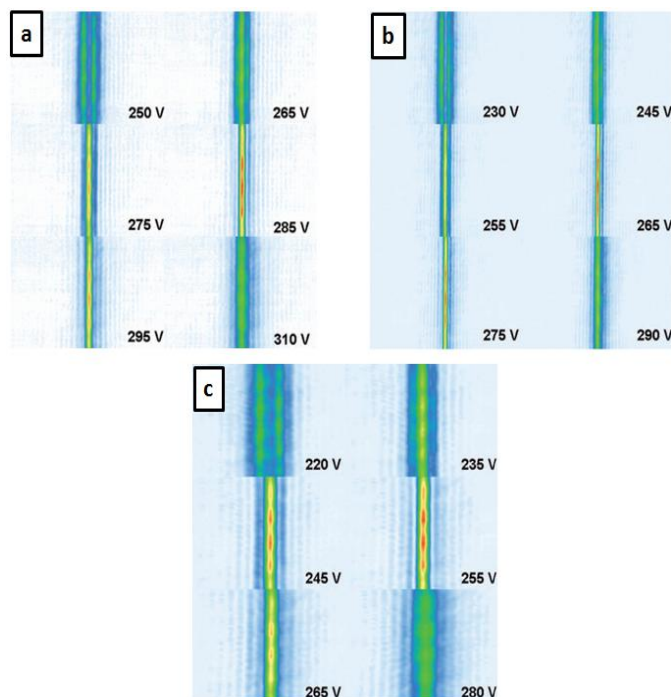


Figure 5.31 Focal spots acquired with different grating voltages:  $\lambda = 633$  nm, (a) zero order, (b)  $m=+1$  (internal order), (c)  $m=-1$  (external order).

The quality of the spectral focusing is clearly changing when the voltage, and therefore the grating radius, is changed. Figure 5.32 shows the full-width-at-half-maximum (FWHM) of the focal spots at different grating voltages, measured in the tangential plane (i.e., the spectral dispersion plane).

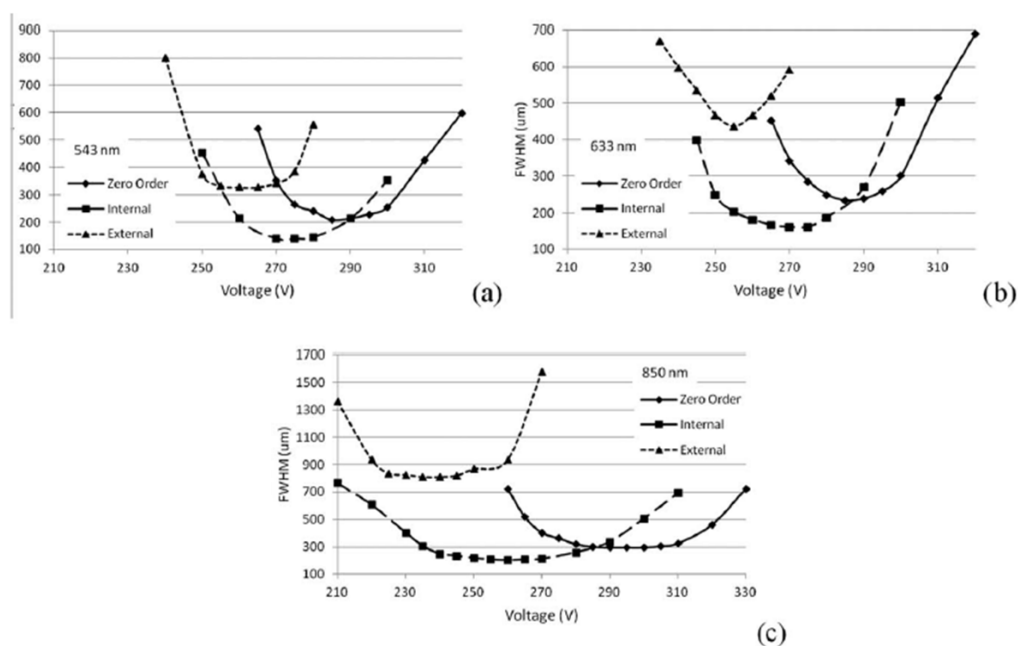


Figure 5.32 Spectral focusing at different applied voltages; the FWHM is measured in the tangential plane. Each of the three panels presents the FWHM at a single wavelength for the internal, external, and zero diffraction order: (a) 543 nm, (b) 633 nm, and (c) 850 nm.

Let us indicate with  $V^{\text{foc}}$  the voltage for which the minimum spot,  $W^{\text{foc}}$ , is reached. The curves show that  $V^{\text{foc}}_{\text{Zero-Order}} > V^{\text{foc}}_{\text{Internal-order}} > V^{\text{foc}}_{\text{External-order}}$ , as predicted from R equation. Moreover, it results  $W^{\text{foc}}_{\text{Internal-order}} < W^{\text{foc}}_{\text{Zero-Order}} < W^{\text{foc}}_{\text{External-order}}$ , in agreement with  $\text{FWHM}(\lambda)$  that will be discussed in the following. It is worth to mention here that, being the spherical grating operated at grazing incidence, it provides focusing only in its tangential plane. The focusing in the grating sagittal plane, that is the direction perpendicular to the spectral dispersion plane, has to be provided by the addition of a grazing incidence mirror after the exit slit that is demanded to provide a stigmatic focusing on the experimental chamber.

The theoretical FWHM of the focal spots at the output of the monochromator and the experimental results are compared in Table 5.2. The theoretical values are obtained by summing quadratically the diffraction contribution  $D(\lambda)$ , the geometrical contribution  $G(\lambda)$ , and the image broadening  $S(\lambda)$  due to the spectral width of the source dispersed by the monochromator:

$$\text{FWHM}(\lambda) = \sqrt{D(\lambda)^2 + G(\lambda)^2 + S(\lambda)^2} = \sqrt{\left(\frac{\lambda q}{\Phi \cos \beta}\right)^2 + \left(\Delta S \frac{\cos \alpha q}{\cos \beta p}\right)^2 + \left(\Delta \lambda \frac{\sigma q}{\cos \beta}\right)^2}$$

where  $\Delta S$  and  $\Delta \lambda$  are, respectively, the FWHM size and the spectral width of the source and  $\Phi$  is the grating diameter. The theoretical values have been calculated assuming  $\Delta S = 70 \mu\text{m}$  for all the cases,  $\Delta \lambda = 1 \text{ nm}$  for the laser diode source emitting at 850 nm, and  $\Delta \lambda \approx 0$  for the HeNe lasers emitting at 543 nm and 633 nm. The experimental data are in good agreement with the theoretical prediction.

Wavelength [nm]	Theoretical/measured FWHM ( $\mu\text{m}$ )		
	Internal	External	Zero
543	124.8/140.4	337.0/327.6	186.4/208
633	136.5/161.2	426.7/436.8	211.4/234
850	177.4/202.8	833.5/811.2	273.7/296.4

Table 5.2 Theoretical FWHM of the focal spots at the output of the monochromator compared with the experimental results



### 5.2.3.1. Time-delay compensated monochromator (TDCM): development and tests

As previously reported a limit of a fixed grating is the pulse-front tilt that gives rise to a difference in the lengths of the optical paths of the rays, due to the diffraction itself, see Figure 5.20. We demonstrated the possibility of overcoming this problem realizing a Time-delay compensated monochromator TDCM based on the use of two active gratings in grazing-incidence. The experimental proof of principle was performed in the near infrared with a Ti-Sapphire laser at 800 nm with a pulse length of 60 fs, since at this wavelength the spatial, spectral and temporal characterization of the light pulses can be easily achieved. The setup of the monochromator consists of an entrance slit, an intermediate slit and two active gratings placed as shown in Figure 5.33. The design parameters are listed in Table 5.3.

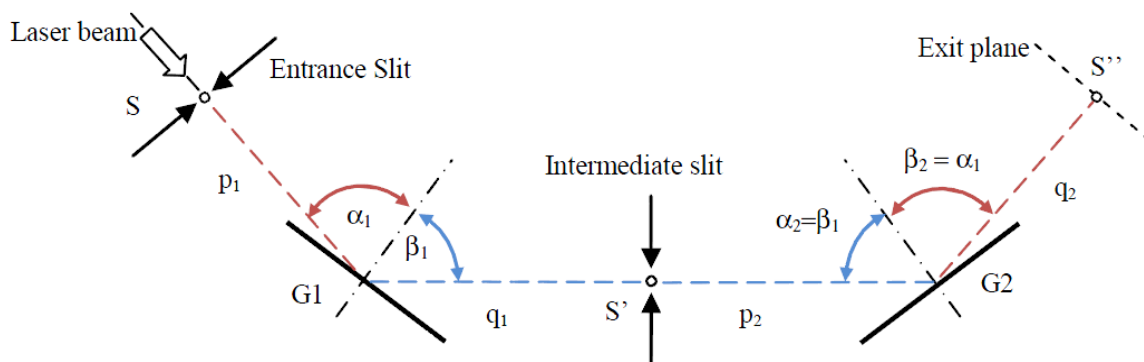


Figure 5.33 Scheme of the TDCM monochromator: S is the source, S' the image of S in the intermediate plane, that is the focal plane of G1; S'' is the image of S' at the exit plane, that is the focal plane of G2;  $p_{1,2}$  and  $q_{1,2}$  are respectively the lengths of the entrance and exit arms of G1,2;  $\alpha_{1,2}$  and  $\beta_{1,2}$  are respectively the incidence and diffraction angles.

$p_1 = q_2$	mm	300
$q_1 = p_2$	mm	500
$K = \alpha_1 + \beta_1 = \alpha_2 + \beta_2$	deg	155
groove density	$\text{mm}^{-1}$	25
Radius and applied voltage @800 nm	mm, V	1850, 150
Grating diameter	mm	15

Table 5.3 Parameters of the Time-delay compensated monochromator TDCM

As previously reported, the wavelength selection is performed through the rotation of the gratings, following the equations:

$$\alpha_1 = \frac{k}{2} + \text{asin} \left[ \frac{m\lambda\sigma}{2\cos(k/2)} \right], \quad \alpha_2 = \frac{k}{2} - \text{asin} \left[ \frac{m\lambda\sigma}{2\cos(k/2)} \right]$$

where  $K$  is the subtended angle,  $\lambda$  the wavelength,  $\sigma$  the grating groove density and  $m$  the diffraction order of G1. G1 is rotated to diffract and focus the desired wavelength on the intermediate plane, G2 is consequently rotated to focus the radiation at the exit plane and compensate for the pulse-front tilt given by G1. The grating radii  $R_{G1}$  and  $R_{G2}$  have to be modified according to the equation:

$$R_{G1} = R_{G2} = (\cos \alpha_1 + \cos \beta_1) \left( \frac{\cos^2 \alpha_1}{p_1} + \frac{\cos^2 \beta_1}{q_1} \right)^{-1}$$

which is the condition to cancel the spectral defocusing. The groove density is constant, therefore, when the surface is bent according to the last equation, the groove density will also be changed. It can be calculated that the variation of the total length of the surface induced by the piezo-actuator when changing from a plane to a sphere with a curvature of few meters is about 10  $\mu\text{m}$  for a grating that is 15-mm long. Therefore, the effect on the variation of the groove density is totally negligible.

The compensation of the pulse-front tilt requires that the two stages of the monochromator are operated in opposite orders, either (G1 internal/G2 external) or (G1 external/G2 internal). Among them, the configuration that has been realized is the G1 internal/G2 external.

The compensation of the pulse-front tilt operated by the TDCM has been demonstrated using a Michelson interferometer in which one arm is equipped with an additional folding mirror [53]. The operation of a standard Michelson interferometer on a pulse with front-tilt  $\Delta t$  is shown in Figure 5.34(a). The two arms act symmetrically on the pulse and the interference fringes appear uniformly at the output on the whole beam spot. On the other hand, the modified configuration presented in Figure 5.34(b) flips the left and the right side of the pulse in one arm of the interferometer and the fringes are observed only in the portions of the two pulses that are overlapped. The measurements are shown in Figure 5.35. The upper row refers to the noncompensated (G1 internal/ G2 zero-order) configuration. As can be clearly seen in the figure, by changing the delay between the two arms of the interferometer, one observes the interference fringes moving along the section of the beam. This is a clear indication of the presence of pulse-front tilt, that is expected to be about 1 ps in good agreement with the experimental results. On the other hand, the compensated configuration (G1 internal/G2 external) does not show any pulse-front tilt; indeed as shown in lower row of Figure 5.35, the intensity of the interference pattern is modulated as a function of the interferometer delay but the fringe envelope does not change position with the delay.

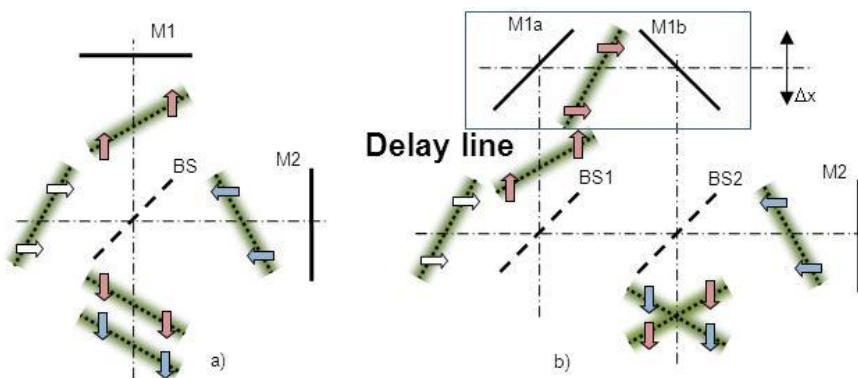


Figure 5.34 Comparison between a standard Michelson interferometer (left) and the modified version used to measure the pulse-front tilt (right).

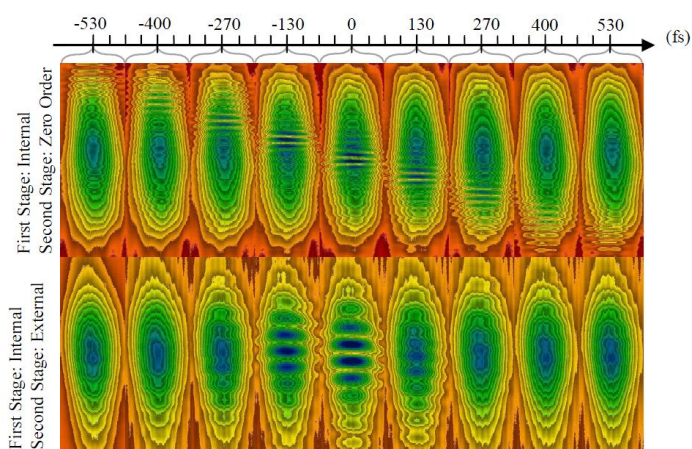


Figure 5.35 Interference fringes acquired using the interferometer for front-tilt detection. Upper row: non-compensated configuration. Lower row: compensated configuration.

#### 5.2.4. Blazed grating

The final device working as a XUV monochromator was realized through the fabrication of blazed gratings on the top a bimorph deformable mirror consisting in a flat silicon substrate glued to a piezoelectric (PZT) disc. The grating initial curvature was spherical with a radius of -2m and the PZT could change its radius of curvature depending on the voltage that is applied to its electrodes, i.e between -150V / 500V. The grating, with a lines density of 600 lines/mm and a blaze angle of 6.4-6.7°, was obtained by nanoimprint lithography NIL on spin coated GZ system film. The master was a PMMA plane ruled reflection grating, with dimensions of 26 x 26 x 6 mm, 600 grooves per mm, 7° nominal blaze angle and coated with a gold coating. The reflection gratings are blazed for specific wavelengths and generally have high efficiency at those wavelengths and are especially useful in systems requiring high resolution.

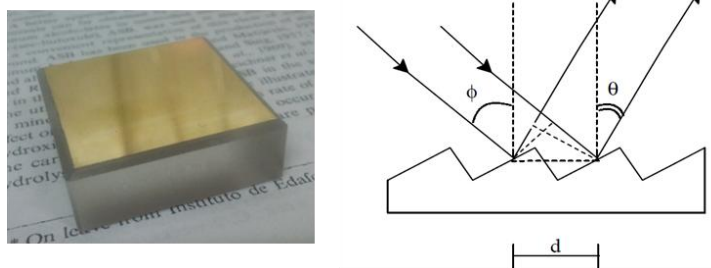


Figure 5.36 Master used for the realization of the deformable blazed grating through NIL process: PMMA blazed grating covered with Au coating; on the right: scheme of the blazed reflection grating.

Before each replication, in order to avoid the master sticking to the film, the stamp was silanized in vacuum with octadecyltrichlorosilane at 150°C, putting the master at around 5 cm from the silanizing precursor. Octadecyltrichlorosilane (Figure 5.37) is an amphiphilic molecule consisting of a long-chain alkyl group (C<sub>18</sub>H<sub>37</sub>-) and a polar head group (SiCl<sub>3</sub>-), which forms self-assembled monolayers (SAMs) on various substrates [54].

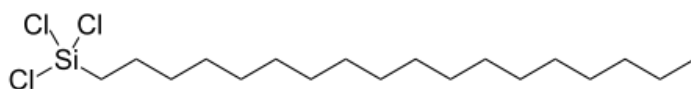


Figure 5.37 Octadecyltrichlorosilane molecular formula

The GZ solution 100g/l was spin coated at 4000 rpm for 30s reaching a film thickness of 1.7μm. In order to improve the film quality (in terms of bubbles and striatures forming during spin coating) the deposition was done by filtering the GZ sol through a 0.2μm filter and spin coating the films by applying an acceleration ramp of 2s before reaching the final speed of 4000rpm.

The NIL procedure was conducted by applying a pressure of 15-30 bar between master and film for 5min at RT and 15min at 80°C, Figure 5.38. The nanoimprint temperature was maintained below 100°C (up to 80°C) in order to avoid the deformation of the PMMA master, whose glass transition temperature is around 105 °C. The obtained blazed grating was then cured at 150°C for 15min and coated with sputtered Au (~100nm) in order to enhance the reflection efficiency.

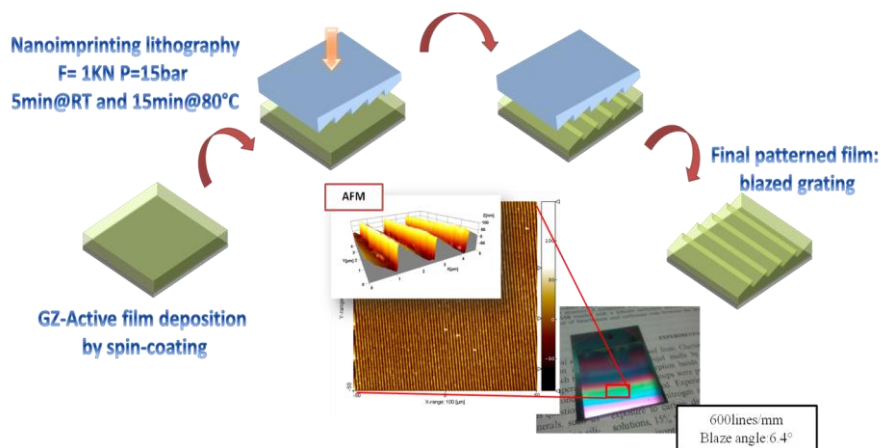


Figure 5.38 Scheme of the NIL process. In the inset: picture and AFM image of the obtained blazed grating

Focusing measurements were performed using the Spherical Grating Monochromator for 5-45 nm reported in Figure 5.39 and Figure 5.40 and operating in  $10^{-5}$  mbar vacuum: a Manson source for the range 5-25 nm with a Hollow cathode lamp suitable for the range 25-45 nm as XUV emitting lamps, a toroidal focusing mirror that refocalize the monochromatized radiation on the center of the experimental chamber, where a sample should be placed, and finally a channel electron multiplier detector (CEM) that collect the reflected light.

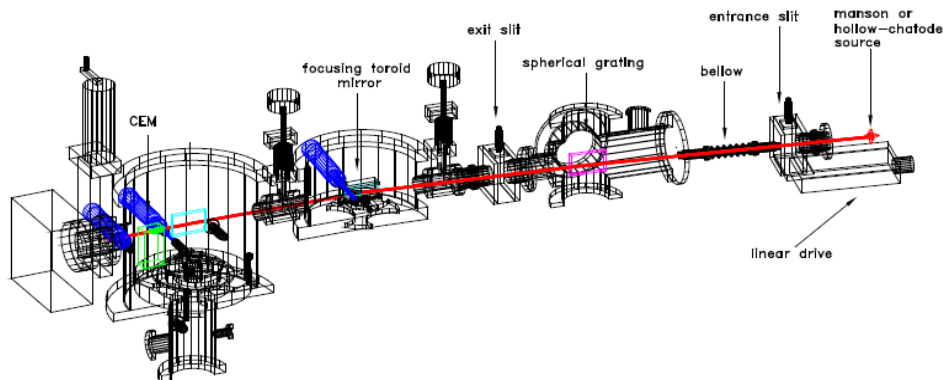


Figure 5.39 Scheme of the Spherical Grating Monochromator for 5-45 nm used for the adaptive grating characterization working in the XUV

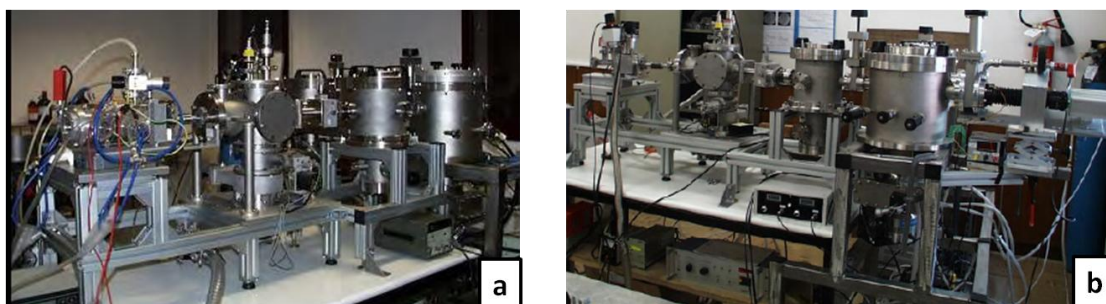


Figure 5.40 The Spherical Grating Monochromator adopted for the focusing measurements: (a) Hollow cathode lamp and (b) experimental chamber

The first results were obtained at the second order of 30.4 nm (diffraction efficiencies around 20%, see Table 5.4) in the configuration with entrance arm around 50 cm and 1 m. The flux of photon collected by the channel electron multiplier detector (CEM) changes as a function of the voltage applied to the PZT showing the focusing capabilities of the blazed diffraction grating working in the XUV spectral region.

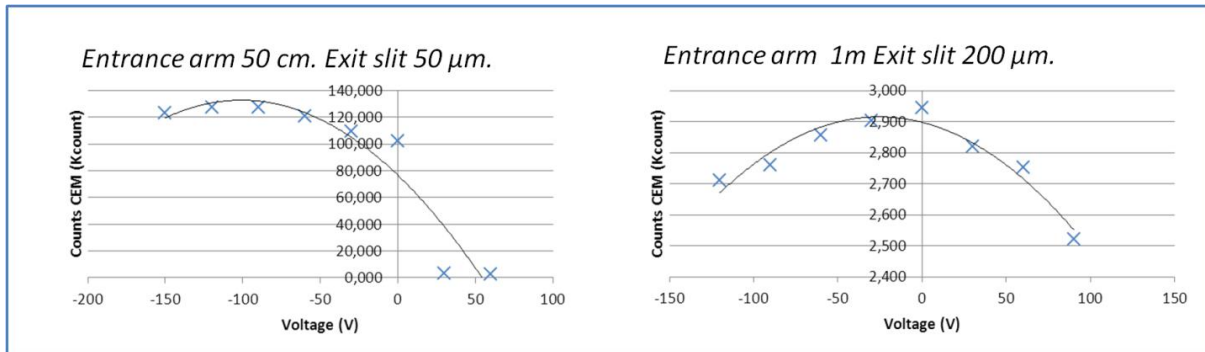


Figure 5.41 Focusing capabilities of deformable blazed grating working with a 30.4nm wavelength: the entrance arm is changed from 50cm to 1m

		0 order	1st order	2nd order	3rd order	4th order
		Efficiency [%]	Efficiency [%]	Efficiency [%]	Efficiency [%]	Efficiency [%]
30.4	5 deg.	30,87	12,35	10,43	2,01	0
	10 deg.	8,84	13,77	19,47	7,18	0,52
46nm	5 deg.	23,61	11,03	13,01	9,46	1,81
	10 deg.	2,9	5,6	14,84	20,22	8,63

Table 5.4 Diffraction efficiencies of the adaptive grating working with 30.4 and 46 nm wavelengths

In conclusion, the main advantage of a configuration with active gratings is the great flexibility to choose the parameters, such as the included angle and the entrance and exit arms, that better match the performance of the monochromator in the spectral interval of operation. Indeed it is possible to increase/decrease the length of the monochromator arms to achieve higher/lower spectral resolution without changing the gratings, which generally are the most expensive components of the monochromator. Furthermore, active gratings directly realized on a plane substrate, with directly patternable advanced resists, are definitely less expensive than conventional gratings realized on toroidal surfaces through the traditional lithographic process and pattern transfer steps.

### ***5.3. Micro- and nano- inserts for micro- injection moulding***

With the rapid development of micro-engineering technologies there is an increasing trend towards product miniaturisation. As already mentioned, micro and nano structured surfaces are present in many everyday life fields and covers a fundamental role in several domains of research, including microelectronics, photonics, microfluidic applications and sensors development. Therefore, on the technological side the development has moved very fast, primarily driven by the need of the electronics industry to create smaller and smaller chips with still larger capacity.

For all technologies, however, developing manufacturing systems that make it possible to produce micro and nano devices at a reasonable price and in large numbers in order to create the operational basis for an industrial production is a continuously increasing challenge. Innovation within the field of micro and nano technology is to a great extent characterized by cross-disciplinary factors and competences, e.i. physics, biology, medicine and engineering have to be united in a common development process. In fact, the ability to integrate into the product development phase considerations regarding materials, processes and production technology and the possibility to exploit the advantages brought about by nano and micro technologies will be the core competence of the companies in future. Therefore, if micro products have to be introduced to a large market it is necessary to develop materials, processes and production technologies that can support an industrial production. Thus it is not only a question of downscaling existing processes and technologies to comprise smaller sizes of components, but in some cases the development of totally new production technologies to replace the conventional processes is necessary. Recently, the mass production with high replication accuracy of polymer parts having micro and nano features on the surface has gained great interest in the scientific community. Polymers low cost, good biocompatibility, high optical clarity and high impact strength make them important for the production of devices for biology, micro-fluidic systems and optics or, for example, of DVD discs used for high-density data storage. To pursue the above discussed goal nanoimprint lithography and hot embossing techniques were explored thanks to their ability to produce patterns with very high resolution and great precision [55], but with low throughput.

Injection moulding is an already industrially consolidated platform for low-cost fabrication of polymer items in large numbers. In the late eighties micro injection moulding technology was firstly introduced from conventional injection moulding in order to satisfy the specific functional and technical requirements of new emerging micro-structured products. Since then,



the micro injection moulding evolution has been considered a process of high potential for fast and accurate mass replication of polymer parts with micro-features, allowing simultaneous complex shaping of the bulk and surface structures in a wide range of polymer materials [<sup>55,56,57</sup>]. Generally, in injection moulding the polymer material is heated and melted and then forced into the tool cavity using high pressure. Usually the tool temperature is relatively low compared to the material. The material solidifies under a maintained pressure before it is ejected out of the tool. In micro injection moulding with respect to traditional injection moulding process, elevated tool temperatures, a cooling of the tool after material injection, prior evacuation of the tool are necessary and the structured surface highly depends on the thermo-rheology of the polymer. Tool temperature was found to have more effect on product quality than melt temperature. Holding pressure also influences the product quality since increased pressure improves mould filling. Moreover, because of the small parts size, many cavities can be implemented into one tool in this way making the process cost effective. Therefore, the replication of micro/nano-scale features also poses challenges for the tooling technologies and a durable master mould with well-fabricated micro/nano-scale structures is a critical point for mass production with the micro injection moulding process. However, competitiveness in a market characterized by low added value products can be achieved reducing technological investments, specifically the ones related to mould realization. The manufacture of the mould generally relies on manufacturing technologies that can create the necessary micro structures (e.g. milling, laser machining, electroforming) [<sup>58,59</sup>]. However, suitable engineered materials need to be developed in order to realize easy and cheap micro and nanostructured inserts as alternative inserts to the metallic tools for micro injection moulding process.

We explored the possibility of fabricating micro- and nano- injection moulding stamps by patterning both the developed Zirconia-based hybrid organic-inorganic sol-gel systems on flat metallic surfaces. The main advantages of using these materials for inserts fabrication are:

- the easier realization through the direct patterning of films with respect to conventionally used micro-machining of metallic bulk
- the possibility of controlling the desired properties of the masters, such as superior mechanical resistance, chemical stability and low thermal dispersion that allows to maintain higher the temperature of the stamps during replication process with respect to metallic materials, thanks to the flexibility of hybrid materials



- the possibility of realizing several structures with no grain size limitations to the final resolution and a better surface finishing, typical problems of metallic insert and of some micro machining tools.

Although many different structures can be realized on the presented HOI systems through UV and nanoimprint lithography in order to obtain micro and nano structured polymer surfaces for various purposes (i.e. biology, optics, medicine, microfluidic devices), we focalized our studies on the development of an industrially viable processes for the realization of moulded polystyrene micro- and nano-patterns that induce mesenchymal stem cells differentiation to osteoblasts for bones regeneration. In particular the stamps fabrication was inserted in the contest of “Nanobones” project in collaboration with the *Laboratory for Precision and Micro Manufacturing (Te.Si.)* of Rovigo and the *Faculty of Pharmacy* of University of Padova, see Scheme 5.3.



Scheme 5.3 Micro- and nano- inserts realization is inserted in the “Nanobones” project in collaboration with *Laboratory for Precision and Micro Manufacturing (Te.Si.)* of Rovigo and the *Faculty of Pharmacy* of University of Padova

### 5.3.1. Stamp inserts realization

The idea of using directly patternable hybrid materials for micro-injection moulding realization arose from the need for easily obtainable inserts to be used for replicating micro- and nano- structured surfaces, demonstrated by the Laboratory for Precision and Micro Manufacturing (Te.Si.) of Rovigo. Different HOI systems have been tested for such a purpose but the best results so far have been obtained with Zirconia based systems developed and optimized in order to be patterned with UV lithography (TMSPM-Zr system) and nanoimprint lithography (GZ system) depending on the final required structures resolution.

The chosen geometry is cylindrical since polystyrene pillars with different diameters ( $\emptyset$ ) and centre to centre distance (I) have to be the final outcome of the I $\mu$ M, according to the work of Kolind et al. [60] that shows how the pillars diameter and pitch rather than the single pillar shape influence the cells growth. Therefore the realization of both the UV mask and the

nanoimprinting stamps was the first step of the micro- and nano- fabrication process. We ordered the UV mask with the structures geometries reported in Figure 5.42, and the nanometer scale silicon master needed for nanoimprint lithography to LaNN (Laboratory for nanofabrication of nanodevices) (Figure 5.43).

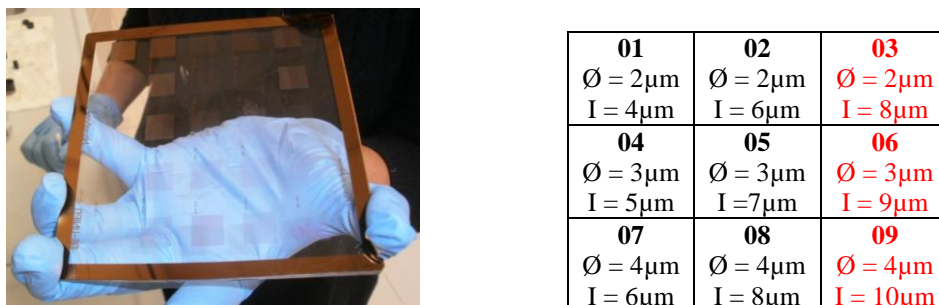


Figure 5.42 on the left: UV mask picture; on the right: structures size and pitch realized on the mask

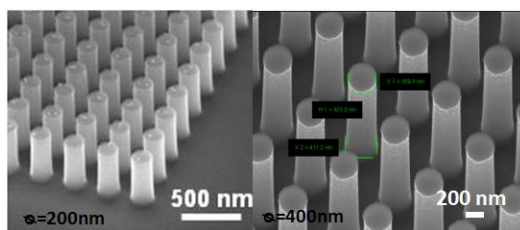


Figure 5.43 On the left: silicon master with Ø=200nm and I=400 nm; on the right: silicon master with Ø=400nm and I=800 nm for nanoimprint lithography process

As it will be discussed below, we firstly realized the following structures geometries:

- 2 µm diameter with 8 µm centre to centre distance (Ø2 – I8)
- 3 µm diameter with 9 µm centre to centre distance (Ø3 – I9)
- 4 µm diameter with 10 µm centre to centre distance (Ø4 – I10)
- 200 nm diameter with 400 nm centre to centre distance; h= 400nm
- 400 nm diameter with 800 nm centre to centre distance; h=620nm

### 5.3.1.1. Micro-structured inserts fabrication

TMSPM-Zr system when used as a resist presents a negative behaviour: the exposed areas undergo polymerization and crosslinking (refer to paragraph 5.1.4.2 for FTIR analysis), thus remaining after development.

Since the Hamamatsu Lightningcure LC5 lamp used for film exposure and patterning was not collimated and no mask aligner was available, we first faced some problems of exposure of the films even under the covered structures (smaller the structures more difficult was to

develop the films up to the substrate). In order to reduce this setup issue and lower the exposure time we adopted three expedients: (1) the resist was exposed a shorter time to UV in combination with a milder development (a mixture of Acetone and Ethanol) compared with Acetone (used for example for digital grating development, see paragraph 5.2.3); (2) TMSPM-Zr 110 g/l solution was added with 1%mol (with respect to TMSPM) of IRGACURE 369 photoinitiator in order to compensate the shorter UV exposure; (3) the lamp fibre was approached to the sample up to 2 cm distance. Films were spin coated at 700 rpm for 30s (thickness around 3  $\mu\text{m}$ ) on lapped 39 Ni Cr Mo 3 steel substrates (failure load of 980 - 1180 MPa, hardness HB 180 – 240) with a surface roughness Ra below 0.050  $\mu\text{m}$  (see Figure 5.44).

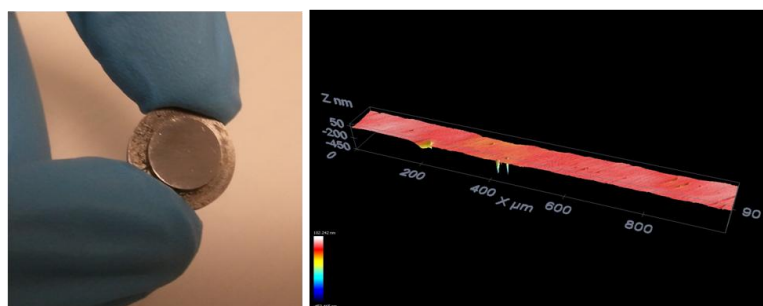


Figure 5.44 Example of flat steel substrate used as inserts for micro-injection moulding and relative surface topography measured with confocal microscopy after lapping.

Holes of 2, 3, 4  $\mu\text{m}$  diameter with height between 1 and 1.6  $\mu\text{m}$  were obtained by exposing the films through the mask with an UV dose of 4  $\text{J}/\text{cm}^2$  and developing the films for 15s in a mixture of Ethanol:Acetone=100:1. The obtained geometries, even if not optimized in terms of structures height (part of the exposed film was removed during development), were first used to optimize the entire process, i.e. replica by injection moulding and stem cells proliferation and differentiation. Higher structures (up to 3  $\mu\text{m}$ ) were obtained by exposing the films to doses up to 9  $\text{J}/\text{cm}^2$ , but results from injection moulding tests are not available so far. After the lithographic step the inserts were thermally treated for 1h at 100°C in order to further promote the resist condensation (of the inorganic component) and polymerization (of the organic part) so as to obtain better mechanical resistance and chemical stability.

SEM pictures (and in the inset some AFM 3D images) of the structures are reported in Figure 5.45.

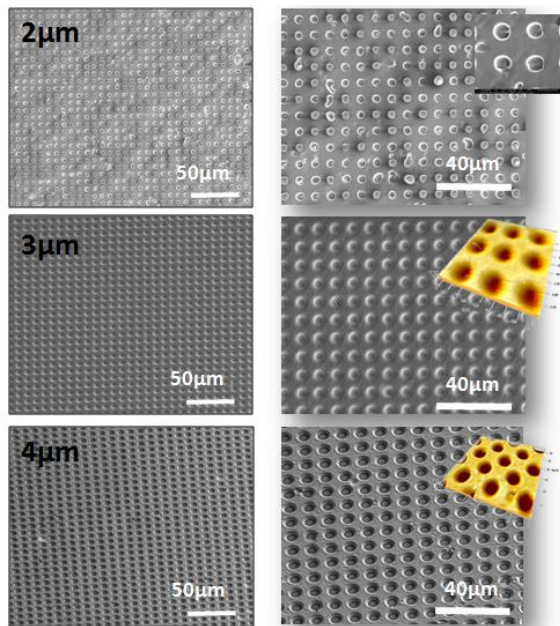


Figure 5.45 Examples of inserts patterned with UV lithography on TMSPM-Zr films with 2 μm, 3 μm, 4 μm structures diameter

5.3.1.2. Nano-structured inserts

The thermally curable GZ system was used as NIL resist in order to realize the nano-structured inserts. Nanoimprint lithography was conducted by applying a pressure of 100 bar for 5 min at RT and 10 min at 120°C between the 8x8 mm<sup>2</sup> Si master and the spin coated (1000 rpm for 5s) GZ film. The patterned films were then treated at 100°C for 1h in order to further condense the structures before using the insert as stamp for micro-injection moulding. SEM images of the obtained inserts are reported in Figure 5.46 and Figure 5.47.

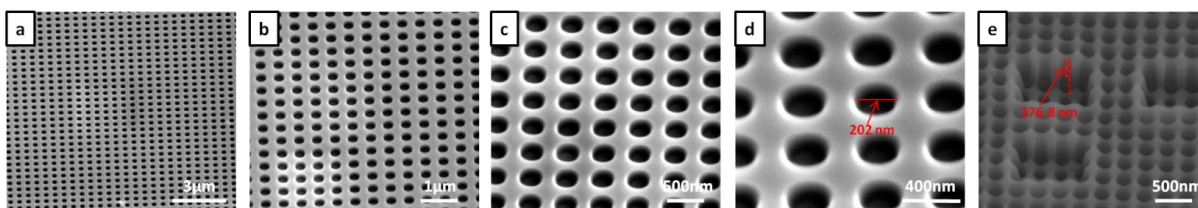


Figure 5.46 SEM images of the nanoimprinted structures of 200 nm diameter with increasing magnification (a-d); cross section image (e)

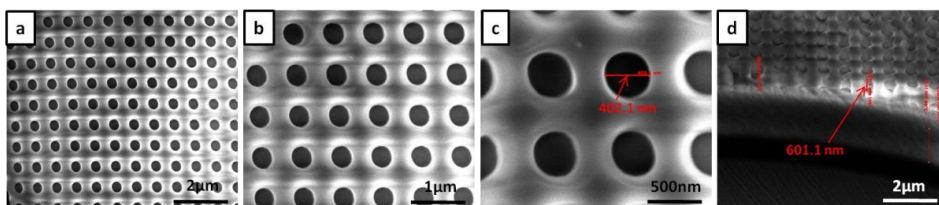


Figure 5.47 SEM images of the nanoimprinted structures of 400 nm diameter with increasing magnification (a-c); cross section image (d)

### 5.3.2. Stamp replication with micro-injection moulding technique

As previously mentioned, micro-injection moulding is the process of transferring a thermoplastic material in the form of granules from a hopper into a heated barrel so that it becomes molten and soft. The material is then forced under pressure inside a mould cavity where it is subjected to holding pressure for a specific time to compensate for material shrinkage. The material solidifies as the mould temperature is decreased below the glass-transition temperature of the polymer. After sufficient time, the material freezes into the mould shape and gets ejected, and the cycle is repeated. A state-of-the-art  $\mu$ IM machine (MicroPower 15, Wittmann-Battenfeld) with a maximum clamping force of 150 kN and a maximum injection speed of 750 mm/s was employed for the moulding process, see Figure 5.48. Unlike conventional injection moulding machines, the MicroPower 15 has an injection system composed of a screw plasticizing unit and a separate plunger injection unit. The plasticizing screw has a diameter of 14 mm and the plunger has a diameter of 5 mm. The mould cavity considered in this study is placed at the end of a trapezoidal cold runner 16mm long, 3 to 2 mm wide and 1.5 thick, connected through a rectangular gate 0.3 mm long, 2.7 mm wide and 0.5 mm thick. The machine characteristics can be found in Table 5.5.



Figure 5.48 On the left: Wittman Battenfeld Micropower 15; on the right: Injection moulding unit

Clamping force	150 kN (15 ton)
Minimum mould height	100 mm
Maximum mould height	300 mm
Dosing screw diameter	14 mm
Injection plunger diameter	5 mm
Injection speed	750 mm/s
Specific injection pressure	3000 bar

Table 5.5 Wittman Battenfeld Micropower 15 characteristics



The obtained micro and nano-inserts were mounted in the micro-injection moulding machine: Figure 5.49 reports the insert where the structured stamp had to be fixed.

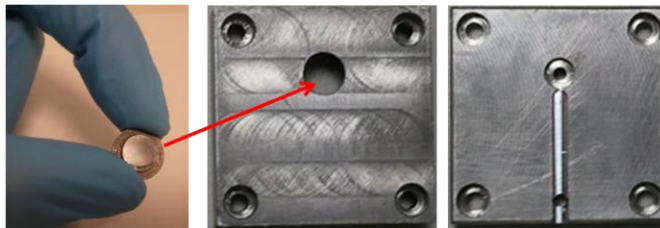


Figure 5.49 Micro structured stamp and final insert that has to be mounted in the micro injection moulding machine

Different polymers or blends were also investigated for maximizing the surface quality in terms of replication, residual stresses and transparency of the final outcome. Since the final aim was to obtain structured substrates for stem cell differentiation the polymeric material chosen was polystyrene (PS), a well-established biocompatible material for on-chip cell culture [61,62]. It is an amorphous, glassy polymer ( $T_g$  around  $100^\circ\text{C}$ ,  $T_f=270^\circ\text{C}$ ) that is generally rigid, relatively inexpensive and transparent and possesses good processing characteristics. It is obtained by radicalic polymerization of styrene monomers: the carbon-carbon pi bond (in the vinyl group) is broken and a new carbon-carbon single (sigma) bond is formed, attaching another styrene monomer to the chain (Figure 5.50).



Figure 5.50 PS polymerization

To investigate the influence of the controllable process variables on the replication capability (screening phase), a three-level full factorial design was carried out. According to literature the following three factors were selected: mold temperature ( $T_{mold}$ ), injection speed ( $V_{inj}$ ) and holding pressure ( $P_{pack}$ ). The range values for each factor (Table 5.6) were defined considering the literature, recommendations of the material supplier and technological limits of the available experimental setup. During injection molding, the melt temperature and the holding time were fixed at  $240^\circ\text{C}$  and 20s, respectively and automatic execution of the process (including part ejection and handling) was performed for each treatment. Firstly, 50

cycles were carried out to stabilize the process. Subsequently, 10 parts obtained from the following 30 cycles have been randomly collected and analyzed.

Factor	Low level	Medium level	High level
$T_{mold}$ [°C]	50	70	90
$P_{pack}$ [bar]	100	150	200
$V_{inj}$ [mm/s]	200	350	500

Table 5.6 Process parameters settings of the screening plan

The analysis of variance (ANOVA) results of the screening plan indicated that the mould temperature markedly affected the replication degree, as reported in literature, while the effect of both injection speed and holding pressure was far less important. The interactions were all negligible. As it can be seen from Table 5.7, in order to maximize the average height of the micro pillars the maximum suitable values for all of the process parameters should be selected, namely  $T_{mold} = 90^{\circ}\text{C}$ ,  $V_{inj} = 500$  mm/s and  $P_{pack} = 200$  bar.

**Estimated Regression Coefficients for pillars height**

Term	Coef	SE Coef	T	P
Constant	0.319720	0.009886	32.341	0.000
V_injection	0.026222	0.005816	4.508	0.000
P_pack	0.094042	0.005816	16.168	0.000
T_mold	0.238988	0.005816	41.089	0.000
V_injection*V_injection	0.007625	0.011470	0.665	0.514
P_pack*P_pack	0.023425	0.011470	2.042	0.055
T_mold*T_mold	0.176858	0.011470	15.419	0.000
V_injection*P_pack	0.002723	0.006503	0.419	0.680
V_injection*T_mold	0.010577	0.006503	1.627	0.119
P_pack*T_mold	0.078952	0.006503	12.141	0.000

Table 5.7 Analysis of variance (ANOVA) results of the screening plan of the controllable process variables

An example of the replica obtained is reported in Figure 5.51.

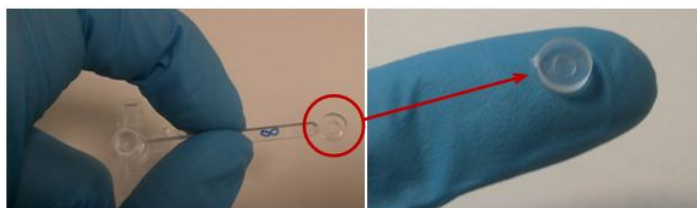


Figure 5.51 image of the final outcome after injection-moulding process

In Figure 5.52 and Figure 5.53 the SEM images at increasing magnifications of the PS replicated surfaces are reported. The injection moulding with the nano-stamps has not been optimized yet, see Figure 5.53, since the polymer doesn't fill all the structures depth: a better optimization of rheology, temperatures and pressures needed is required.

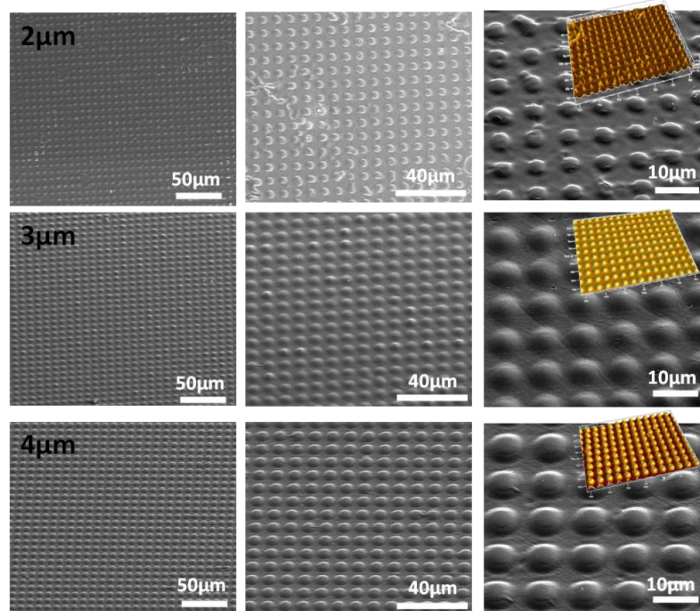


Figure 5.52 SEM images of the PS replicated micro-inserts

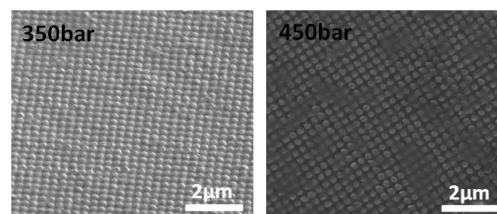


Figure 5.53 SEM images of the PS replicated nano-inserts

### 5.3.3. *Mesenchymal Stem Cells (MSC) differentiation: literature background*

Recently, the interest in the basic understanding of cell–substrate interaction has grown increasingly as it has now been recognized to play a key role in the differences observed in cell behaviour. For this reason it represents a crucial factor in the fields of tissue engineering, drug development and regenerative medicine. Cells in their natural environment are surrounded by nanostructures, for example when contacting with other cells (membranes have nano-size features) or with the extra-cellular matrix (ECM), formed by biomolecules configured in different geometrical arrangements (nanopores, nanofibers, nanocrystals). Cell behaviour is then determined not only via intrinsic cell signals, but also via extrinsic cell



signals coming from the cell–cell contact and the cell–ECM components. These signals can be chemical (growth factors such as cytokines) or mechanical (tensile forces caused by the cell interacting with micro- or nano-structured surfaces). Influencing cell behaviour, from proliferation to differentiation, using the material design of the substrate or implant topography, is a desirable approach for many regenerative medicine applications since a surface provides physical, geometrical, mechanical, and structural signals which act together as an intelligent entity for guiding cellular responses. Therefore, nowadays biomaterials not only have to be bioinert and provide mechanical support, as well as to be bioactive (elicit a desired cell response), but they should also provide reproducible influence on cells at the molecular level.

The effects of a solid substrate elasticity on cells behaviour is well established and studied: a prototypical system is reported in Figure 5.54. A tissue cell is shown attached via receptor-engaged contractile ‘stress fibers’ linked to the cytoskeleton not to rigid plastic or glass but to an elastic substrate of tunable stiffness given by the elastic modulus  $E$ , as it happens in vivo where adhesive ligands mediate attachment and cells are immersed in serum full of nutrients and growth factors. Gels that mimic the elasticity of tissue have been revealed to be significant on adhesion, spread, cytoskeletal organization, and even on the differentiation of human adult derived stem cells (as reported in Figure 5.55).

Therefore the elasticity typical of solid tissue can be as influential to tissue cell structure and function as soluble chemical factors, revealing to exist an important biophysical interplay of cells and their microenvironment [63].

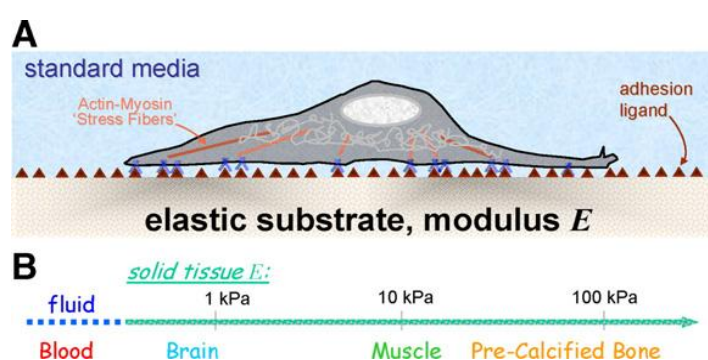


Figure 5.54 Cells on elastic substrates that model tissue elasticity. A) Sketch of a model in vitro environment of a cell on a substrate of elasticity  $E$ , coated with ligands that are specifically recognized by cell adhesion receptors. Force sensing and transduction is mediated by these contacts. Biochemical stimuli are also provided by factors in the surrounding media. B) Elasticity of various solid tissues, and blood as a “fluid tissue” [63].

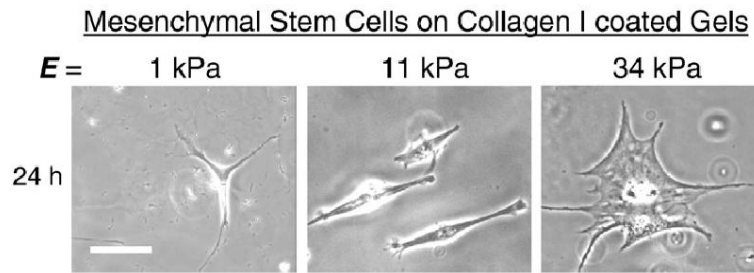


Figure 5.55 Morphology of naive, low passage MSCs (upper panel) 24 h after plating on PA gels of different stiffness closely matches that of cell lineages found within each microenvironment. Naive MSCs are initially small and round but a dominant fraction indicated here (lower panel) develops increasingly branched, spindle, or polygonal shapes within days of plating when grown on matrices with respective elasticities of 1 kPa, 11 kPa, and 34 kPa. Results for mitomycin C treated cells are shown with diagonally-hatched bars. Scale bar is 20  $\mu\text{m}$ .

As an example Y.L. Wang and coworkers, using polyacrylamide (PA) gels in which the Young's modulus  $E$  could be tuned by polymer crosslinking, showed that gel substrate elasticity directly influences how cells spread, establish adhesive contact, migrate, contract, and organize key intracellular structures such as focal adhesions [64].

However, cells respond to physical stimuli provided not only by material intensive property, such as elasticity, but also on extensive factors, such as roughness and topographic geometry. Topography was first identified to influence cell behaviour as early as 1911 when R.G. Harrison observed the guidance of cells along the fibers of a spider's web [65]: the cells followed the fibers of the web in a phenomenon called stereotropism or physical guidance. Since this discovery, numerous studies have been found in literature analyzing cell behaviour on various micro- and nano- features such as lines, wells, holes and more. Investigation into the topographical effect on cell behaviour identified that topography, independently from substrate chemistry, can have not only a strong effect on cell morphology [66,67] (see Figure 5.57), but it can also influence cell adhesion [68], orientation [69] (see Figure 5.56), migration, proliferation [70], vitality [71], cytoskeletal organization, gene expression and differentiation [72]. However, despite the large number of papers published on this topic, significant general trends in cell behaviour are challenging to establish due to differences in cell type, substrate material, feature aspect-ratio, feature geometry and parameters measured. A paper published by Martinez et al. [73] reviewed many works and information on the influence of micro- and nano-structured artificial substrates on cell behaviour, analyzing the possible trends. Moving towards this direction Kolind et al. [60] demonstrated the use of a highly versatile combinatorial screening approach to identify the effect of 169 distinct surface topographies, consisting of pillars, on fibroblast proliferation and mechanical response. Altering the inter-

pillar gap size of the structures a significant change in fibroblast proliferation was observed: larger (4-6  $\mu\text{m}$ ) inter-pillar gap sizes reduced fibroblast proliferation and elicited a strong elongation leading to a disruption of the actin cytoskeleton anchored primarily to focal adhesions located between the pillars, while smaller (1-2  $\mu\text{m}$ ) interpillar gap sizes, on the contrary, caused the fibroblasts to proliferate comparable to cells on a nonstructured surface with cells having a clear actin cytoskeleton attached to focal adhesions located mostly on top of the pillars.

More recently, even the influence of substrate nanotopography on cell gene expression and differentiation has been pointed out. As an example, Dalby et al. [74] demonstrated that a nanopitted topographical PMMA pattern having a fundamentally square geometry, but with a controlled level of disorder, has the ability to promote the differentiation of Skeletal stem cells (SSCs) down an osteoblastic lineage (Figure 5.58)

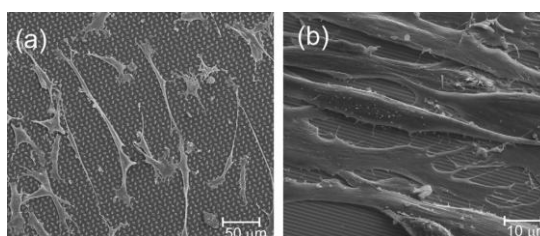


Figure 5.56 Scanning electron microscopic (SEM) images of rat mesenchymal stem cells cultured on (a) non-symmetric PMMA structured surface, feature size 2  $\mu\text{m}$  and (b) surface structured with 2  $\mu\text{m}$  wide lines [73].

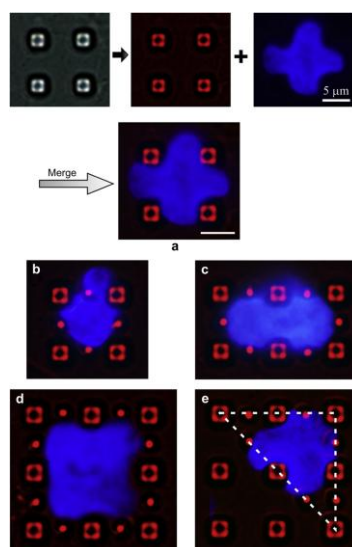


Figure 5.57 Micrographs of BMSCs on the PLGA micropillars of designed pillar patterns. In (a), a process of merging a fluorescent micrograph of a cell nucleus and the converted image of a brightfield micrograph of the corresponding micropillar pattern is demonstrated. Blue and green pixels were filtered in converting the brightfield image. The bars indicate 5  $\mu\text{m}$ . In (b)-(e), some merged images of typical cell nuclei and the associated topographic patterns with mixed micropillars are presented. Blue and red colors indicate cell nuclei and micropillars, respectively. The dashed line in (e) marks the initially aimed region of the material pattern unit. The probabilities of the cell nuclei of specific shapes are summarized in Fig. 8. (For interpretation of the references to colour in this figure legend, the reader is referred to the web version of this article.) [67]

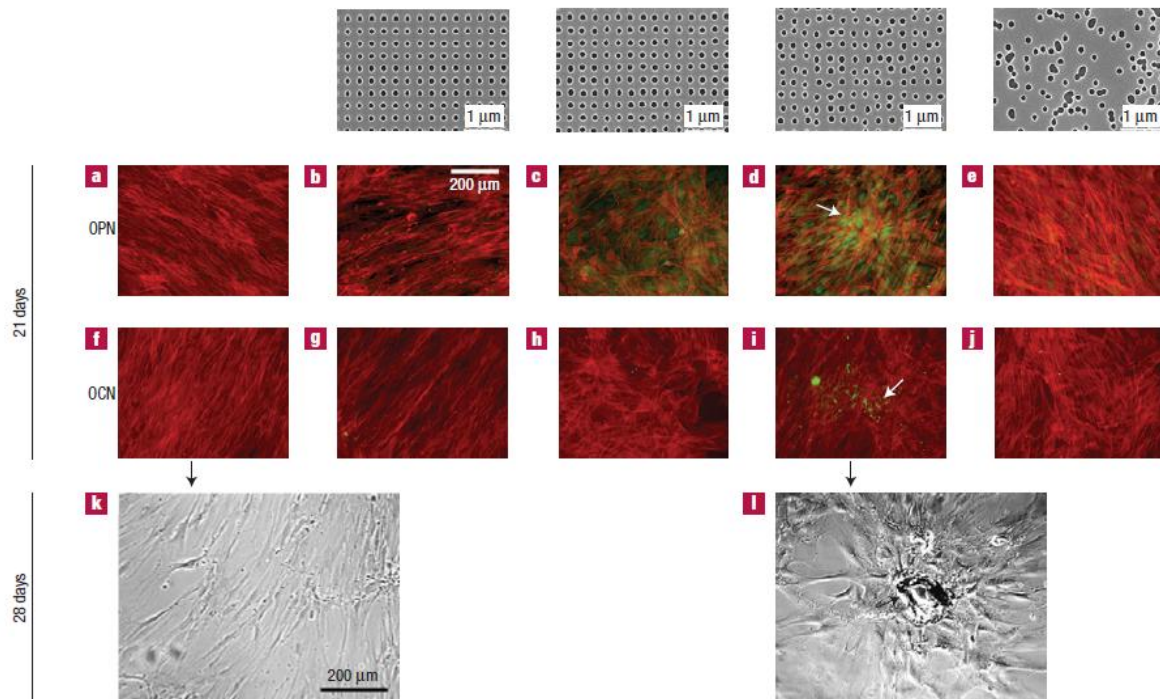


Figure 5.58 OPN and OCN staining of MSC cells after 21 days and phase-contrast/bright-field images of alizarin-red-stained cells after 28 days. The top row shows images of nanotopographies fabricated by EBL. All have 120-nm-diameter pits (100 nm deep, absolute or average 300 nm centre–centre spacing) with square, displaced square 20 ( $\pm 20$  nm from true centre), displaced square 50 ( $\pm 50$  nm from true centre) and random placements. a–j, MSCs on the control (a,f), note the fibroblastic appearance and no OPN/OCN positive cells; on SQ (b,g), note the fibroblastic appearance and no OPN/OCN positive cells; on DSQ20 (c,h), note OPN positive cells; on DSQ50 (d,i), note OPN and OCN positive cells and nodule formation (arrows); on RAND (e,j), note the osteoblast morphology, but no OPN/OCN positive cells. k,l, Phase-contrast/bright-field images showing that MSCs on the control (k) had a fibroblastic morphology after 28 days, whereas on DSQ50 (l), mature bone nodules containing mineral were noted [74].

In the fields of tissue engineering and regenerative medicine, it is then crucial to recapitulate this microenvironment in order to mimic *in vivo* cellular processes and assure an optimized *in vitro* cell and tissue growth. In particular, biomechanical cues presented in the form of micro- and nano-topographies are known to be of utmost importance in regulating cell behaviour. Pillars at the micro- and nano- scale are required to lower the substrate stiffness sensed by the cells with the aim of mimicking the elasticity of biological microenvironment such as brain ( $\sim 0.5$  kPa), intermediate stiffness tissues such as muscle ( $\sim 10$  kPa, transverse and in a relaxed state), and rigid tissues such as pre-mineralized collagenous bone ( $\geq 30$  kPa), as depicted in Figure 5.54B.

In particular we focalized our attention on Mesenchymal stem cells (MSCs) differentiation into osteoblast, since MSCs are multipotent cells that have the capacity to differentiate into stromal lineages such as adipocyte, chondrocyte, and osteoblast cell types by generating the appropriate intermediate progenitors for each through controlling the required matrix elasticity and topography [75]. We took the cue from the work of I.H. Jaafar et al. [76] who

described the injection moulding of nanostructured polystyrene (PS) surfaces and their application in the stimulation of stem cells differentiation. In this work the mold tools were obtained through traditional lithographic techniques, through resist deposition, development and pattern transfer on the silicon substrate with plasma etching. Differently from Jaafar et al.'s work, in order to simplify the overall manufacturing process and more and more approach the final step of industrialization, we realized the  $\mu$ IM stamps with directly patternable engineered materials, as previously reported.

#### 5.3.4. *Mesenchymal Stem Cells (MSC) growth and differentiation on PS micro and nano patterned replica*

We focalized our studies on MSCs differentiation in osteoblast for bone regeneration. Osteoblasts are specialized fibroblasts that secrete and mineralize the bone matrix. Osteoblast differentiation *in vitro* and *in vivo* can be characterized in three stages: (a) cell proliferation, (b) matrix maturation, and (c) matrix mineralization. [77] The matrix maturation phase (b) is characterized by maximal expression of alkaline phosphatase (AP) and once mineralization is completed, calcium deposition can be visualized using adequate staining methods.

Hereinafter there will be reported only the results obtained with the micrometric structured substrates since the nanopatterned replicas have not been optimized yet.

The cells were spread on top of the micro-structured substrates in 96 wells (some flat PS substrates were also used in order to control the process), see Figure 5.59.

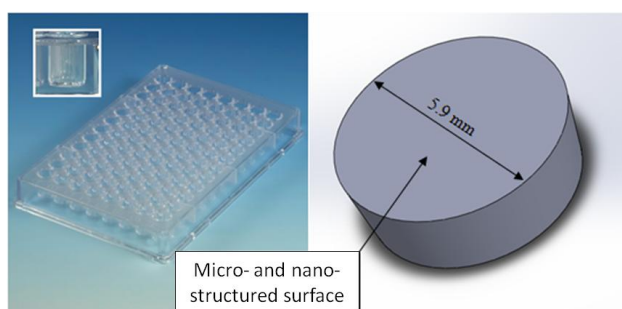


Figure 5.59 The plate with the 96 wells were the micro-structured substrates were inserted for cells growth

In a first step, cell growth monitoring was performed through MTS vitality test. This chromogenic assay involves the biological reduction by viable cells of the tetrazolium compound 3-(4,5-dimethylthiazol-2-yl)-5-(3-carboxymethoxyphenyl)-2-(4-sulfophenyl)-2H-tetrazolium (or MTS) in the presence of the electron coupling agent phenazine methosulfate



(PMS). The formazan product of MTS reduction is soluble in tissue culture medium and presents an absorbance maximum at 490-500 nm in phosphate-buffered saline. This reaction only takes place when mitochondrial reductase enzymes are active, and therefore the conversion can be directly related to the viability of cells in culture. The MTS reagent alone generally results in very low background absorbance values in the absence of cells. MTS tests and measurements of absorbance at 490nm revealed that cells proliferate on every kind of substrates, both on the flat and on the microstructured ones (Figure 5.60).

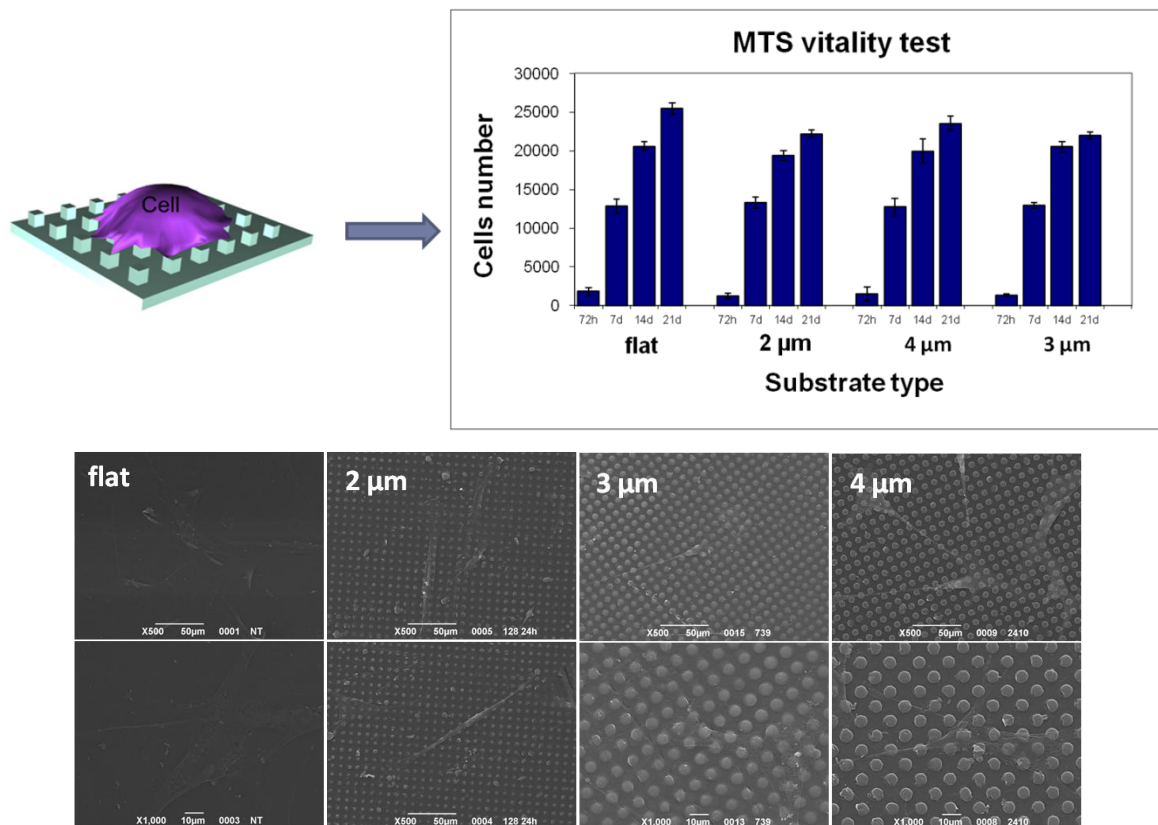


Figure 5.60 Results of cell growth on a flat surface and on 2-3-4  $\mu\text{m}$  PS replica. On the top: the results of MTS Viability Assay. On the bottom: SEM images of the MCSs growth after 24 hours on flat and microstructured surfaces.

However, besides cell proliferation, the other important issue was guiding cell growth through differentiation in osteoblast cells. Osteoblasts can be induced to produce vast extracellular calcium deposits *in vitro*, a process called mineralization. Calcium deposits are an indication of successful *in vitro* bone formation and can specifically be stained bright orange-red using Alizarin Red S. Alizarin tests on our samples revealed calcium formation mainly on cell growth on microstructured substrates, as could be seen in Figure 5.61.

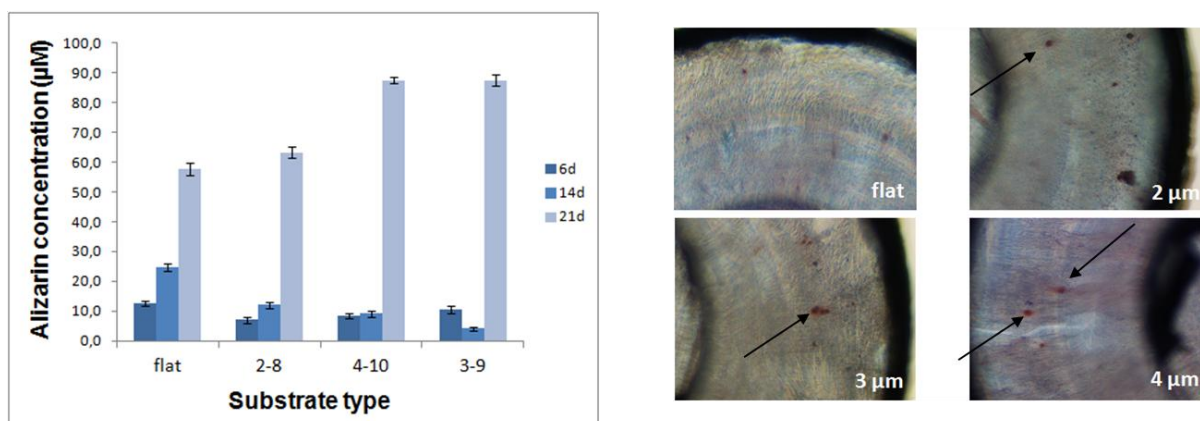


Figure 5.61 Alizarin Red S test on flat and microstructured surfaces (2-3-4 µm) after 6, 14 and 21 days. On the right: examples of optical images showing the presence of calcium (red colored for Alizarin test) on microstructured surfaces.

Proliferation of osteoblasts will be further studied revealing alkaline phosphatase (AP) activity (but the results are not available yet), which is greatly enhanced during *in vitro* bone formation. AP can be easily detected using BCIP/NBT (5-Bromo-4-chloro-3-indolyl phosphate/nitro blue tetrazolium chloride) as a substrate, since it stains cells blue-violet when AP is present.

Summarizing, a simple, cost-effective and high-throughput method of obtaining micro- and nano- patterned polystyrene surfaces for bone regeneration by injection moulding technique on directly patterned sol-gel surfaces inserts was presented. The advantages offered by micro-injection moulding process, that make it commercially applicable with potential for further developments in the future are: full-automation with short cycle times, cost-effectiveness for mass-production process, very accurate shape replication and good dimension control, low maintenance costs of capital equipment when compared to lithographic methods, and applicability of the large amount of industrial information and „know-how available from conventional injection moulding that, within certain limitations, may be scaled down to micro-injection moulding. [78] In particular, thanks to directly patternable resists with high chemical stability and mechanical resistance neither micro machining tools nor lift-off and RIE [79] processes were needed to obtain the injection moulding stamps.

## References

- <sup>1</sup> Simone Dal Zilio, Gioia Della Giustina, Giovanna Brusatin, Massimo Tormen, *Microelectronic Engineering* **2010**, 87, 1143–1146.
- <sup>2</sup> D. Hoebbel, M. Nacken, H. Schmidt, *Journal of Sol-Gel Science and Technology* **2001**, 21, 177.
- <sup>3</sup> G. Schottner, *Chemistry of Materials* **2001**, 13, 3422.
- <sup>4</sup> H. Schmidt, *Journal of Non-Crystalline Solids* **1994**, 178, 302.
- <sup>5</sup> S. J. L. Ribeiro, Y. Messaddeq, R. R. Goncalves, M. Ferrari, M. Montagna, M.A. Aegerter, *Applied Physics Letters* **2000**, 77, 3502.
- <sup>6</sup> G. Philipp, H. Schmidt, *Journal of Non-Crystalline Solids* **1984**, 63, 283.
- <sup>7</sup> G. Schottner, *Chemistry of Materials* **2001**, 13, 3422.
- <sup>8</sup> M. Mennig, K. Endres, M. Schmitt, H. Schmidt, *J. Sol-Gel Sci. Tech.* **1997**, 218, 373.
- <sup>9</sup> P Innocenzi, A. Martucci, M. Guglielmi, L. Armelao, S. Pelli, G.C. Righini, G. Battaglini, *Journal of Non-Crystalline Solids* **1999**, 259, 182.
- <sup>10</sup> P. Innocenzi, G. Brusatin, F Babonneau, *Chemistry of Materials* **2000**, 12, 3726.
- <sup>11</sup> P. Innocenzi, G. Brusatin, M. Guglielmi, R. Signorini, R. Bozio, M. Maggini, *Journal of Non-Crystalline Solids* **2000**, 265, 68.
- <sup>12</sup> P. Innocenzi, G. Brusatin, A. Abbotto, L. Beverina, G. A. Pagani, M. Casalboni, F. Sarcinelli, R. Pizzoferrato, *J. Sol-Gel Sci. Tech* **2003**, 26, 967.
- <sup>13</sup> G. Brusatin, P. Innocenzi, A. Abbotto, L. Beverina, G. A. Pagani, M. Casalboni, F. Sarcinelli, R. Pizzoferrato, *Journal of European Ceramic Society* **2004**, 24, 1853–1856.
- <sup>14</sup> K. Tadanaga, K. Ueyama, T. Sueki, A. Matsuda, T. Minami, *J. Sol-Gel Sci. Techn.* **2003**, 26, 431–434.
- <sup>15</sup> Y. Castro, M. Aparicio, R. Moreno, A. Duràn, *Journal of Sol-Gel Science and Technology* **2005**, 35, 41–50.
- <sup>16</sup> T. Scherzer, *Journal of Polymer Science: Part A: Polymer Chemistry* **2004**, 42, 894–901.
- <sup>17</sup> F. Krausz, M. Ivanov, *Rev. Mod. Phys.* **2009**, 81(1), 163–234.
- <sup>18</sup> G. Sansone, L. Poletto, M. Nisoli, *Nat. Photonics* **2011**, 5(11), 655–663.
- <sup>19</sup> T. Sekikawa, T. Okamoto, E. Haraguchi, M. Yamashita, T. Nakajima, *Opt. Express* **2008**, 16(26), 21922–21929.
- <sup>20</sup> W. Li, X. Zhou, R. Lock, S. Patchkovskii, A. Stolow, H. C. Kapteyn, M. M. Murnane, *Science* **2008**, 322(5905), 1207–1211.



- 
- <sup>21</sup> H. Wang, M. Chini, S. Chen, C.-H. Zhang, F. He, Y. Cheng, Y. Wu, U. Thumm, and Z. Chang, *Phys. Rev. Lett.* **2010**, 105(14), 143002.
- <sup>22</sup> P. Jaeglè, *Coherent Sources of XUV Radiation*, Springer, **2006**.
- <sup>23</sup> Paul et al., 2001; Kienberger et al., 2004; Schultze et al., 2007
- <sup>24</sup> G. Sansone, L. Poletto, M. Nisoli, *Nat. Photonics* **2011**, 5, 655.
- <sup>25</sup> Kenichi L. Ishikawa, Cap.0 High-Harmonic Generation, InTech
- <sup>26</sup> Krzysztof Jakubczak, Cap. 4, High-order Harmonic Generation, InTech
- <sup>27</sup> T. Sekikawa, T. Okamoto, E. Haraguchi, M. Yamashita, and T. Nakajima, *Opt. Express* **2008**, 16, 21922.
- <sup>28</sup> L. Poletto, F. Frassetto, *Appl. Opt.* **2010**, 49(28), 5465–5473.
- <sup>29</sup> L. Poletto, F. Frassetto, P. Villoresi, *J. Sel. Top. Quantum Electron.* **2012**, 18(1), 467–478.
- <sup>30</sup> L. Nugent-Glandorf, M. Scheer, D. A. Samuels, V. Bierbaum, S. R. Leone, *Rev. Sci. Instrum.* **2002**, 73(4), 1875.
- <sup>31</sup> P. Villoresi, *Appl. Opt.* **1999**, 38, 6040.
- <sup>32</sup> M. Ito, Y. Kataoka, T. Okamoto, M. Yamashita, T. Sekikawa, *Opt. Express* **2010**, 18, 6071.
- <sup>33</sup> H. Igarashi, A. Makida, M. Ito, T. Sekikawa, *Opt. Express* **2012**, 20, 3725.
- <sup>34</sup> J. A. R. Samson and D. L. Ederer, *Vacuum ultraviolet spectroscopy*, Academic Press, **2000**.
- <sup>35</sup> R.K. Tyson, *Principles of adaptive optics - Third edition* (CRC Press, Taylor and Francis Group, **2011**).
- <sup>36</sup> E. Steinhaus, S. G. Lipson, *J. Opt. Soc. Am.* **1979**, 69, 478.
- <sup>37</sup> S. Bonora, I. Capraro, L. Poletto, M. Romanin, C. Trestino, P. Villoresi, *Rev. Sci. Instrum.* **2006**, 77, 093102.
- <sup>38</sup> S. Bonora, D. Coburn, U. Bortolozzo, C. Dainty, S. Residori, *Opt. Express* **2012**, 20, 5178.
- <sup>39</sup> E.J. Fernandez, L. Vabre, B. Hermann, A. Unterhuber, B. Povazay, W. Drexler, *Opt. Express* **2006**, 14, 8900.
- <sup>40</sup> J.W. Hardy, *Adaptive Optics for Astronomical Telescopes* (Oxford Series in Optical and Imaging Sciences, **1998**).
- <sup>41</sup> F. Bortoletto, C. Bonoli, P. Panizzolo, C.D. Ciubotaru, F. Mammano, *PLoS ONE* **2011**, 6, e22321.
- <sup>42</sup> A. Roorda, F. Romero-Borja, W.J. Donnelly, H. Queener, T.J. Hebert, M.C.W. Campbell, *Opt. Express* **2002**, 10, 405.

- <sup>43</sup> P. Villorresi, S. Bonora, M. Pascolini, L. Poletto, G. Tondello, C. Vozzi, M. Nisoli, G. Sansone, S. Stagira, S. De Silvestri, *Opt. Lett.* **2004**, 29, 207.
- <sup>44</sup> S. Bonora, F. Frassetto, S. Coraggia, C. Spezzani, M. Coreno, M. Negro, M. Devetta, C. Vozzi, S. Stagira, L. Poletto, *Appl. Phys. B* **2011**, 106, 905.
- <sup>45</sup> D. Brida, C. Manzoni, G. Cirimi, M. Marangoni, S. Bonora, P. Villorresi, S. De Silvestri, G. Cerullo, *J. Opt.* **2010**, 12, 013001.
- <sup>46</sup> O. Solgaard, F. S. A. Sandejas, and D. M. Bloom, *Opt. Lett.* **1992**, 17(9), 688–690.
- <sup>47</sup> C. W. Wong, Y. Jeon, G. Barbastathis, S. G. Kim, *Appl. Opt.* **2003**, 42(4), 621–626.
- <sup>48</sup> R. A. Guerrero, M. W. C. Sze, J. R. A. Batiller, *Appl. Opt.* **2010**, 49(19), 3634–3639.
- <sup>49</sup> S.-J. Chen, C. T. Chen, S. Y. Perng, C. K. Kuan, T. C. Tseng, D. J. Wang, *Nucl. Instrum. Methods Phys. Res. A* **2001**, 467, 298–301.
- <sup>50</sup> H. S. Fung, J. Y. Yuh, L. J. Huang, T. C. Tseng, S. Y. Perng, D. J. Wang, K. L. Tsang, S. C. Chung, *Ninth International Conference on Synchrotron Radiation Instrumentation AIP Conf. Proc.* **2007**, 879, 563–566.
- <sup>51</sup> J. Ma, Y. Liu, T. He, B. Li, J. Chu, *Appl. Opt.* **2011**, 50, 5647-5654.
- <sup>52</sup> T. Namioka, *J. Opt. Soc. Am.* **1959**, 49, 446–460.
- <sup>53</sup> C. Radzewicz, J. S. Krasinski, M. J. la Grone, M. Trippenbach, Y. B. Band, *J. Opt. Soc. Am. B* **1997**, 14(2), 420–424.
- <sup>54</sup> Mingji Wang, Kenneth M. Liechti, Qi Wang, J. M. White, *Langmuir* **2005**, 21, 1848 – 1857.
- <sup>55</sup> M Hecke, W K Schomburg, *J. Micromech. Microeng.* **2004**, 14, 1–14
- <sup>56</sup> N Zhang, J S Chu, C J Byrne, D J Browne, M D Gilchrist, *J. Micromech. Microeng.* **2012**, 22, 065019.
- <sup>57</sup> M. Matschuk, H. Bruus, N. B. Larsen, *Microelectronic Engineering* **2010**, 87, 1379–1382.
- <sup>58</sup> E.M. Kjær, B.B. Johansen, H.H. Sørensen, H.K. Rasmussen, U.R. Arlø, *Proc. of the 1st Euspen topical conference on fabrication and metrology in nanotechnology* **2000**, 1, 259-267.
- <sup>59</sup> L. Alting, F. Kimura, H. Hansen, G. Bissacco, *CIRP Annals - Manufacturing Technology* **2003**, 52, 635-657.
- <sup>60</sup> K. Kolind, A. Dolatshahi-Pirouz, J. Lovmand, F. S. Pedersen, M. Foss, F. Besenbacher *Biomaterials* **2010**, 31, 9182-9191.
- <sup>61</sup> P. M. van Midwoud, A. Janse, M. T. Merema, G. M. M. Groothuis, E. Verpoorte, *Anal.Chem.* **2012**, 84, 3938–3944.

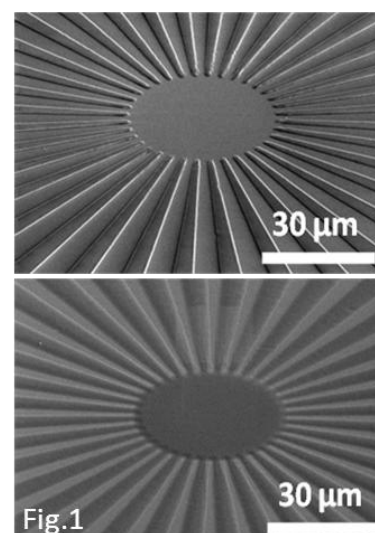
- 
- <sup>62</sup> A. S. Johnson, K. B. Anderson, S. T. Halpin, D. C. Kirkpatrick, D. M. Spence, R. S. Martin, *Analyst* **2013**, 138, 129.
- <sup>63</sup> F. Rehfeldt, A. J. Engler, A. Eckhardt, F. Ahmed, D.E. Discher, *Advanced Drug Delivery Reviews* **2007**, 59, 1329–1339.
- <sup>64</sup> R.J. Pelham, Y.L.Wang, *Proceedings of the National Academy of Sciences of the United States of America* **1997**, 94 (25), 13661–13665.
- <sup>65</sup> R.G.Harrison, *Science* **1911**, 34, 279–281.
- <sup>66</sup> R.G. Flemming, C.J. Murphy, G.A. Abrams, S.L. Goodman, P.F. Nealey, *Biomaterials* **1999**, 20,573–588.
- <sup>67</sup> Z. Pan, C. Yan, R. Peng, Y. Zhao, Y. He, J. Ding, *Biomaterials* **2012**, 33, 1730-1735.
- <sup>68</sup> K. Matsuzaka, X. F. Walboomers, M. Yoshinari, T. Inoue, J. A. Jansen, *Biomaterials* **2003**, 24, 2711–2719.
- <sup>69</sup> J.B. Recknor, J.C. Recknor, D.S. Sakaguchi, S.K. Mallapragada, *Biomaterials* **2004**, 25, 2753–2767.
- <sup>70</sup> B.G. Keselowsky, L. Wang, Z. Schwartz, A.J. Garcia, B.D. Boyan, *J.Biomed. Mater.Res.A* **2007**, 80A(3), 700–710.
- <sup>71</sup> C.S. Chen, M. Mrksich, S. Huang, G. M. Whitesides, D. E. Ingber, *Science* **1997**, 276,1425–1428.
- <sup>72</sup> A. Bruinink, E. Wintermantel, *Biomaterials* **2001**, 22,2465–2473.
- <sup>73</sup> E. Martinez, E. Engel, J.A. Planell, J. Samitier, *Ann Anat* **2009**, 191, 126—135.
- <sup>74</sup> M. J. Dalby, N. Gadegaard<sup>1</sup>, R. Tare, A. Andar, M. O. Riehle,P. Herzyk, C. D. W. Wilkinson, R. O. C. Oreffo, *Nature Materials* **2007**, 6.
- <sup>75</sup> A.J. Engler, S. Sen, H.L. Sweeney, D.E. Discher, *Cell* **2006**, 126, 677–689.
- <sup>76</sup> I.H. Jaafar, M. A. Ammar, S.S. Jedlicka, J. P. Coulter, *Polymer Process Engineering* **2009**
- <sup>77</sup> G.S. Stein, J. B. Lian, *Academic Press*. **1993**, 47–95.
- <sup>78</sup> U. M. Attia, S. Marson, J. R. Alcock, *Microfluidics and Nanofluidics* **2009**, 7, 1-28.
- <sup>79</sup> K. S. Brammer, C. Choi, C. J. Frandsen, S. Oh, S. Jin, *Acta Biomaterialia* **2011**, 7, 683–690.



## Conclusions

The main objective of this thesis project was the simplification and decrease of costs and time of the overall micro- and nano- fabrication process with respect to traditional lithographic procedures, in order to obtain better final features quality. This aim has been achieved through the development of new organic–inorganic sol–gel materials as directly patternable resists possessing engineered and advanced properties, according to their main final applications.

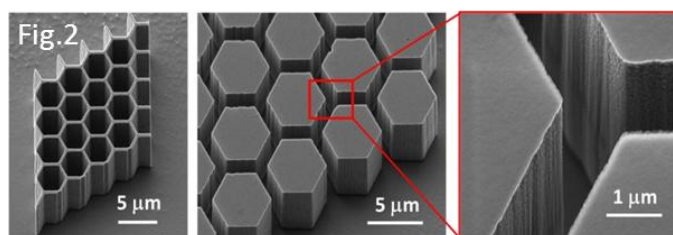
**TiO<sub>2</sub>** was patterned in a one-step process starting from hybrid organic-inorganic (HOI) based sol-gel systems with up to 90% of titania, obtained by hydrolysis and condensation of Ti-isopropoxyde (in situ system) or by loading a sol with 15 nm ex-situ synthesized titania nanoparticles (ex situ system). Minor contents of silica precursors (such as 3-glycidoxypropyltrimethoxysilane, GPTMS) and organic monomers were added to improve film quality, increase layer thickness and improve processing properties (control of rheology and resist contrast). This approach enabled us to fabricate large area titania micro and nanoscale patterns directly through photolithography and nanoimprint lithography without need for transfer processes: gratings with lines width down to 2-3  $\mu\text{m}$  were obtained with the former technique, while features with smallest sizes of 50 nm and up to 630 nm deep were realized with the latter. The novelty of both fabrication approaches lies in the exploitation of titania photocatalytic character, responsible of the structural change of the film when exposed to UV light (during the lithographic process for photolithography and after pattern realization with thermal NIL), which enables to realize almost inorganic and partially crystalline structures, without the need for high temperature treatments. UV-treatment of imprints at doses up to 86J/cm<sup>2</sup> resulted in the loss of organics, but no lateral shrinkage, loss of integrity or aspect ratio was observed. The refractive index of the realized structures could be easily tuned by UV exposure (between 1.74 and 1.8@632nm for in-situ and in the range 1.60-1.64 for ex-situ), an eventual thermal treatment at 300°C or 500°C led to a refractive index up to 2 and 2.1@632nm, respectively.



Deep comprehension of resist structure evolution during optical lithographic process experiments allowed to reveal the high versatility of the in-situ synthesized resist, that showed both positive and negative tone (Figure 1) with lithographic contrast up to 19, simply changing the process parameters.

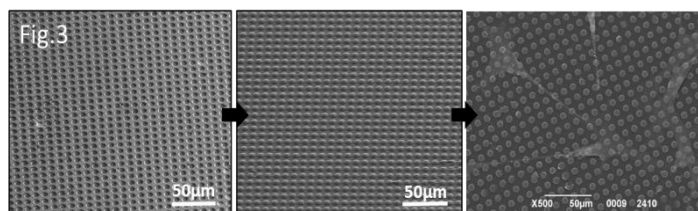
The second spin-on resist developed was  $\text{Al}_2\text{O}_3$ -based, optimized to possess outstanding etching properties; it was developed starting from aluminum-tri-sec-butoxide and a phenyl modified silane precursors. This new resist combines the exceptional properties of alumina as etching mask with the benefit of a simple processability typical of polymeric resists and with the further advantage of being directly patternable by several lithographic techniques: UV, X-ray, Electron Beam, and Nanoimprint Lithography. This spin-on resist is unique, as it is spin coated from a sol whose main part consists of an alumina precursor, which after deposition reaches an adequate condensation degree transforming into an alumina-like organically modified film, without the need to be loaded with a solid fraction (nanoparticles, nanocrystals). Hence, the desired directly patternable etching mask is produced in one step, eliminating the need for complex synthesis or post-processing. The exposure of the spin-coated films to UV light, X-rays and electron beam modify the film degrading the organic component of the system and promoting hydrolysis and condensation of the inorganic network. The deep study and understanding of material modifications and of all the parameters involved during the different lithographic techniques processes allowed to obtain a resist which exhibits both positive and negative tone behaviour, an ultimate achievable resolution below 20 nm for isolated structures (and dense pattern down to 50 nm CD). The striking feature of this material is the selectivity over 100:1 towards the underlying silicon in a fluorine based non cryo-cooled continuous plasma etching process (Figure 2). It is worth

underlying that the use of such material for high resolution deep silicon etching would be time and cost effective compared to pattern transfer materials generally used,



since the etching property exhibited is generally achievable only with more complex lithographic processes using ceramic or metallic intermediate layers (i.e.  $\text{SiO}$ ,  $\text{SiN}$ ,  $\text{SiGe}$ ,  $\text{Cr}$ ,  $\text{Al}$ ).

Finally, hybrid materials belonging to  $\text{ZrO}_2$ -based systems, organically modified with 3-glycidoxypropyltrimethoxysilane (GPTMS) and 3-(Trimethoxysilyl)propyl methacrylate (TMSPM), were developed. GPTMS and TMSPM are organically modified alkoxides containing an epoxy ring and a double bond  $\text{C}=\text{C}$ , respectively, and whose inorganic part is an alkoxy-silane polymerizable via hydrolysis and condensation reactions at room temperature, thus leading to a glass like material. On the one hand, the *GPTMS-modified Zr system* (named GZ) has been used as NIL resist that undergoes densification with thermal treatment. On the other hand, *TMSPM-based Zr* is a photosensitive system that can be used as directly patternable resist for optical lithography since the polymerizable organic function of TMSPM, i.e.  $\text{C}=\text{C}$  bond of the methacrylic group, undergoes radical polymerisation upon UV irradiation (with or without a photoinitiator addition). Both materials were exploited for two unusual and smart applications: the realization of a double-grating monochromator for ultrafast pulses in the XUV region, using micro and nano deformable gratings, and the fabrication of micro- and nano-patterned stamps as alternative inserts to the metallic ones for micro injection moulding, with the final aim of producing micro and nano structured polystyrene surfaces for osteo-inductive differentiation of mesenchymal stem cells (Figure 3).



In conclusion, this thesis work allowed to develop new materials as innovative resists but exploited in unusual ways: not as sacrificial materials but actively working with a specific role or as part of a device. In fact, this research has been carried out in the direction of developing advanced materials that simplify production processes, as in the case of the long and complex lithographic processes generally used for pattern transfer, improving materials and device performances, as in the case of gratings for adaptive optics, and allowing new products development, as for micro and nano injection moulding, otherwise sometimes impossible or extremely expensive.

The experience gained throughout the PhD work in Hymat lab (Padova) together with the possibility of joining different research labs in Italy and abroad have then prepared the ground for starting new studies on materials which have been considered too distant from lithography so far. As future perspective, this new field of research will address to explore different, new and unusual applications, such as MOF lithography through microfluidic channels or imprinting unusual materials like innovative TR-polymers.





## *Future perspectives*

### *a) Ongoing experiments on titania and alumina systems*

The presented thesis work is not meant to be concluded with the reported results. Our aim is to continue on studying the developed materials for different purposes.

As it regards the *titania resist* we have already started to test it with other different lithographic techniques. In fact it has to be kept in mind that the initial goal was to develop resists with several ambitious properties: direct patternability as they already possess the final required properties, patternability with various lithographic techniques in order to widen the range of usability and applications, eventually positive and negative tone behaviour.

Titania resist, in particular the most promising in-situ system, has been already tested with other different lithographic techniques, but the process hasn't been optimized yet; among them:

- two photon photolithography (TPP), a technique that allows creating 3D sub-100 nm structures which would be very complex or even impossible to fabricate with conventional lithographic methods, with the aim of fabricating high refractive index micro-optics components of reduced size on the top of optics fibers for biological investigations [<sup>1</sup>];
- electron beam lithography (EBL) in order to obtain nanostructures;
- interferential lithography (IL) that allows to obtain sub-micron features without the need for optical masks;
- extreme ultraviolet lithography (EUVL).

Figure 1 reports the first results of the obtained lithographies.

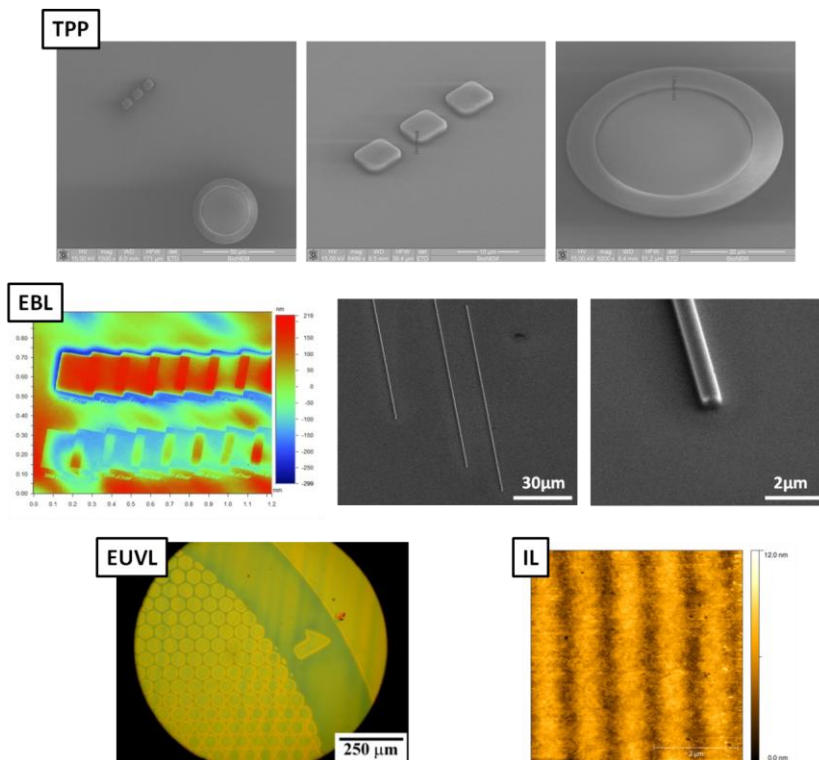


Figure 1. First results of titania patterns obtained with TPP, EBL, EUVL and IL

Alumina system has been tested with EUV lithography as well. The results are reported in Figure 2.

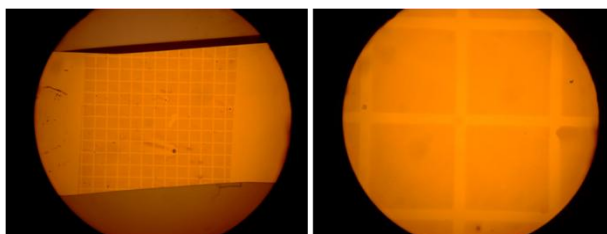


Figure 2. Alumina patterns obtained with EUVL: 2.5× and 20× magnification

Moreover, both titania and alumina resists are being tested as etching masks for FTO with different plasma recipes. Images in Figure 3 show the final pattern that has to be transferred into FTO substrate in order to obtain FTO electrodes.

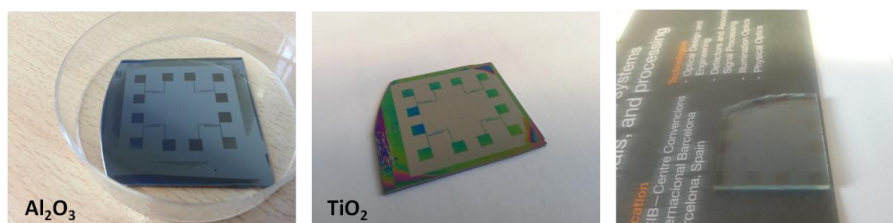


Figure 3. Alumina and Titania etching masks patterns on silicon and on FTO substrate

### ***b) Patterning of smart porous material***

Two different studies were also conducted in collaboration with *Commonwealth Scientific and Industrial Research Organisation (CSIRO) of Melbourne* on the patterning of smart porous material: metal–organic frameworks (MOFs) and TR-polymers.

#### *MOFs growth and patterning*

*MOFs* are a fascinating class of solid-state inorganic–organic hybrid materials. Their huge porosity and the easy tunability of their pore size and shape from the microporous to the mesoporous scale, obtained by changing the connectivity of the inorganic moiety (metal ions or metal-ion clusters) and the nature of the organic polydentate bridging ligands (usually carboxylate, sulfonate, or phosphonate), make them interesting for storage, separation, catalysis, drug delivery, sensors and biomedical applications.

In particular, the majority of research on MOFs so far has been devoted to the facile synthesis of MOFs through pre-synthesized nanocrystals [2,3,4,5,6,7,8], heterogeneous nucleation on different nucleating agents [9,10,11,12] and pseudomorphic replication [13,14,15]. More recently, the development of new efficient protocols to control MOFs positioning and patterning (from microfluidics [16] and contact printing [17] to X-ray [18], optical lithography [19] and imprinting technique [20]) have been demonstrated to be necessary to totally exploit MOF properties and expand MOFs technological applications into miniaturized devices, such as microfluidic or lab-on-a-chip devices [21], which have to be obtained in the fastest, easier, cost-effective method as possible.

We are still studying and investigating a fast nucleation kinetics, high reproducible and technologically scalable synthesis and patterning of metal organic frameworks obtained with a broad band of linkers (terephthalic acid, 2-aminoterephthalic acid, 1,3,5-benzenetricarboxylic acid, 2,6-naphthalene-dicarboxylic acid, 4,4'-biphenyl-dicarboxylic acid, 1,2,4,5-benzenetetracarboxylic acid) by exploiting the heterogeneous MOF formation mechanism on zinc oxide nanoparticles. Figure 4 reports the SEM images of the different MOFs obtained.

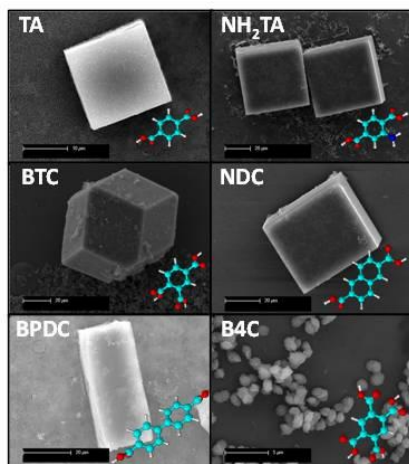


Figure 4. SEM images of the different MOFs prepared with diverse ligands for 1h@95°C, together with the corresponding ligand structures

Moreover, the great advantage of the studied synthesis approach is the possibility of decreasing the MOFs synthesis temperature from 95°C to room temperature with a synthesis time still under half an hour. Figure 5 shows the SEM images and SAXS results obtained at Australian Synchrotron (in terms of nucleating time, i.e. time after the addition of the ZnO NPs at which a SAXS pattern could be collected from the MOF growing solution) of btc-MOFs and nh<sub>2</sub>ta-MOFs synthesized at decreasing temperature.

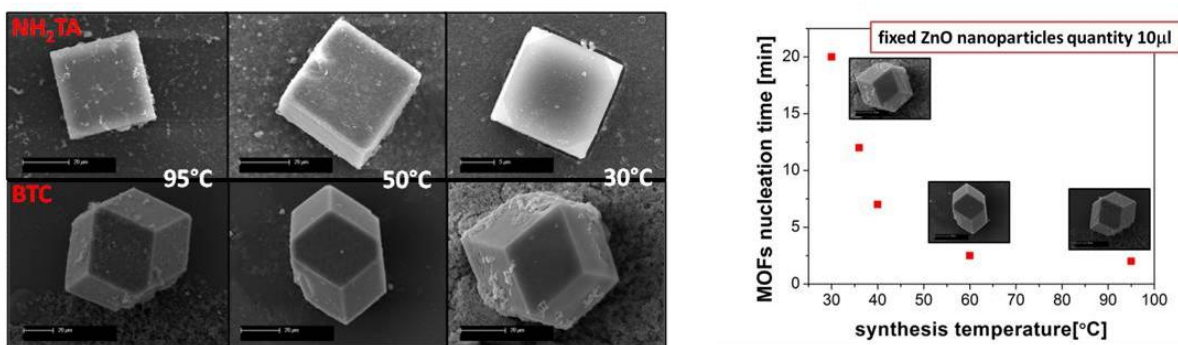
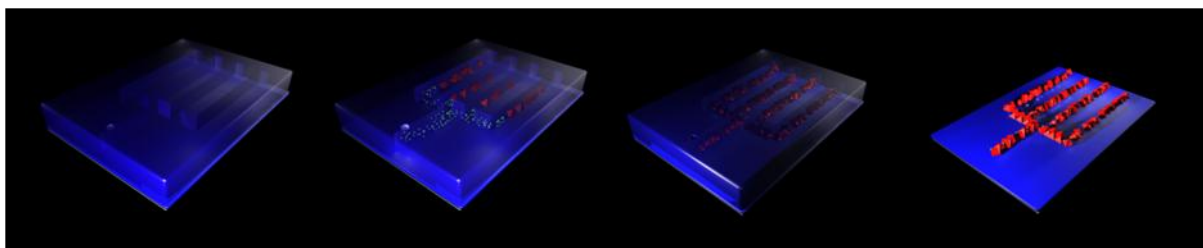


Figure 5. On the left: nh<sub>2</sub>ta-MOFs and btc-MOFs synthesized at different temperatures; on the right: MOFs nucleating time vs synthesis temperature for btc-MOFs and SEM images of the corresponding crystals grown (inset images). The nucleating time is the time after the addition of the ZnO NPs at which a SAXS pattern could be collected from the MOF growing solution.

The strategy of using nanoparticles as nucleating agents has been also used for the positioning and growth of MOF crystals on controlled and selected surface areas of a substrate through injection of the starting MOF solution, added with ZnO NPs, into PDMS microfluidic channels placed in close contact with the substrate, Scheme 1. First results of MOFs patterns are reported in Figure 6.



Scheme 1. Positioning of MOFs (red) by injecting the growth solution added with ZnO NPS into microfluidic channels pressed on a substrate

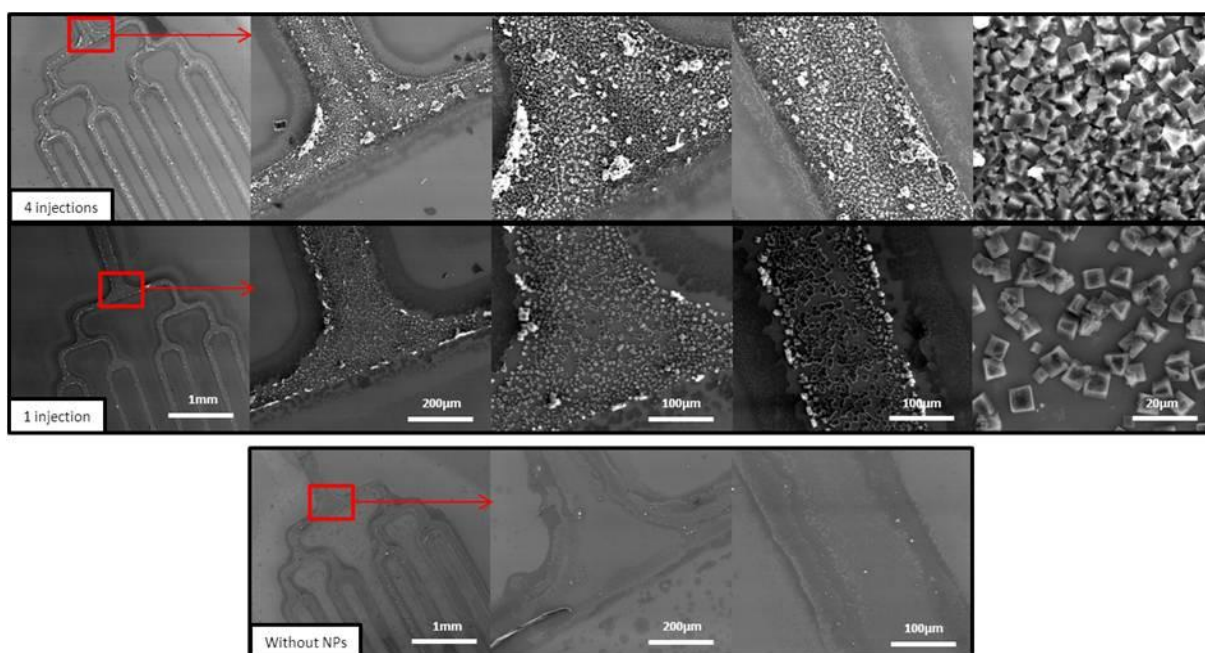


Figure 6. MOFs patterns obtained through several injections of the growth solution into the microfluidic channels of the PDMS mold: from the left increasing magnification of a particular of the pattern. The last image on the right shows the MOFs interconnection after 4 injections. Without ZnO NPS no MOFs formation into the channels can be detected.

### *TR-polymer nanoimprint lithography*

Thermally rearranged (TR) polymers are engineered microporous polymers [22,23] that possess interconnected microcavities in a glassy polymer matrix rendered via a solid-state conversion of polyimide to polybenzoxazole during thermal rearrangement (typically at 450 ° C). [24] This thermal treatment, increasing polymer fractional free volumes and cavity sizes, enhances gas permeation properties and lowers the dielectric constant  $k$  of the polymeric film from 2.1 to 1.6. Therefore, combining TR-polymers with lithography, such as NIL, would provide a simple but powerful method to fabricate micropatterned devices with the unique properties provided by these rigid-rod type polymers [25]. Optimization of NIL was conducted on polyimide films by imprinting with a 200nm-high master possessing several micro- structures.

The best results have been obtained with the following conditions: temperature=270°C, pressure=100bar, Figure 7.

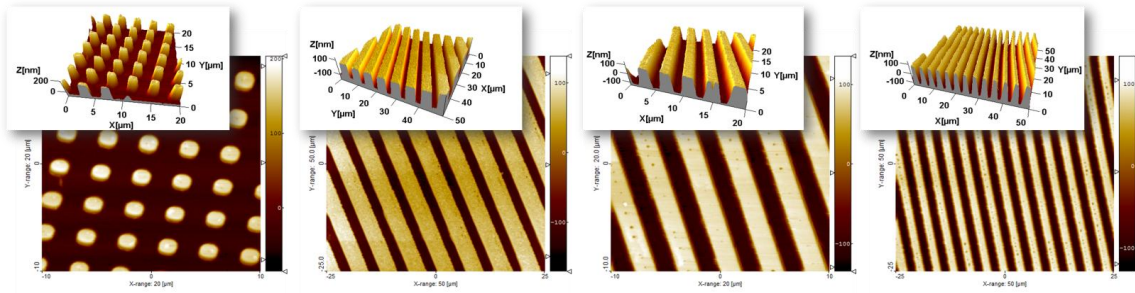


Figure 7 AFM of polyimide nanoimprinted structures (nanoimprint conditions: T=270°C, P=100bar)

## References

- <sup>1</sup> C. Liberale, G. Cojoc, P. Candeloro, G. Das, F. Gentile, F. De Angelis, E. Di Fabrizio, *IEEE Photonics Technology Letters* **2010**, 22(7), 474–476.
- <sup>2</sup> V. Guerrero, Y. Yoo, M. C. McCarthy, H. Jeong, *J. Mater. Chem.* **2010**, 20, 3938–3943.
- <sup>3</sup> Y. Hu, X. Dong, J. Nan, W. Jin, X. Ren, N. Xu, Y. Moo Lee, *Chem. Commun.*, **2011**, 47, 737–739.
- <sup>4</sup> J. Nan, X. Dong, W. Wang, W. Jin, *Microporous and Mesoporous Materials* **2012**, 155, 90–98.
- <sup>5</sup> J. Nan, X. Dong, W. Wang, W. Jin, N. Xu, *Langmuir* **2011**, 27, 4309–4312.
- <sup>6</sup> D. Jiang, A. D. Burrows, R. Jaber, K. J. Edler, *Chem. Commun.* **2012**, 48, 4965–4967.
- <sup>7</sup> P. Horcajada, C. Serre, D. Grosso, C. Boissière, S. Perruchas, C. Sanchez, G. Férey, *Adv. Mater.* **2009**, 21, 1931–1935.
- <sup>8</sup> A. Demessence, P. Horcajada, C. Serre, C. Boissière, D. Grosso, C. Sanchez, G. Férey, *Chem. Commun.* **2009**, 7149.
- <sup>9</sup> D. Buso, K. M. Nairn, M. Gimona, A. J. Hill, P. Falcaro, *Chem. Mater.* **2011**, 23, 929–934.
- <sup>10</sup> D. Buso, A. J. Hill, T. Colson, H. J. Whitfield, A. Patelli, P. Scopece, C. M. Doherty, P. Falcaro, *Cryst. Growth Des.* **2011**, 11, 5268–5274.
- <sup>11</sup> P. Falcaro, A. J. Hill, K. M. Nairn, J. Jasieniak, J. I. Mardel, T. J. Bastow, S. C. Mayo, M. Gimona, D. Gomez, H. J. Whitfield, R. Riccò, A. Patelli, B. Marmiroli, H. Amenitsch, T. Colson, L. Villanova, D. Buso, *Nature Communications* **2010**, 2.
- <sup>12</sup> Z. Xie, J. Yang, J. Wang, J. Bai, H. Yin, B. Yuan, J. Lu, Y. Zhang, L. Zhou, C. Duan, *Chem. Commun.* **2012**, 48, 5977–5979.
- <sup>13</sup> J. Reboul, S. Furukawa, N. Horike, M. Tsotsalas, K. Hirai, H. Uehara, M. Kondo, N. Louvain, O. Sakata, S. Kitagawa, *Nature Materials* **2012**, 11, 717–723.
- <sup>14</sup> W. Zhan, Q. Kuang, J. Zhou, X. Kong, Z. Xie, L. Zheng, *J. Am. Chem. Soc.* **2013**, 135, 1926–1933.
- <sup>15</sup> Y. Yue, Z. Qiao, X. Li, A. J. Binder, E. Formo, Z. Pan, C. Tian, Z. Bi, S. Dai, *Cryst. Growth Des.* **2013**, 13, 1002–1005.
- <sup>16</sup> D. Witters, N. Vergauwe, R. Ameloot, S. Vermeir, D. De Vos, R. Puers, B. Sels, J. Lammertyn, *Adv. Mater.* **2012**, 24, 1316–1320.

- <sup>17</sup> R. Ameloot, E. Gobechiya, H. Uji-I, J. A. Martens, J. Hofkens, L. ALaerts, B. F. Sels, D. E. De Vos, *Adv. Mater.* **2010**, 22, 2685.
- <sup>18</sup> C. Dimitrakakis, B. Marmiroli, H. Amenitsch, L. Malfatti, P. Innocenzi, G. Greci, L. Vaccari, A. J. Hill, B. P. Ladewig, M. R. Hill, P. Falcaro, *Chem. Commun.* **2012**, 48, 7483
- <sup>19</sup> G. Lu, O. K. Farfa, W. Zhang, F. Huo, J. T. Hupp, *Adv. Mater.* **2012**, 24, 3970
- <sup>20</sup> C. M. Doherty, G. Greci, R. Riccò, J. I. Mardel, J. Reboul, S. Furukawa, S. Kitagawa, A. J. Hill, P. Falcaro, *Adv. Mater.* **2013**, 25, 4701–4705.
- <sup>21</sup> P. Falcaro, D. Buso, A. J. Hill, C. M. Doherty, *Adv. Mater.* **2012**, 24, 3153–3168.
- <sup>22</sup> D. Wu, F. Xu, B. Sun, R. Fu, H. He, K. Matyjaszewski, *Chem. Rev.* **2012**, 112, 3959 – 4015.
- <sup>23</sup> N. Du, H. B. Park, G. P. Robertson, M. M. D al-Cin, T. Visser, L. Scoles, M. D. Guiver, *Nat. Mater.* **2011**, 10, 372 – 375.
- <sup>24</sup> H. B. Park, C. H. Jung, Y. M. Lee, A. J. Hill, S. J. Pas, S. T. Mudie, E. Van Wagner, B. D. Freeman, D. J. Cookson, *Science* **2007**, 318, 254 – 258.
- <sup>25</sup> S. H. Han, C. M. Doherty, B. Marmiroli, H. J. Jo, D. Buso, A. Patelli, P. Schiavuta, P. Innocenzi, Y. M. Lee, A. W. Thornton, A. J. Hill, P. Falcaro, *Small* **2013**, 9, 2277–2282.



## *Acknowledgments*

You never walk alone...the greatest things you can achieve are always the result of collaboration and synergy with people around you.

First of all I want to thank Prof. Giovanna Brusatin, not only an enthusiastic far-seeing supervisor and researcher, but also a friend, a sister and...a “mum” as I always love to call her.

I also want to express my sincere gratitude to Prof. Massimo Guglielmi for encouraging me and supporting me from the beginning of this PhD adventure.

A special thanks goes to my mates and friends from Hymat Laboratory, Gioia and Laura, for their useful help, their constant support, their inspiring advices..for the chats and good time together. I also want to thank all the people (PhD students, post-doc., technicians, professors, researchers,...) from “Material group” of Industrial Engineering Department: Michela, Giovanni, Marco B., Marta, Mauro, Laura, Marco S., Marco A., Liz, Ines and people that have already moved to different laboratories abroad (Giulio, Enrico, Giovanni) for being always good friends, even after kilometers of distance. I have learnt a lot from you all!

Thanks also to people from TASC laboratory in Trieste (Gianluca, Alessandro, Massimo) for helping me and collaborate with me for obtaining outstanding results and lithography fabrications: benefiting from your knowledge and help was a great opportunity for me.

Thanks to special collaborators: Stefano Bonora, Vaida Auzelyte, Marco Sorgato, Enrica Guidi and Giovanni Lucchetta for the great research work together.

A special thanks goes to Dr. Paolo Falcaro (and of course his beautiful family!) for the chance to work with him at CSIRO in Melbourne, and to Dr. Luca Malfatti...with them I have learnt what it means playing with science, loving it and enjoying work as a part of life!

The people working at Micro Resist Technology, especially Gabi, Tina and Anna are acknowledged for their hospitality and the support offered to me during my stay in Berlin.

Thanks to “Mouge” Musical company and the fantastic “musical” friends, especially the ones who were really close to me when I went through difficult moments..without Music my life wouldn’t have been the same! Thanks for laughing, crying, being moved from the same great passion!

## Acknowledgments

---

Thanks to all my friends, the ones that are still with me, the ones that have gone..everybody in his own way has helped me to be who I am and to achieve this important result.

A special thanks goes to Claudio for giving me the gift of beautiful moments together, for your love, for believing in me in everything I do, from work to passion, and for supporting me in whatever can make me happy..I love you!

Last but, of course, not least, the greatest thanks goes to my family, my parents and my “fratellino”, for making me feeling really loved and always pushing me to overcome difficulties...without you nothing would have been possible!